



UNIVERSITÀ
DEGLI STUDI
DI PADOVA

Sede Amministrativa: Università degli Studi di Padova

Dipartimento di Ingegneria Industriale

CORSO DI DOTTORATO DI RICERCA IN INGEGNERIA INDUSTRIALE

CURRICOLUM: MATERIALI

CICLO XXXIV

Laser Powder Bed Fusion of Pure Copper and CuCrZr Alloy for Power Exhaustion Solutions

Coordinatore del corso: Ch.mo Prof. Giulio Rosati

Referente curricolare: Prof. Paolo Sgarbossa

Supervisore: Prof.ssa Irene Calliari

Co-Supervisore: Dott. Adriano Pepato

Dottorando : Massimiliano Bonesso

ACKNOWLEDGEMENTS

Several people have helped me during these three (and a half) years of research, and first of all, I would like to dedicate them a few lines.

At the end of my master's degree, I no longer intended to continue my studies. It was only thanks to my supervisor Professor Irene Calliari that I changed my mind. She believed in me and gave me this incredible opportunity, so I sincerely thank her.

Special thanks go to Dott. Adriano Pepato for welcoming me into his research group and for having involved me in multiple projects that have allowed me to grow intellectually and professionally. If I had a research topic, it was only thanks to him.

My sincere thanks go to Razvan Dima, Marco Romanato and all the Mechanics Design group of INFN - Padova for practical support and countless tips. Many thanks also to Loris Ramina and the Mechanics Workshop group for the infinite amount of work they have done for me.

I would like to acknowledge the research group at DII for helping with all the laboratory stuff. Thanks to Alessio Settimi, Claudio Gennari, Luca Pezzato, and Mattia Franceschi. An honourable mention also goes to prof. Simone Mancin for his contribution, without which my research would not have been complete.

I want to thank my colleagues from the DIAM group, especially Giacomo Favero and the *little boys*: Mattia Lago and Marco Marigo. Pietro Rebesan was first a colleague but now is a special friend. His passion and resourcefulness for research made him my role model to become a good researcher.

I could conclude this research project thanks to my loving family, that has always supported me and helped me during difficult moments. Thanks to all my friends for encouraging me during my studies.

Finally, I want to dedicate this thesis to my fiancée Sara who has supported me starting from my first year of university. Your encouragement, care, and patience are the real authors of this thesis. It would not be possible without you.

Massimiliano Bonesso

PREFACE

The work presented in this doctoral thesis was conducted at the Padua Section of the National Institute for Nuclear Physics and at the Department of Industrial Engineering, University of Padua, between October 2018 and March 2022. During this period, the work carried out was funded through two research grants: between October 2018 and May 2021 through the SATELLES project (Call 19739 - collaboration between INFN and the Italian Space Agency) and between July 2021 and March 2022, the DTT (Divertor Tokamak Test) project (Call 23109 - collaboration between INFN and DTT).

Abstract

Additive Manufacturing (AM), also known as three-dimensional (3D) printing, differs from traditional manufacturing methods in that the material is added rather than subtracted to achieve the desired solid geometry. AM procedures are free of the limitations of conventional manufacturing methods, allowing for the creation of unique geometries and intricate interior systems.

The nature and aggregate state of the feedstock and the binding mechanism between the joined layers of material are used to classify AM processes. In AM of metals, a powder feedstock, or more rarely a wire, is fully melted by the energy input of a laser or electron beam and transformed layer by layer into a solid part.

The feedstock material is metal powder in the laser powder bed fusion (LPBF) process, and the energy input is a laser beam. A laser beam scans the powder bed at a predetermined speed selected locations during the procedure, fusing the powder to the solid material underneath. After laser radiation in one layer is completed, the powder bed is lowered by the defined layer thickness, and a new layer of powder is dropped and levelled. The process repeats until the part is entirely built.

State of the art in metal powder bed fusion has progressed to the point that it is transitioning from a quick prototype to production technology. Parts can be fabricated at near full density (99.5%) with mechanical properties equivalent to conventionally produced metals. Therefore, the rapid

manufacturing process needs a thorough understanding of the process itself, the microstructure created by the process parameters, and the qualities of the generated parts.

Every additive manufacturing process has its own set of process parameters, which influence the quality of manufactured components in combination with material properties and environmental conditions. As new technologies and applications develop, the spectrum of metals accessible for use in AM continues to expand. Currently, the most common metallic materials are steels, pure titanium and titanium alloys, aluminium casting alloys, nickel-based super-alloys, and cobalt-chromium alloys.

The main objective of this project is to characterize copper and copper alloys for the LPBF process. The thermal properties of Cu make it ideal for heat exchange applications, and the design freedom provided by AM technologies could improve the performance by the increment of volume ratio. However, pure copper's high thermal conductivity (401 W/m*K at 27 °C) is also one of the reasons why (coupled with its high reflectivity) it is not easy to process via LPBF. In particular, copper is one of the materials with the highest reflectivity toward near-infrared radiation, which corresponds to the emitted wavelength region of commonly adopted lasers in LPBF systems (continuous wave fibre lasers). In addition, the high conductivity leads to a higher tendency of melt pool instability during LPBF due to the rapid dissipation of the deposited heat input. Both these defects reduce the amount of energy available for melting, leading to high porosity and low mechanical and electrical properties.

Two leading solutions can be found in the literature to overcome the low energy issue: increasing the laser power up to 1 kW or utilising a green laser source. However, these approaches for printing pure copper are not suitable for commercially available LPBF machines, which have a low laser power (400W Max) and laser wavelength of around 1080 nm. The characterization procedure of copper was carried out using the EOSINT M280, which possesses the laser characteristics mentioned above. As a result, two alternative options have been investigated: using powder with a different particle size distribution and oxidizing the powder to increase its absorptivity. Finally, the precipitation hardened copper alloy CuCrZr was studied. The CuCrZr alloy's key feature is its high mechanical properties while maintaining high conductivity. For this reason, the CuCrZr alloy represents a viable pure copper substitute in high thermal conductivity applications.

In this research, the main application of the LPBF of copper and copper alloy is the manufacturing of accelerating electrostatic grids, a component of the negative ion beam source of the Neutral Beam Injector (NBI) system. The grids are subjected to highly focused power densities and hence require continuous active cooling to guarantee proper heat removal and temperature control. The accelerator grids represent a critical component as they have a rather complex design, with tiny cooling channels, apertures for the negative ions and grooves for the embedded magnets. The grids' geometry could be optimized through additive manufacturing, realising complex internal cooling channels for higher heat transfer efficiency. This research activity has designed a feasible alternative AM shape of the cooling channels. Prototypes of AM single channels have been manufactured using the tuned process parameters, and the pressure drop was experimentally measured using different water flow rates.

Finally, the characterization of pure copper parts using high-power infrared and green lasers was performed. The high quality of the parts enabled the production of the first accelerator grids prototypes with an additive manufacturing approach.

Structure of the Thesis

The thesis is organised into seven chapters. The **first chapter** contains an overview of the main metal additive manufacturing technologies, focusing on the LPBF process and its thermo-physical phenomena. The chapter then presents the state of the art of the LPBF of pure copper and CuCrZr alloy, and it concludes by showing this thesis' main application: the implementation of the LPBF process for the manufacturing of acceleration grids. The **second chapter** reports the experimental apparatuses used during the research period. The **third chapter** investigates the influence of the particle size distribution on the manufacturability of copper via LPBF. The results obtained using oxidized powder are shown in the **fourth chapter**. **Chapter five** deals with the characterization of the CuCrZr alloy produced via LPBF and the effect of the heat treatments applied to it. Finally, the research activity that led to the development of an additive manufacturing design for the acceleration grids is presented in **chapter six**. **Chapter seven** reports the conclusion of the thesis.

PREFAZIONE

Il lavoro presentato in questa tesi di dottorato è stato svolto presso la Sezione di Padova dell'Istituto Nazionale di Fisica Nucleare e presso il Dipartimento di Ingegneria Industriale dell'Università di Padova, tra ottobre 2018 e marzo 2022. Durante questo periodo, il lavoro svolto è stato finanziato attraverso due assegni di ricerca: tra ottobre 2018 e maggio 2021 attraverso il progetto SATELLES (Bando 19739 – collaborazione tra INFN e l'Agenzia Spaziale Italiana) e tra luglio 2021 e marzo 2022 attraverso il progetto DTT (Divertor Tokamak Test) (Bando 23109 – collaborazione tra INFN e DTT).

Abstract

La produzione additiva (AM-Additive Manufacturing), nota anche come stampa tridimensionale (3D), differisce dai metodi di produzione tradizionali in quanto il materiale viene aggiunto anziché sottratto per ottenere la geometria solida desiderata. Le procedure AM sono prive dei limiti dei metodi di produzione convenzionali, consentendo la creazione di geometrie uniche e complessi sistemi interni.

Per classificare i processi AM sono utilizzati la natura e lo stato aggregato della materia prima e il meccanismo di adesione tra gli strati di materiale aggiunto. Nella produzione additiva di metalli, una materia prima in polvere, o più raramente un filo, viene completamente fusa dall'immissione di energia di un raggio laser o di elettroni e trasformata, strato dopo strato, in una parte solida.

Nel processo Laser Powder Bed Fusion (LPBF) la materia prima è polvere metallica e l'energia è immessa da un raggio laser. Durante il processo manifatturiero, il raggio laser scansiona il letto di polvere in posizioni preselezionate a una velocità predeterminata, fondendo la polvere con il materiale solido sottostante. Completata la scansione di uno strato, il letto di polvere viene abbassato di un definito spessore e un nuovo strato di polvere viene depositato. Il processo viene ripetuto fino a quando la parte non è completa.

Lo stato dell'arte nella fusione a letto di polvere metallica è progredito al punto da passare dalla prototipazione rapida ad una tecnologia di produzione. Le parti possono essere fabbricate a densità quasi totale (99,5%) con proprietà meccaniche equivalenti a quelle dei metalli prodotti convenzionalmente. Pertanto, il processo di produzione rapida richiede una comprensione approfondita del processo stesso, della microstruttura creata dai parametri di processo e delle qualità delle parti generate.

Ogni processo di produzione additiva ha il proprio insieme di parametri di processo, che influenzano la qualità dei componenti fabbricati in combinazione con le proprietà dei materiali e le condizioni ambientali. Con lo sviluppo di nuove tecnologie e applicazioni, lo spettro di metalli accessibili per l'uso in AM continua ad espandersi. Attualmente, i materiali metallici più comuni sono vari tipi di acciaio, titanio puro e leghe di titanio, leghe da colata di alluminio, superleghe a base di nichel e leghe di cobalto-cromo.

L'obiettivo principale di questo progetto è caratterizzare rame e leghe di rame per il processo LPBF. Le proprietà termiche del rame lo rendono ideale per applicazioni di scambio termico e la libertà di progettazione fornita dalle tecnologie AM potrebbe migliorare le prestazioni mediante l'incremento del rapporto volumetrico. Tuttavia, l'elevata conducibilità termica del rame puro ($401 \text{ W/m}^{\circ}\text{K}$ a 27°C) è anche uno dei motivi per cui (insieme alla sua elevata riflettività) è difficile da elaborare attraverso LPBF. In particolare, il rame è uno dei materiali con la più alta riflettività nei confronti della radiazione del vicino infrarosso, che corrisponde alla regione di lunghezza d'onda emessa dai laser comunemente adottati nei sistemi LPBF (laser in fibra ad onda continua). In aggiunta, l'elevata conduttività porta a una maggiore tendenza all'instabilità della pozza di fusione a causa della rapida dissipazione dell'apporto di calore depositato. Entrambi questi difetti riducono la quantità di energia disponibile per la fusione, portando a un'elevata porosità e basse proprietà meccaniche ed elettriche.

In letteratura si possono trovare due soluzioni all'avanguardia per superare il problema della bassa energia: aumentare la potenza del laser fino a 1 kW o utilizzare una sorgente laser verde. Tuttavia, questi approcci per la stampa di rame puro non sono adatti per le macchine LPBF disponibili in commercio, che hanno una bassa potenza laser (400 W max) e una lunghezza d'onda del laser di circa 1080 nm. La procedura di caratterizzazione del rame è stata eseguita utilizzando la stampante EOSINT

M280, che possiede le caratteristiche laser sopra menzionate. Di conseguenza, sono state studiate due opzioni alternative: utilizzare polvere con una distribuzione granulometrica diversa e ossidare la polvere per aumentarne l'assorbimento. Infine, è stata studiata la lega di rame CuCrZr che indurisce per precipitazione. La caratteristica chiave della lega CuCrZr sono le sue elevate proprietà meccaniche pur mantenendo un'elevata conduttività. Per questo motivo, la lega CuCrZr rappresenta un valido sostituto del rame puro nelle applicazioni ad alta conducibilità termica.

In questa ricerca, l'applicazione principale della stampa additiva di rame e lega di rame tramite LPBF è la produzione di griglie elettrostatiche acceleranti, un componente della sorgente di fasci di ioni negativi del sistema Neutral Beam Injector (NBI). Le griglie sono sottoposte ad un'elevata densità di potenza altamente focalizzata e quindi richiedono un raffreddamento attivo continuo per garantire una corretta rimozione del calore e il controllo della temperatura. Le griglie dell'acceleratore rappresentano un componente critico in quanto hanno un design piuttosto complesso, con minuscoli canali di raffreddamento, aperture per gli ioni negativi e scanalature per i magneti incorporati. La geometria delle griglie potrebbe essere ottimizzata attraverso la produzione additiva, realizzando complessi canali di raffreddamento interni per una maggiore efficienza di trasferimento del calore. Questo studio ha progettato e simulato una possibile forma AM alternativa dei canali di raffreddamento. Questa attività di ricerca ha progettato una possibile forma alternativa dei canali di raffreddamento. Sono stati realizzati prototipi di singoli canali AM utilizzando i parametri di processo ottimizzati e la perdita di pressione è stata misurata sperimentalmente utilizzando diverse portate d'acqua.

Infine, è stata eseguita la caratterizzazione di parti in rame puro prodotto utilizzando laser infrarosso e verde ad alta potenza. L'elevata qualità delle parti ha consentito la produzione dei primi prototipi di griglie di accelerazione con un approccio di produzione additiva.

Struttura della tesi

La tesi è organizzata in sette capitoli. Il primo capitolo contiene una panoramica delle principali tecnologie di produzione additiva dei metalli, concentrandosi sul processo LPBF e sui suoi fenomeni termofisici. Il capitolo poi presenta lo stato dell'arte della produzione di rame puro e della lega CuCrZr

tramite LPBF, e si conclude mostrando la principale applicazione di questa tesi: l'implementazione del processo LPBF per la realizzazione di griglie di accelerazione. Il secondo capitolo riporta gli apparati sperimentali utilizzati durante il periodo di ricerca. Il terzo capitolo indaga l'influenza della distribuzione granulometrica sulla producibilità del rame tramite LPBF. I risultati ottenuti utilizzando la polvere ossidata sono mostrati nel quarto capitolo. Il quinto capitolo tratta la caratterizzazione della lega CuCrZr prodotta tramite LPBF e l'effetto dei trattamenti termici applicati ad essa. Infine, nel capitolo sei viene presentata l'attività di ricerca che ha portato allo sviluppo di un design additivo per le griglie di accelerazione. Il capitolo sette riporta la conclusione della tesi.

TABLE OF CONTENTS

ACKNOWLEDGEMENTS	i
PREFACE	ii
Abstract	ii
Structure of the Thesis.....	iv
PREFAZIONE	v
Abstract	v
Struttura della tesi.....	vii
TABLE OF CONTENTS	ix
LIST OF FIGURES.....	xii
LIST OF TABLES	xviii
1 LASER METAL ADDITIVE MANUFACTURING OF COPPER	1
1.1 Overview of metal additive manufacturing systems	1
1.1.1 Powder bed fusion (PBF)	1
1.1.2 Direct energy deposition (DED).....	3
1.1.3 Sheet lamination	4
1.1.4 Binder Jetting (BJ).....	4
1.2 Laser Powder Bed Fusion.....	5
1.2.1 Process sequence	7
1.2.2 Fundamental thermo-physical phenomena in LPBF	9
1.2.3 Processing parameters	17
1.3 Copper and copper alloys in LPBF	21

1.3.1	Influence of material's properties on the LPBF process	21
1.3.2	Challenges in processing copper via LPBF	22
1.3.3	LPBF of the CuCrZr copper alloy	28
1.3.4	Application: manufacturing of accelerator grids	34
2	MATERIALS AND METHODS	39
2.1	LPBF setup	39
2.2	Material characterization	40
2.3	Characterization of CuCrZr surface roughness	47
3	INFLUENCE OF PARTICLE SIZE DISTRIBUTION ON LPBF MANUFACTURABILITY OF COPPER.....	48
3.1	Introduction	48
3.2	Materials and methods.....	53
3.2.1	Powder characterization	53
3.2.2	Experimental plan.....	61
3.3	Result and discussion	62
3.3.1	Single scan tracks	62
3.3.2	Tuning of process parameters.....	64
3.3.3	2.3 Mechanical and thermal properties.....	72
3.3.4	Lateral surface roughness	77
3.4	Summary	78
4	LPBF OF OXIDIZED PURE COPPER POWDERS	80
4.1	Side effects of studying the influence of temperature of the platform	80
4.1.1	Scan strategies	80

4.1.2	Preheating of the platform	82
4.2	LPBF of surface oxidized pure copper powder	86
4.2.1	Materials and methods.....	86
4.2.2	Experimental results and discussion.....	87
4.3	Summary	98
5	LPBF OF CUCRZR ALLOY	100
5.1	Thermo-mechanical characterization	100
5.1.1	Introduction	100
5.1.2	Material and methods	101
5.1.3	Experimental results	103
5.2	Surface roughness improvements.....	125
5.3	Summary	134
6	DEVELOPMENT OF AN AM DESIGN FOR ACCELERATOR GRIDS.....	135
6.1	Preliminary AM design and prototypes of accelerator grids.....	135
6.2	Pure copper single-channel prototypes.....	139
6.3	Characterization of pure copper produced using high-power infrared and green lasers 142	
6.4	Production of accelerator grids prototypes.....	147
7	CONCLUSIONS	150
	APPENDIX A	154
	REFERENCES.....	156

LIST OF FIGURES

Figure 1.1 Schematic illustration of a typical LPBF machine.....	6
Figure 1.2 Scheme of a part attached to the platform, support structures in red.....	8
Figure 1.3 (a) Top view and (b) transverse micrograph of three single scan tracks produced using increasing scan speeds. The lowest scan speed produced a more regular scan track, while increasing the scan speed led to the balling phenomenon. All the scan tracks weakly penetrate the substrate [25]...	10
Figure 1.4 Scheme of the fluid forces acting on a transversal section of a melt pool [31].	11
Figure 1.5 Electron backscatter diffraction crystallographic characterization of two perpendicular views for an AlSi10Mg LPBF part [42]. The front view (on the left) shows the grain alignment in the build direction.....	15
Figure 1.6 Cracks and delamination of M2 HSS parts produced by LPBF [54].	16
Figure 1.7 (a) Correlation between the energy input and relative density. (b) Process window of LPBF 6511 stainless steel [60].	19
Figure 1.8 Various scanning strategy: (a) uni-directional, (b) bi-directional, (c) island or chess, and (d) rotation scan of a bi-directional scan strategy [65].	20
Figure 1.9 Various raw metals' spectral absorbance [80].	24
Figure 1.10 Damage of the optical mirror due to back-reflections after 12h of high laser power exposition [88].	26
Figure 1.11 Yield strength and thermal conductivity of selected high-performance Cu alloys [103]. .	29
Figure 1.12 Liquidus and Solidus of the Cu – Cr phase diagram [107].	30
Figure 1.13 Scheme of the tokamak configuration [122].	35
Figure 1.14 Schematic of a neutral beam injector system [123].	36
Figure 1.15 (a) Cooling circuit and water temperature of the G4 MITICA grid. (b) Peak temperature of copper due to localized heat loads [127].	37
Figure 2.1 Hall Flowmeter Funnel [130].	41

Figure 2.2 Thermal conductivity and tensile specimens manufactured in horizontal and vertical directions.	44
Figure 2.3 Experimental Van der Pauw (VdP) four-probe set-up.	45
Figure 2.4 Geometry of the machined tensile specimens tested using MTS 858 Mini Bionix II.	45
Figure 3.1 Schematic representation of the relationship between the properties of the powder and the final part's property [140].	48
Figure 3.2 Multiple scattering of the laser beam between the powder particles [152].	51
Figure 3.3 Example of a particle size distribution obtained using the laser diffraction method [156].	52
Figure 3.4 Effect of element impurities (or additions) on the conductivity of pure copper [157].	54
Figure 3.5 Particle size distribution of the powder B (top) and powder C (bottom).	55
Figure 3.6 Secondary electron image of copper powder A with a focus on agglomerates and superficial defects.	57
Figure 3.7 Secondary electron image of copper powder B with a focus on an agglomerate of fine particles. The yellow arrows indicate deformed particles.	58
Figure 3.8 Secondary electron image of copper powder C; the red arrows indicate melt ejections while the yellow arrows indicate deformed particles.	58
Figure 3.9 EDS analyses on powder C: (a) spherical particle; (b) particle with irregular shape.	60
Figure 3.10 Laser reflectance measurements of the pure copper powders with different PSDs.	61
Figure 3.11 Scan strategies employed for the wall production: bidirectional scan strategy (on the left); contours addition (on the right).	62
Figure 3.12 Width of SSTs as a function of scan speed at 370 W of laser power.	64
Figure 3.13 Relative density of the samples manufactured with different scan speeds and hatching distances for the three different powder suppliers. a) Powder A; b) Powder B; c) Powder C.	66
Figure 3.14 Optical microscope analyses of the highest density specimens after etching in the horizontal XY plane: a) Powder A; b) Powder B; c) Powder C.	70
Figure 3.15 Optical microscope analysis of the highest density specimens produced using powder C after etching in the vertical XZ plane.	71

Figure 3.16 EDS analysis of pure copper printed samples: (a) Powder A, (b) Powder B. No oxygen peak was detected.	72
Figure 3.17 Micro-hardness values for each highest density sample.	73
Figure 3.18 Stress-strain curves of one copper tensile specimen for each powder lot.	75
Figure 3.19 (a) Micrograph of a vertical cross-section of a sample produced using powder C. (b) and (c) illustrate a lack of fusion porosity oriented perpendicular and parallel to the loading direction [168].	76
Figure 4.1 Relative densities of powder C samples manufactured using different scanning strategies.	81
Figure 4.2 Relative densities of powder C samples manufactured with different scanning strategies using a preheated building platform at 150 °C.	83
Figure 4.3 Oxidized powder recovered after manufacturing samples using a 150 °C preheated platform.	84
Figure 4.4 Comparison of relative densities obtained using oxidized copper powder and “virgin” powder with different scan strategies.	85
Figure 4.5 On the left: PSD of the reused powder. On the right: comparison between the D values of the virgin and recycled powder.	87
Figure 4.6 XRD spectra of pure and oxidized copper powders, with a focus on the 35°-39° range, showing the Cu ₂ O peak evolution.	90
Figure 4.7 Laser reflectance measurements of pure copper and oxidized powders.	91
Figure 4.8 Morphology and EDS analysis of the starting pure copper powder.	92
Figure 4.9 Morphology (TOP) and cross section (BOTTOM) of powder oxidized at 150 °C for 15 h. On the right of each figure are reported the EDS pecks of oxygen and copper.	92
Figure 4.10 Morphology (TOP) and cross section (BOTTOM) of powder oxidized at 200 °C for 1 h. On the right of each figure are reported the EDS pecks of oxygen and copper.	93
Figure 4.11 Relative densities of pure and oxidized copper samples manufactured with different scan speeds and hatching distances.	94
Figure 4.12 Micrograph of a cross section of the samples with the highest density obtained using pure copper powder oxidized at 150 °C.	95

Figure 4.13 Micrograph of a cross section of the samples with the highest density obtained using pure copper powder oxidized at 200 °C.	95
Figure 4.14 Micro-hardness values for pure and oxidized copper.	97
Figure 5.1 Morphology of the CuCrZr powder and EDS analysis.	103
Figure 5.2 Laser reflectance measurements of pure copper (powder A) and CuCrZr.	104
Figure 5.3 Relative densities of CuCrZr samples manufactured using different laser powers and scan speeds.	106
Figure 5.4 Relative densities of CuCrZr samples manufactured using different scan speeds and hatching distances.	106
Figure 5.5 Microstructural analyses of XY sections of an AB sample (TOP) and a DAH sample (BOTTOM).	107
Figure 5.6 Microstructural analyses of XY sections of an SA sample (TOP) and a SA+AH sample (BOTTOM).	108
Figure 5.7 Microstructural analyses of XZ section of (a) DAH sample and (b) SA+AH sample.	110
Figure 5.8 XRD-spectra of CuCrZr alloy in various heat-treated states, with close up view of the detected Cr peaks.	111
Figure 5.9 Micro-hardness of LPBF CuCrZr samples in the as-built state and after various heat treatments.	113
Figure 5.10 Stress-strain curves of CuCrZr manufactured in horizontal and vertical direction in AB, DAH, and SA+AH states.	114
Figure 5.11 Tensile fracture morphologies of (A-B) AB H, (C-D) AB V, (E-F) DAH H, (G-H) DAH V, (I-L) SA+AH H, (M-N) SA+AH V.	117
Figure 5.12 Thermal conductivities of CuCrZr samples in different heat-treating states and manufacturing orientations.	119
Figure 5.13 Thermal conductivities of copper samples obtained with Hot Disk and Laser Flash methods.	120

Figure 5.14 Experimental setup components: (a) pure copper heater cone made, (b) test sample and reference samples, (c) water cooler made by 3D printed pure copper.	121
Figure 5.15 On the left: the final experimental setup connected with all components. On the right: the experimental setup covered with glass wool.	122
Figure 5.16 Calibration experimental tests at different heat fluxes imposed. The red and black data points are referred to as the test sample and reference sample, respectively.	123
Figure 5.17 Temperature gradients obtained in the reference sample (Black) and in the CuCrZr samples (Green). On the left: SA + AH. On the right: DAH.	125
Figure 5.18 Sample geometry diagram used for roughness measurements: isometric (left), front (top right), side (bottom right) view. Dimensions in mm.	127
Figure 5.19 On the left: scheme of the used scan strategy. On the right: Sa parameters of US and DS surfaces at different beam offsets. The contour scan speed was 1000 mm/s.	127
Figure 5.20 SEM images of US surfaces of samples manufactured using (a) 1 contour at 1000 mm/s (Sa= 25 μm) (b) no contour (Sa= 21 μm).	128
Figure 5.21 Sa parameters of US and DS surfaces with varying scanning speed and contour number. NC indicates the number of contours. Blue curves are downskin surfaces while the warm colour curves are upskin surfaces.	130
Figure 5.22 Trend of Sa parameter as the orientation of the surface varies (contour speed set at 1000 mm/s). The "dash-point" line in (a) represents the trend of the Sa parameter according to the model of G. Strano, with layer thickness at 30 μm and λ equal to 0.66.	131
Figure 5.23 The contour scan speed effect on the US (red curve) and DS (blue curve) surfaces. The inclination angle was 55°.	132
Figure 5.24 Isometric views of the volume reconstructed from the CT scans of the specimen printed with a contour scan speed of 100 mm/s, in which a) DS b) US surfaces can be observed; c) surface topography of the US surface of the same specimen.	133
Figure 6.1 CAD geometries of AM cooling channels. On the left: Alternate Channels. On the right: Crossed Channels.	136

Figure 6.2 On the left: AM grids attached to the platform. On the right: AM grid after electro-discharging.	137
Figure 6.3 Pressure drops of Crossed and Alternate channels at various water flow rates.	138
Figure 6.4 On the left: CT scan of crossed channel grid. On the right: focus on the highest scan deviation from the CAD geometry.....	139
Figure 6.5 CAD design of the cooling channels: (a) test specimen design, (b) reference straight channel, (c) DUNED channel and (d) NICE channel [156].	140
Figure 6.6 Image of the three cooling channels manufactured vertically [156]......	141
Figure 6.7 Plot with calibrated CFD and experimental results for the three different geometries [156].	142
Figure 6.8 (a) cross section micrograph of pure copper AMCM M 290-1 1kW sample; (b) cross section micrograph of pure copper TRUMPF TruPrint 5000 sample.....	144
Figure 6.9 Stress-Strain curves of pure copper samples manufactured with TRUMPF TruPrint 5000.	146
Figure 6.10 Stress-Strain curves of pure copper samples manufactured with AMCM M 290-1 1kW.	146
Figure 6.11 On the left: TruPrint 5000 accelerator grid prototype (250 x270x18 mm). On the right: AMCM M 290-1 1kW accelerator grid prototype (200x210x18 mm)......	147
Figure 6.12 On the left: CAD design of the “Power Test” prototype. On the right: a section showing the DUNED cooling channels.	148
Figure 6.13 (a) CAD design of the “Leak Test” prototype. (b) Grid produced using EOS M290 1 kW. (c) Grid produced using TruPrint 5000. (d) CT scan of the “Leak Test” grid manufactured using TruPrint 5000.	149

LIST OF TABLES

Table 2.1 Technical specifications of the employed EOSINT M280 LPBF machine.....	39
Table 3.1 Chemical composition of the copper powders.	53
Table 3.2 Particle size distribution of the copper powders.....	54
Table 3.3 Single scan tracks produced at 370 W laser power and increasing scan speed from 100 to 850 mm/s.	63
Table 3.4 Results of tensile test on LPBF copper.	73
Table 3.5 Thermal conductivities of LPBF copper.	76
Table 3.6 Effect of the contour scan strategy on the lateral surface roughness of samples produced with copper powders with different PSD.	78
Table 4.1 Comparison of the relative densities obtained using a different preheating temperature of the platform.	83
Table 4.2 Fabrication parameters of the LPBF process.....	87
Table 4.3 Oxygen levels of oxidized powders at different times and temperatures.	89
Table 5.1 Chemical composition of the starting CuCrZr copper powder.	101
Table 5.2 Powder characteristics provided by the producer.....	101
Table 5.3 Fabrication parameters of the LPBF process.....	102
Table 5.4 Tensile test results of CuCrZr manufactured in two printing directions and at different heat-treating states.....	113
Table 5.5 Results of the electrical resistivity measurements of heat-treated CuCrZr sample with different surface roughness.	118
Table 5.6 Thermal conductivity results for bulk C10100 copper samples.	124
Table 5.7 Thermal conductivity of DAH and SA+AH CuCrZr samples obtained with the experimental setup. The C10100 values shown in figure 5.13 were used as k_{ref} . The obtained k_{TOP} are compared with the theoretical k calculated using the Wiedemann-Franz relationship (k_{W-F}).	124

Table 6.1 Results obtained from CFD simulations of the acceleration grids prototypes. A straight channel prototype was designed to have reference results.	136
Table 6.2 Porosity level of 3D printed pure copper measured with Archimedes method and optical analysis	143
Table 6.3 tensile test results of pure copper manufactured in two printing directions with AMCM M 290-1 1kW and TRUMPF TruPrint 5000.....	145

CHAPTER 1

1 LASER METAL ADDITIVE MANUFACTURING OF COPPER

1.1 Overview of metal additive manufacturing systems

Additive manufacturing (AM), more commonly known as 3D printing, is an alternative technological approach to traditional subtractive manufacturing, where the material is deposited layer by layer to form the final parts. This method enables the production of complex shapes directly from a computer-aided design model (CAD) in short development times.

Many distinct terminologies and definitions have been used during the development of additive manufacturing technology, frequently connected to specific application areas and trademarks. The several names that manufacturers provide in commercially available systems generate ambiguity. For example, LPBF (Laser Powder Bed Fusion), SLM® (Selective Laser Melting), LMF (Laser Metal Fusion), DMP (Direct Metal Printing), and DMLS (Direct Metal Laser Sintering) are some of the terms are used to describe the same additive manufacturing technology.

The ISO/ASTM 52900 standard [1] was published in 2015 in response to the ever-increasing number of new terms to provide essential knowledge of AM concepts and clarify its terminology. AM can be subdivided into several different technologies depending on the material and feedstock form, the principle for fusion or bonding and the machine architecture. The standard divides additive manufacturing into seven process categories, four of which pertain to metal AM.

1.1.1 Powder bed fusion (PBF)

The PBF is based on melting a powder feedstock by exposure to power radiation. A levelling system spreads the powder over a substrate plate in a defined thickness, creating a powder bed layer.

The levelling system can be a blade, brush or roller. Alternatively, the powder is distributed evenly directly from the powder container by moving it across the substrate plate.

The power source is either a laser or an electron beam. When the exposure process is finished, the build platform is lowered by the thickness of the layer to apply the next powder layer. The following layer merges with the previously generated layer upon re-exposing it. The given procedure is repeated until the entire component geometry is developed. The powder that has not been exposed stays loose and can be reprocessed.

Although both Laser Powder Bed Fusion (LPBF) and Electron Beam Melting (EBM) systems use the same powder-bed technique, the hardware configurations vary significantly. In this Section, the EBM is described, while the LPBF process is described in detail in [Section 1.2](#).

The EBM system is essentially a high-powered scanning electron microscope (SEM) [2]. An electron gun emits electrons that are then collimated and accelerated to ~60 keV kinetic energy [3]. Electromagnetic lenses focus the electron beam, while a magnetic coil controls the scanning directions of the beam. The typical electron beam diameter is between 100 μm and 200 μm . One of the main differences between EBM and LPBF is that EBM works in a vacuum environment because even air molecules can deviate the electron beam. The typical pressure of residual gases in an EBM machine's vacuum chamber is 10^{-5} mbar [4]. This feature guarantees a low level of external contamination, an essential benefit for processing highly reactive materials, such as titanium alloy.

Another critical difference is that, during the beam-material interaction, electrostatic charge effects arise in the powder due to the extremely low electrical conductivity of the powder [5]. Each layer is preheated to a temperature where the particles softly sinter to hold the powder in place, avoiding electrostatic repulsion. The pre-heating is performed by projecting the defocused beam on the powder bed several times at low power and high scanning speed. Furthermore, pre-heating the powder bed lowers the part's thermal gradient, reducing the thermal stresses in the component. Therefore, parts manufactured with the EBM process do not need stress relief after the heat treatment [6]. The addition of low pressure of inert helium gas during the melting process also prevents the accumulation of

electrical charges in the powder [3]. Once the process is finished, the powder is passed through a powder recovery system to remove and recover sintered powder from around the parts [7].

The electron beam offers a higher scanning speed and power output than the laser beam. While the high scan speed enables the pre-heating feature, higher power output allows the use of thicker layer thickness (in the range of 50 – 200 μm)[8], resulting in faster build rates [9]. The particle size distribution (PSD) stays in the range of 45- 150 μm , a PSD bigger than the one used in LPBF [4]. The use of larger particles reduces the prices of the feedstock material [2], but it also leads to inferior surface finishing [6] and lower resolution. In addition, the resolution of EBM is lower than LPBF due to its larger beam size. The beam diameter determines the least attainable feature: smaller diameters of the heat source result in smaller melt pools, leading to a higher resolution.

1.1.2 Direct energy deposition (DED)

The unique feature of the DED technology is that a focused source of energy melts the material as it is deposited. According to the form of the feedstock, the DED process can be classified into powder and wire feeding types. The most commonly used metal DED technique is the powder-based DED system, which uses a laser as energy source [10]. The wire feeding DED process can be further classified depending on the source of thermal energy used: electric arc, plasma arc, laser beam or electron beam.

Compared to the PBF process, DED processes have a higher production rate at the cost of lower resolution and surface quality [11]. However, unlike PBF methods, DED processes can build arbitrary shapes on even and uneven substrates. In fact, among the essential DED applications are the addition of features, the reparation of a component, and the surface coating. Another functionality that distinguishes DED from other AM systems is changing the chemical composition of the manufactured parts locally by simultaneously feeding different powders, which enables the fabrication of heterogeneous material with optimized properties [11].

Finally, laser DED can be paired to computer numerical control (CNC) for operation in tandem, forming hybrid CNC-AM systems. This is possible because the laser DED module can be easily

integrated with the CNC machine, allowing for the rapid manufacturing of items with a machined surface finish directly from the hybrid process and without post-processing machining.

1.1.3 Sheet lamination

The sheet lamination process is the only metal AM technique that uses sheets as feedstock material [1]. The sheets are bonded together layer by layer to build the final part. A feed roller supplies the sheet material, which is then cut with a laser in the profile required to create the part's contour. Ultrasonic consolidation is the most common bonding technique [12]: it bounds metallic sheets together using an ultrasonic welding operation. The process forms a near-net-shape part, and then a three-axis CNC milling machine is used to mill it to its final dimensions [13].

Compared to other metal AM techniques, the sheet lamination process is less expensive since metal sheets are cheaper than fine powders or wires. Additionally, it is feasible the production of large parts with a fast production rate [14]. On the other hand, the geometric freedom is restricted: the technique cannot produce complex overhangs, and the tool paths available for machining processes may limit other features.

Unique features of the ultrasonic consolidation process are the possibility to fabricate layered composite materials with different metals (multi-material structures) [15] and the insertion of electrical circuits or optical fibres between two metallic strata [16], which are a challenge for other AM techniques.

1.1.4 Binder Jetting (BJ)

Binder jetting is a multi-step AM process since it requires multiple operations to fabricate a part. The first step is the printing process, followed by three post-processing operations that consolidate the part to the intended basic material properties.

The printing process provides the basic geometric shape called “*Green Body*”. Green body manufacturing occurs similarly to how parts are produced in PBF processes. However, in the BJ process, the consolidation of the powder does not occur through the melting of the powder. In this case, one or

more nozzles inject a liquid-state binder on top of the powder bed, consolidating the powder within and between sliced layers.

The primary post-processing operations are curing, debinding, and sintering. First, the curing of the binding agent is performed to slightly enhance the green body's mechanical properties for better handling. Afterwards, the part is heated at low temperatures and long times to burn out the binder (debinding process). The temperature is then raised to sinter the metal particles, eliminating the voids and improving the mechanical properties.

Dividing the manufacturing process into multiple steps leads to many advantages but also some drawbacks. The BJ machines are less expensive and require a low capital investment [12]. Materials with high thermal conductivity, high optical reflectivity and low thermal stability can be more easily processed in BJ since the process does not use a high energy beam to fuse the part. Moreover, support structures that act as heat sinks or mechanical anchors for overhang geometries are not required to produce the green body. Therefore, it is possible to design more possible geometries (e.g., internal cavity) [17]. The main limitation of the BJ process is the low mechanical properties of the printed components due to their high residual porosity. Other disadvantages are the fragility of as-printed green bodies, which are prone to failure, and post-thermal treatments might distort more prominent parts and increase the lead time remarkably [18].

1.2 Laser Powder Bed Fusion

The typical configuration of the LPBF system is shown in Figure 1.1, which is the configuration of the LPBF machine used for this research project. Another standard design has a powder hopper as a powder dispenser system; however, the basic principle is the same. The process begins with the downward movement of the building platform. The thickness of the layer with which the CAD component was sliced determines the building system's step movement. Then, the powder dispenser system moves in the vertical direction, and the recoating system distributes a layer of powder over the building platform by moving in the horizontal direction. The excess powder ends in a collector container.

The optical system creates and positions the laser beam. The galvanometric scanning mirrors control the laser's position, and a focusing objective (F-theta objective) focuses the laser beam onto a flat field. The laser scans portions of the powder bed that correspond to the cross-section of the CAD model. It melts the powder and anchors the solid part to the building platform. Then the platform is lowered again, and a new layer of powder is formed. The sequence of procedures is repeated, layer by layer, until the component is complete.

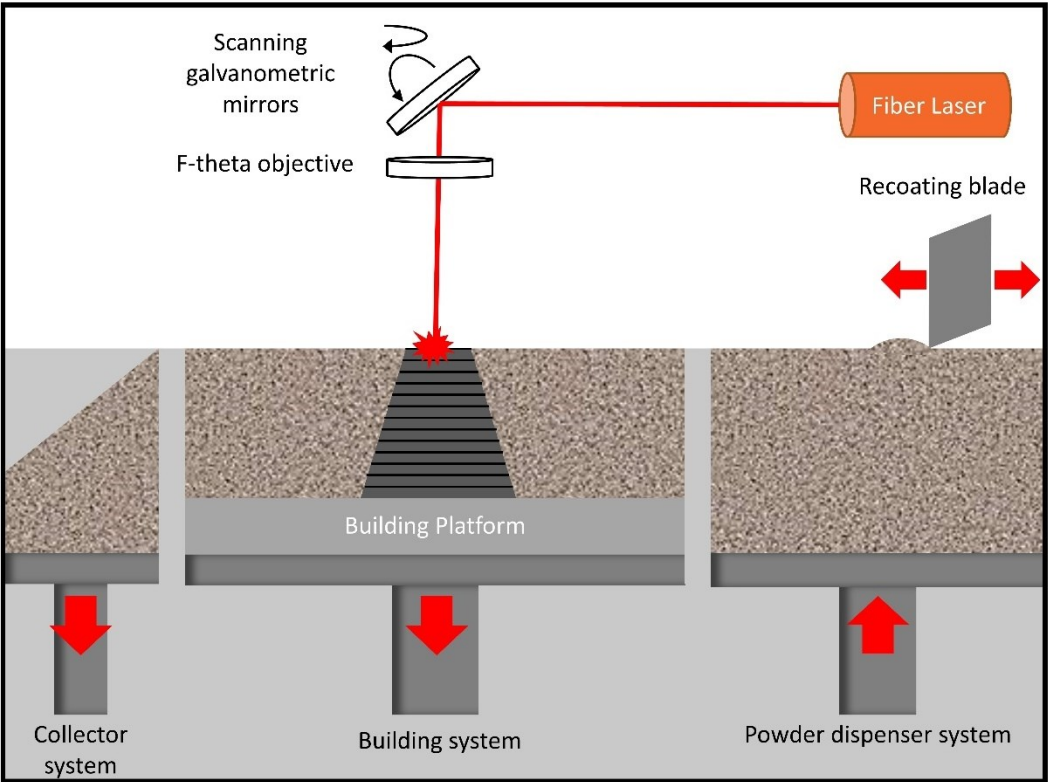


Figure 1.1 Schematic illustration of a typical LPBF machine.

The printing process takes place in an inert environment to hinder the oxidation reactions activated by the high temperature. A flux of inert gas, commonly nitrogen or argon, is delivered across the powder bed to form the inert atmosphere. The gas flux also removes all of the process by-products generated during the powder's melting, such as metal vapour and spatters. Metal vapour may affect the laser beam properties (energy, spot diameter, or intensity profile) [19], and spatters can generate defects if their trajectory ends over the fused parts.

1.2.1 Process sequence

The printing process is only one of many sequence steps that have to be performed to obtain the final part. The production begins with the design of a model through CAD software. Compared to standard processes, designing for LPBF offers greater geometrical freedom. The LPBF process can produce geometries that are difficult to accomplish with conventional methods, such as undercut or internal and complex surfaces. Despite this, several process restrictions must be considered when designing an AM part. For example, when manufacturing hollow parts, the removal of the powder must be taken into consideration; thus, at least one hole should be added for the removal of the powder. The minimum wall thickness and clearance are also important geometrical factors.

The slicing and positioning of the model are then performed by AM build preparation software. These programmes usually require a mesh as a form of input. Therefore, the model is converted to an STL (Stereo-lithography format) file, which represents the model only through its surface, discretely arranged in a series of triangles. Because the mesh size affects the accuracy of the finished item, it is critical to use the appropriate number of facets.

The orientation of the parts over the building platform significantly influences their quality [20]. One key factor is the positioning of supports. A representation of a supported part attached to the platform is shown in Figure 1.2. The object's surface can be horizontal, vertical, or inclined, depending on the orientation. Downward-facing surfaces are known as *downskin*, whereas upward-facing surfaces are known as *upskin*. As a general rule, support structures are placed on the downskin when the inclination angle between the surface and the platform is less than 45° . Many factors, including the LPBF machine setup, process parameters, and material used, determine the degree's exact value.

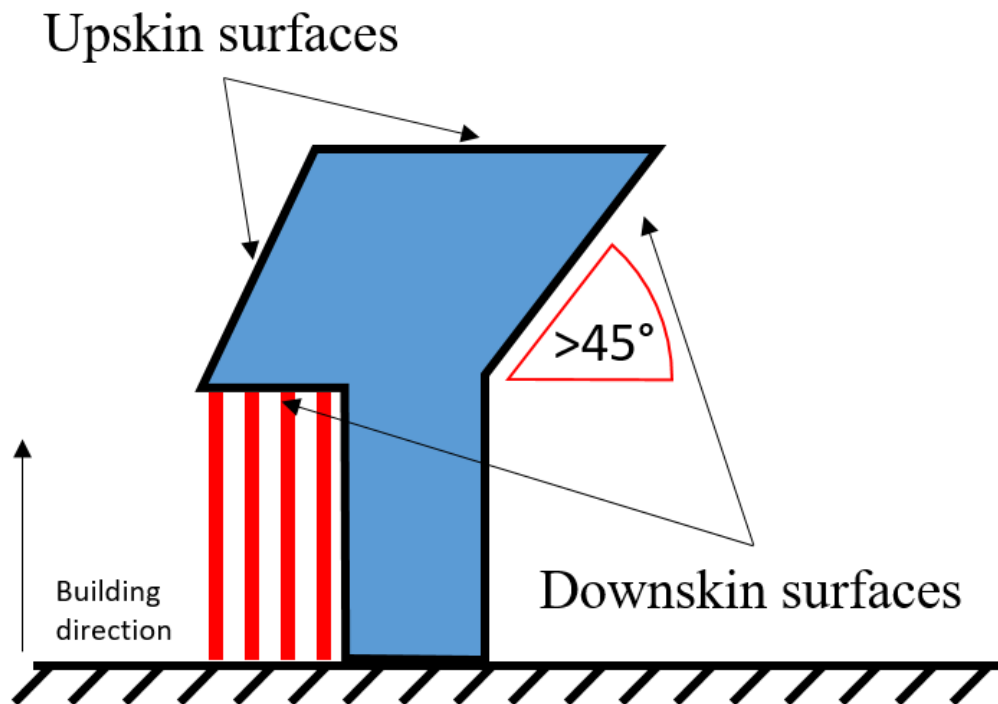


Figure 1.2 Scheme of a part attached to the platform, support structures in red.

Support structures have the function of supporting overhanging features and fixing the part on the building platform. They are also utilized to reduce component distortion by dissipating heat, lowering internal tension, and preventing part deformation.

Supports are one of the most significant limitations of the LPBF technology, as they have several drawbacks. Supports structures increase the overall time for obtaining the final part since they require time to manufacture and then have to be manually removed during post-processing operations. It is also critical that the supports can be easily removed with a tool or hand, which further constrains the geometric freedom. Furthermore, because they are not reusable, they usually result in waste feedstock material, raising the price of the part. Finally, when a support structure is removed, it may be detrimental to the surface quality [21].

Therefore, while positioning the part, the designer should consider an orientation that minimizes the use of supports. Another technique to decrease the number of supports is to improve the topology of the oriented component by converting overhangs into inclined surfaces that do not require support. In

addition, the support's design and qualities can be improved to decrease material consumption and post-processing time [22].

After positioning and generating supports, the file is transferred to the LPBF machine, where the material and process parameters are set. Before the manufacturing process, the LPBF machine needs to be prepared by an operator. The powder container is loaded with the feedstock material, the baseplate is positioned, and the processing chamber is filled with inert gas. Following that, the samples may be manufactured.

The post-processing operations start with removing the un-melted powder, which is subsequently sieved, and the withdrawal of the baseplate. The parts are then cut from the build plate using a wire electrical discharge machining or a band saw. Following that, all supports will be removed (manually or by milling operations). Before removing the elements from the platform, the baseplate may be subjected to different AM-post treatments, such as the stress relief heat treatment. Many LPBF components may need final machining to add holes, smooth surfaces, and other details. If necessary, further procedures such as hot isostatic pressing, chemical milling, vibro-finishing, abrasive blasting, and others may be undertaken.

1.2.2 Fundamental thermo-physical phenomena in LPBF

The characteristics of a manufactured part depend on the production technology. A laser-build part will have different properties than a part made with the same material but produced with another method. The manufacturing process affects the microstructure and defects of the built component, which determines the object's mechanical and physical properties. Therefore, it is crucial to understand the governing process physics to guarantee the reliability of the process and the quality of the products, especially for highly engineered metallic components.

Several articles that present different thermo-physical models to describe the LPBF process are available in the literature [23]–[26]. The LPBF process is governed by many physical mechanisms, making it challenging to model. The LPBF process is multiscale in nature: material transformation occurs in milliseconds and involves a small volume (particles with an average diameter of 30 μm), yet

the whole part has a dimension in the tens of cubic centimetres and is manufactured over hours or days [27]. Therefore, the LPBF models are consequently suited to investigate physical processes at their respective scales, typically macroscale, mesoscale, and microscale [28].

1.2.2.1 MESOSCALE PHENOMENA

The mesoscale phenomena concern the powder particles and the melt pools. The fusion of the powder and the melt pool thermal fluid dynamics are fundamental phenomena, as they are correlated with the creation of defects and the quality of the surface [24].

➤ Melt pool's shape

The laser beam heats and melts the powder, which starts to coalesce due to the capillary forces. The shape of the melt pool can vary depending on the process parameter and environment. It can take on various forms, ranging from a quasi-stationary melt pool to a sequence of spherical droplets known as balling phenomenon and frequently referred to as Rayleigh instability [25]. The formation of discontinuous scan tracks significantly hinders the uniform deposition of a new powder layer on the substrate surface. Due to inadequate inter-layer bonding and thermal stresses, the balling phenomenon can lead to porosity and even delamination [29]. Figure 1.3 displays examples of single scan tracks with different shapes.

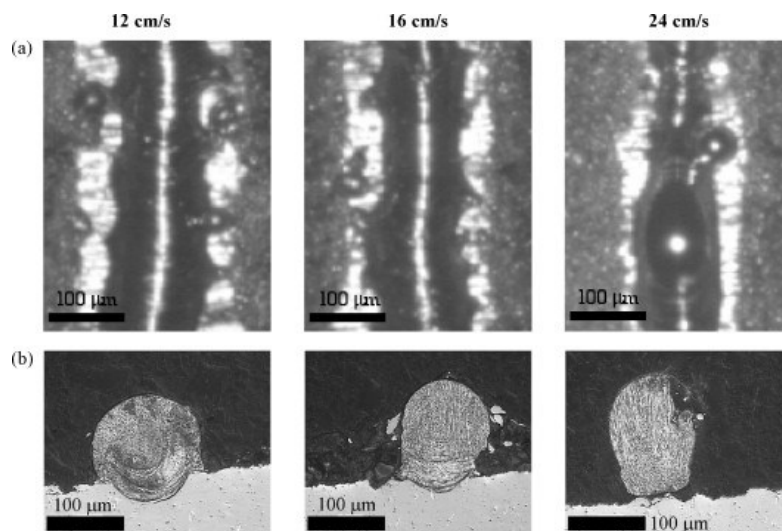


Figure 1.3 (a) Top view and (b) transverse micrograph of three single scan tracks produced using increasing scan speeds. The lowest scan speed produced a more regular scan track, while increasing the scan speed led to the balling phenomenon. All the scan tracks weakly penetrate the substrate [25].

Poor wettability of the underlying substrate with the melt can also produce the balling phenomenon, leading to the problems stated above. Material, temperature, surface roughness, and surface chemistry significantly impact wetting behaviour. Depending on the material, oxidation of the powder particles or substrate surface severely reduces the melt’s wetting behaviour [30]. Therefore, reducing the oxygen content in the processing chamber and preventing the oxidation of the powder by proper handling and storing the powder is essential.

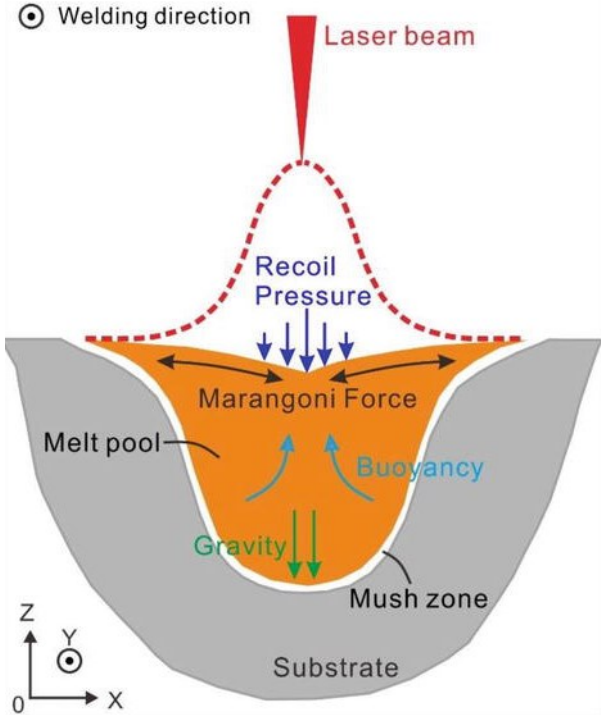


Figure 1.4 Scheme of the fluid forces acting on a transversal section of a melt pool [31].

The Marangoni flow and the recoil pressure are the primary determinants of melt pool instability [23]. Figure 1.4 displays a scheme of the fluid forces acting on a cross-section of a melt pool. During the fusion process, the laser re-melts the underlying material, while the fusion of the powder forms a metal structure with a dome shape (or balls if the balling phenomenon happens). Depending on the entity heat source, the shape of the section may range from being semi-circular (as shown in Figure 1.3) to a keyhole (high penetration depth).

➤ **Marangoni convection**

The temperature within the melt pool is exceptionally high and not uniform. The peak temperature is at the centre of the melt pool (the centre of the laser-heated zone), while the surrounding regions are colder. The temperature gradient causes a gradient in the surface tension of the liquid metal, which usually decreases with increasing temperature and creates the conditions for Marangoni convection. The Marangoni convection is the mass transfer along an interface between two fluids caused by a surface tension gradient. Thus, the melted metal flows outwards from the centre of the melt pool towards the high surface tension region.

➤ **Buoyancy forces**

Another contribution that promotes the outwards flow is the temperature-induced buoyancy forces [32], which are also generated by temperature inhomogeneity. The colder liquid metal on the edges sinks, while the hotter liquid metal in the centre floats.

➤ **Recoil pressure**

Generally, the temperature below the laser spot is higher than the boiling point, resulting in strong metal vaporization. The recoil pressure generated by the gas expansion drives the liquid metal down and outward and develops a cavity just beneath the laser beam, which then collapses to form the shape shown in Figure 1.4.

High recoil pressure is the cause of two common defects in LPBF: the keyhole porosity and the spatter generation. Zhao et al. [33] have directly observed the keyhole formation by real-time monitoring the fusion process with X-ray imaging. High recoil pressure resulting from excessive heating generates deep depressions in the melt pool. These deep cavities often incompletely collapse, leaving voids with a spherical form or keyhole porosity.

Spatters are the melt ejections from the melt pool and its vicinity. The convection forces, generated by high vapour recoil pressure and the Marangoni effect, can overcome the surface tension and form droplet spatters. If the ambient gas flow does not clear the spatters, they will fall back into the

powder bed, potentially altering the local particle distribution and contributing to structural defects in the finished products [34].

➤ **Denudation zone**

The depression region that forms at the laser spot also can generate lateral gas that pulls the particles from the sides, creating a denudation zone on the side of the melt pool (an area deprived by the particles) [35].

A different type of spatter particle generates from the denudation zone. The quick expansion of the gas entrainment between the particles (generated by the depression region) can accelerate them. If these particles pass near or across the laser beam, they partially melt and become spatter [36].

➤ **Metal evaporation**

Significant evaporation of alloying elements occurs from the molten pool because of the high temperatures experienced during LPBF. Because certain alloying elements are more volatile than others, selective vaporization of alloying elements frequently causes a considerable change in the alloy's composition [37].

1.2.2.2 MICROSCALE PHENOMENA

Three essential parameters determine the solidification microstructure of a given process: the temperature gradient G , solidification rate R and undercooling ΔT [38]. The manner of solidification is determined by the G/R ratio, whereas the product GR (i.e. the cooling rate) determines the scale of the solidification microstructure. The solidification microstructure can be divided into planar, cellular, columnar dendritic or equiaxed dendritic (listed with decreasing G/R values) [39]. The LPBF process is characterized by relatively high thermal gradients and cooling rates. Hooper measured thermal gradients in the range of 5-20 K/ μm and cooling rates in the range of 1-40 K/ μs during the processing of the Ti6Al4V alloy [40]. The high GR product of this process leads to a fine-grained structure compared to traditional manufacturing (e.g. casting) [8], while the solidification mechanism also depends on the feedstock material used. Planar growth is characteristic of Ti-6Al-4V alloys [41], the cellular-dendritic

microstructure is typical of LPBF aluminium components [42]–[44], whereas columnar dendrites are more common with nickel-based alloys [45].

The rapid solidification of the melt pool performed during the manufacturing of numerous layers generates a specific grain structure and crystallographic texture that is characteristic of the LPBF process. The microstructure inside each melt pool depends on the intensity and direction of the thermal gradients at the border, while the macrostructure depends on the reciprocal position of the scan tracks. Therefore, both the processing parameters and scan strategy deeply influence the final grain structure [46], [47].

Grain growth occurs in a direction parallel to the heat flow direction. Since the melt pools are former over large part, the heat flows radially from the centre towards the borders. The maximum heat flow direction is normal to the solidifying surface of the melt pool, parallel to the $\langle 001 \rangle$ build direction. This favours the growth of grains with $\langle 001 \rangle$ orientation, forming columnar grains and crystallographic texture in the parts. Since there is no nucleation barrier to solidification, epitaxial grain grown from the bottom of the melt pool is usually observed [47]. In fact, it is often possible to identify grains that span multiple layers/melt pools. The scan tracks' partial re-melting further increases the morphological texture since it allows new solid material to form by maintaining the neighbouring grains' crystallographic orientation [46].

In addition, the part's geometry also affects the temperature gradients of the melt pool. The powder dissipates less heat than the bulk material, and small features accumulate heat. As a result, the microstructure of LPBF-fabricated components is impacted by the part's shape and might vary within a produced part [48]. An example of the columnar grains generated by the LPBF process is shown in Figure 1.5.

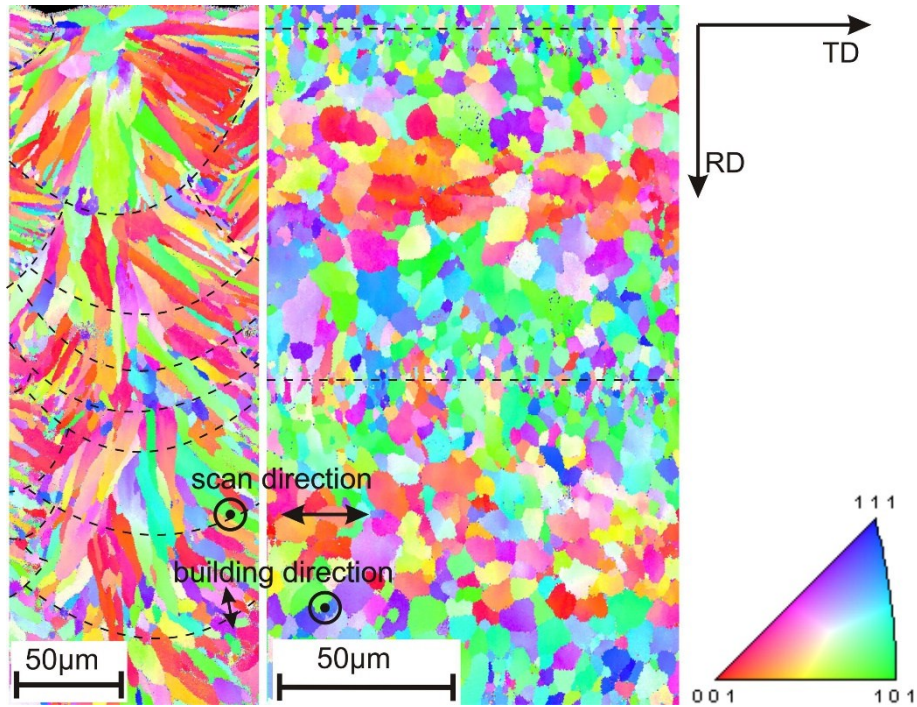


Figure 1.5 Electron backscatter diffraction crystallographic characterization of two perpendicular views for an AlSi10Mg LPBF part [42]. The front view (on the left) shows the grain alignment in the build direction.

Furthermore, each layer's thermal cycle is quite complicated. During the printing process, solidified microstructures in preceding layers are continuously exposed to heat cycles from succeeding layer deposition, resulting in a variance of thermal histories for each layer [45]. Repeated heat cycles can cause various effects, including microstructural banding or changes in microstructure across deposition layers [49]. Due to strong temperature gradients, materials exhibit rapid solidification far from equilibrium conditions. Rapid solidification decreases element partitioning and increases solid solubility, leading to metastable phases [50], which may even vary for each layer of the deposited material.

It is interesting to note that by selecting an appropriate set of parameters and designing a tailored scan strategy, it is possible to control and change the microstructure of a manufactured component [39].

1.2.2.3 MACROSCALE PHENOMENA

The mesoscale and microscale phenomena determine the macroscopic properties of the part. The typical columnar grain structure oriented along the build direction often results in macroscopic behaviour that is significantly anisotropic. Moreover, each layer is subjected to a different thermal cycle,

which leads to a change of microstructure in the build direction. These cycles may result in a coarsening of the bottom layers' microstructure, a reduction in brittle non-equilibrium phases, and, as a result, more ductile material properties [26]. Poor bonding between adjacent layers is also the cause of mechanical anisotropy. It leads to weaker mechanical properties in the building direction than in the scanned planar direction [14].

Besides the mechanical anisotropy, the high residual stresses are another mechanical feature of LPBF-manufactured parts. Residual stresses are created due to strong temperature gradients, substantial volumes of thermal expansion and shrinkage or non-uniform plastic deformation during the heating and cooling cycle [51]. During the manufacturing, the bulk material constrains the shrinkage of the solidifying melt pool. The stresses in the deposited scan track are tensile in all directions while the substrate is under compression [52]. The underlying solid microstructure and the consequent macroscopic material behaviour dictate the intensity of these stresses. On the part scale, the tensile stresses at the top cause bending, resulting in significant vertical stresses. These tensile residual stresses are on the side surfaces and are balanced by compression in the middle [52]. In addition, the magnitude of the residual stresses increases with the number of layers. It increases with increasing Z values and reaches its maximum at the top surface [53].

If the stress concentration is high enough, it may affect the strength of the material and cause part distortion, cracks, or delamination of the part. An example of LPBF cracks is shown in Figure 1.6.

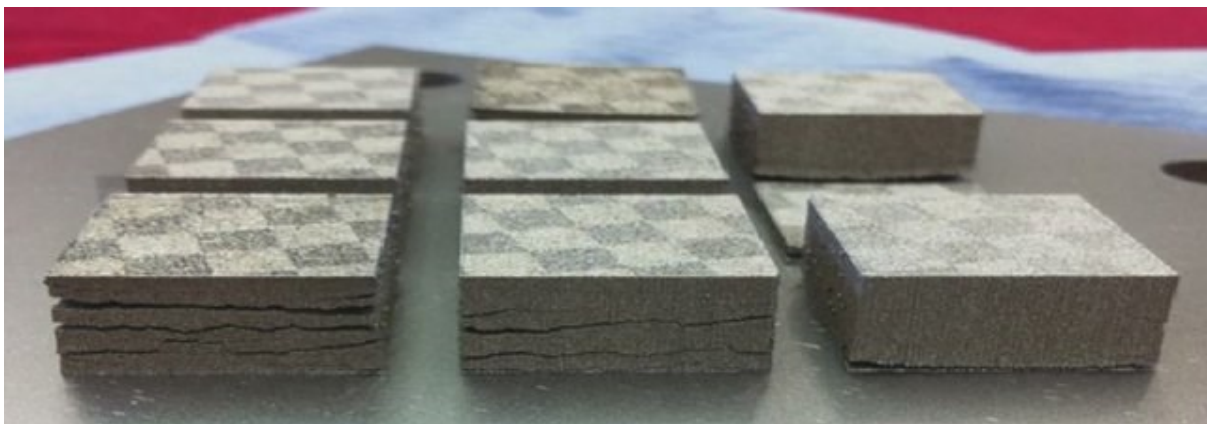


Figure 1.6 Cracks and delamination of M2 HSS parts produced by LPBF [54].

The warping of the top surface might happen during the manufacturing and block the recoating blade movement, causing a premature job failure. If the thermal stresses are not removed from the part, the removal of the component from the baseplate causes severe distortions. Since the baseplate no longer limits the distortions, the residual stress relaxes by shrinkage and bending deformation. For this reason, the LPBF parts are commonly stress relieved prior to the removal from the platform. The thermal stresses can be reduced by tuning the processing parameters [55] and pre-heating the baseplate [56].

1.2.3 Processing parameters

As already mentioned, several factors influence the properties of a component produced by LPBF. They can be divided into two groups, the processing parameters and the properties of the feedstock material [57]. The chemical composition and physical qualities of the feedstock material and the properties of the powder, such as the morphology and particle size distribution, are among the properties of the feedstock material.

Once a material is selected for processing LPBF, a tuning of the processing parameters is performed. Some processing parameters, such as those related to laser qualities like laser wavelength and laser spot geometry, are fixed. However, most of them may be tuned to get the optimal material qualities at the highest productivity. The selection of the processing parameters is a challenging task as the increase in productivity is often at the expense of quality. Often the machine manufacturer offers complete parameter sets dedicated to specific materials. Despite this, many studies in the LPBF sector focus on fine-tuning processing parameters for novel metal alloys or investigating the effects of laser-related factors on microstructure development and final attributes (surface quality, fatigue resistance, etc.).

Finding the process window for the in-process parameters is frequently the first step in tuning the processing parameters. The process window is the set of parameters that leads to a stable melt pool and hence to a dense, defect-free component. The laser power P [W], the scan speed v [mm/s], and the layer thickness t [μm] are the parameters that mainly influence the mechanism of melt pool formation. The process window is often found by testing several combinations of different scan speeds and laser

power at a determined layer thickness. The laser power is the amount of energy applied per unit of time, while the scan speed is the rate at which the laser moves across the build area. Both parameters determine the amount of energy that is absorbed by the powder. The thickness of the consolidated layer determines the amount of feedstock material that must be melted. As a result, it specifies the total amount of energy required to melt the powder completely while simultaneously maintaining strong interlayer adhesion.

The scanning strategy and its related parameters have also a high influence on the quality of the final product. One of the most important scan-related parameters is the hatching distance h [μm], i.e. the distance between two adjacent scan tracks. In order to avoid lack of fusion porosities, the melt pools must overlap the underneath layer and the adjacent tracks. Tang et al. [58] calculated that the overlap must be at least as large as the layer thickness. Nevertheless, an excessive overlap increases the production time and generates rough surfaces [59].

These parameters define to a large extent the energy that is applied to a unit of volume of the processed material, commonly called volumetric energy density E_{Vol} [J/mm^3], given by Equation (1.1).

$$E_{Vol} = \frac{P}{h \cdot v \cdot t} \quad (1.1)$$

Despite not having physical meaning, this parameter is useful for comparing different combinations of parameters. An example of a schematic representation of the process window and the use of energy density as a comparative parameter is reported in Figure 1.7.

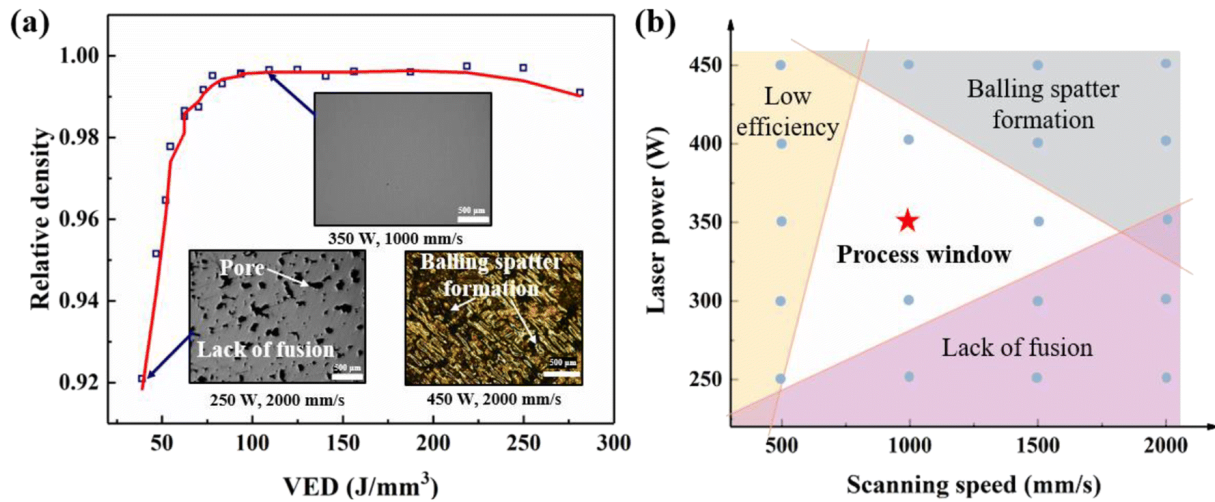


Figure 1.7 (a) Correlation between the energy input and relative density. (b) Process window of LPBF 6511 stainless steel [60].

Besides the process window, the sets of parameters define three other melting regimes. Two regimes are determined by the amount of energy applied to the material. If the energy input is insufficient (due to low laser power or high layer thickness, for example), the powder layer may not be entirely melted, or the melt pool may not penetrate enough the solid metal below. The un-melted powder remains underneath, resulting in increased porosity and the possibility of delamination. The creation of keyhole porosity, on the other hand, occurs when the energy input is excessive. In fact, the relative density starts decreasing at too high energy densities [61]. Aside from keyhole porosity, high energy densities cause significant accumulated thermal stresses and component deformation, preventing the LPBF recoating system from operating [62]. Finally, the third region regards the formation of an unstable melt pool. High scan speed and high laser power often lead to melt pools with high capillarity instability and the balling effect. For this reason, it is not possible to increment the process productivity by simply increasing the P/v ratio. Another kind of balling occurs at low energy input. Because the small amount of liquid precludes sufficient formation of sintering necks between metal agglomerates, no adequate bonding between neighbouring balls occurs [29]. Aversa et al. define these scan tracks as “irregular”[63].

Finally, the spatial moving pattern of the laser influences the thermal gradients and hence the quality of the part. The scanning strategy significantly affects the microstructure, mechanical properties,

and residual stresses [64]. Several scan strategies with different paths exist, but the most common ones use straight, parallel lines. Sketches of common scanning strategies are shown in Figure 1.8.

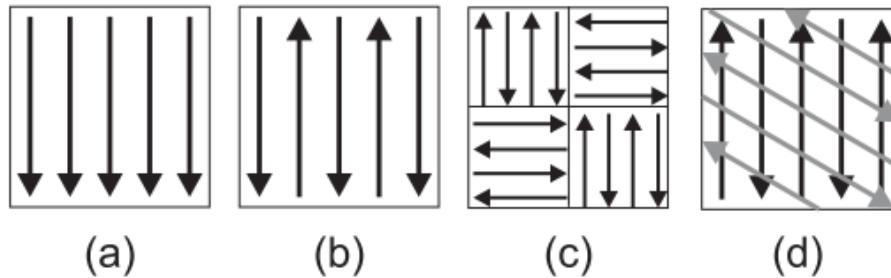


Figure 1.8 Various scanning strategy: (a) uni-directional, (b) bi-directional, (c) island or chess, and (d) rotation scan of a bi-directional scan strategy [65].

A scanning strategy might be uni-directional (Figure 1.8a) or bi-directional (Figure 1.8b). The difference is that in the bi-directional scanning strategy (also commonly called “zigzag” scan), the moving direction of the laser alternates, whereas in the uni-directional, it is always the same. The bi-directional scan strategy is the most common one, as the alternating vector leads to a more homogenous temperature distribution and less residual stress [66]. Also, the length of the scan vector is critical. The time interval between two lengthy adjacent scanning vectors is long, leading to significant temperature gradients due to the cooling of the first track [67]. Therefore, the scanning vectors are generally short and subdivided into small sections, which might be stripes or islands (as illustrated in Figure 1.8c).

Another strategy to reduce the thermal stresses of the part is by rotating the laser scan direction between layers [64]. The use of the rotation scan strategy helps prevent the formation of an anisotropic microstructure [42]. This effect is increased when the rotation angle is a prime number since it reduces the periodicity of the scanning directions [68].

The scan strategy has a significant impact on the surface roughness as well. Tian et al. [69] discovered that both the contour and skywriting scan strategies improved the quality of the side surface. The contour scan strategy is an additional laser scanning of the borders of the part, generally performed after the melting of the “body”. The re-melting, or partial re-melting, of the surface inhomogeneity, leads to smoother side surfaces. Instead, the skywriting scan strategy does not involve the scanning

pattern. It consists in activating the laser only at a constant speed. The galvanic mirrors need to accelerate the laser to reach the desired nominal speed value. The laser scan speed is lower than the nominal value during this operation, so the energy input is higher. This might lead to keyhole porosity, higher surface roughness, and less geometrical precision. However, these issues can be avoided by accelerating the scanner mirrors a specified distance before the scan vectors' actual start point and turning on the laser only after the acceleration phase is completed (the skywriting strategy). A similar process occurs with the deceleration phase.

Finally, it is worth highlighting the re-melting scan approach. It consists of scanning each layer twice, removing valleys and peaks, and generating a flat surface useful for adding the subsequent layer [70]. The part roughness of top surfaces is improved, and the part density increases, but the processing time is longer.

The process parameters and scan strategy can also be tuned according to the part's geometry. The regions at the borders (side, upskin and downskin surfaces) are in contact with the less thermal-conducting powder. This difference in heat conductivity leads to heat accumulation and so to larger melt pools. Therefore, it is crucial to reduce the energy input of these parts, especially for the downskin surface. In this region, the melt pools are supported by the powder bed, and large melt pools cause dross formation and part deformation (warping) [69], [71]. Moreover, it is possible to reduce the minimum allowable self-supporting angle of downskin surfaces by tuning the process parameters of this region [71].

1.3 Copper and copper alloys in LPBF

1.3.1 Influence of material's properties on the LPBF process

The material properties are the main driving factor in material selection for a specific application. However, the material selection must also consider the manufacturing process because material and production processes are not always compatible. For example, cast iron cannot be forged.

This is also valid for the LPBF process, as many alloys are not “printable”. The capacity of an alloy to avoid the production of defects typical of the LPBF process is referred to as "printability" [37]. Depending on the material’s properties, a material might be more prone to cracking, compositional change, formation of lack of fusion porosity, and distortion during the LPBF process. For example, in the case of aluminium alloys, mainly near eutectic Al-Si alloys, such as AlSi10Mg, are generally used in the LPBF process since these alloys are less susceptible to the solidification-cracking phenomenon [50], [72]. Properties of the liquid metal, such as the contact angle, viscosity and interface energies, determine the shape of the melt pool, its stability and the wettability with the substrate. The energy that the material requires to be fully melted is driven by physical properties like specific heat capacity, the latent heat of fusion and the melting temperature. Other properties, like the linear coefficient of thermal expansions and the thermal diffusivity, influence the residual stress generated upon cooling. Finally, the laser absorption coefficient is essential in deciding the final product's quality. The absorption determines the amount of energy that the material receives. It depends on the laser wavelength and on the material’s morphology. A more detailed description is presented in [Section 3.1](#).

Commercially accessible alloys for the LPBF process are often repurposed from traditional production processes, such as casting and powder metallurgy. These alloys are well known to the end-users, and the feedstock material is available in large quantities. However, because these alloys are not suited to the LPBF process's unique thermo-mechanical processing, the process’ full potential is not exploited [73]. Therefore, one research field in this sector is the design of alloys with properties suited for the LPBF process.

1.3.2 Challenges in processing copper via LPBF

Copper and its alloys have unique features that make them the ideal material in several applications. Copper is the non-precious metal with the highest conductivity. It is the conductor of choice for electrical applications because of its high electrical conductivity, ductility, and excellent resistance to oxidation and corrosion. Moreover, copper's great electrical conductivity is matched by its outstanding thermal conductivity, making it the preferred material for heat exchangers. Copper alloys

can be used in applications that demand good mechanical properties and excellent conductivity. Indeed, the mechanical properties of pure copper may be enhanced by alloying it with the appropriate elements. Due to the ease with which copper can create alloys with other elements, an extensive range of materials is available for a wide range of uses.

Examples of popular applications of copper and copper alloys are motors, alternators and wires for the generation, transmission and distribution of electrical power, heat exchangers and components for air conditioners and refrigerators, plumbing tubes and fittings for their high corrosion resistance, as well as a variety of aesthetic applications in the architecture and jewellery industries [74].

The design of freedom that the LPBF process offers could be implemented in the applications mentioned above, especially for electrical and heat exchange fields. Traditional hand-made coils for electrical motors and heat induction coils may now be built with a customizable form, enhancing efficiency while lowering manufacturing time [75]–[77]. As a result, electric motors might be smaller and lighter, making them more appropriate for aerospace and automotive applications. Another possible application is the fabrication of photoinjector cathodes with high radio frequency performance [78]. Also, heat transfer applications, such as heat exchangers and heat sinks, benefit from the ability to fabricate complicated, porous, and conformal shaped components. Indeed, it is possible to enhance the efficiency of heat exchangers by forming fine features that increase the surface to volume ratio and by designing parts with complex channels for optimized conformal cooling [76].

The use of LPBF to manufacture pure Cu components has not been as widely applied as it has been for more established materials such as aluminium, titanium, and steel, despite the process's great potential. This is due to the unique features of pure copper, which make it difficult to process by LPBF. The main limitations are its high thermal conductivity and its high reflectivity towards near-infrared wavelength.

The high thermal conductivity of pure copper (401 W/(mK) at 27 °C) promotes rapid heat dissipation from the melt pool. The combination of high heat fluxes with pure copper's

low surface tension forces may easily induce Plateau-Rayleigh instabilities in the molten pool and hence the balling effect [79]. In addition, the intense heat dissipation prevents the thermal accumulation necessary to melt the powder fully [76].

The material's reflectivity determines the amount of energy deposited in the material for the melting process. The interactions between radiation and matter are reflection, transmission, and absorption. Reflectance (R), transmittance (T), and absorptance (A) are the fractions of the aforementioned interactions, and their sum is equal to one. The transmittance is null if the interaction between the laser radiation and metal powder is considered, and therefore the absorptance can be defined as equation (1.2):

$$A = 1 - R \tag{1.2}$$

Only the absorbed radiation transfers its energy to the material, while the energy of the reflected radiation is lost to the surroundings.

The absorbance and reflectance depend on the material, morphology, and radiation wavelength.

Figure 1.9 depicts the wavelength dependency of the absorption rate of several raw materials.

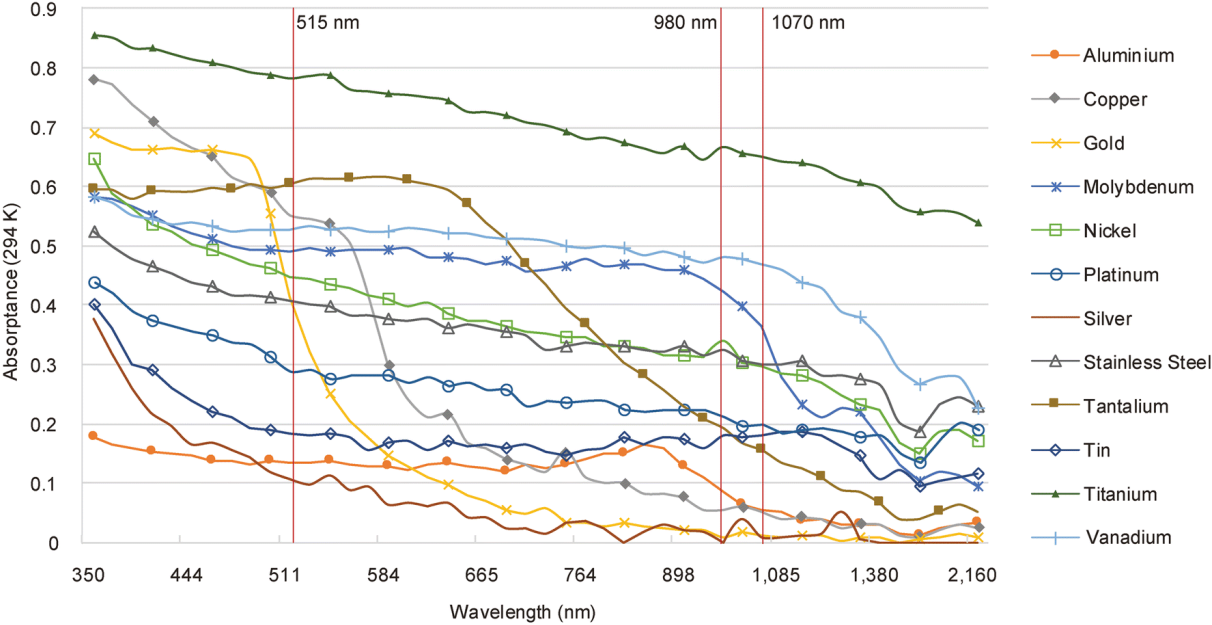


Figure 1.9 Various raw metals’ spectral absorbance [80].

The absorptance of most metals rises as the wavelength decreases. As a result, short-wavelength laser sources, such as solid-state Nd/Yb:YAG1 rod or Yb fibre lasers with a wavelength of around 1 μm , are commonly used in LPBF machines. Unfortunately, the reflectivity of pure copper (or highly conductive materials in general) is still high in the near-infrared range (up to 98%) [81].

On the other hand, the powder's reflectivity is lower than the bulk material due to the scattering of the laser light between the powder particles. Sinico et al. [82] have measured the optical reflectance of two batches of pure copper powders with different particle size distributions and measured reflectance of $\sim 70\%$ at a wavelength of 1070 nm. A more extensive investigation of the impact of the powder's particle size distribution on the powder's reflectivity is presented in [Section 3](#).

Another contribution to reducing the energy input is the energy dissipation during the melting process. According to Yan et al. [83], 20% of the total energy input is lost through convection, radiation and evaporation.

The combination of high thermal conductivity and reflectivity leads to parts with high residual porosity due to the lack of fusion problem [84]. Few approaches to overcome this problem have been offered, and they either involve the modification of the laser or the starting powder.

The first investigated method was to raise the energy input by increasing the laser power. The maximum achievable laser power of the first commercial LPBF machines was low, generally below 200W [85]. Therefore, the first published studies report low densities of the produced parts. Lykov et al. [85] obtained a maximum relative density of 88% using an LPBF system equipped with a 200W CO₂ laser source, while Trevisan et al. [84] obtained a lower density (83%) by using a 200W Yb-fibre laser. Even though the reflectance of pure copper is higher for CO₂ laser, the system used by Lykov et al. [85] had a smaller laser beam diameter (35 μm vs 100 μm), which led to higher power densities and thus higher energy input.

Subsequently, researchers have started developing in-house LPBF machines equipped with much stronger fibre lasers (up to 1 kW), which has led to an increase in the degree of densification. When utilizing 800 W of laser power and a scan speed of 300 mm/s, Ikeshoji et al. [86] produced a

relative density of 96.6%, whereas Colopi et al. [87] obtained a similar result (97.8%) when using 600 W of laser power and a scan speed of 1000 mm/s.

Despite these results, the use of a high laser power might be inconvenient due to the back-reflections. Jadhav et al. [88] performed a tuning of the process parameter on an LPBF machine equipped with a 1 kW laser source, with a beam diameter of 40 μm . They were able to manufacture dense parts (relative density higher than 98%) with electrical conductivity of 88% of the International Annealed Copper Standard (IACS - 58 MS/m corresponds to 100% IACS for electrical conductivity). However, the prolonged use of an extremely high laser power density can cause damage to the optical coating of the laser mirror, as shown in Figure 1.10.

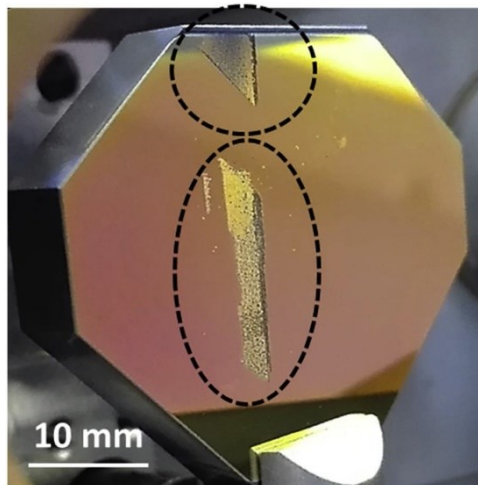


Figure 1.10 Damage of the optical mirror due to back-reflections after 12h of high laser power exposition [88].

While increasing laser power has been found to improve component relative densities, other factors can also help to improve manufacturability. Another study by Colopi et al. [89] has analysed the influence of the material of the baseplate on the manufacturing process. It was found that using a low conductive material as a substrate improves the manufacturability of pure copper since less heat is dispersed. Therefore, it is better to use a steel baseplate than a copper one. The scanning strategy was evaluated, a slight increase in relative density was obtained using a multi-pass scan strategy: from 98.7% with one passage to 99.1% with two passages at half energy density.

Another studied approach is to reduce the laser spot diameter to increase the laser power density. Silbernagel et al. [77] performed a tuning of the process parameter using a 200W Yb-fibre laser with a

laser spot diameter of 35 μm . The highest density measured was 85.8%, using 200 W of laser power, 300 mm/s of scan speed, and 45 μm of layer thickness. The highest electrical conductivity measured was 50.3% IACS, achieved using a 1000 $^{\circ}\text{C}$ heat treatment. Jadhav et al. [90] performed a similar research work using a fibre laser with a laser spot diameter of 37.5 μm and maximum laser power of 500 W. The tuning of the process parameters involved a layer thickness of 30 μm and a hatching distance of 90 μm . According to the results, 500 W of laser power is required to attain a density greater than 99%. In the as-built state, the copper components had an electrical conductivity of 94% IACS, a tensile strength of 211 MPa, yield strength of 122 MPa, and an elongation at break of 43%. Finally, Qu et al. [91] presented a research work using an even smaller laser spot (25 μm) and a combination of a fine powder (5-25 μm) with a small layer thickness (10 μm). Despite employing a low laser power (200W), a high relative density (99.6%) was obtained due to the use of a reduced layer thickness. The electrical conductivity of the as build part was 76.1% IACS, which can be further increased to 96% IACS after a heat treatment at 1000 $^{\circ}\text{C}$ for 12 h.

Another line of research investigates the processability of pure copper under lower laser wavelengths, mainly using blue (450nm) and green (515 nm) lasers. The absorptance of pure copper highly increases below 600 nm, reaching 55% at 515 nm and 65% at 450 nm, as illustrated in Figure 1.9 [80]. Nonetheless, research is currently limited due to the scarcity of high-power green and blue lasers with laser spot diameters adequate for LPBF. Asano et al. [92] studied the laser metal deposition (LMD) of pure copper using a blue laser with a beam spot of 400 μm and managed to produce continuous scan tracks, while Prasad et al. [80] investigated the LMD on different substrates using a 1kW green laser with a spot size of 1.7 mm.

Recently, the Trumpf Company has connected its TruDisk 1020 disk laser (515 nm, 1kW max power) with its LPBF machines to process pure copper [93]. In a research work conducted by Gruber et al. [94], a Trumpf LPBF machine was used (TruPrint 1000 Green Edition) to produce pure copper samples. The manufactured samples had relative density above 99.8%, electrical conductivity of 100% IACS and mechanical properties in the range of soft annealed copper. The primary drawback was the

lack of geometrical accuracy: due to the laser focus diameter of 200 μm , features of 500 μm were challenging to accomplish.

Coating the surface of the powder with materials with a greater absorptivity is an alternative option for increasing copper absorptance. However, adding solute elements causes lattice distortion, which increases the scattering of lattice electrons and drastically reduces the thermal and electrical conductivity [95]. A straightforward approach is to oxidize the feedstock powder, Jadhav et al. [96] heat-treated pure copper powder in the air to form a surface oxide layer and used it as feedstock material to manufacture copper samples. The results show that it is possible to obtain dense samples using a low energy density of 463 J/mm^3 . The specimens showed improved tensile strength (270 MPa) with acceptable ductility (28%) and electrical conductivity of 89% IACS. According to the authors, the low solubility of oxygen in the copper matrix led to the formation of nanometric copper oxide particles, which increased the mechanical properties and debased the electrical conductivity to a lower extent. Lindström et al. [97] improved the densification of copper by coating the powder with thin layers of tin and nickel using an immersion deposition method, but the properties of the as-built samples are not reported. Also, Jadhav et al. [98] coated the pure copper particles with a nanometric (62 ± 14 nm) layer of tin using the immersion deposition method. Performing the coating under an argon atmosphere led to lower sulphur pick up, which reduced the generation of porosity and cracks during the manufacturing process. The as-built samples were dense with a good combination of high mechanical properties and high electrical and thermal conductivity. Jadhav et al. [99] also improved the optical absorption (from 29% to 67%) and flowability of copper powder by mixing it with 0.1 wt% carbon nanoparticles. The relative density of the manufactured specimens was 98%. However, segregation of carbon nanoparticles and other impurities were observed along the grain boundaries. This led to a deterioration of the mechanical properties and reduced electrical conductivity.

1.3.3 LPBF of the CuCrZr copper alloy

Copper alloys have proven to be more printable than pure copper due to their reduced reflectivity and thermal conductivity. Clearly, copper alloys are manufactured at the expense of pure copper's

outstanding thermal and electrical conductivity. Several published works present the characterization of LPBF products produced using commercially available pre-alloyed copper alloys and low power LPBF machines; examples are CuSn10 [100], CuSn15 [101], and Cu7.2Ni1.8Si1Cr [102].

By either dispersion or precipitation, particle strengthening is ideal for producing high strength, high conductivity copper alloys. Figure 1.11 shows the room temperature strength and thermal conductivity of some high-performance particle-strengthened copper alloys.

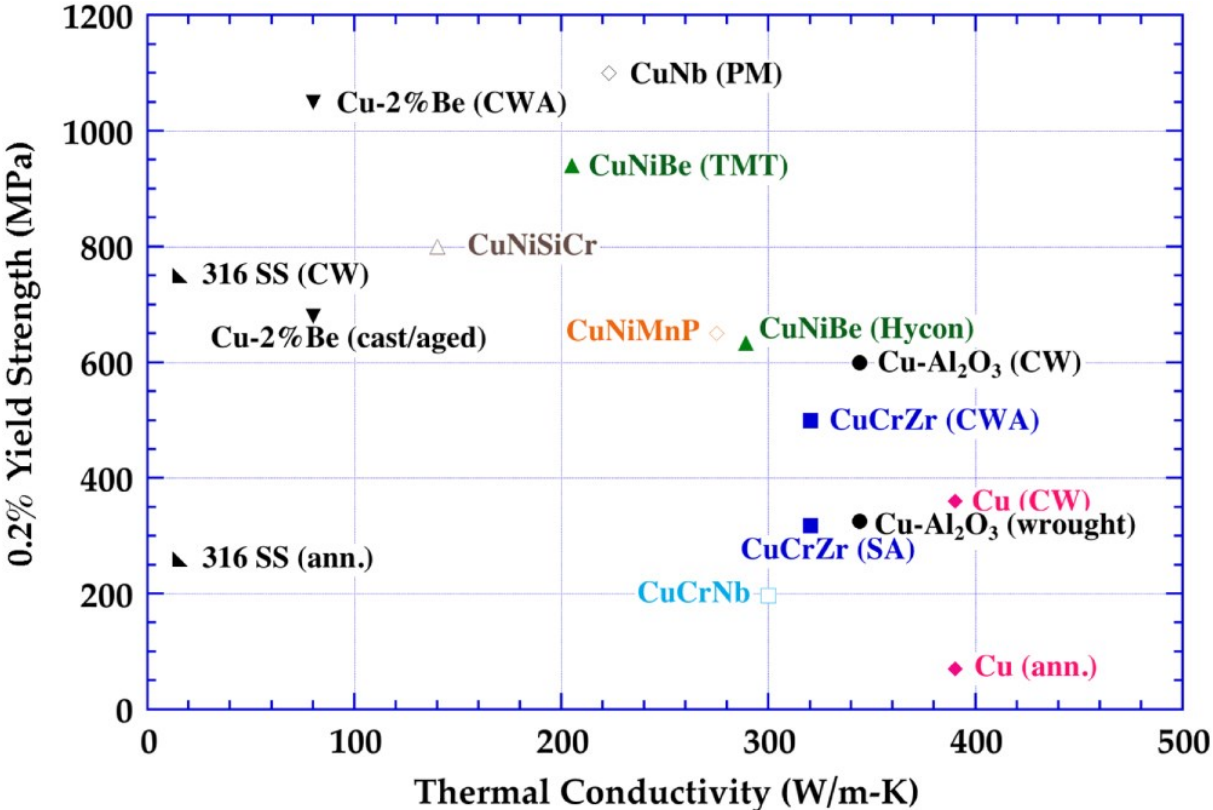


Figure 1.11 Yield strength and thermal conductivity of selected high-performance Cu alloys [103].

The presence of fine particles dispersed throughout the copper matrix blocks the movement of the dislocations, increasing the material’s yield strength [103]. Alloy elements, on the other hand, debase the thermal conductivity to a lesser level while not in solution, and therefore the conductivity of the copper alloy remains high [104].

1.3.3.1 Strengthening mechanism of the Cu-Cr system

The good trade-off between strength and conductivity of the Cu - Cr alloys, mainly CuCr and CuCrZr, has attracted the attention of many researchers in the LPBF field. CuCr and CuCrZr are

precipitation-hardening alloys that achieve particle strengthening by fine-scaled coherent Cr precipitates formed by high-temperature solution annealing plus intermediate temperature ageing [105]. In CuCrZr alloys, a low amount of Zr is added to suppress the tendency for embrittlement (by fixing the elemental sulphur) and to improve the hot ductility [106].

The Cu-Cr phase diagram is shown in Figure 1.12. It is a two-component eutectic system. The elements are completely miscible in the liquid state, but below the eutectic temperature, a two-phase equilibrium based on Cu and Cr solid solutions exists.

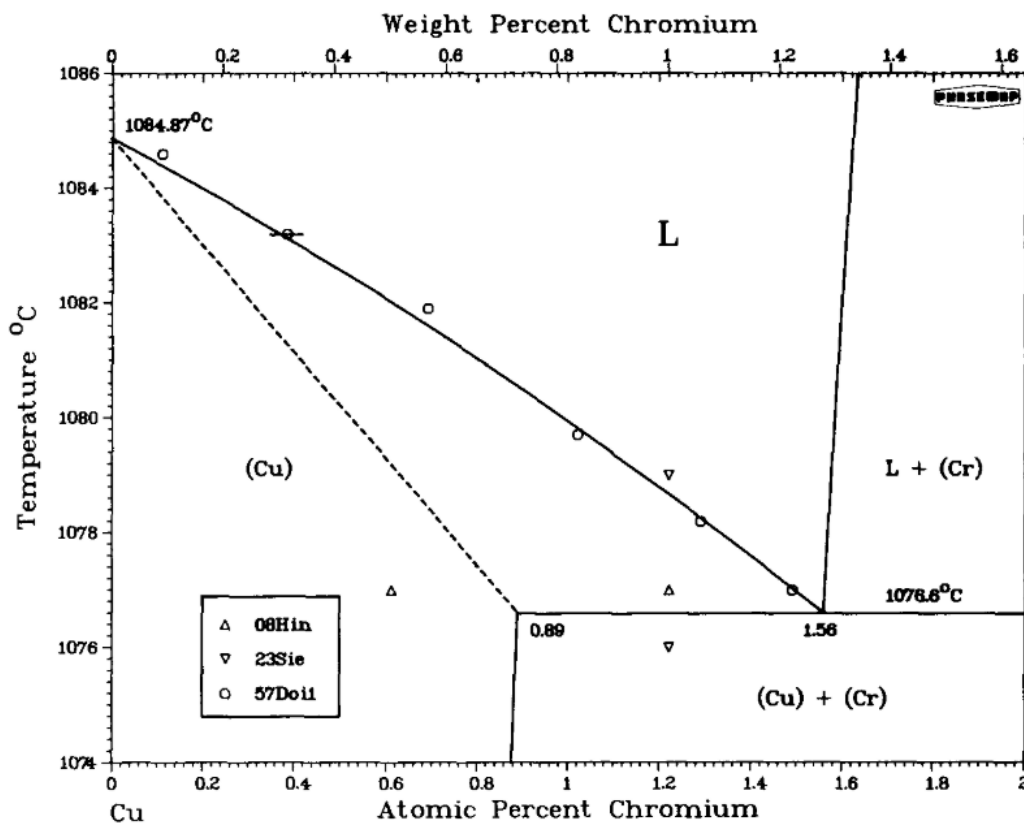


Figure 1.12 Liquidus and Solidus of the Cu – Cr phase diagram [107].

Chromium has low solubility in the copper matrix at room temperature (0.03 wt%) [108], with the highest equilibrium solubility (0.71 wt%) at 1070 °C [109]. Because of the change in solubility, when a Cu-Cr solid solution is cooled to room temperature, precipitation of Cr occurs. However, this operation leads to the formation of coarse precipitates. A fine distribution of Cr precipitates is preferred since narrower particle spacing leads to a greater increase in the material's strength [108]. Heating a

supersaturated solid solution is one approach to get a fine dispersion of precipitates. A supersaturated solid solution occurs when the concentration of the solute element exceeds the equilibrium concentration. The Cu-Cr supersaturated solid solution can be obtained through rapid solidification or solution annealing heat treatment: heating the material at a high temperature to dissolve the precipitates followed by fast cooling. The rapid cooling prevents the Cr to precipitate, forming a solution in a metastable state. Then, the material is heated at an intermediate temperature in a heat treatment called precipitation hardening (or age hardening/ageing). At this temperature, the Cr atoms are thermally activated, and the nucleation of the Cr phase occurs. Because time and temperature affect the diffusion of the solute Cr, it is critical to choose the best time and temperature combination. A high time-temperature combination will result in a coarse distribution of precipitates, whereas a low combination will result in too small precipitates that will not improve the mechanical properties effectively.

1.3.3.2 Current developments on LPBF of CuCrZr alloy

LPBF of Cu – Cr samples has proven to be less problematic than pure copper. Besides lowering the conductivity and increasing the material's strength, the addition of Cr also reduces the reflectivity [110]. Several researchers have investigated the processability of CuCr and CuCrZr through the LPBF process during the last few years. These studies mainly focus on the process parameters tuning, the microstructural analyses, the characterization of the alloy's physical and mechanical properties, and the effect of the heat treatments on them.

Uhlmann et al. [111] reported one of the first process parameter tunings. The research was performed on an LPBF machine SLM 250 using CuCr1Zr powder as feedstock material. A three-stage qualifying method (single scan tracks, followed by thin walls and blocks for the last step) was applied to find an appropriate set of process parameters. The optimal combination of parameters ($P = 350\text{W}$, $v = 300\text{ mm/s}$, $h = 80\text{ }\mu\text{m}$, $t = 50\text{ }\mu\text{m}$ and baseplate preheating at $200\text{ }^\circ\text{C}$) lead to a relative density of 99.5%. They also observed an inhomogeneous distribution of precipitates, mainly concentrated along the boundaries of heat-affected zones and recommended a solution annealing heat treatment to homogenize the microstructure.

Other researchers have also performed the tuning of the process parameters. The parameter tuning mainly concerns the laser power, the scan speed, and the hatching distance. When using laser power lower than 400W, the layer thickness is usually kept constant at 20 μm or 30 μm . Increasing the laser power leads to higher densities, while the hatching distance and scan speed have their optimal values depending on the layer thickness [112]–[116]. Jahns et al. [115] have also investigated the effect of the process parameters on surface quality. The surface roughness was between 8 and 16 μm on the side surface (i.e. the surface whose normal is perpendicular to the building direction) and 7 and 14 μm on the top surface (surface whose normal is parallel to the building direction). However, the parameters that led to samples with the highest relative densities also resulted in the roughest surface.

The microstructure depends on the heat treatment applied to the material. As-built components show a partially recrystallized microstructure with elongated grains along the printing direction smaller globular grains [111]–[114], [117]. The solution annealing heat treatment leads to a more homogenous recrystallized microstructure and removes the visible scan tracks [113], [117], [118]. Wallis et al. [113] have investigated the effect of different heat treatments on the microstructure and properties of the CuCrZr alloy processed by LPBF. Since the solidification rate in the LPBF process is high, a supersaturated solid solution is formed in the as-built state. Therefore, it is possible to avoid the solution annealing heat treatment (SA) and directly perform the age-hardening (DAH) heat treatment. The microstructure showed no particular variations from the as-built state with the DAH heat treatment, and the precipitates were too fine to be observed by SEM. Coarser precipitates formed at the grain boundaries were observed in the solution annealed + age-hardened condition (SA +AH). Furthermore, compared to a SA + AH heat treatment, DAH resulted in improved mechanical and thermal properties, with a hardness of ~ 200 HV1 and thermal conductivity of 300 W/mK. The highest UTS was obtained with the DAH heat treatment; compared to the as-built condition, it increased from 287 to 466 MPa, while the ductility decreased from 33% to 12%. Wegener et al. [117] also analysed the possibility of avoiding the solution annealing heat treatment. The results show that the highest combination of

hardness and electrical conductivity (151 HV 10 and 77% IACS) is obtained through the DAH heat treatment at 450 °C for 120 min.

In three separate studies, Jadhav et al. [110], [119], [120] improved the absorptance of the CuCr powder. In [119], adding carbon nanoparticles to CuCr0.3 powder improved the optical absorption from 44% to 56%. However, the segregation of carbon nanoparticles along the melt pool boundaries led to melt pool instability. Therefore, no improvement in densification was observed. In [110], the authors modified the particle's surface of CuCr1 powder by outward diffusion of chromium in the presence of a nitrogen atmosphere at elevated temperatures, reaching an optical absorption of ~70%. This allowed for the production of dense parts with a lower energy density input, limiting the risk of damaging the optical mirrors. However, for the fabrication of >98% dense parts, a minimum laser power of 400 W was required. After a SA+AH heat treatment, the parts exhibited good mechanical properties (331 MPa of yield strength) and high thermal (370 W/(mK)) and electrical (81 % IACS) conductivity. Finally, in [120], a further improvement of the densification of CuCr1 powder was obtained by the carburisation of the particles' surface. Heat-treating a 0.1 wt% carbon-mixed CuCr1 powder in an argon atmosphere produced a thin layer of chromium carbide (Cr_3C_2) and metallic chromium. Although the powder showed a lower optical absorption (62%) than the nitrogen treated CuCr1 powder, a laser power of 300W was sufficient for fabricating parts with a relative density higher than 98%. The authors attributed this opposite behaviour to the different thermal stability of the chromium nitride phases present on the surface of the nitrogen treated CuCr1 powder. CrN phases decompose at lower temperatures and have lower melting temperatures than the chromium carbide phase. Therefore, while processing the nitrogen-treated CuCr1 powder, a substantial reduction in the effective laser absorption may happen. Moreover, the precipitation of chromium carbide obtained with the SA+AH heat treatment led to better thermal (381 ± 6 W/(mK)) and electrical ($93 \pm 1\%$ IACS) conductivity but to lower mechanical properties (yield strength of 143 MPa). A higher strength was obtained with an optimized DAH heat treatment, reaching a yield strength of 347 MPa and tensile strength of 458 MPa.

Finally, since the rapid solidification rates in the LPBF process enable the formation of a supersaturated solution, studies with higher Cr content have been performed [95], [108]. The results suggest that increasing Cr concentration improves mechanical properties at the expense of conductivity.

1.3.4 Application: manufacturing of accelerator grids

The National Institute for Nuclear Physics (INFN), the Italian scientific organisation devoted to the investigation of matter's fundamental constituents, has several research lines dedicated to the study of subnuclear, nuclear, and astroparticle physics. Nuclear fusion is one of the research lines of the INFN-ENERGY research projects. In this research work, the characterization of pure copper and copper alloys generated using LPBF is primarily focused on that initiative.

1.3.4.1 Nuclear Fusion

The demand for energy production has been increasing for more than 50 years, with the only exceptions in the early 1980s and 2009, during the financial crisis. Transitioning from fossil fuels to low-carbon energy is problematic since these new forms of production must displace current fossil fuels and, in addition, fulfil the increased demand [121]. This challenge has refocused international research on nuclear fusion. Nuclear fusion energy might be a novel approach to generating environmentally friendly power, emits no greenhouse emissions, is inherently safe, has plentiful fuel supplies, and leaves no nuclear waste for future generations.

Fusing two or more nuclei into a heavier one releases a high amount of energy. The total mass of the products is lower than the reactants. As predicted by Einstein's equation $E = \Delta mc^2$, the mass variation is turned into energy in the form of radiation or kinetic energy of the particles. The Coulomb barrier between charged particles must be overcome to allow the fusion process to happen. Since the Coulomb barrier scales with the squared effective nuclear charge, light reactants (mainly deuterium, tritium, and helium-3) are utilized.

The only method to achieve nuclear fusion is for the matter to be in a plasma state, which must be adequately contained in terms of gravitational, magnetic, and inertial confinement. The tokamak configuration is currently the most promising technology for producing controlled thermonuclear fusion

power. The word tokamak comes from the Russian acronym meaning *toroidal chamber with magnetic coils*. Indeed, the tokamak design uses a strong magnetic field created by coils arranged in a toroidal configuration to confine the plasma. Figure 1.13 shows a schematic representation of such configuration.

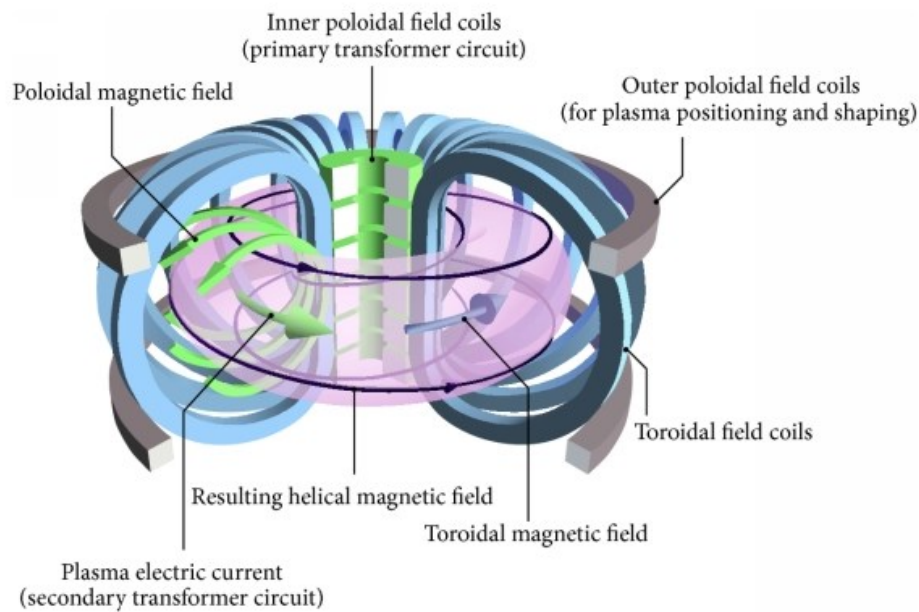


Figure 1.13 Scheme of the tokamak configuration [122].

The fusion devices of important research projects such as ITER (International Thermonuclear Experimental Reactor), DEMO (DEMONstration Fusion Power Plant), and DTT (Divertor Tokamak Test facility) are all based on the tokamak configuration.

The confined plasma must be heated to an exceedingly high temperature for sufficient fusion reactions to occur. Neutral Beam Injectors (NBIs) are one of three auxiliary heating systems used to heat the plasma. The accelerator grids are one of the system's components. In this research project, the possible improvement of the design of such parts through the LPBF technology is studied.

1.3.4.2 Neutral Beam Injector System

In many fusion studies across the world, neutral beam heating is regarded as the fundamental approach for supplying extra power. Accelerated neutral particles can penetrate the plasma's strong magnetic field. Inside the plasma, the particles ionize (and therefore are trapped by the magnetic field) and deliver energy to ions and electrons through collisions, thus heating the plasma. The only way to

create an accelerated neutral beam is to do it indirectly. The particles are first created as positive or negative ions within an ion source. These ions can then be accelerated as an ion beam using an electrostatic accelerator with a high electric field between separate grids. The accelerated particles are then neutralised with a neutral gas stripper. Before being fed into the plasma, the resultant beam is filtered in a residual ion dump by utilising an electric field to deflect the residual ions. Figure 1.14 shows a schematic representation of the NBI.

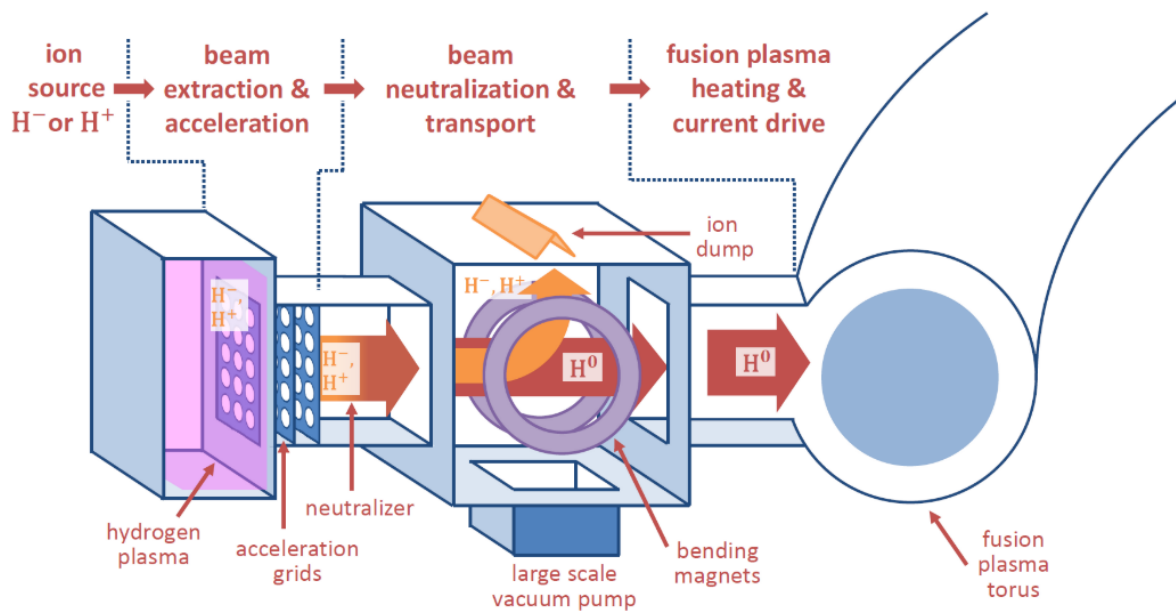


Figure 1.14 Schematic of a neutral beam injector system [123].

The neutralisation of high energy beams is efficient only if negative ions are used. The neutralisation efficiency of positive ion beams rapidly decreases with the beam energy [124]. As a result, the ITER and DEMO experimental reactors rely on accelerated negative ions to reach high performances.

1.3.4.3 Accelerator Grids Design

The accelerator's purpose is to accelerate the ion beam by creating a strong electric field between different grids. The number and design of such grids depend on the operating condition of the tokamak. For example, the SPIDER (source for the production of deuterium ion extracted from RF plasma) accelerator has three grids, the MITICA (Megavolt ITER injector concept advancement) accelerator has

seven, and the DTT accelerator is composed of five grids. The first two grids are the Plasma Grid (PG) and Extraction Grid (EG) and represent the extraction system of the ion beam. The successive grids, the Acceleration Grids (AG), compose the acceleration system. These grids have increasing potential and accelerate the negative ion beam. The last grid is the Ground Grid (GG), whose potential is 0 kV. The improvement of the grids' design considered in this thesis was developed following the design presented for the MITICA experiment. Agostinetti et al. [125] presented a detailed description of such grids.

One of the drawbacks of using negative ion beams is that electrons are co-extracted from the plasma source, making the design of the accelerator grids far more complex. Before they accumulate too much energy, the co-extracted electrons must be halted in the initial part of the accelerator. As a result, a series of magnets inside the EG create high localised magnetic fields, causing almost all co-extracted electrons to impact the EG itself. Other magnets are embedded on the AG grids to immediately stop other electrons generated inside the accelerator (mainly electrons generated by stripping reactions). The collision of the accelerated electrons with the accelerator grids generates extremely high and localized heat loads, which might damage the grids [126]. Therefore, the grids contain cooling channels to exhaust the heat loads on the grids. The heat loads' position lies around the beam apertures; the exact location depends on the type of accelerator and grid type. The main reason why the acceleration grids are made in pure copper is for the exhaustion of such high heat loads. Figure 1.15 shows an example of the cooling circuit and the peak temperatures of an accelerator grid.

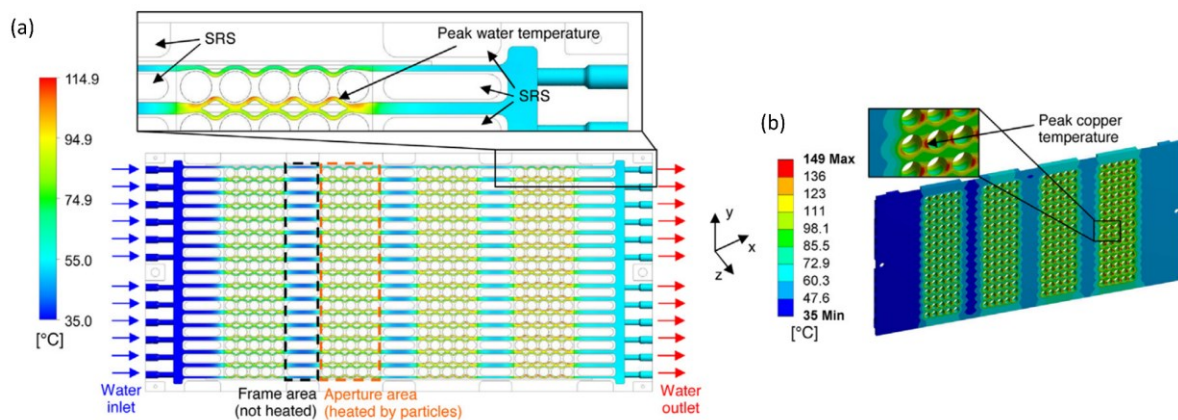


Figure 1.15 (a) Cooling circuit and water temperature of the G4 MITICA grid. (b) Peak temperature of copper due to localized heat loads [127].

Several research activities investigate the optimization of the cooling circuit [125]–[128]. Reducing the peak temperature is essential for several reasons. The mechanical properties of copper degrade with the temperature, and if the temperature is too high, the grid might deform. In addition, high peak temperatures reduce the fatigue life of the material [127]. Finally, if not adequately cooled, the grids might misalign due to different thermal expansion between the grids.

The impact of the LPBF technology on the improvement of the grids' design is straightforward. While standard manufacturing processes only allow for the creation of basic cooling channel geometries, the LPBF methodology allows for the creation of cooling channels with conformal designs that pass near the heat loads, increasing the cooling efficiency of the grids. Moreover, the traditional manufacturing procedure of the accelerator grids is highly complex and hence expensive. They require multiple milling steps, followed by copper electrodeposition for closing the cooling channels and the magnets slots [129]. With the LPBF process, the cooling channels and the magnets slots can be produced in just one step. The milling of the exterior surface and the polishing of the cooling channels are the only post-process procedures required with this process.

CHAPTER 2

2 MATERIALS AND METHODS

2.1 LPBF setup

All the specimens were manufactured by an EOSINT M280 powder bed machine equipped with a 400W ytterbium fibre laser. The technical specifications of the LPBF machine are summarized in Table 2.1.

Table 2.1 Technical specifications of the employed EOSINT M280 LPBF machine.

Technical Data	EOSINT M280
Building volume	250 x 250 x 325 mm
Laser source	Ytterbium fibre laser; 400 W
Precision optics	F-theta lenses; high-speed scanner
Scan speed	up to 7.0 m/s
Focus diameter	100 μm
Minimum layer thickness	20 μm
Power supply	200 – 240 V
maximum power consumption	5.5 kW
Compressed air supply	7,000 hPa; 20 m ³ /h
Argon supply	4,000 hPa; 100 l/min during the inertization of the building chamber, up to 2.5 l/min during the manufacturing
Machine dimensions (w x d x h)	2200 mm x 1070 mm x 2290 mm
Net weight	approx. 1250 kg (without powder)

The calibration of the laser beam resulted in a slightly inferior beam focus from the one reported in the technical specifications: it was 82 μm rather than 100 μm . It had a Gaussian profile with a wavelength of 1064 nm. Stainless steel (AISI 304L) platforms were used as substrate and were heated to 40 ° C. Compared to copper platforms, steel guarantees higher thermal stability due to the lower thermal conductivity, and higher relative densities are obtained for the same energy input [89]. Argon or nitrogen gas was employed as a protective gas during the production process, and the oxygen concentration was controlled below 0.2%. Each specimen was settled on at least 3 mm support structures. A high-speed steel recoating blade was used to distribute the powders. Unless otherwise specified, the scan strategy adopted was a bidirectional (zigzag) 5 mm stripe pattern with a rotation angle of 67° between neighbouring layers.

2.2 Material characterization

❖ Optical and scanning electron microscope

The microstructure of the studied materials was observed using a Leica DMRE optical microscope. The samples have been ground on silicon carbide papers (500 – 4000) and polished using a 1 μm diamond suspension. A solution of 1 ml HCl, 2.5 g FeCl₃, and 100 ml EtOH was used to etch all the samples.

The morphology of the powder, the melt pools, the as-built surfaces, and the fracture surfaces of CuCrZr samples were observed with a Cambridge Leica Stereoscan LEO 440 scanning electron microscope (SEM) using secondary electrons equipped with a Philips PV9800 EDS probe.

❖ X-ray diffraction

A Bruker D8 x-ray diffractometer equipped with a CuK α X-ray tube was employed to perform peak shape analysis to evaluate the oxidation level of the oxidized powder and to detect the precipitates of heat-treated CuCrZr samples. Diffraction spectra were collected using a step size of 0.025° within the 30–80° 2 θ range for the oxidized powder and within 40–80° 2 θ for CuCrZr samples. Peak detection

was performed using the Savitzky-Golay finite impulse response (FIR) smoothing filter of polynomial order 3 and frame length 21.

❖ Powder flowability

The powder flowability was tested with the Hall flowmeter funnel (Figure 2.1) according to ASTM B213-17 [130].

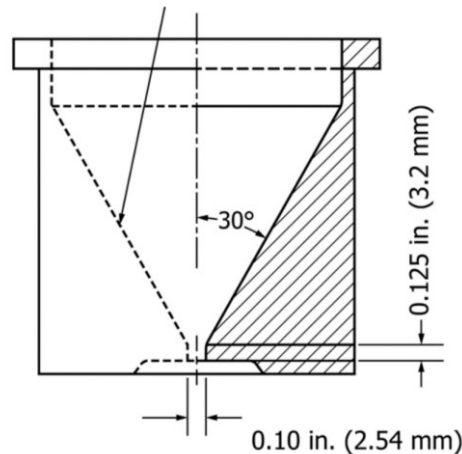


Figure 2.1 Hall Flowmeter Funnel [130].

50g of powder is run through an orifice with a 2.54 mm diameter, and the flow time is measured from the start of the flow until all the powder is passed through the orifice.

The same apparatus was used to measure the apparent density of only powder A following the ASTM-B212 standard [131]. This standard uses the Hall flowmeter funnel to measure the apparent density of the powder: the powder is run through the funnel into a cylindrical brass cup with a capacity of 25 mm³, and the mass of the powder is weighted. The ratio between the mass of the powder and the cylinder's capacity is the powder's apparent density.

❖ Optical absorption

The characterization of the optical absorption was carried out on a Jasco V-570 spectrophotometer with integrating sphere ISN-470, with a range of 200 – 850 nm. The measurements were performed on tables produced with 10 g of virgin powder. The results of the optical absorptivity are not analysed in their absolute value but only as a comparison between the powders since it was not

possible to measure the absorptivity at 1064 nm, i.e. the wavelength of the infrared laser used in this study.

❖ Particle Size Distribution

A Mastersizer 2000 laser diffraction particle size analyser has been used to measure the particle size distribution. The description of the technique is presented in [Section 3.1](#).

❖ Density measurements

The relative density measurements have been performed on cubes with a side of 10 mm (copper samples) and on cylinders with 10 mm of diameters and 10 mm of heights (CuCrZr samples). The samples' density was determined using the Archimedes method using an analytical balance MettlerToledo® ME104 (capacity 120g, 0.1 mg readability) following ASTM B311-17 standard [132].

The samples were first sawed off the platform, and the rough surface in contact with the supports was then polished. The samples were dried the night before each weighted step in an oven at 60 °C. Each sample's mass was measured three times in air and five times in deionized water, ensuring no air bubbles were attached to the surface during the water measurements. The density was calculated using the following Equation (2.1):

$$\rho_{bulk} = \frac{m_{dry} * \rho_{water}}{m_{dry} - m_{water}} \quad (2.1)$$

where ρ_{bulk} is the density of the specimen in g/cm³, m_{dry} is the mass weighed in air, m_{water} is the mass weighed in deionized water, and ρ_{water} is the density of the deionized water (the temperature of the water was monitored during the measurements, and the density is varied according to it). A drop of a wetting agent was added to the water to lessen the effects of surface tension. The relative density ρ_{rel} is the ratio between the obtained density ρ_{bulk} and the theoretical one ρ_{Theo} :

$$\rho_{rel}[\%] = \frac{\rho_{bulk}}{\rho_{Theo}} \quad (2.2)$$

The theoretical density of pure copper used for this research work was 8.96 g/cm³ [133]. As a reference density for pure copper, literature offers a range of theoretical densities between 8.91 g/cm³

and 8.96 g/cm³. It was decided to take the highest number to be more conservative. The theoretical density of CuCrZr used as a reference was 8.89 g/cm³.

An alternative way to measure the relative density of the components was to analyse the cross-section of the samples. The software ImageJ was used to quantify the percentage of porosity of each section. The inbuilt “default” function (a variation of Ridler and Calvard's 1978 IsoData method) was used for auto-thresholding [134]. The micrographs were recorded using a Leica DMRE optical microscope with a magnification of 100. The reported measurements are the average of six values.

❖ Thermal diffusivity

The thermal diffusivity has been measured by means of a Transient Hot Disk TPS 2500 S. The instrument is based on the Hot Disk technique. An accurate description of the procedure can be found in the literature [135]. A sensor disk is placed between two disks of 40 mm diameter and 8 mm thickness of the analysed material to perform the measurements. The sensor disk is a double spiral made of nickel, is insulated with a Kapton film, and is used as a transient heater and as a precise temperature transducer. The measure is repeated ten times, and the average value is reported. The instrument uncertainty is 5%. The thermal conductivity has been calculated as follows:

$$\lambda = a * c_p * \rho \quad (3.3)$$

where λ is thermal conductivity (W/(m*K)), a is thermal diffusivity (mm²/s), c_p is the heat capacity of pure copper (0.385 J/g/K) [133], and ρ is the density of the specimen (g/cm³). The disks have been printed in both vertical and horizontal directions to determine the thermal conductivity anisotropy of CuCrZr. Figure 2.2 shows the build job with the oriented disks.



Figure 2.2 Thermal conductivity and tensile specimens manufactured in horizontal and vertical directions.

❖ **Electrical resistivity**

The electrical resistivity measurements presented in this paper have been obtained using a Van der Pauw (VdP) four-probe set-up. The VdP system uses four small Au contacts located at the periphery of a flat film specimen. A current is applied between two tips while the other two measure the voltage drop; in this way, the resistivity measurements are independent of leads and contact resistivity. The shape of the specimen must be flat with a uniform thickness. A detailed description of the procedure used to measure the electrical resistivity can be found in [136].

Four square samples of 100 mm side length and 0.75 mm thickness have been printed vertically to avoid the excessive use of supports. A single contour scan strategy was adopted to have a higher thickness precision. The tips holes were located at the edges of the square. Figure 2.3 shows the experimental setup.

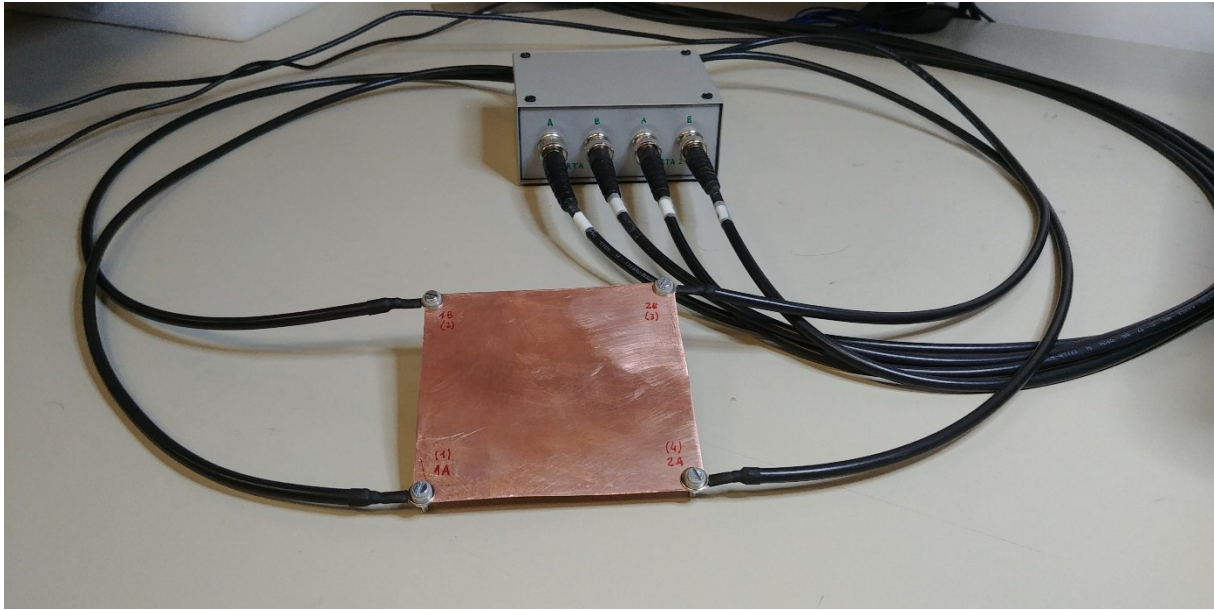


Figure 2.3 Experimental Van der Pauw (VdP) four-probe set-up.

❖ Mechanical properties

Micro-hardness measurements were performed on the samples on a Leitz Miniload 2 (Leica Microsystem S.r.l., Milan, Italy) micro-hardness tester with a 300 g load. The reported results are an average of 5 measurements.

Tensile tests have been performed in accordance with ASTM E8/E8M-16a standard [137] on cylindrical dog bone tensile specimens. The tensile samples have been in horizontal (XY plane) and vertical (XZ plane) directions. The specimens have been machined to a gauge length of 24 mm and a 6 mm diameter. Figure 2.4 displays the geometry of the samples. All the specimens have been tested on an MTS 858 Mini Bionix II with a displacement rate of 0.45 mm/min.

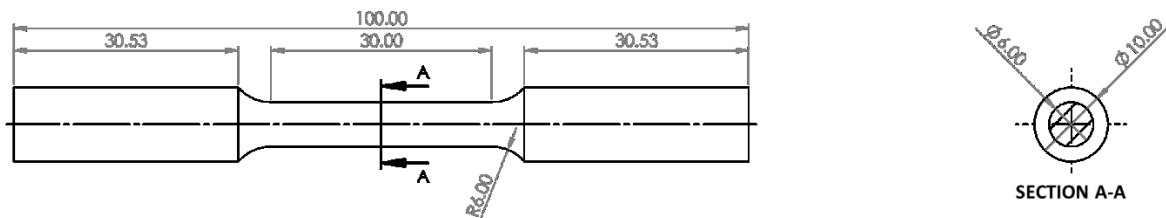


Figure 2.4 Geometry of the machined tensile specimens tested using MTS 858 Mini Bionix II.

For the tensile test shown in Section 3, four specimens of pure copper components for each condition have been tested, and the strain was measured with an MTS extensometer 632.29F-30 with a gauge length of 5 mm.

For the CuCrZr samples, two specimens for each condition have been tested. Two MTS extensometers have been applied: an MTS 632.13F-20 with a gauge length of 10 mm for the determination of Young's module and an MTS 634.12F-24 with a gauge length of 25 mm for the determination of the elongation at break. The reported yield strength and tensile strength have been measured with both extensometers.

For the pure copper samples provided by the EOS and TRUMPS companies, an MTS extensometer 634.12F-24 with a gauge length of 25 mm was used to measure the strain. After the fracture, the elongation at break was measured by fitting the two halves of the test specimen together and measuring the distance between gauge marks that were applied before the test. Due to damage to the surface created during milling, a horizontal EOS sample was discarded.

❖ **Surface roughness analysis**

The lateral surface roughness of copper parts was measured on thin walls with dimensions 20×2×10 mm using a portable roughness gauge RUGOSURF 10G, following the ISO 4288:1998 standard [138]. The Ra roughness value is reported; it is defined as the arithmetic mean value of the deviations of the actual profile of the surface with respect to the mean line. The measurements have been repeated eight times through the build direction, and the average values are reported. Hydraulic tests

The hydraulic tests were carried out in an experimental setting at the University of Padua's Department of Management and Engineering. The test rig consists of a water loop where the fluid temperature and flow rate may be adjusted and regulated separately. The water temperature was monitored using calibrated T-type thermocouples with an accuracy of ± 0.05 K, while the pressure drops were recorded using a differential pressure transducer with an uncertainty ($k=2$) of $\pm 0.065\%$ of the full scale (FS= 1 bar). The tests were done with a water flow rate ranging from 1 to 14 l/min, and several

curves were obtained by increasing and lowering the water flow rate to validate the repeatability of the results successfully.

2.3 Characterization of CuCrZr surface roughness

The characterisation was carried out at the University of Padua's TE.SI. Laboratory. The surface roughness measurements have been performed using the Sensofar S neox v3 optical profilometer and following the ISO 25178 standard [139]. The equipment uses the Focus-Variation approach to capture a series of light reflected images from the surface at various heights. The surface topography is then constructed using an algorithm that recognises the regions in focus in each image and relates them to the height at which the image was taken.

The S_a surface roughness parameter is reported. S_a is the arithmetic mean of the surface deviations, and it is defined as:

$$S_a = \frac{1}{A} \iint_A |z(x, y)| dx dy \quad (3.4)$$

where $z(x,y)$ is the surface height in the (x,y) position and A is the analysed area.

THE Nikon MCT225 Metrology CT system was used for selected specimens' X-ray computed tomography scans. An X-ray beam scans the component, which is rotated around its z-axis, and a detector creates a series of 2D greyscale images. These images show the intensity of the captured beam, which is attenuated depending on the material and thickness of the component. A three-dimensional matrix can be generated using an algorithm, with each cell, or voxel, having a grey value. The scanned object's surface, components, internal flaws, and materials may then be identified using this matrix.

powder, which is the second level. The flowability and packing density are two crucial characteristics of the powder's behaviour. The powder packing density is defined as the ratio between the volume of the particles and the volume of the container that houses them (in the LPBF case, the layer volume), and the powder flowability is the displacement of powder particles with respect to each other or along the container wall surface. Finally, the third level describes the behaviour of the powder while being processed. The significant aspects addressed for the LPBF method are the spreadability (the powder's ability to be spread homogeneously) and the interaction between the powder bed and the laser beam.

High flowability and high packing density are required powder properties for the LPBF process to guarantee successful material deposition and component densification [141]. Powder with good flowability is desired because it ensures a homogeneous distribution of the powder without variations of packing density in the powder bed. The packing density of the powder bed, on the other hand, affects the total amount of energy that reaches the underlying layer. The heat penetration of a loosely packed powder is reduced because the effective powder layer thickness is larger [142], preventing an effective re-melting of the previous layer or even of the powder itself [143]. In addition, a densely packed powder shows higher thermal conductivity due to the increased coordination number and points of contact between the particles [144]. Impurities of the powder may affect the powder's behaviour as well. For example, powder with high moisture content has reduced flowability [145].

During the LPBF, the interaction between the laser and the powder can result in powder contamination due to various events (spatter, partial fusing, oxidation, agglomeration) [146]. Reusing the un-melted powder several times will deviate its characteristics from its initial state and affect the bulk characteristic of the printed parts [146], [147].

Compared to particles with irregular shapes, particles with a spherical morphology have superior flowability and packing density and are hence favoured for this application. The particles' morphology depends on the atomization technique. The most common atomization techniques in the powder metallurgy industry are the water and gas atomization processes. While the gas atomization method produces spherical particles, water atomized powders have a more irregular shape due to the faster

cooling rates and shorter time for spheroidization [148]. Moreover, water atomized powders have a higher oxygen content level, which further reduces the densification process as it increases the surface tension of the melt pool, resulting in narrower scan tracks and reducing the wettability [149], [150].

While the morphology selection is straightforward because of the advantages of spherical particles, choosing the size and distribution of the powder is more complex. In fact, the granulometry of the powder has opposing effects on flowability and packing density. The packing density benefits from a wide range of particle sizes since small particles may fill the air spaces between bigger particles in the powder bed. Moreover, the presence of a significant number of fine particles can enhance the densification process, as an inferior energy input is required to melt them [142]. On the other hand, smaller particles tend to agglomerate more because of the cohesive Van der Waals forces and the increased inter-particle friction forces, limiting the powder flowability and hence hindering the formation of a homogenous layer [141], [151]. The PSD impacts surface quality as well; a narrow distribution of fine particles allows for the deposition of thinner layers, which improves the part's surface roughness [143]. In addition, the presence of larger particles might degrade the surface's quality by attaching to it [147].

Finally, the PSD plays a critical role in the interaction of the material with the laser beam. As already mentioned, the absorptance of material in powder form is significantly higher due to multiple scattering of the laser between the particles [152], as shown in Figure 3.2. In addition, when fine particles are utilized, the optical absorption is further increased since they have a more extensive surface area to absorb more laser energy [153].

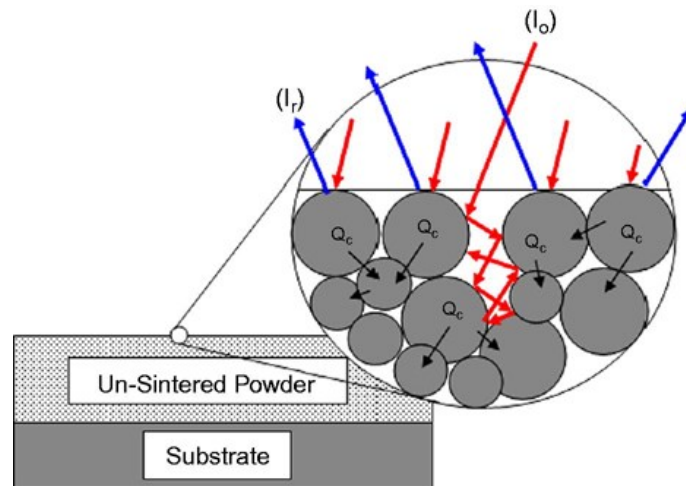


Figure 3.2 Multiple scattering of the laser beam between the powder particles [152].

King et al. [27] simulated the interaction of a laser beam using different PSD and material properties. The calculations show that the PSD has little effect on optical absorption for low-reflective materials, whereas highly reflective materials' optical absorptions are quite sensitive to the particle structure. In particular, it is crucial to have a high packing density to reduce the interaction of the laser beam with the highly reflecting substrate. The fine grains displaced between the inter-particle pores scatter the laser rays and prevent them from being reflected from the flat substrate. In contrast, Khan and Dickens [152] measured the reflectivity of copper powder with different PSD. The results revealed that a lower packing density favours absorption because the spaces between the particles allow more irradiation to permeate through, resulting in a higher optical penetration depth. Therefore, using a higher packing density increases the probability of irradiating particle surfaces, but it also limits the beam transmission to the underlying substrate. This problem could be minimized by reducing the layer thickness, a feature that is possible when fine powders are used [141].

Several techniques are available to measure the particle size distribution of the powder. The simplest one is to sieve the powder using a series of decreasing mesh sizes; the amount of powder retained in each sieve will describe the PSD [154]. The laser diffraction approach is the most common since it is faster and more reliable [141]. This approach provides a PSD spectrum by analysing the scattered rays of a laser beam travelling through a diffuse dispersion of particles. The computed PSD are reported as equivalent spherical diameters since the particles are considered spherical [155].

Therefore, this method is less reliable when analysing powders with irregular surfaces [141]. Figure 3.3 shows an example of a PSD obtained using the laser diffraction method. The DXX value represents a particle diameter, and the XX values indicate the volume percentage of powder with a diameter lower than the reported one. For example, D10 = 15 μm means that 10% of the powder has a diameter lower than 15 μm . Thus, the D50 is the median.

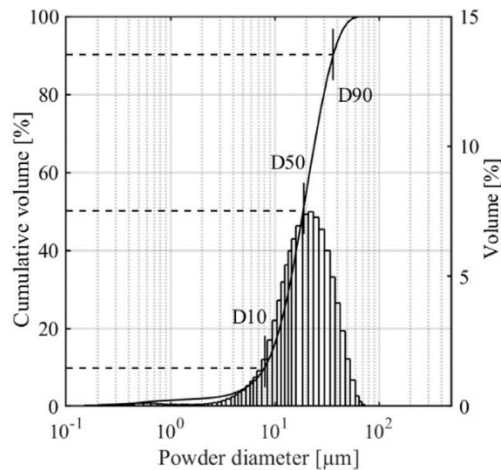


Figure 3.3 Example of a particle size distribution obtained using the laser diffraction method [156].

Since the PSD affects the critical factors that prevent the printing of pure copper (the reflectivity and thermal conductivity of the powder), designing the granulometry of the powder could be beneficial for the densification process. Using a powder with a higher packing density could improve the absorptivity at the expense of higher thermal conductivity. Sinico et al. [82] enhanced the fusion behaviour of copper powder particles and the concomitant part density by using a finer PSD of 10–35 μm . Compared to a standard PSD (15–45 μm), finer distribution improved relative density from 88.4% to 98.1%. The SLM machine used in that study was a SISMA mysint100 PM, equipped with a 200 W laser power and a spot diameter of 30 μm . Despite the densification enhancement, it was impossible to fabricate near full density samples due to the low laser power.

This work continues the research on the PSD effect on the processability of pure copper powder using a 370 W LPBF machine. The effect of hatching distance and laser scan speed on the relative density was analysed. A contour scan strategy has been tested for the improvement of the

lateral surface finishing. Finally, the optimal process parameters were used to manufacture samples to characterise mechanical and thermal properties.

3.2 Materials and methods

3.2.1 Powder characterization

The present research tested gas-atomized copper powders with three different particle size distributions. The powders were supplied from different producers, labelled A, B, and C. The manufacturers have provided chemical composition and laser diffraction data of the powders. Table 3.1 reports the chemical composition of the three powders.

Table 3.1 Chemical composition of the copper powders.

	Cu wt%	O wt%	Zn wt%	P Wt%	Sn Wt%
POWDER A	99.96	0.032			
POWDER B	99.95				
POWDER C	99.57	0.25	0.07	0.06	0.05

Company A and B provided electrolytic tough pitch (ETP) copper powder with 99.95% pure copper. The chemical composition of powder C presented a higher concentration of impurities: O 0.25%, Zn 0.07%, P 0.06%, and Sn 0.05%.

Even low levels of contamination have a massive impact on the conductivity of pure copper; Figure 3.4 shows the effect of various elements. Zinc and oxygen do not hinder conductivity as much as tin and phosphorous. Especially phosphorous has a severe negative effect on pure copper's conductivity. Therefore, Powder C has reduced conductivity compared to powder A and B, a critical factor that contributes to improving the densification process.

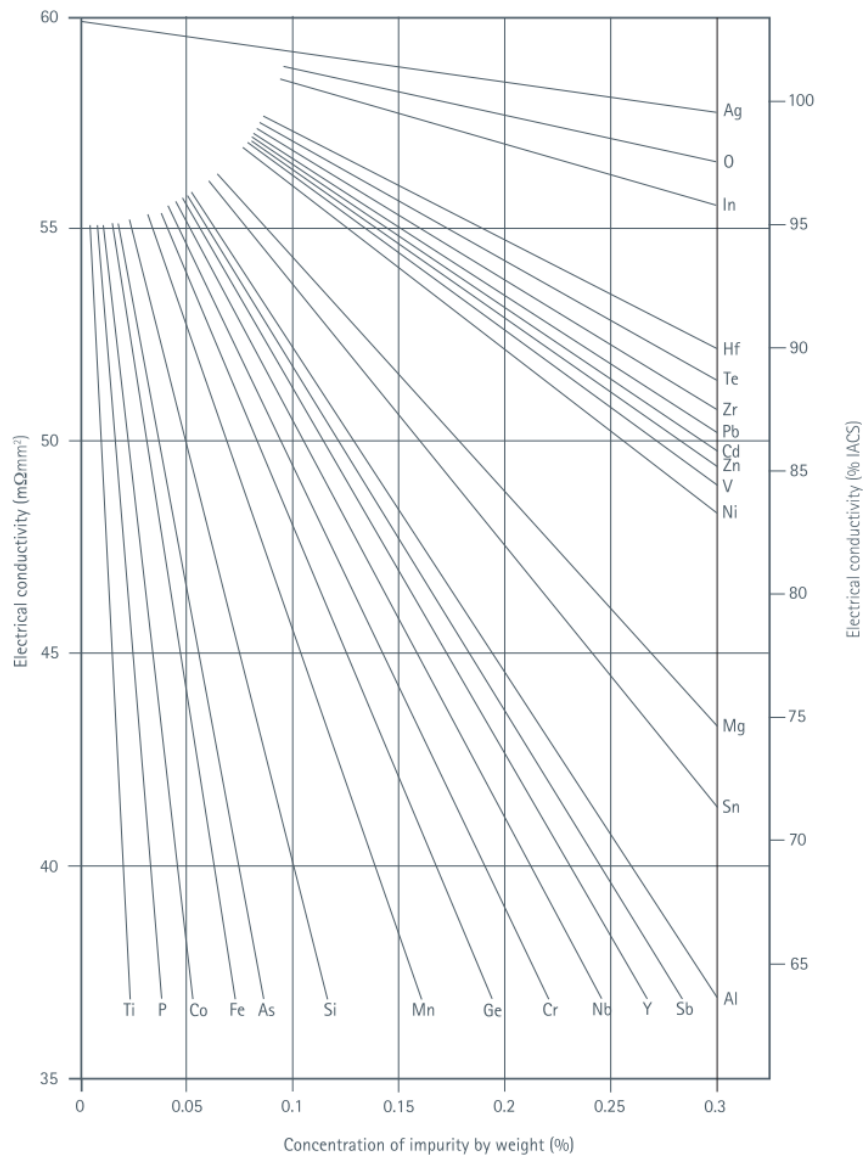


Figure 3.4 Effect of element impurities (or additions) on the conductivity of pure copper [157].

The particle size distributions of the copper powders are reported in Table 3.2 and Figure 3.5. Company A only reported the D values, while Companies B and C also reported the cumulative curves.

Table 3.2 Particle size distribution of the copper powders.

	D10 [μm]	D50 [μm]	D90 [μm]	SPAN (D90-D10)/D50
POWDER A	18.5	27.4	40.6	0.81
POWDER B	8.1	18.7	36.4	1.51
POWDER C	12.5	19.5	28.2	0.81

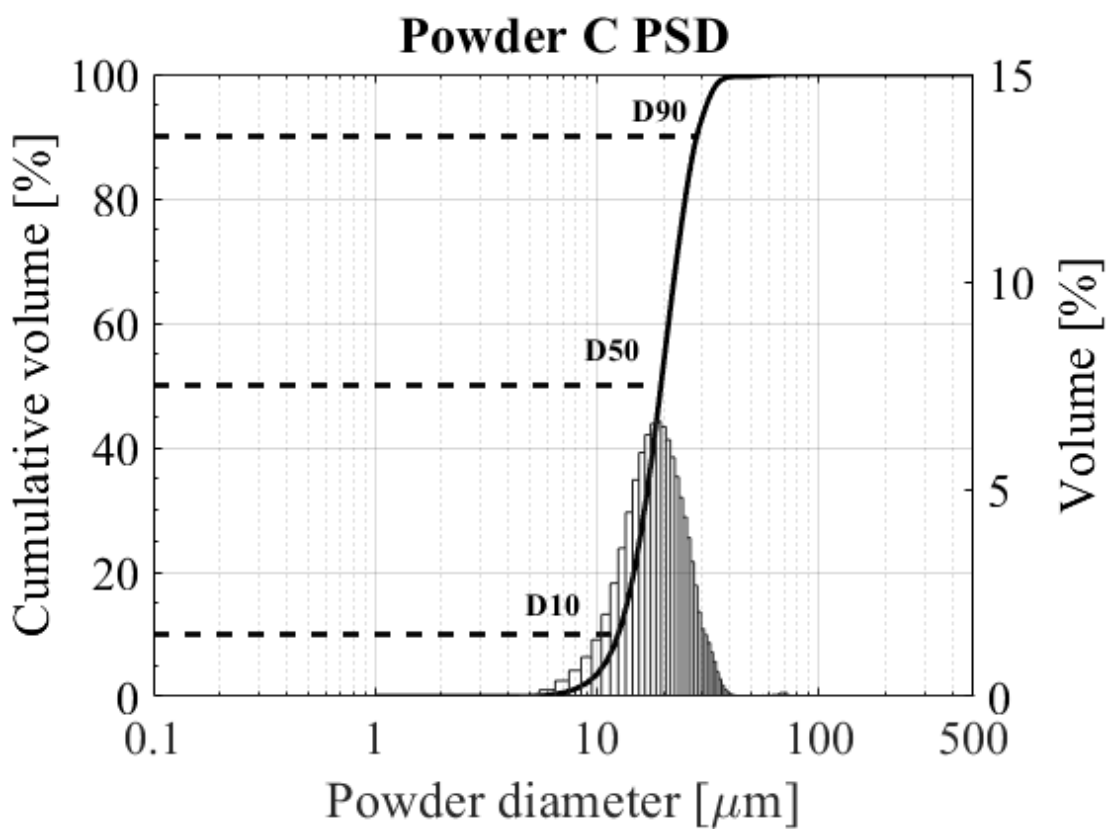
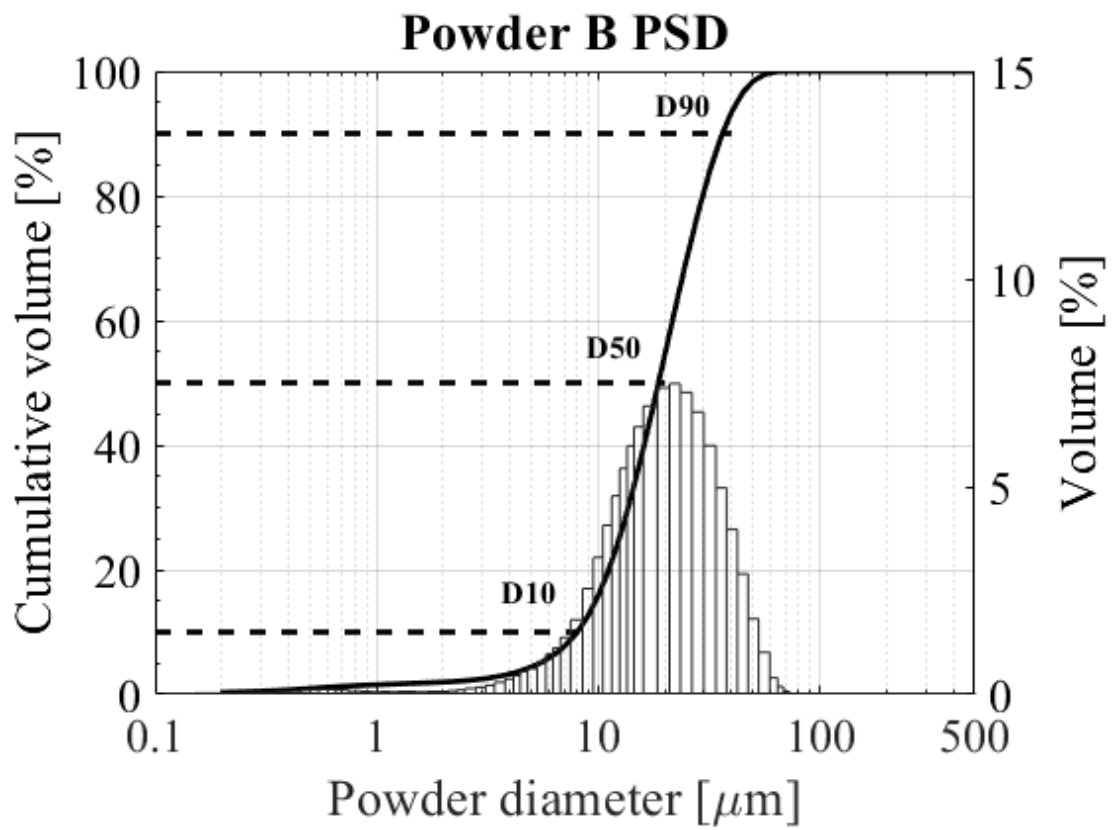


Figure 3.5 Particle size distribution of the powder B (top) and powder C (bottom).

The D10-D90 distribution of powder A is 18.5 - 40.6 μm . This distribution is commonly called 15-45 μm and is the standard distribution that several companies offer for the LPBF process. The SPAN index $\left(\frac{D_{90}-D_{10}}{D_{50}}\right)$ indicates the width of a Gaussian distribution and is 0.81 for both powder A and C. However, Powder C has much finer particles, with a distribution between 12.5 and 28.2 μm . A broader distribution was shown by powder B: the D10-D90 distribution is 8.1 – 36.4 μm , and the SPAN index is 1.51. Powder B presents more fine particles than the other powders ($D_{10} < 10 \mu\text{m}$), these particles can settle between the bigger particles and increase the packing density.

The powder flowability was tested with the Hall flowmeter funnel. Only the powder with standard PSD (powder A) presented a flow rate of $19.1 \pm 1.2 \text{ s}/50\text{g}$, while the powders with finer particles did not flow, even when using the dynamic method. Despite being ASTM's recommended characterisation technique for metal powders for AM, Spierings et al. [158] claim that it is not a suitable approach for quantitative findings. The operator filling method affects the result, and it does not represent the spreading behaviour used in the LPBF machines. However, it can be helpful as a comparison between different powders. The presence of finer particles has incremented the interparticle friction and blocked the flow of powders B and C.

Nevertheless, this does not mean that the powders cannot be used for the LPBF process. In a research activity performed by Engeli et al. [159], a powder with similar PSD to powder B yielded good flowability. The results obtained showed that a SPAN index of 1.5 is the higher limit for yielding enough flowability to form homogenous layers. Indeed, no powder flowability issues have been observed during the recoating.

Since only powder A was fluid enough to run through the Hall flowmeter funnel, it was only possible to measure the apparent density of powder A, which resulted in $4.69 \pm 0.01 \text{ g}/\text{cm}^3$.

The presence of fine particles reduces the flowability, but also the morphology of the powder has a negative effect. Less spherical particles or satellites attached to the particles are common morphology defects that hinder flowability [151], [159].

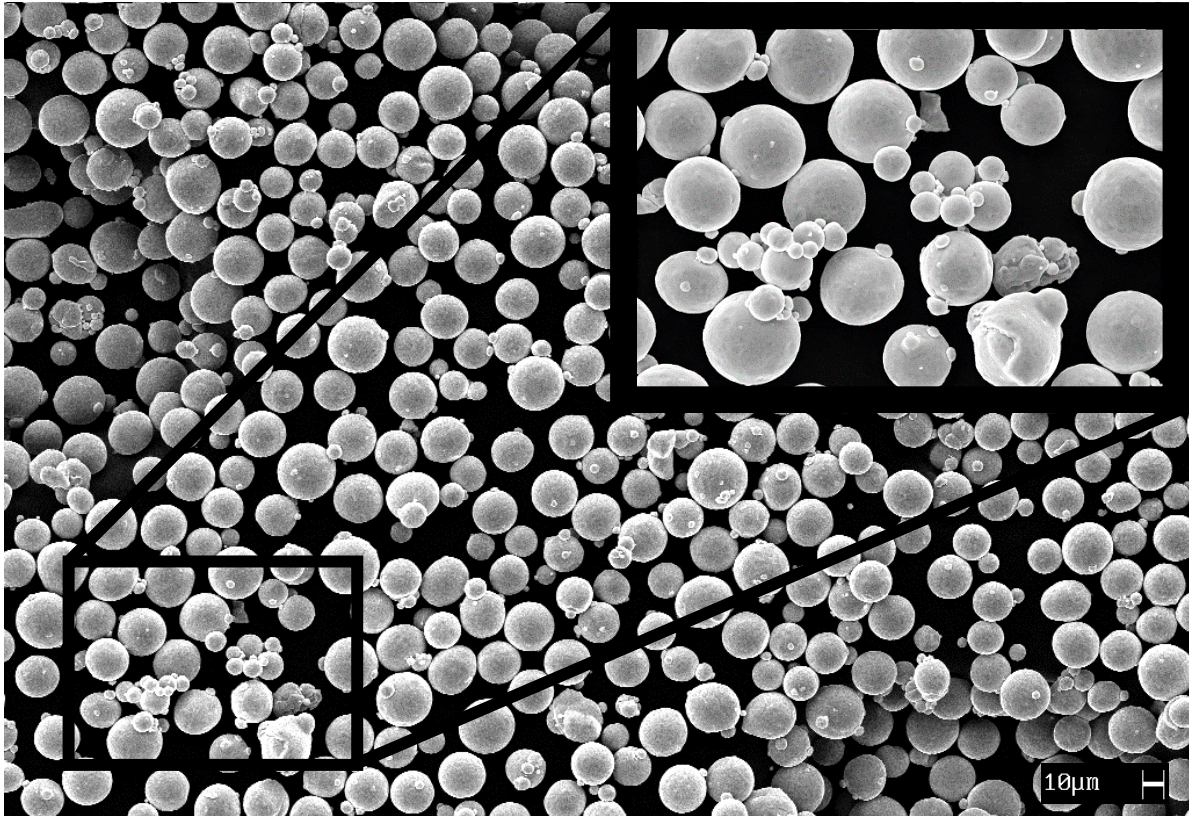


Figure 3.6 Secondary electron image of copper powder A with a focus on agglomerates and superficial defects.

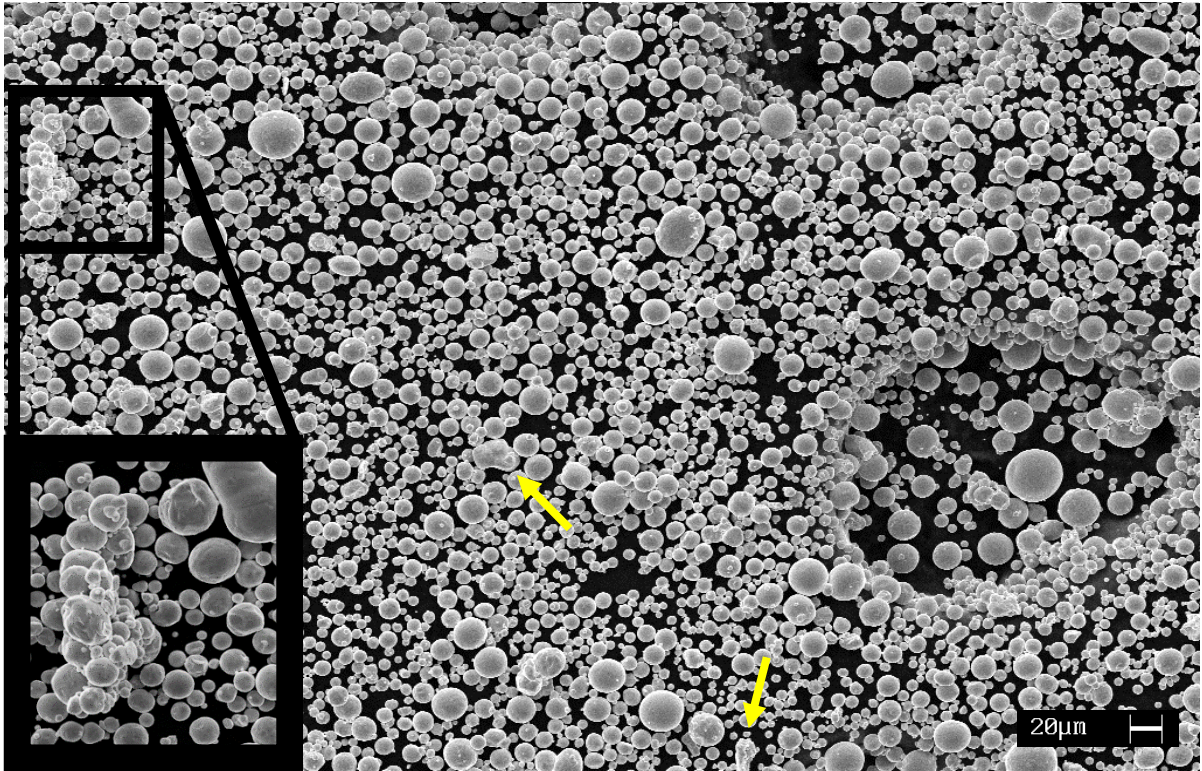


Figure 3.7 Secondary electron image of copper powder B with a focus on an agglomerate of fine particles. The yellow arrows indicate deformed particles.

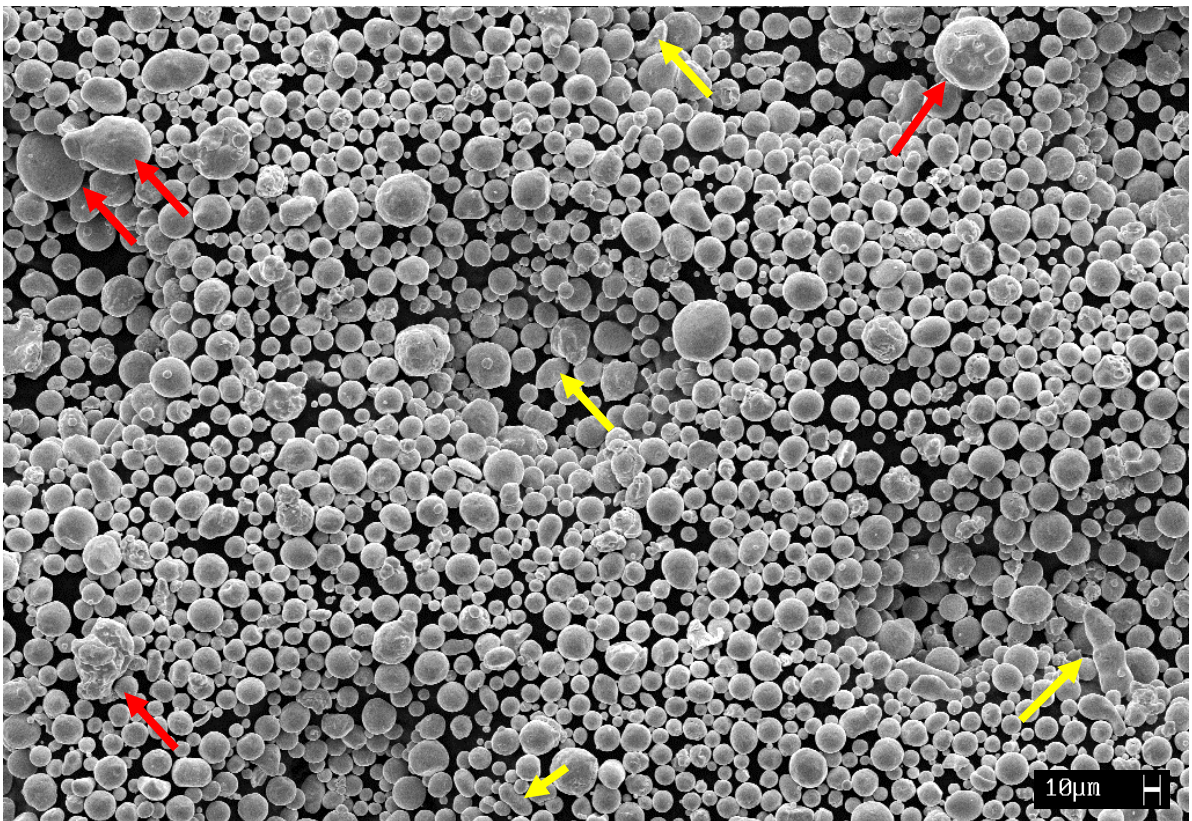


Figure 3.8 Secondary electron image of copper powder C; the red arrows indicate melt ejections while the yellow arrows indicate deformed particles.

Figure 3.6, Figure 3.7, and Figure 3.8 show the morphology of powder A, B, and C, respectively. The images were obtained after the first manufacturing process in order to check any defects caused by the manufacturing (spatters, semi-molten powder) and recycling procedures (handling operations of the powder and sieving). The circularity of the powders was measured using the ImageJ software.

Powder A consists of spherical particles with a circularity of 0.88 ± 0.03 and smooth surfaces. This powder presented the lowest amount of defects; however, agglomerates of fine particles, deformed particles and satellites were observed. Less spherical particles were observed in powder B. The measured circularity was 0.81 ± 0.04 . Because of the increased number of fine particles, powder B had the most agglomerates, which were significantly larger than those seen in powder A. These agglomerates might have formed due to melt ejections colliding in mid-flight or settling on the powder bed while still molten. While powder B presented some deformed particles, the highest amount of irregular particles was observed in powder C (indicated in both images with yellow arrows). Gasper et al. [160] described the mechanism that causes these particles to form: these are spattering particles that travel through the laser beam and are heated to the same degree as melt ejections, resulting in severe deformations. Although the particles in powder C were spherical, the large proportion of deformed particles resulted in a circularity value of 0.80 ± 0.05 . Furthermore, many melt ejections with bigger diameters than powder particles were found in powder C (indicated with the red arrows).

Figure 3.9 reports the Energy Dispersive X-ray Spectroscopy (EDS) analysis performed on the particles to check the chemical composition. It was found that many particles with irregular surfaces were oxidized. At the melt pool, oxide spots develop, and when expelled, these oxides remain attached to the spatter particles [160].

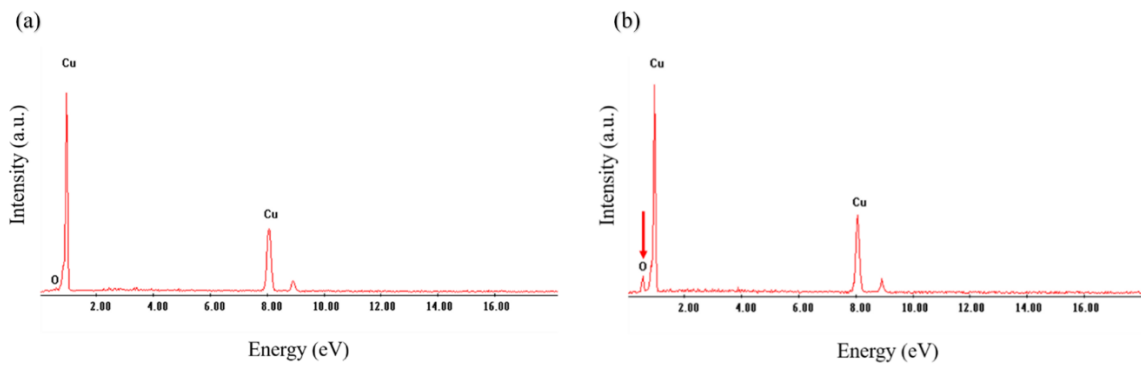


Figure 3.9 EDS analyses on powder C: (a) spherical particle; (b) particle with irregular shape.

The measurements of the optical reflectivity of the copper powders in the 400-850 nm wavelength range are shown in Figure 3.10. Although all powders had varied absorptance behaviours, powders A and B had similar reflectivity in the infrared spectrum, $\sim 65\%$ at 850 nm. Sinico et al. [82] presented similar results: at 850 nm, they obtained a $\sim 65\%$ reflectivity for the powder with standard distribution and $\sim 68\%$ for the distribution 10 – 35 μm . According to their findings, if the absorptance behaviour of powders A and B is the same as the one presented by Sinico et al. [82], both powders should have a reflectance of $\sim 68\%$ at 1064 nm. Other research works have obtained similar results measuring the optical absorptivity of pure copper [96], [120]. However, the reflectivity of powder A seems to increase at a higher pace in respect of powder B, so probably its value is slightly higher at 1064 nm. A possible explanation for this phenomenon is that powder A consisted of bigger particles that exposed a larger surface area, which increases the reflectivity. Furthermore, because the powders were compacted into tables, the packing density for all distributions was likely identical, and thus the penetration depth for all powders was minimal.

Finally, powder C exhibited the lowest reflectivity, $\sim 55\%$ at 850 nm. It is most likely that the chemical impurities in the composition, rather than the PSD, are the primary source of this discrepancy. Therefore, the less pure chemical composition of powder C benefits the densification process, as both the reflectivity and thermal conductivity are reduced.

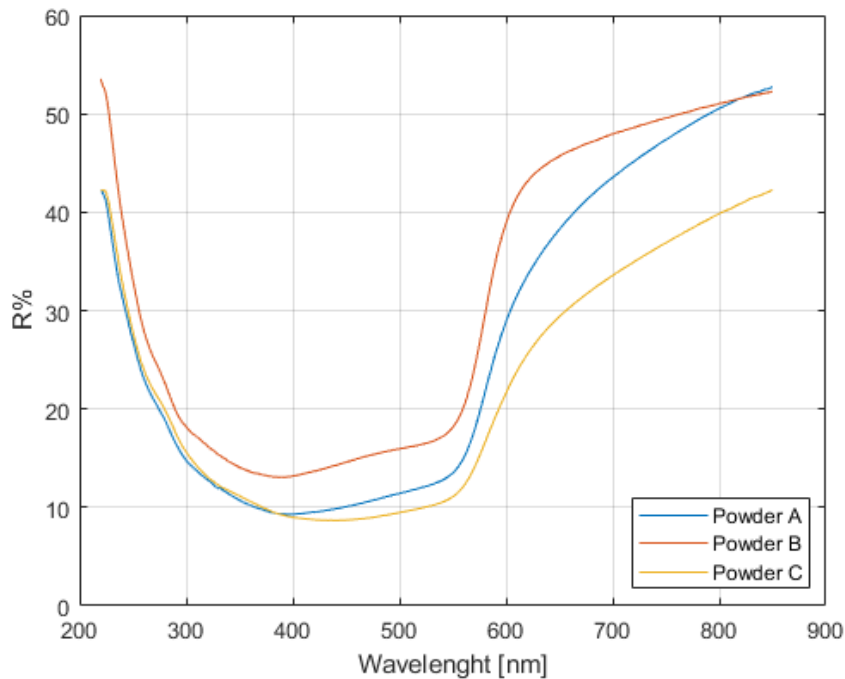


Figure 3.10 Laser reflectance measurements of the pure copper powders with different PSDs.

3.2.2 Experimental plan

The tuning of the process parameters was performed only for the hatching distance (h) and the scan speed (v), while the laser power (P) and the layer thickness (t) were kept at 370 W and 20 μm to maximize the volumetric energy density input (E).

The decision on the range of scan speed and hatching distance to test was the initial stage in the process parameter tuning approach. The influence of the scan speed on the melt pool width was analysed by producing 16 single scan tracks (SSTs) on top of four cubes. The cubes were produced using a laser power of 370W, a layer thickness of 20 μm , a scan speed of 400 mm/s, and a hatching distance of 0.08 mm. It was decided to manufacture the SSTs over the manufactured samples to ensure the same physical conditions that develop during the melting process. Because the heat conductivity of the stainless steel platform differs from that of the fabricated copper, manufacturing the SSTs over the building platform would have generated different results. In addition, it ensured the same effective layer thickness that develops during the manufacturing process. The scan speed was varied in 50 mm/s increments between 100 and 850 mm/s, and the laser power was kept constant at 370W. This test was performed using the

powder C. The stability of the melt pool was observed with an SEM microscope, and the width was measured using the ImageJ software. After this step, 16 blocks for each powder have been manufactured by varying four values of hatching distance and scan speed. Selected specimens with the highest density have been polished and chemically etched to be observed at the optical microscope.

The tuned parameters have been used to manufacture specimens for thermal conductivity measurements and tensile tests.

Finally, the lateral roughness of thin walls manufactured with the tuned parameters and the contour scan strategy was measured. The samples were manufactured utilizing two scan strategies: one that was utilized for the usual creation of the samples and another that included contour scans. The laser traced two contours scan, one on the original CAD geometry contour and one with a hatch distance of 0.08 mm towards the inside. Figure 3.11 reports the two scan strategies employed to produce the thin walls.

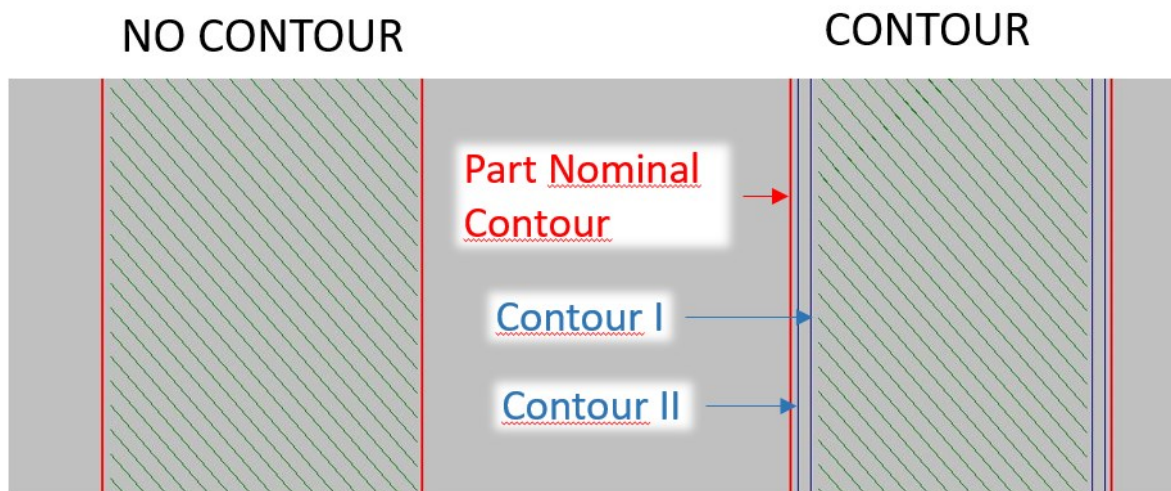


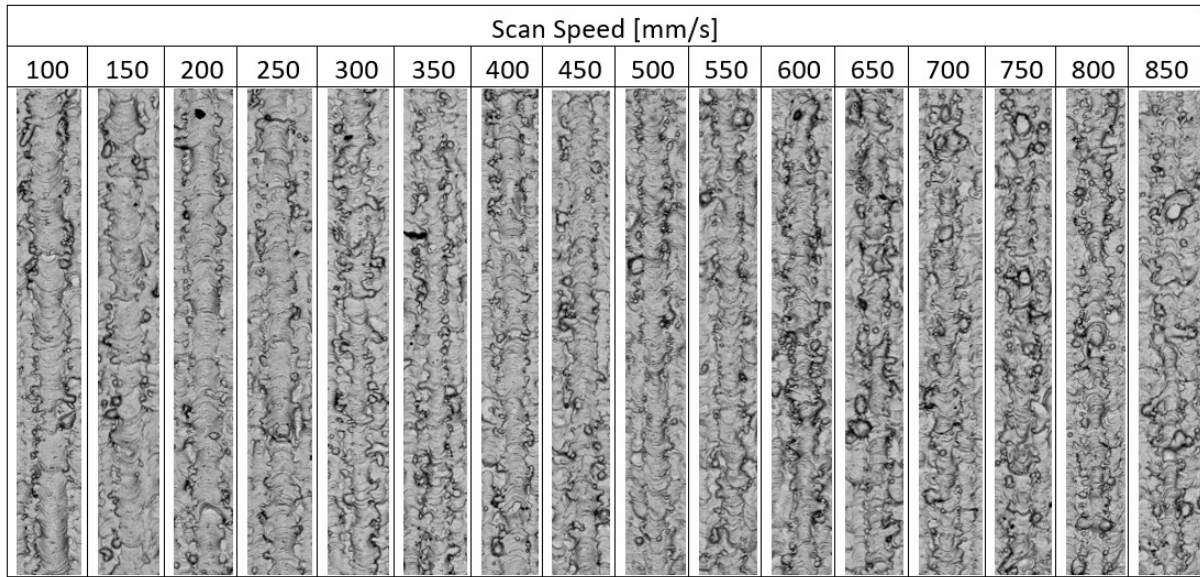
Figure 3.11 Scan strategies employed for the wall production: bidirectional scan strategy (on the left); contours addition (on the right).

3.3 Result and discussion

3.3.1 Single scan tracks

Table 3.3 reports the SSTs manufactured over the copper cubes at different scan speeds using a laser power of 370 W.

Table 3.3 Single scan tracks produced at 370 W laser power and increasing scan speed from 100 to 850 mm/s.



The scan speed deeply influences the melt pool morphology and stability of the SST. As the scan speed increases, the amount of volumetric energy input decreases, firstly resulting in narrower tracks but eventually leading to melt pool inhomogeneity, such as the balling effect or melt pool interruptions.

Below 300 mm/s, the melt pools appear to be continuous, wide, and without evident morphology issues. Since the laser has a Gaussian distribution, the energy input diminishes radially. The melt pools produced at 300 and 350 mm/s show a high amount of partially melted particles on the side. This occurs because the radial energy input is high enough to melt the particles, but the melt pool's capillary forces are not strong enough to incorporate them into the melt pool. The larger particles on the side of the SSTs are not melted at faster scan speeds (up to 550 mm/s), and thus only thin particles are observed, resulting in slightly more homogeneous melt pools. At 600 mm/s, the SST becomes highly inhomogeneous, and the balling effect is observed. Over that value, the SSTs become discontinuous, finally becoming a series of fragmented droplets. Indeed, the width of the past four SSTs was impossible to measure.

Based on these observations, it was decided to test scan speed between 200 and 500 mm/s (using 100 mm/s increments). Scan speeds below 200 mm/s would limit the building rate so that the LPBF process's efficiency would be jeopardized.

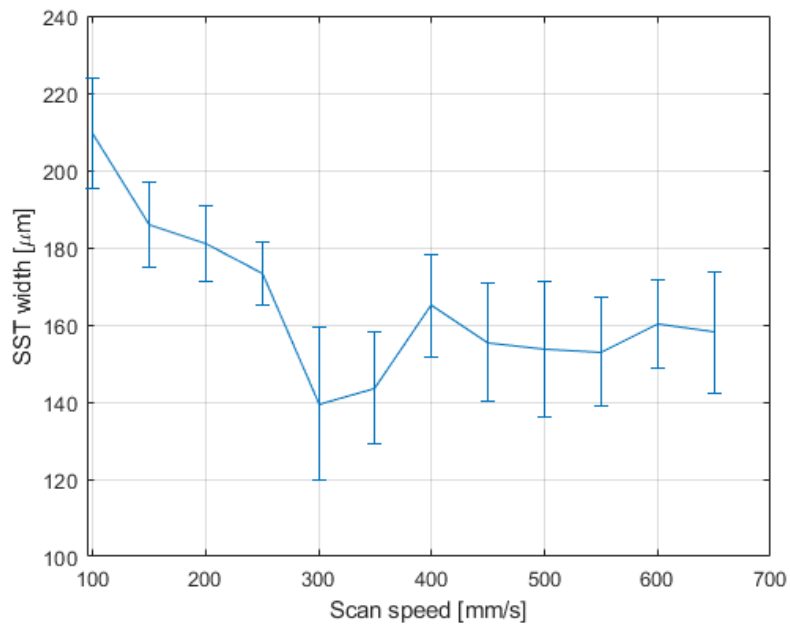


Figure 3.12 Width of SSTs as a function of scan speed at 370 W of laser power.

Figure 3.12 shows the correlation between the width of the SSTs and the laser scan speed. The width ranges between $\sim 210 \mu\text{m}$ at 100 mm/s and $\sim 155 \mu\text{m}$ at 450 mm/s and above. An overlap ratio of about 50% between adjacent melt pools is required to avoid lack of fusion porosity and yield a low surface roughness [161]. For this reason, it was decided to test the hatching distance at values near half of the width of the melt pool, between 80 and 0.110 μm (with 10 μm increments).

3.3.2 Tuning of process parameters

3.3.2.1 Relative density

The results of the parameters optimisation for the realization of dense copper parts are reported in Figure 3.13. All the density specimens have been manufactured in acceptable condition, without evident defects.

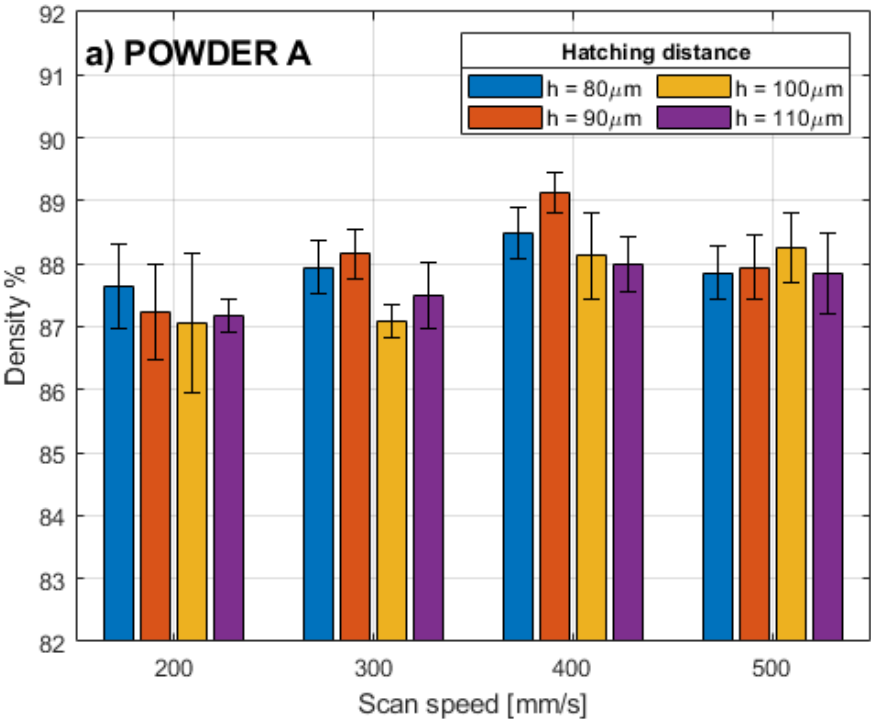
The modification of the parameters did not involve a high variation of the measured relative densities (2% maximum) for each powder, while higher differences were observed between powders.

The results obtained using powders A and B are very similar. The obtained relative densities were in the range of 87 – 89 % for both powders, with a slight increase toward higher scan speeds. The

hatching distance has essentially little effect; only a slight decrease in relative density was observed as hatching distances were increased due to the low overlap between melt pools.

The high reflectivity of the melt pools could explain why there was no increase in densification. Reducing the hatching distance should increase the energy input (see Equation (1.1)) and, as a result, the component density. However, for short hatching distances, the laser beam location is, to a great extent, over the highly reflecting melt pool, decreasing the total energy input. Therefore, the hatching distance's influence on the densification process has been negated due to a compromise between these opposing effects.

The highest density obtained using powder A was 89.1% with a scan speed of 400 mm/s and a hatching distance of 90 μm , while powder B yielded an 88.5 % maximum relative density using 500 mm/s of scan speed and 80 μm of hatching distance.



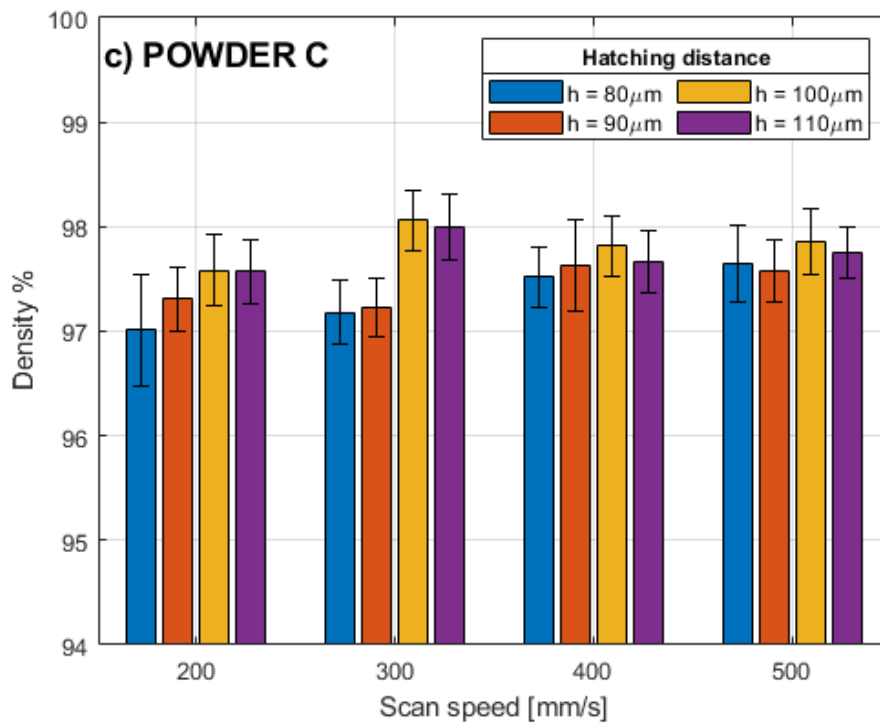
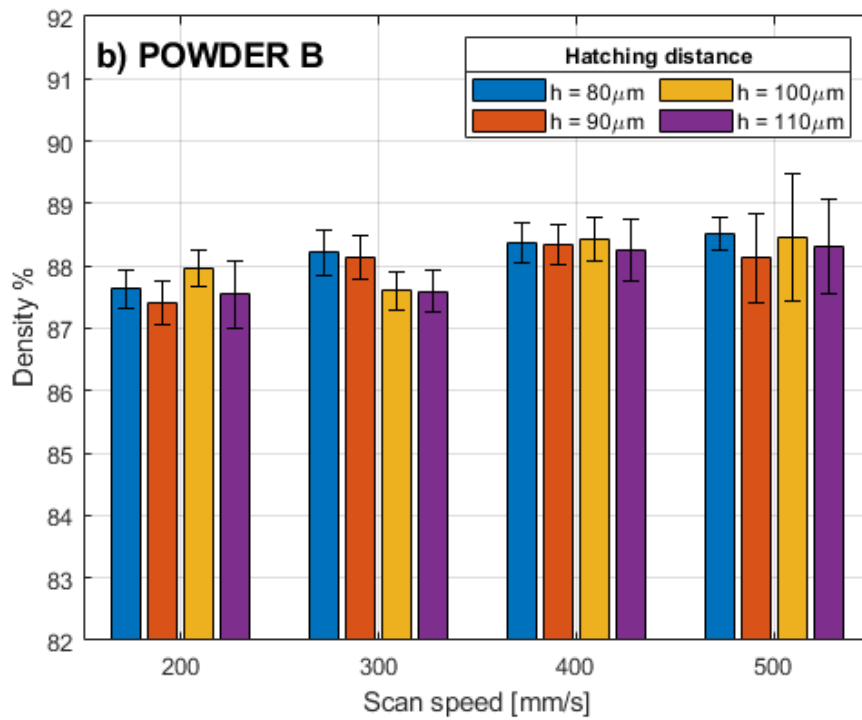


Figure 3.13 Relative density of the samples manufactured with different scan speeds and hatching distances for the three different powder suppliers. a) Powder A; b) Powder B; c) Powder C.

Higher densities have been obtained using the less thermal-conducting and reflecting powder C. Even for this case, minor variations of relative densities were obtained by varying scan speed and hatching distance. By tuning these parameters, it was possible to increase the relative density from 97% to 98%; the maximum relative density obtained with this powder was 98.06%, with a scan speed of 300 mm/s and a hatching distance of 100 μm . Due to the difference in chemical composition, it is not possible to evaluate the effect of the fine PSD on the densification process. In fact, the high amount of impurities has reduced the reflectivity of the powder (it is 10% lower than powder A and B at 850 nm), and the presence of a low amount of phosphorous has reduced the thermal conductivity of the powder, decreasing the dissipation of the heat [98], [153].

However, the thin distribution of powder C could be best suited for being spread while using a 20 μm of layer thickness. The powder layer's effective thickness is greater than the solidified layer's thickness. It achieves a steady-state around the seventh layer [162], and it can be calculated using the following Equation (3.1):

$$t_{eff} = \frac{t}{\rho_{pow}} \quad (3.1)$$

where t_{eff} is the effective powder layer thickness after $> \sim 7$ layers, t is the layer thickness, and ρ_{pow} the relative packing density of the powder (ratio between the powder's density and the material's bulk density). The apparent density of powder A was 4.69 g/cm³, which resulted in an effective layer thickness of 38.2 μm . Since the D90 of powder A was 40.6 μm , the larger particles may not be able to fit in the layer, leading to spreading problems that might have enhanced the porosity of the parts. Powder B, whose D90 was 36.4 μm , but apparent density was likely higher due to the presence of fine particles, might also be influenced by the same issue. The lower D90 of powder C (28.2 μm), on the other hand, suits the thickness of the powder layer nicely and so this problem does not exist.

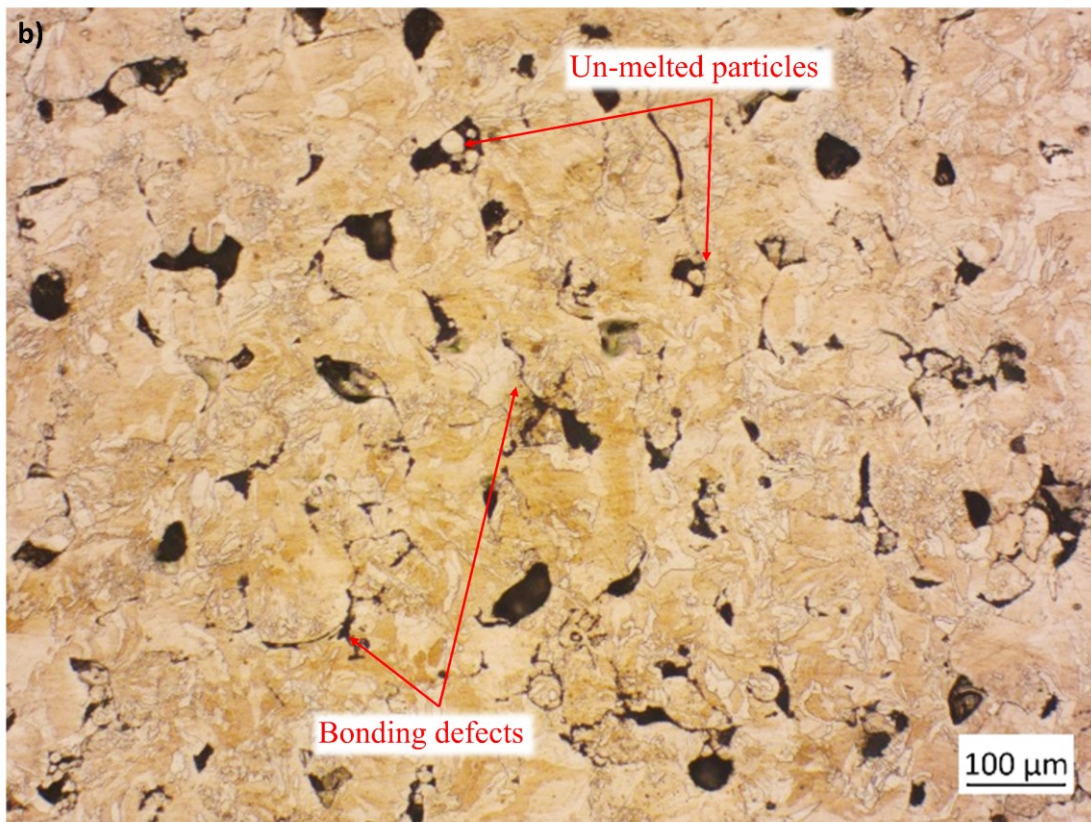
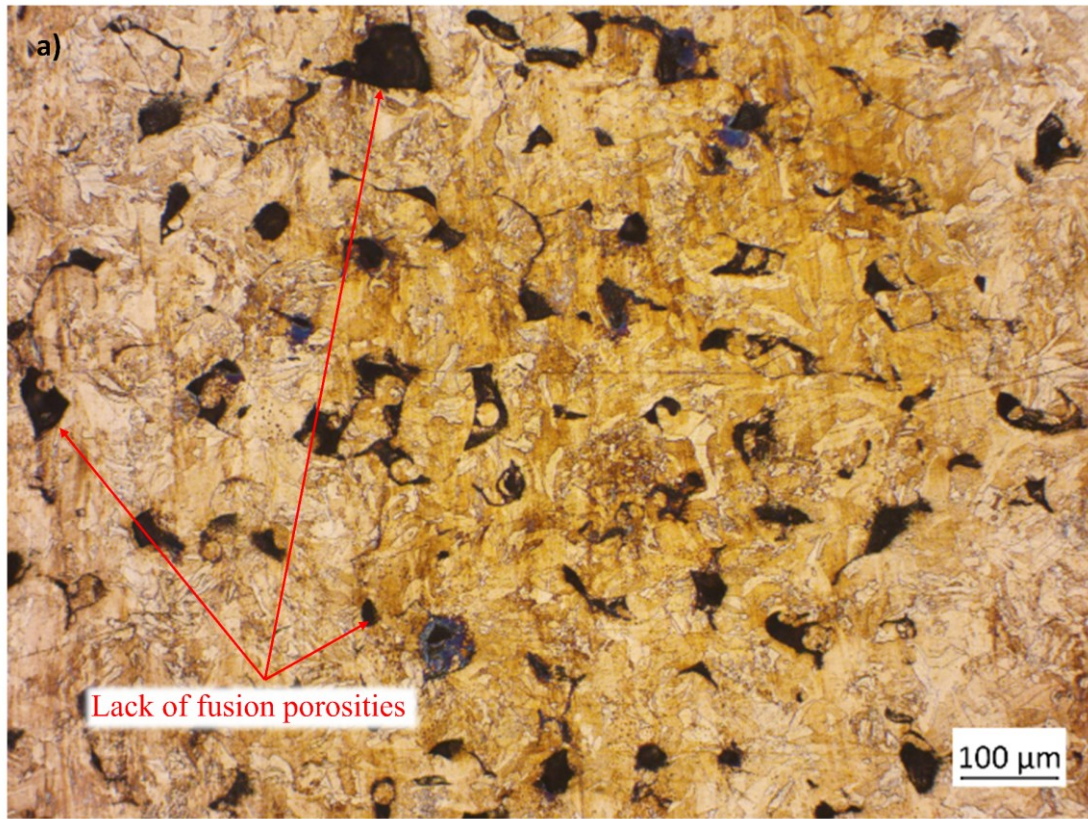
However, Wischeropp et al. [163] used two distinct layer thicknesses to measure the actual layer height of two different powders and found that the actual thickness is between 4 and 5.5 times the layer thickness. According to their results, this problem should not subsist even for powders A and B.

An issue that occurred during the weighing in water of samples made with powder A and B is worth addressing. Due to the water filling the open porosities, air bubbles continued to develop on the surface of the samples during the first set of tests. As a result, the weighted mass continued to rise as the buoyant force exerted by the air bubbles decreased. In the porosity range of 6-8%, the pores start becoming interconnected [164], and the interior pores become connected to the surface. As specimens produced using powder A and B presented high levels of porosity, the first measurements obtained were ~5% higher than the presented results due to the problem described above. The stated results in Figure 3.13 were acquired by measuring the mass within the first few seconds after the sample was settled, allowing insufficient time for the water to be absorbed.

3.3.2.2 *Optical inspection*

Optical images of the horizontal section (XY plane) of the highest density samples for each powder batch are reported in Figure 3.14. As expected, powders A and B presented similar microstructures and defects concentrations, as they showed similar densities. Several lack of fusion porosities may be seen in both sections. They are characterized as porosities with irregular shapes and different dimension sizes, with equivalent spherical diameters (calculated with the software ImageJ) ranging from a few micrometres to ~ 80 μm . More extensive lack of fusion porosities often presents on their inside un-melted fine particles or semi-molten particles incorporated by the melt pools.

Samples produced using powder C, on the other hand, showed smaller lack of fusion porosities in a lower concentration. The specimen section produced using powder C also illustrates the presence of small circular pores associated with gas entrapment. Because of the fast cooling rate during the solidification process, the gas existing between the powder particles does not come out of the melt pool before solidification [165].



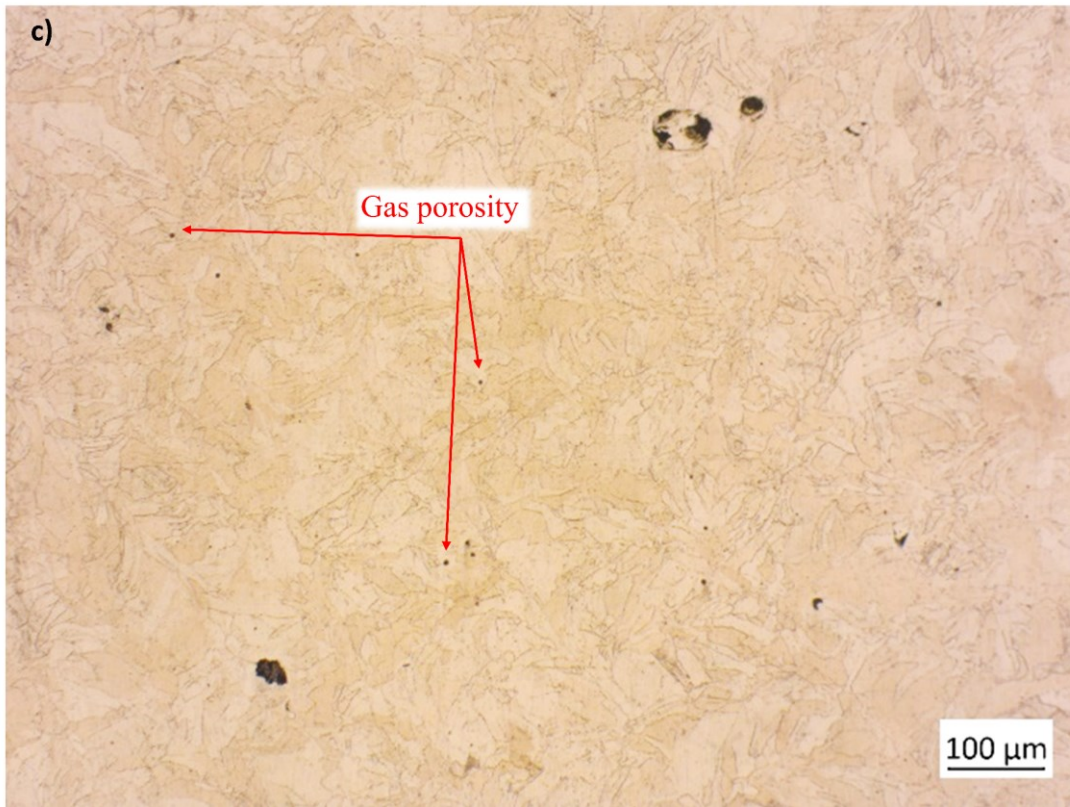


Figure 3.14 Optical microscope analyses of the highest density specimens after etching in the horizontal XY plane: a) Powder A; b) Powder B; c) Powder C.

The microstructure observed in the three specimens showed similar features. In comparison to standard production procedures, the overall microstructure is quite fine [84]. The very small grains are the result of the high cooling rate that occurs during the solidification process. However, also bigger grains are observed. The recurrent fusing of layers creates a local heat treatment, which induces partial recrystallization and increases grain size locally [117].

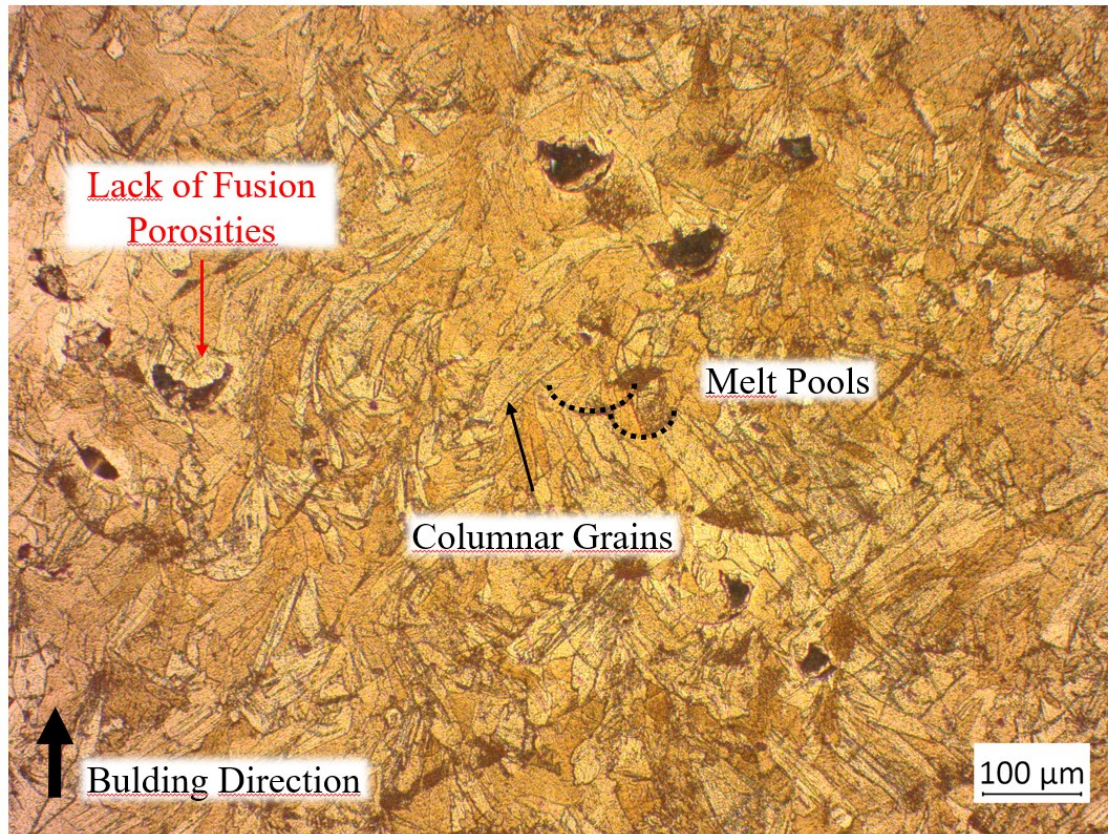


Figure 3.15 Optical microscope analysis of the highest density specimens produced using powder C after etching in the vertical XZ plane.

Figure 3.15 shows the section micrograph of the etched surface parallel to the building direction of the sample produced using powder C. From this orientation, it is possible to observe the elongated grain that grows epitaxially across the melt pools in the vertical direction. The thermal gradients that develop during the melting of the powder drive the grain growth towards the vertical direction, forming an anisotropic microstructure. The columnar grains result slightly inclined with respect to the vertical direction. The change in growth direction is obtained thanks to the 67° rotation angle given to each layer, which changes the direction of the laser track and, as a result, the direction of heat flux in the material. Therefore, the rotation angle helps reduce the microstructural anisotropy of the material.

Finally, bonding defects between melt pools were observed in samples produced with powders A and B. The lack of adhesion between the scan track could be due to the oxidation of the surface of molten scan tracks. The copper oxides have a higher melting temperature compared to pure copper and could stabilize the surfaces and act as physical barriers to wetting [166]. This issue might emerge as a

result of probable pollution of the oxygen content in the process chamber atmosphere. However, the chemical composition near such surfaces was controlled via EDS analysis, and no oxygen peak was detected (as shown in Figure 3.16). Therefore, these cold weld lines are probably due to the high cooling rate of pure copper: the adjacent melt pool is already too cold to bond together due to their reduced temperature.

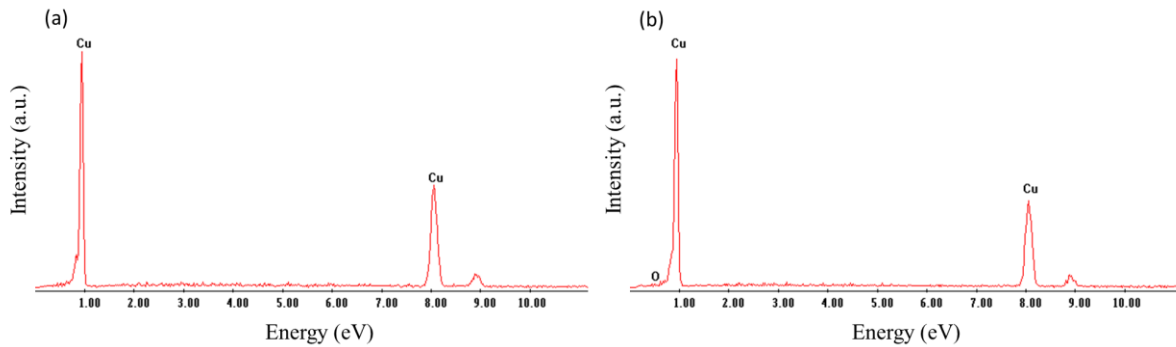


Figure 3.16 EDS analysis of pure copper printed samples: (a) Powder A, (b) Powder B. No oxygen peak was detected.

3.3.3 2.3 Mechanical and thermal properties

3.3.3.1 Micro-hardness

The average values of five micro-hardness measurements are reported in Figure 3.17. As expected, the densest sample showed the highest value of 61.7 HV, more than double the others, respectively 27.6 HV with powder A μm and 27.3 HV with powder B.

Annealed unalloyed copper has a hardness in the range between 40 and 120 HV, depending on the level of cold working[153]. The value obtained with powder C is in the range of annealed pure copper (between 40 and 65 HV) and is in agreement with the micro-hardness obtained by Jadhav et al. [90]. Their research obtained a micro-hardness of 66 HV with a 99.3% dense pure copper.

The low values observed with powder A and B are due to the high concentration of lack of fusion porosities. The pores within the material collapse under the applied load, which causes the reduction of micro-hardness [167].

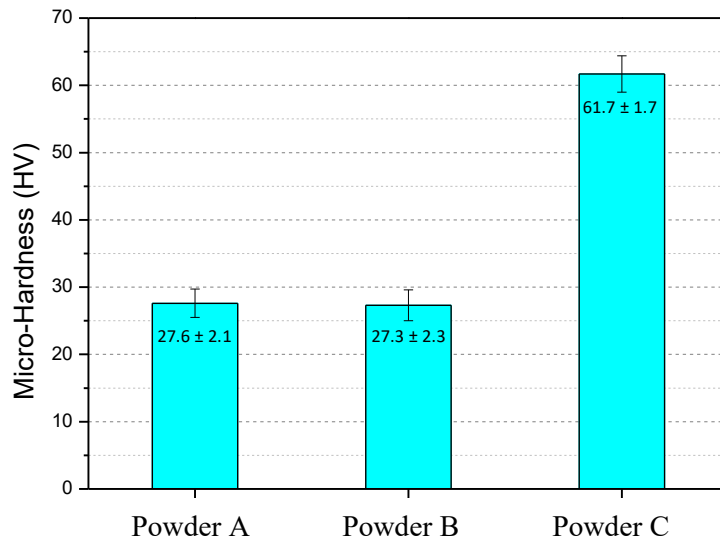


Figure 3.17 Micro-hardness values for each highest density sample.

3.3.3.2 Tensile test results

The average results of tensile tests are reported in Table 3.4, and stress-strain curves of representative samples are shown in Figure 3.18. The mechanical properties of all the specimens built in the horizontal direction were higher than those manufactured in the vertical direction.

Table 3.4 Results of tensile test on LPBF copper.

	E [GPa]	$\sigma(0,2\%)$ [MPa]	UTS [MPa]	EB [%]
Powder A H	109.2 ± 1.9	113.3 ± 0.5	160.2 ± 1.7	-
Powder A V	85.2 ± 1.5	89.0 ± 1.2	102.8 ± 1.8	9.5 ± 0.9
Powder B H	101,8 ± 3.1	97.5 ± 2.4	138.8 ± 2.5	13.8 ± 1.8
Powder B V	77.2 ± 2.2	74.3 ± 0.5	83.9 ± 1.9	8.2 ± 0.5
Powder C H	155.4 ± 1.5	254.8 ± 3.0	312.7 ± 2.7	-
Powder C V	149.8 ± 0.7	237.8 ± 4.3	259.3 ± 13.3	1.8 ± 0.9

The samples made with powder B had the lowest mechanical properties, which was unexpected given that their density was identical to that of the ones made with powder A. Between powder A and B, a ~15 MPa yield strength gap was discovered in both vertical and horizontal samples. In the UTS measured values, this disparity is amplified to a maximum of ~20 MPa.

The occurrence of a single larger defect (caused by a distribution fault) that would weaken the specimen's strength could not explain the difference in mechanical properties since the findings revealed low standard deviation values, implying that the results are almost constant.

The un-melted fine particle observed in Figure 3.14 could explain the difference in mechanical behaviour. Powder B is characterized by a higher concentration of fine particles, which might fill the lack of fusion porosities during the manufacturing process. However, the energy input is too low to re-melt the layer underneath and melt the particles. While the relative density of the part might increase, these particles do not bring any improvement in the mechanical properties.

As observed with the micro-hardness measurements, samples produced with powder A and B showed inferior mechanical properties compared to annealed pure copper, while the yield strength values obtained with powder C could be compared to pure copper with ~20% cold working deformation [153]. Considering the lowest mechanical properties obtained in the vertical direction, samples produced with powder C have ~240 MPa of yield strength, ~260 MPa of UTS, low elongation at break at ~2% and Young Module of 150 GPa. The material's strength is higher than other pure copper parts produced via LPBF. Yan et al. [83] obtained a relative density of 99.1% and UTS of 248 MPa, while Jadhav et al. [90] obtained 99.3 % dense parts with UTS of 211 MPa. This is due to the solid solution strengthening generated by the alloy elements present in the chemical composition.

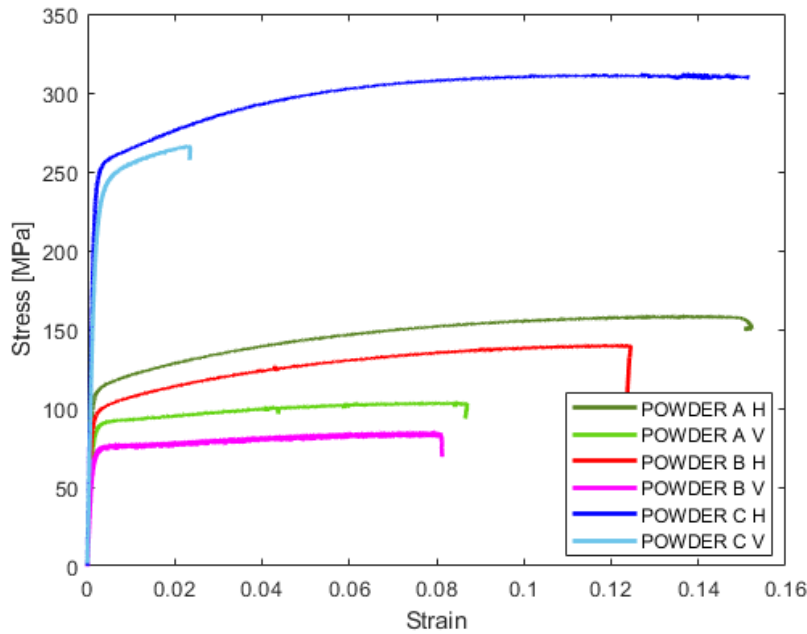


Figure 3.18 Stress-strain curves of one copper tensile specimen for each powder lot.

The mechanical anisotropy is caused by the presence of lack of fusion porosities, which severely diminishes the interlayer bonding. Of course, parts that are built vertically are manufactured with more layers, so their mechanical properties are severely affected. In fact, the samples with higher porosities exhibited higher reductions of mechanical properties: the reduction of the yield strength was 21% with powder A, 24% with powder B, and only 7% with powder C (densest sample). However, the elongation at break (EB) percentage of the vertical sample produced with powder C was drastically reduced below 3% (the percentage elongation of the sample manufactured horizontally was higher than the maximum displacement of the extensometer, so the value is not reported).

The brittle behaviour in the vertical direction is due to the orientation of lack of fusion porosities. Figure 3.19 illustrates how the shape and relative position of the lack of fusion porosities with the loading direction influences the EB. Lack of adhesion between layers forms pores with an extended shape. The angle between the major axis of the pore and the tensile direction may vary from 0° in the case of horizontal samples and 90° for vertical specimens. The 90° arrangement increases stress concentrations at the pore apexes, leading to crack initiation or ductile void expansion, whereas the 0°

configuration minimises stress concentrations [168]. Vertical specimens often break at a lower EB % when exposed to tensile force.

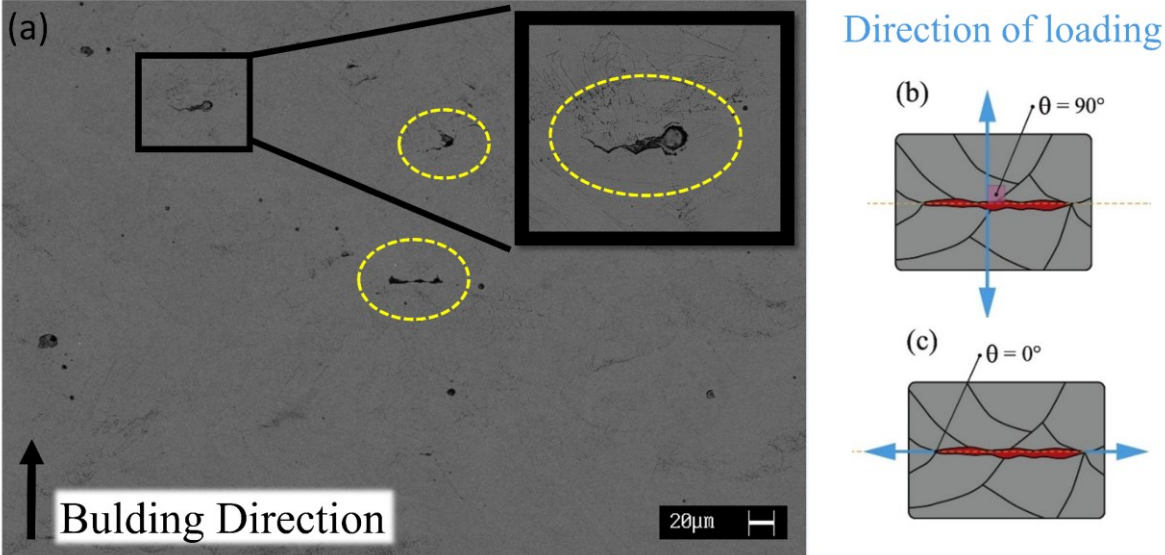


Figure 3.19 (a) Micrograph of a vertical cross-section of a sample produced using powder C. (b) and (c) illustrate a lack of fusion porosity oriented perpendicular and parallel to the loading direction [168].

3.3.3.3 Thermal conductivity measurements

Table 3.5 reports the values of thermal conductivities obtained from the measurements of the thermal diffusivities of the samples.

Table 3.5 Thermal conductivities of LPBF copper.

	Thermal conductivities [W/mK]
POWDER A	136.9 ± 0.4
POWDER B	139.1 ± 0.4
POWDER C	227.8 ± 2.5

All the samples exhibited lower thermal conductivity than pure copper (401 W/(m·K) at 27°C). The reason for the low values measured on the samples obtained with powders A and B can be attributed to the high concentration of lack of fusion porosities. Porosity reduces the thermal conductivity of copper [164], and furthermore, the presence of un-melted particles with oxidized surfaces may also hinder the thermal conductivity. As shown in Figure 3.9, the spatter particles have oxidized surfaces. If these

particles remain englobed into the copper matrix, the less conducting oxide on their surface could further reduce the thermal conductivity.

The sample manufactured using powder C showed a thermal conductivity of 227.8 W/mK. In this case, the conductivity reduction could be due to the chemical composition of the starting powder and the presence of porosities and un-melted particles (in less amount).







3.3.4 Lateral surface roughness

Table 3.6 reports the lateral surface roughness measurements. The effect of the contour scan strategy strictly depends on the PSD of the powders. Powders with larger particles did not show any improvement in the reduction of surface roughness; the average surface roughness measured was ~11 μm , regardless of the scan strategy performed. A significant improvement was found with the PSD 13-28 μm , from 12 μm to 2.9 μm with the contour scan strategy.

This improvement could be attributed to two main reasons: the stable melt pool formation and the fine PSD. As reported in Table 3.3, powder C forms stable melt pools at low scan speed while powders A and B develop irregular scan tracks due to their higher reflectivity, which hinder the formation of a smooth surface.

Fine powder particles can improve the surface quality in different ways. If a small particle remains attached to the surface, it hinders the surface quality to a lesser extent than larger particles. In addition, the force required to displace small particles is less since they weigh less. As a result, particles near the melting zone are either integrated into the melting pool by convection forces or ejected by recoil pressure. This leads to a reduction of semi-melted particles attached to the surface and hence to a reduced roughness.

Table 3.6 Effect of the contour scan strategy on the lateral surface roughness of samples produced with copper powders with different PSD.

	POWDER A PSD (19-41 μm)	POWDER B PSD (8-36 μm)	POWDER C PSD (13-28 μm)
NO CONTOUR R_a [μm]	11.7 \pm 0.9 	11.1 \pm 0.8 	12.0 \pm 0.7 
CONTOUR R_a [μm]	11.5 \pm 0.7 	10.9 \pm 0.7 	2.9 \pm 0.7 

3.4 Summary

This work investigates the fabrication by LPBF of copper parts using powders with different particle size distributions. The results show that the PSD affects the performance of the printed parts in terms of density, surface roughness, mechanical and thermal properties.

The results show that while using a low laser power (<400W), the PSD has a low influence on the densification process. Both the standard PSD and the broader PSD led to a maximum relative density lower than 90 %, despite using the lowest layer thickness and maximum laser power. The parts produced with these powders showed similar thermal conductivities and surface roughness. The only difference between the parts was found in the mechanical properties: samples produced using powder B presented a ~14% yield and tensile strength reduction. This was probably due to the higher concentration of unmelted particles englobed inside the bulk.

Superior performances were observed with powder C. A fine PSD and a higher concentration of impurities, which decreases the thermal conductivity of the powder and improves the densification, characterized the powder. A relative density of 98.1% has been obtained by varying scan speed and hatching distance. An improvement of the surface finishing was possible by using a contour scan

strategy (R_a from 12 to 2.9 μm). The reduction of lack of fusion porosities granted better thermal and mechanical properties. In fact, despite the lower purity of the starting powder, the measured thermal conductivity of the printed parts was higher ($\sim 228 \text{ W}/(\text{m}\cdot\text{K})$). The mechanical properties of the printed parts can be compared with a 20% cold-worked pure copper.

Finally, samples produced vertically had lower mechanical properties than those produced horizontally. Samples produced with powder A and B showed higher yield strength and tensile strength reductions, while vertical samples produced with powder C presented higher reductions of percentage elongation.

CHAPTER 4

4 LPBF OF OXIDIZED PURE COPPER POWDERS

4.1 Side effects of studying the influence of temperature of the platform

To further improve the relative density obtained using powder C, the effect of the scan strategy and the temperature of the building platform were investigated. Usually, the scan strategy and the temperature of the building platform are tested to study the residual stress in more brittle materials such as Ti6Al4V [169], [170], tool steel [171] and Cr [172]. These strategies seek to raise the temperature of the powder bed, hence reducing the thermal gradient and, as a result, residual stresses. However, these factors might improve the densification process because pure copper absorptivity increases with temperature [173]. Moreover, a powder bed at a higher temperature will require less energy input to obtain a dense part, and lower thermal gradients lead to more stable melt pools [89]. When adopting a shorter scan length, the short time interval between tracks results in a more uniform thermal distribution, minimal thermal gradient, and overall high ambient temperature throughout the process [172]. Wegener et al.[117] have observed a ~2% increase in porosity when manufacturing a CuCrZr sample with a double-length scan path, and Lykov et al. [174] obtained higher pure copper densities when using a pre-heated baseplate. In addition, an alternative to increasing the temperature of the powder is to pre-scan the area with a low energy input [89].

4.1.1 Scan strategies

The scan strategies tested for this research were the chess scan strategy (depicted in Figure 1.8 c) and the stripe scan strategy with a rotation angle of 67° (Figure 1.8 d). For this test, the scanning parameters were 370 W of laser power, 20 μm of layer thickness, 400 mm/s of scan speed, and hatching distance of 100 μm , while the width of the path track was varied. Furthermore, two multi-passage stripe scan strategies were performed by scanning each layer twice. The first scan passage is referred to as pre-

sintering since the energy input is insufficient to melt the material, while the second scan had the above parameters and a stripe width of 5 mm. The parameters used for the pre-sintering scan were scan speed of 1200 mm/s, hatching distance of 100 μm , and laser power of 100 W and 200 W, respectively. Figure 4.1 shows the calculated relative densities.

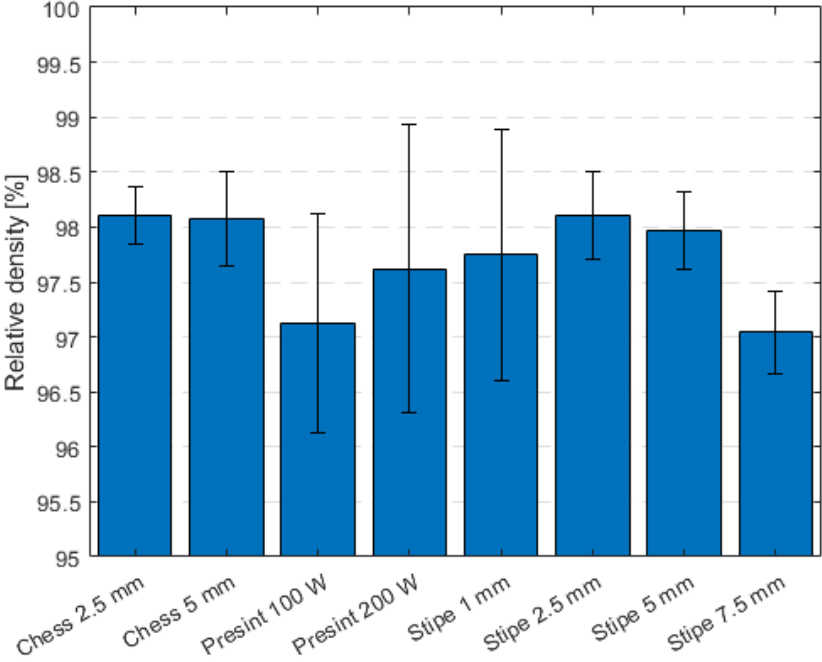


Figure 4.1 Relative densities of powder C samples manufactured using different scanning strategies.

While it was discovered that the scan strategy affects the copper powder's densification behaviour, the results revealed that the evaluated scan techniques did not significantly enhance the densification process. The optimal range of scan path width is between 2.5 mm and 5 mm since both chess, and stripe scan strategies yielded a relative density of ~98% in this range. The relative densities obtained out of this range were lower; the stripe width of 7.5 mm led to a relative density of 97%, while the stripe width of 1 mm generated a relative density of 97.6 %. The employed scan strategies are bi-directional, implying that each scan track begins near the preceding one's hot finishing point and finishes near its colder starting point (Figure 1.8 b). Because lengthier melt pool paths take longer to complete, the beginning point of the preceding scan path will be colder because it has had more time to cool. Because of its excellent heat conductivity, pure copper accentuates this effect even more. The high

thermal gradients that are generated could lead to melt pool instability and hence lack of fusion defects. On the other hand, using a too short scan path track increases the melt pool boundaries concentration, which has been observed to be a preferential location for the lack of fusion porosities.

Despite increasing the total amount of energy added to each layer, the addition of the pre-sintering scan strategy led to lower relative densities. Colopi et al. [89] reported similar results when using a 1 kW infrared laser. A porosity increment of ~1% was measured when a 100 W pre-sintering scan strategy was performed. The volumetric energy input with the adopted scan parameters is 42 J/mm^3 , which is probably too low even to start the sintering process, and a possible side effect is the ejection of the finer particles due to the recoil forces applied by the laser, reducing the packing density of the powder bed.

4.1.2 Preheating of the platform

Density specimens were manufactured on a $150 \text{ }^\circ\text{C}$ preheated platform to examine the influence of the building platform temperature. Similarly to what was performed in Section 3, the scan speed and hatching distance were modified, with the scan speed ranging from 200 mm/s to 800 mm/s with 200 mm/s increments and the hatching distance ranging from $80 \text{ }\mu\text{m}$ to $140 \text{ }\mu\text{m}$ with $20 \text{ }\mu\text{m}$ increments. The laser power was kept at 370 W , and the layer thickness was $20 \text{ }\mu\text{m}$. The tested range of both parameters was expanded towards a lower energy input since preheating the platform should reduce the required energy to melt the material. The relative densities attained are depicted in Figure 4.2.

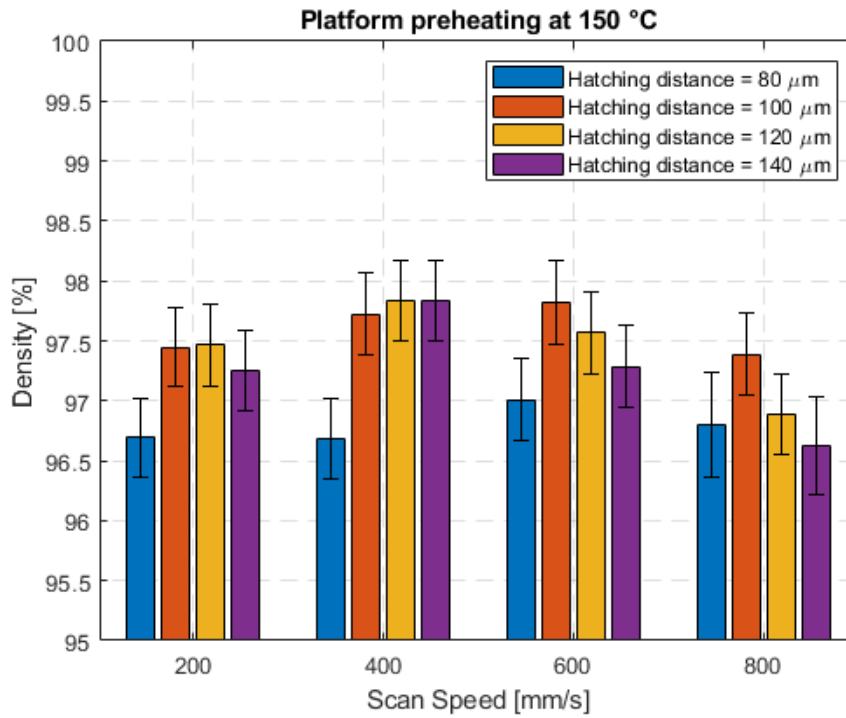


Figure 4.2 Relative densities of powder C samples manufactured with different scanning strategies using a preheated building platform at 150 °C.

The samples manufactured using a preheated platform had a relative density between 96% and 98%, with the higher values obtained at 400 mm/s and 600 mm/s. Overall, the results are not far from the ones obtained using a 40 °C platform. Table 4.1 reports the relative densities of samples manufactured using the same parameters but with different preheating of the platform. The results show that the parts manufactured using a 40 °C baseplate temperature are slightly denser. However, the deviation is <0.5% which is inside the standard deviation of the measurements.

Table 4.1 Comparison of the relative densities obtained using a different preheating temperature of the platform.

Scan speed [mm/s]	Hatching distance [μm]	Platform temperature		Deviation
		150 °C	40 °C	
		Relative density [%]	Relative density [%]	
200	80	96.70	97.01	0.3%
200	100	97.44	97.58	0.1%
400	80	96.69	97.12	0.4%
400	100	97.72	98.14	0.4%

Using a higher platform temperature enables a faster manufacturing process since high relative densities were achieved using a longer hatching distance or a faster scan speed, but the densification process was not improved. Indeed, the relative density of each manufactured sample did not exceed 98%.

A major problem with using a high preheating temperature was found while recovering the unmelted powder. Figure 4.3 shows an image of the powder.

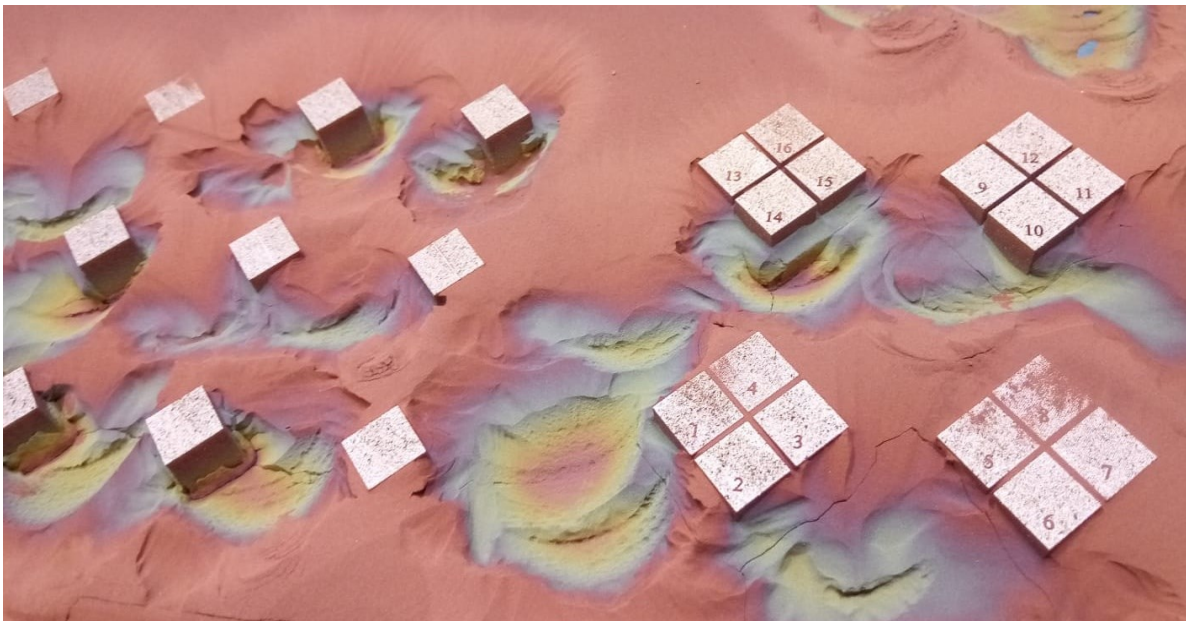


Figure 4.3 Oxidized powder recovered after manufacturing samples using a 150 °C preheated platform.

Severe oxidation of copper particles was observed near the building platform and the printed parts. The manufacturing of the parts was performed in an inert environment, argon gas was fluxed into the processing chamber, and the oxygen level was kept below 0.2 % during the manufacturing process. However, the air between the powder particles was likely retained even throughout the powder bed distribution, causing the particle to oxidise while approaching the platform at 150 °C. An X-Ray Diffraction (XRD) analysis was performed on the oxidized powder and on a sample that was not used in during the manufacturing at 150 °C. Cu_2O oxide peak was present in both XRD spectrums; the “virgin” sample showed a 2.1 % Cu_2O concentration, while the oxidized sample had a 3.7 % Cu_2O concentration. The Cu_2O concentration of the “virgin” powder corresponds to the chemical analysis

reported in Table 3.1. In fact, 2.1% of Cu_2O corresponds to 0.23% of oxygen concentration inside the part.

Instead of despatching the oxidized powder, it was decided to use it to produce a few density samples (the amount of powder was too low to produce several samples). Four density samples were manufactured (10 mm side cubes), two with the pre-sintering scan strategies described above and two using a hatching distance of 100 μm and scan speeds of 400 and 600 mm/s ($P=370\text{W}$, $t=20\ \mu\text{m}$). The results of the relative density are reported in Figure 4.4.

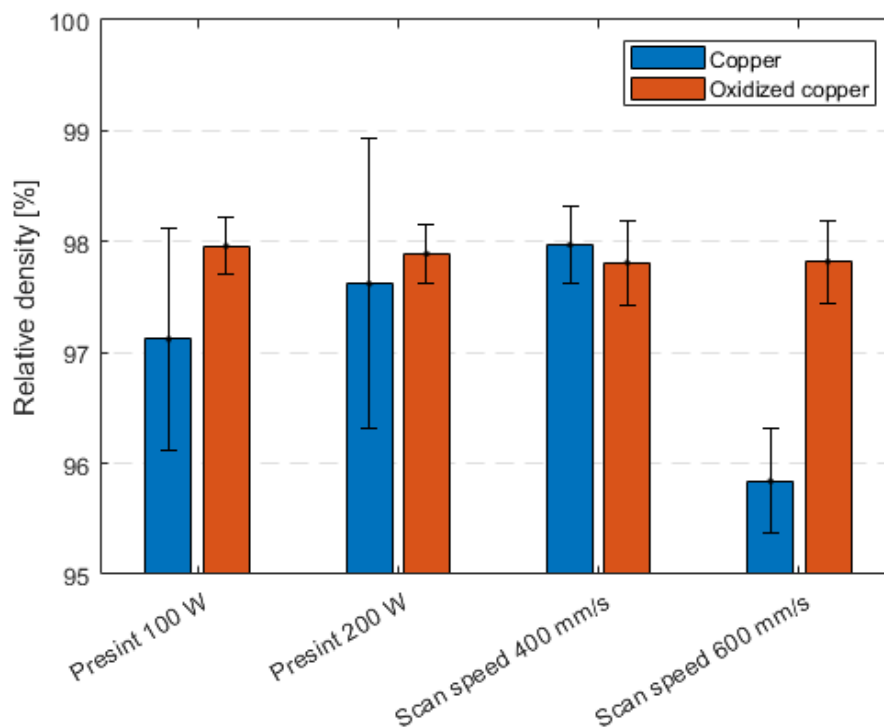


Figure 4.4 Comparison of relative densities obtained using oxidized copper powder and “virgin” powder with different scan strategies.

The oxidized powder yielded better results than the pure one. Regardless of the scan approach or processing parameter utilised, the relative density of the oxidised powder remained nearly constant at ~97.9%. However, it was not still possible to reduce the porosity under the 2% threshold. Copper oxide has an increased absorptivity of the infrared wavelength, and therefore the powder could absorb more energy and improve densification [96]. The presence of the copper oxide at the surface of the particles seemed not to compromise the densification. Therefore, to further analyse the improvement of

the densification behaviour while using an oxidized powder, it was decided to perform controlled oxidation of the pure copper powder A (the pure copper powder with standard 15-45 μm distribution) and use it for manufacturing density specimen. The following sections present the description of the oxidation of the powder and the obtained results.

4.2 LPBF of surface oxidized pure copper powder

The research work for this test was subdivided into three steps. Firstly, small batches of powder were heat-treated at different times and temperatures to analyse the oxidation behaviour and the evolution of the absorptivity of powder. Afterwards, two heat treatments were selected and employed to oxidize two 6 kg batches of powder that were used to manufacture density specimens at various scan speeds and hatching distances. Finally, the micro-hardness and thermal conductivity of the highest density samples were measured.

4.2.1 Materials and methods

The oxidation of the powder was performed in a stat furnace by spreading a thin layer of powder up to 2 mm in large shallow trays. This has been found to help the oxidation of as many particles as possible and prevent cold sintering o the particles simultaneously. Preliminary studies revealed that a significant rise in oxygen content took many hours of heat treatment at 150°C, whereas the oxidation reaction happens significantly faster at 200°C. The higher temperature has been set to 200°C since powders treated at higher temperatures are prone to sintering. The oxygen concentration was measured with the inert gas analysis using an Eltra N/O. The fabrication parameters are listed in Table 4.2.

Table 4.2 Fabrication parameters of the LPBF process

LPBF Parameters	Values
Layer thickness [μm]	20
Laser Power [W]	370
Scan Speed [mm/s]	200, 300, 400, 500
Hatching distance [μm]	80, 90, 100, 110
Protective atmosphere	N ₂
Scanning strategy	Bidirectional, 67° Rotation angle

For optical porosity analysis, the micrographs of the cross-section were analysed using the software ImageJ. The Archimedes method requires knowing the theoretical density of the sample. Since it was not possible to measure the density of the oxidized powder, it was decided to use optical analysis instead.

4.2.2 Experimental results and discussion

❖ Powder Oxidation

Before the oxidation of the powder, the PSD of powder A was recorded using the laser diffraction method. The results are reported in Figure 4.5.

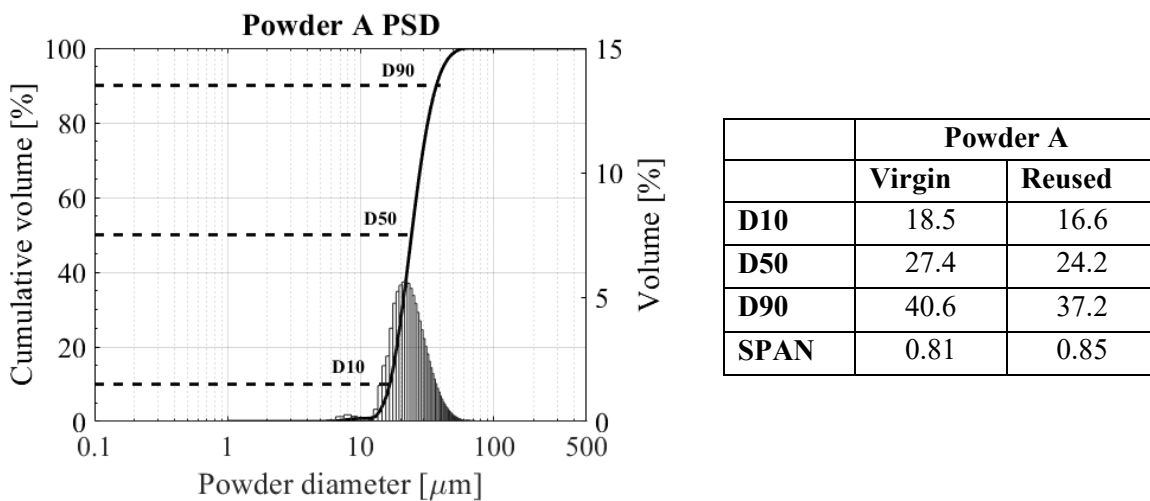


Figure 4.5 On the left: PSD of the reused powder. On the right: comparison between the D values of the virgin and recycled powder.

The reused powder is formed by finer particles with a slightly wider distribution. The reduction percentage of the particles' diameter appears to be almost constant at ~ 10%. Several researchers have studied the influence of powder recycling on the morphology of the particles and their distribution [136]. As already mentioned, the interaction between the laser and the powder bed may affect the morphology of the powder, resulting in less spherical particles [156]. However, the correlation between the multiple reuses of the powder and its PSD is less clear since it has been observed that reused powders can have coarser [175]–[177], constant [178], or narrower distributions [179], [180]. Factors that might increment the PSD are the formation of agglomerates and satellites [175] and the melting of the smaller particles [177]. Powder A was used five times before being characterised, and each time it was sieved with a 230 mesh vibrating sieve (63 μm aperture). As a result, bigger particles, agglomerates, and deformed particles were removed from the utilised powder each time, lowering the PSD of the powder.

The oxygen concentration of the starting powder and after each heat treatment is reported in Table 4.3. There was a modest increase in oxygen concentration in the initial powder; the virgin powder had 320 ppm of oxygen, while the reused powder had ~470 ppm of oxygen. The oxidation of the powder is due to the handling and sieving operations. The powder was in contact with air during these activities, causing oxidation of the particles.

The heat treatment performed at 120 °C showed only a low increment of oxygen content, 544 ppm, after a 12 h heat treatment. The oxidation kinetics is parabolic in this temperature range, implying that the diffusion mechanism controls the oxidation process [181], [182]. The native oxide layer present in the particle acts as a barrier to the oxygen molecules, limiting their diffusion.

Choudhary et al. [183] discovered that the oxidation of copper begins at 150 °C: over this temperature, the thermal energy of oxygen molecules is high enough to overcome the diffusion barrier. Indeed, the concentration of oxygen measured in the samples heat-treated at 150 °C is significantly higher. Heat-treating for 12 h and 15 h led to an oxygen content of 1675 ppm and ~2000 ppm, respectively. At 200 °C, the oxidation of copper powders is much faster: at 30 min, the oxygen level already is 1300 ppm, and it reached ~ 9000 ppm after a 6 h heat treatment.

Table 4.3 Oxygen levels of oxidized powders at different times and temperatures.

Temperature [°C]	Time [h]	Oxygen concentration [ppm]
-	-	467,9
120	12	544
150	12	1674,7
150	15	1958,2
200	0,5	1303,7
200	1	1965,2
200	2	3998,4
200	4	6642,9
200	6	8967,9

Figure 4.6 shows the X-ray diffraction spectra of the pure and oxidized copper at 150 °C and 200 °C for various durations. All the powders showed sharp diffraction peaks at about 43.5°, 50.5°, and 74.4 °, attributed to pure copper reflection planes (111), (200), and (220), respectively. The progressive formation of the diffraction peak at 37 ° may be seen. It starts being distinguishable only above 2000 ppm of oxygen content. This diffraction peak is attributed to the copper oxide Cu₂O, while the diffraction peak of copper oxide CuO was not observed.

Copper oxidation starts with the formation of cuprous oxide Cu₂O, which can further oxidize to form cupric oxide CuO. Equations (4.1) and (4.2) show the oxidation reactions:



The CuO phase starts forming at a temperature above 300 °C [183], [184], and therefore it can be assumed that it was not formed during the oxidation process.

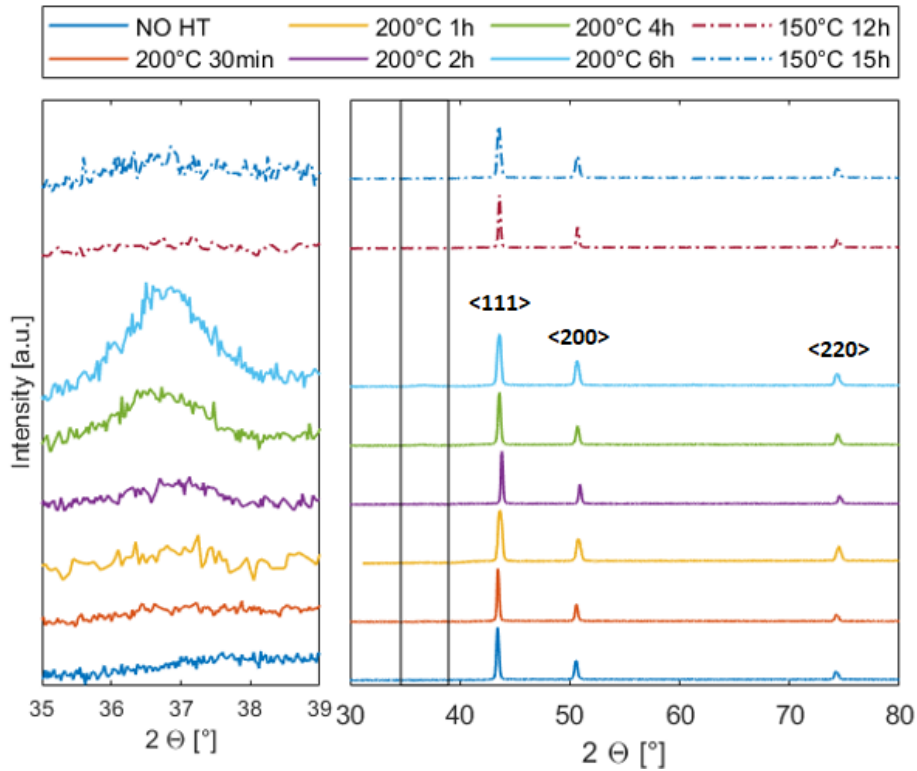


Figure 4.6 XRD spectra of pure and oxidized copper powders, with a focus on the 35°-39° range, showing the Cu_2O peak evolution.

The optical reflectivity of the oxidized powder is shown in Figure 4.7, along with the reflectivity of the starting powder. Oxidized powders show lower reflectivity levels than pure copper powder: at 800 nm, the reflectivity of pure copper is ~ 63 %, while the oxidized powder ranges between ~35 % and 27%, depending on the oxidation level. The oxidized powders with oxygen content below 2000 ppm show similar behaviour, the reflectance curve of powder oxidized at 150 °C and 200 °C for less than an hour almost overlap. Over 2000 ppm, the reflectivity declines less; at 4000 ppm, the optical reflectivity at 800 nm is reduced to 30%, and at 6600 ppm, it is reduced by a further 3%. The absorptivity is unaffected by subsequent oxidation of the powder.

The reduction of reflectivity is due to the multiple reflections that occur in the oxidized layer, increasing the absorption probability of the laser wavelength and hence the optical absorption of the powder [96].

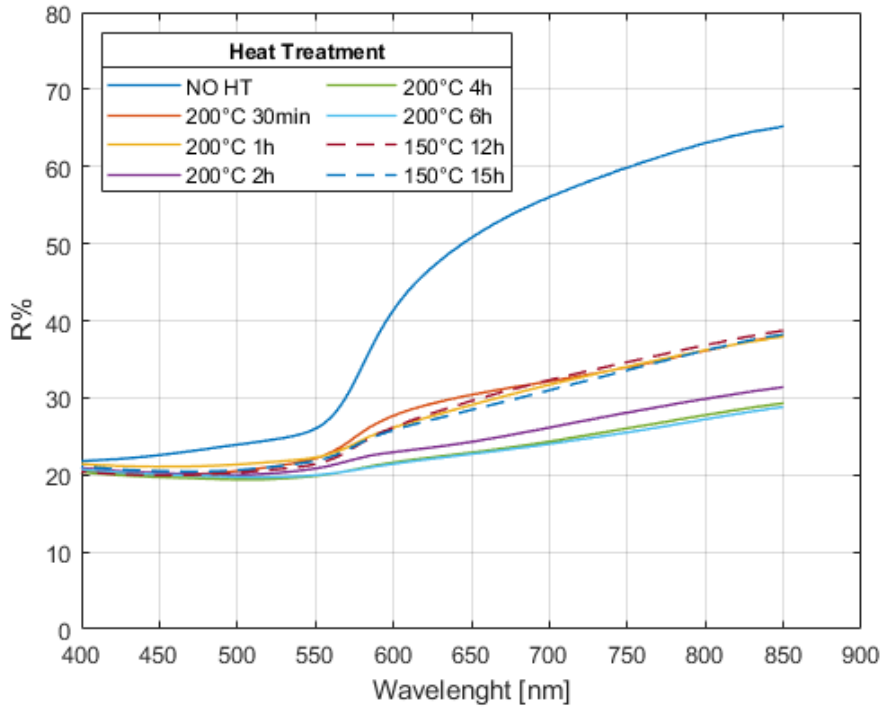


Figure 4.7 Laser reflectance measurements of pure copper and oxidized powders.

Heat treatments at 150°C for 15 hours and 200°C for 1 hour were performed on batches of 6 kg to test the printability of the oxidized powder. Because both heat treatments resulted in powders with almost the same oxygen content reflectivity, the decision to test both powders was made to see which heat treatment was optimal for increasing the powder's printability.

The morphology of the powders is shown in Figure 4.8, Figure 4.9, and Figure 4.10. The heat-treated powders were mounted in epoxy resin for cross-sectional analysis. The particles were polished down to a 1 μm diamond finish. In order to check the oxidation of the particles, EDS analyses were performed on the particles' surfaces and by scanning the area of the cross-section of the mounted particles.

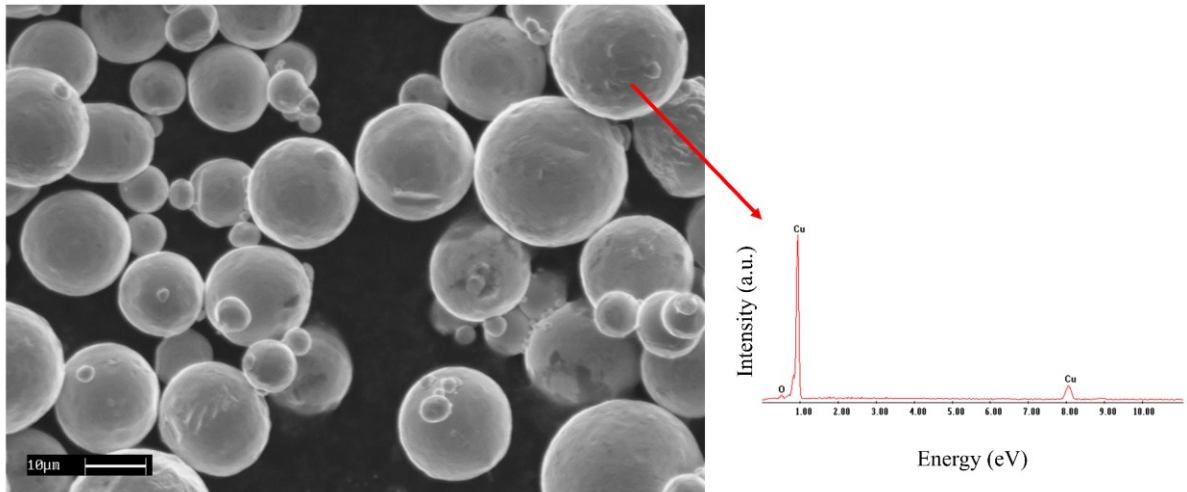


Figure 4.8 Morphology and EDS analysis of the starting pure copper powder.

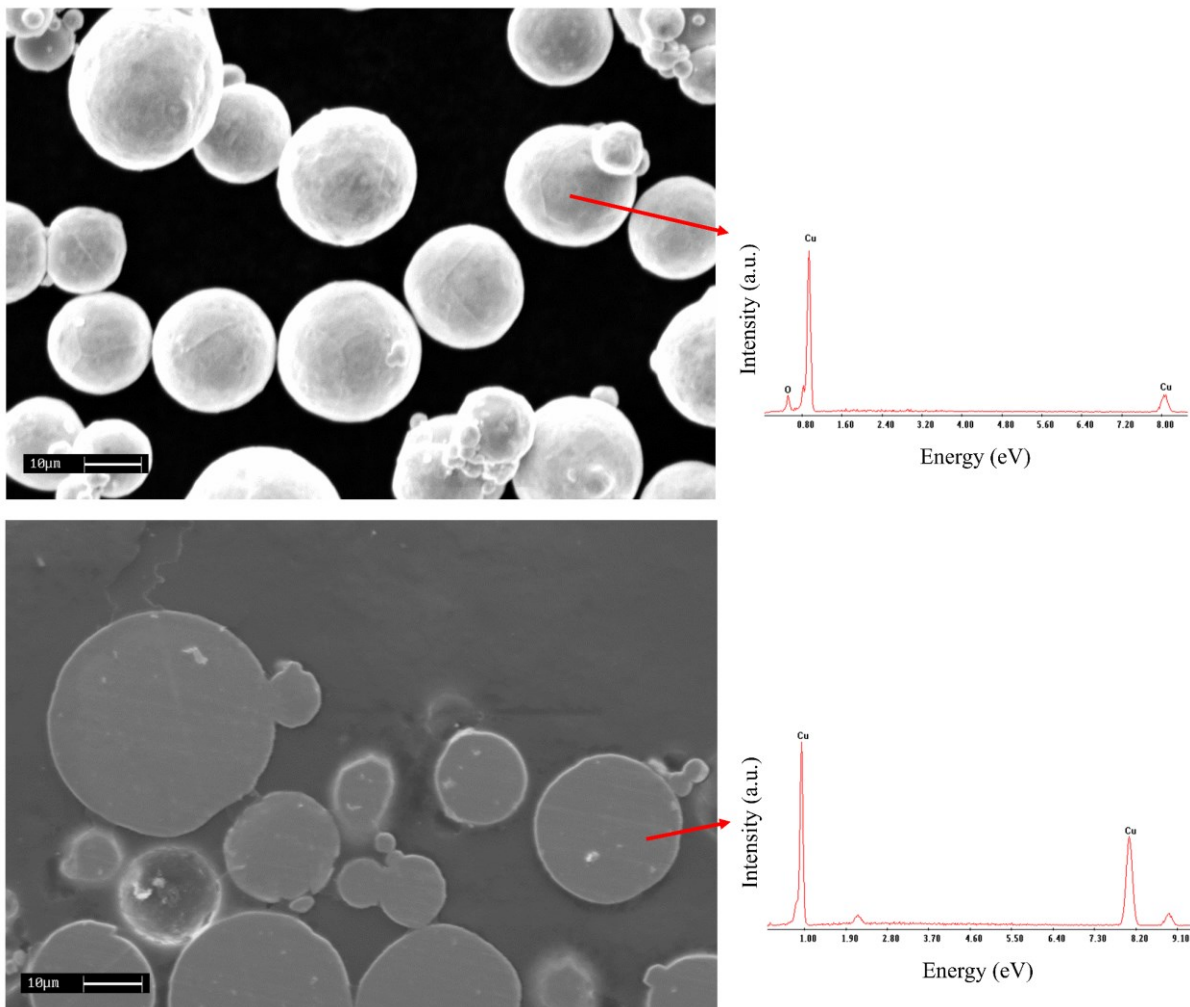


Figure 4.9 Morphology (TOP) and cross section (BOTTOM) of powder oxidized at 150 °C for 15 h. On the right of each figure are reported the EDS pecks of oxygen and copper.

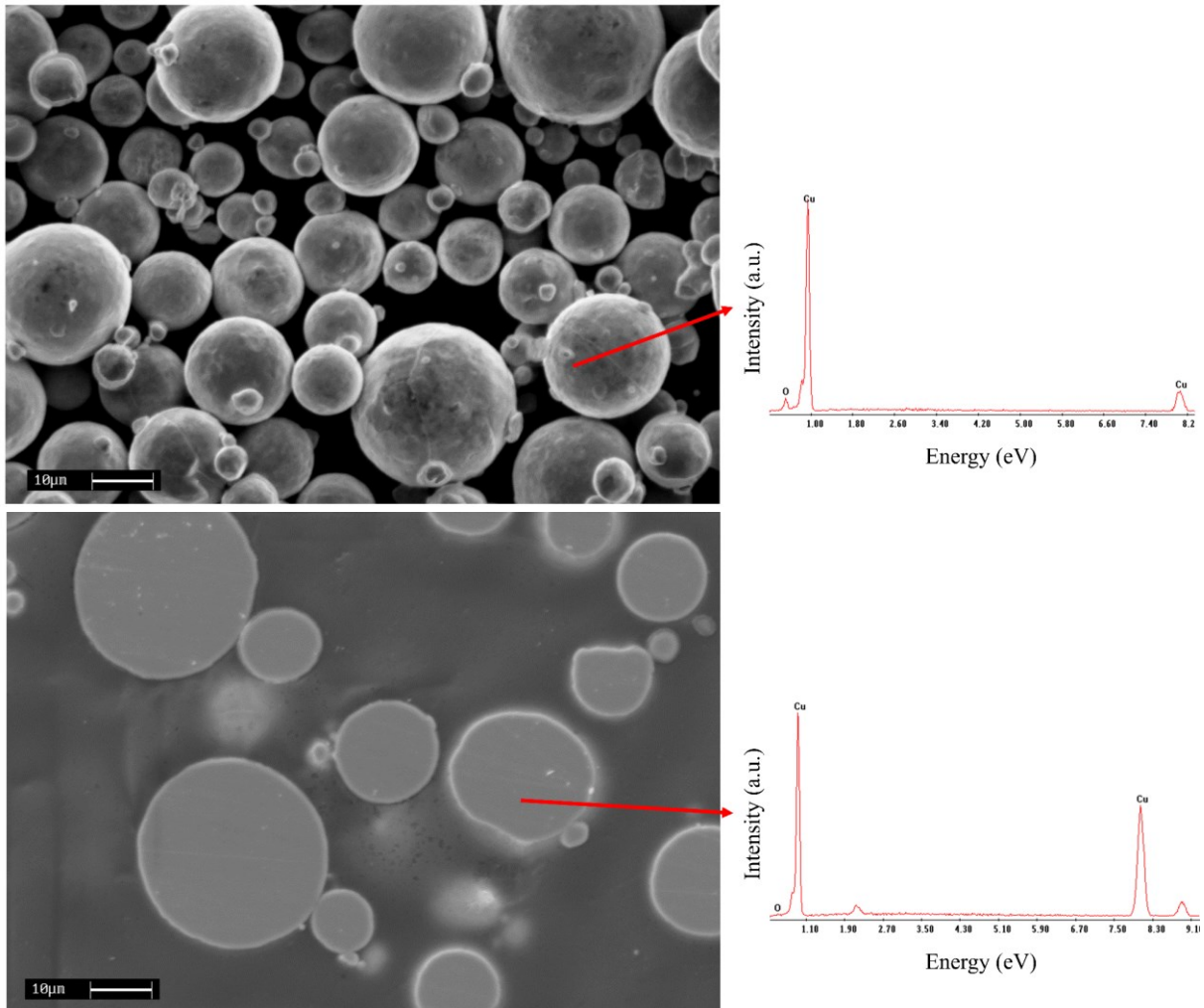


Figure 4.10 Morphology (TOP) and cross section (BOTTOM) of powder oxidized at 200 °C for 1 h. On the right of each figure are reported the EDS pecks of oxygen and copper.

The comparison between the starting powder and the heat-treated one shows that the shape of the powder was not affected by the high temperatures. The particles maintained a spherical shape, but deformed particles had been observed in both starting and heat-treated powders. This was due to the interaction between laser and powder particles in previous LPBF processes. The only morphological difference observed was the surface of the particles: the surface of the oxidized particles appears to be rougher compared to the starting powder. The presence of oxides on the surface (as detected by EDS analyses) modifies its texture, making the particles less smooth. The EDS analyses at the cross-sections reveal that the oxidation is only at the surface and does not extend into the particle's mass.

❖ Tuning of the process parameters

Figure 4.11 shows the comparison of the relative densities obtained using the oxidized powders and the stating one.

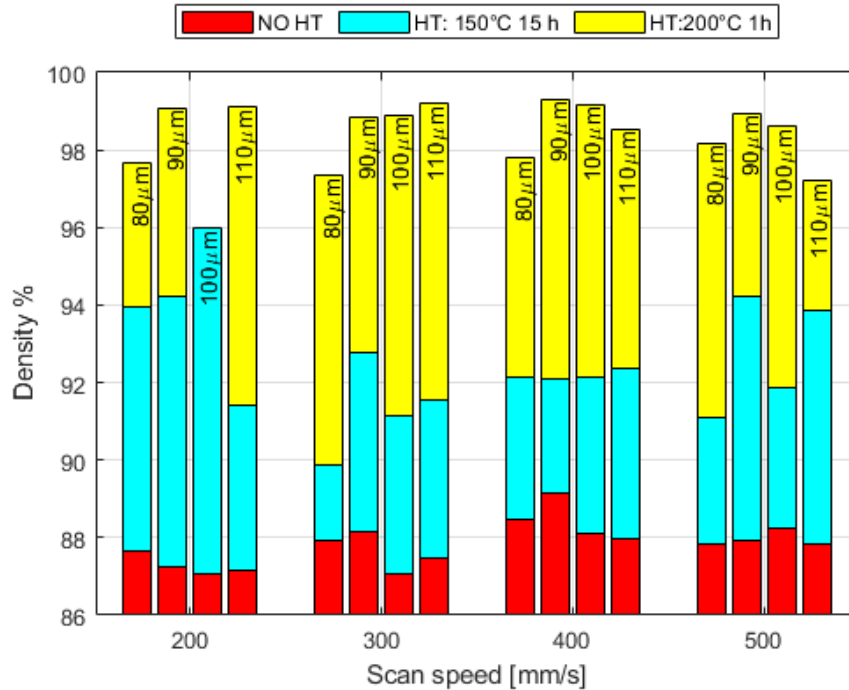


Figure 4.11 Relative densities of pure and oxidized copper samples manufactured with different scan speeds and hatching distances.

The oxidized powder yielded higher densities for each combination of scan speed and hatching distance. Only one sample failed to build during the manufacturing process, and therefore the result is not reported (oxidized powder at 200 °C with $v = 200$ mm/s and $h = 100$ μm).

The powder oxidized at 200 °C yielded the highest increment of relative density. Depending on the process parameters, reductions between 9% and 11% of porosity were measured. At scan speeds of 200 mm /s and 300 mm /s, the relative density increases with the hatching distance since the melt pools are wider, and the optimal overlap ratio is achieved at higher distances. Because the scan tracks are narrower, the opposite behaviour is observed at $v = 400$ mm/s and 500 mm/s. The highest relative density was 99.32%, and it was obtained using 400 mm/s of scan speed and 90 μm hatching distance.

Lower porosity reductions were attained while using the powder oxidized at 150 °C. The highest relative density measured was 96.1% at 200 mm/s of scan speed and 100 μm of hatching distance.

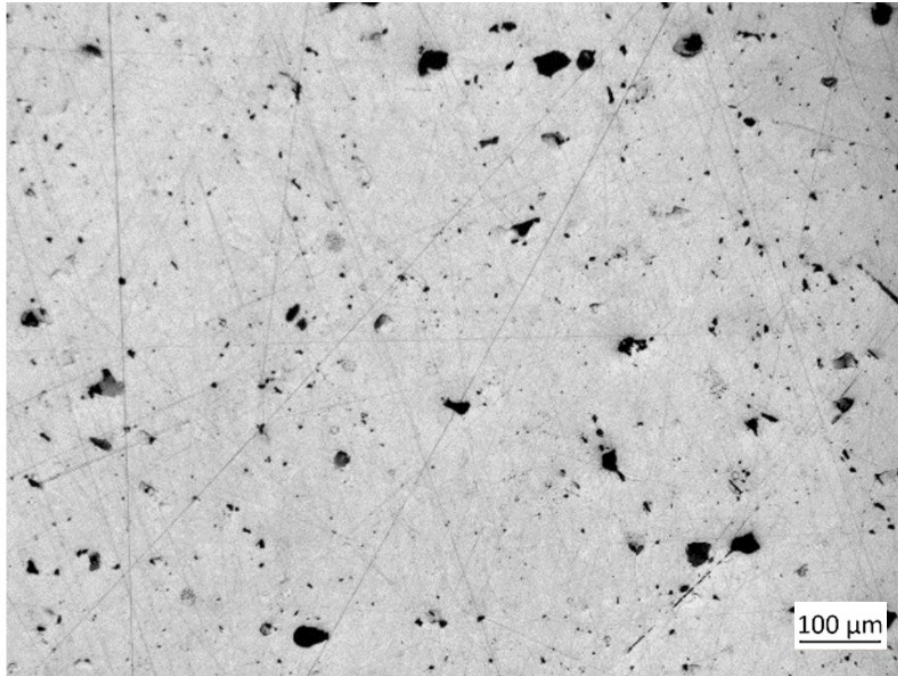


Figure 4.12 Micrograph of a cross section of the samples with the highest density obtained using pure copper powder oxidized at 150 °C.

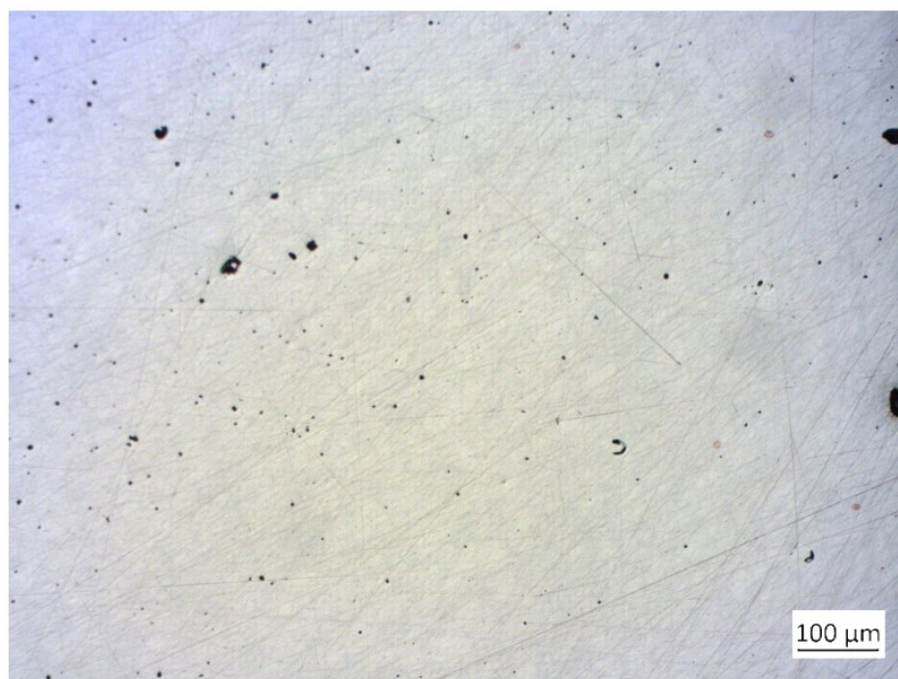


Figure 4.13 Micrograph of a cross section of the samples with the highest density obtained using pure copper powder oxidized at 200 °C.

Figure 4.12 and Figure 4.13 show the cross-section micrographs of the highest density samples obtained using oxidized powder at 150 °C and 200 °C, respectively. Pores with highly irregular shapes were observed in Figure 4.12, and these pores are the results of poor melting of scan tracks. The energy input is not high enough to form stable melt pools, and their partial overlap causes residual porosity in the parts.

Figure 4.13, on the other hand, displays tiny pores with a circular shape, which might be due to the gas entrapment and the keyhole phenomenon. Gas entrapment porosities are small gas bubbles trapped during solidification [165]. The high solidification rate of pure copper favours this typology of porosity since the bubbles have less time to the surface. The keyhole porosity forms at the bottom of the melt pool because of the coalescence of the entrapped gas [39]. The keyhole phenomenon is usually observed when the energy input is very high [10] or when the re-melting scan strategy is employed [185]. The typology of porosity and the failed manufacturing of the sample at low scan speed indicate that the energy input utilized was too high. While 370 W of laser power is insufficient to melt the powder oxidized at 150 °C fully, it is high enough to obtain the opposite defects when using the oxidized powder at 200 °C.

Even though the oxygen content and reflectivity spectra were comparable, the studied samples indicate an opposing densification behaviour. Different reflectivity levels at 1080 nm are thought to be the primary source of this inverse trend. It is also likely that when large volumes of powder are oxidised, the oxidation of the powder particles differs from that achieved in small batches. On a static furnace, the particles that lay on top of the powder bed will oxidise more than the ones at the bottom. Higher temperatures inside the static furnace would generate more air turbulence, improving oxygen diffusion between the particles and hence oxidizing them homogeneously.

❖ Thermo-mechanical characterization

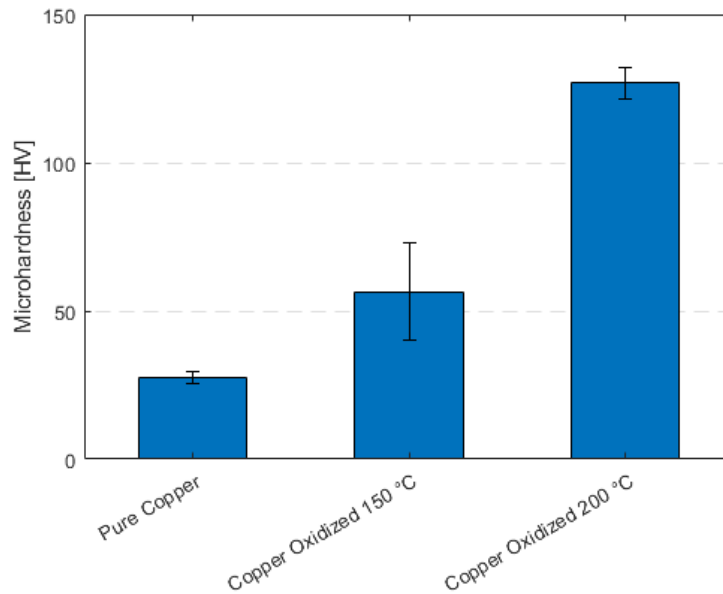


Figure 4.14 Micro-hardness values for pure and oxidized copper.

Micro-hardness measurements were performed on the highest density samples, and the results are shown in Figure 4.14. The reduced porosity of the parts manufactured using the 200 °C heat-treated powder yielded a micro-hardness of 126.8 ± 5.2 HV, while the ones produced with powder oxidized at 150 °C had a micro-hardness of 56.4 ± 16.4 HV. As expected from the relative density measurements, the pieces with reduced porosity also showed higher micro-hardness. The part with higher porosity also shows a higher standard deviation. This is because when the micro-hardness measurement is performed, a pore below the surface of the material might collapse under the applied load, leading to a larger imprint and hence to a lower micro-hardness. As a result, the size of the imprint might vary greatly depending on its location. The porosity of the pure copper component was high enough to be evenly distributed inside the copper matrix. Hence the standard deviation is lower.

Compared to the pure copper parts, which had micro-hardness of 27.6 HV, the samples with the highest density showed a micro-hardness ~4 times higher. According to Jadhav et al. [96], this extreme increment of mechanical properties is not only attributed to the increase in density but also to the presence of nanometric copper oxide precipitates that strengthen the material. Therefore, the

oxidation of the powder can also be a strengthening method for the production of pure copper parts reinforced with copper oxides particles.

Since the oxidized powder at 200 °C yielded the highest density, it was used to produce thermal diffusivity specimens (two disks of 40 mm diameter and 8 mm thickness). Oxidizing the powder led to an increment of thermal conductivity from 137 W/(mK) to 196 W/(mK), which is almost half of the conductivity of pure bulk copper (~400 W/(mK)). This high discrepancy could be due to the oxygen content in the printed parts.

However, in a similar research activity conducted by Jadhav et al. [96], the 2000 ppm of oxygen concentration resulted in only a slight reduction of electrical conductivity. They measured electrical conductivity of 89.9 % IACS (International Annealed Copper Standard). Raab et al. [186] measured both electrical and thermal conductivity of pure copper samples produced via Electron Beam Melting. They found that additively manufactured copper follows the Wiedemann-Franz relationship (4.3):

$$\frac{\lambda}{\sigma} = L * T \quad (4.3)$$

where λ is the thermal conductivity (W/mK), σ the electrical conductivity (S/m), L the Lorenz number ($2.41 \times 10^{-8} \text{ W}\Omega\text{K}^{-2}$) and T the temperature. Since the thermal and electrical conductivities are proportional, high electrical conductivities should correspond to high thermal conductivities. Using the electrical conductivity obtained by Jadhav et al. [96], the resulting thermal conductivity should be 377 W/(mK). Despite being only a rough estimation, as the value of the Lorenz number is roughly constant, this calculation shows that the thermal conductivity should be much higher. [Section 5.1.3.6](#) presents a deep investigation of the thermal conductivities of copper components.

4.3 Summary

Heat treating pure copper powder at temperatures above 150 °C in air produces a superficial oxide layer that reduces the copper reflectivity. At 150 °C, the oxidation reaction occurs slower than 200 °C and longer durations are required to oxidize the powder. The oxidation yielded a considerable reduction of reflectivity: at the 800 nm wavelength, the reflectivity decreased from ~ 63 % (pure copper)

to ~35 %. Despite not being the wavelength of the fibre laser (1080 nm), it is safe to assume that this reduction persists at higher wavelengths. The observed copper oxide was Cu_2O , and no trace of CuO was detected. LPBF of oxidized powder yielded higher relative densities, but only with the powder oxidized at 200 °C it was possible to obtain dense samples. The samples produced with oxidized powder had higher microhardness and thermal conductivity. Therefore, when using LPBF with low laser power (<370 W), the oxidation of pure copper powder is a viable solution to print parts with better thermo-mechanical properties.

CHAPTER 5

5 LPBF OF CUCRZR ALLOY

5.1 Thermo-mechanical characterization

5.1.1 Introduction

The characterization of pure copper parts produced using a low power LPBF machine has demonstrated that it is not possible to achieve dense parts with good thermo-mechanical properties. Only the oxidation of pure copper particles, or a less pure composition, enabled the fabrication of low porosity parts. While adding oxygen or phosphorus to pure copper could be a good solution for various heat exchange applications, it could be a problem for the purpose of this research. The accelerator grids work in a vacuum chamber, and the presence of O and P might lead to outgassing problems.

As a result, the option was to divert to copper alloys already used in vacuum operation, with stronger mechanical properties to compensate for the loss of conductivity. Particle reinforced copper alloys were the ideal contender to substitute pure copper, as they combine high conductivity with good mechanical properties. It was decided between the existing high-performance copper alloys to test the CuCrZr alloy since it has one of the highest thermal conductivity and was commercially available in powder form.

The CuCrZr alloy requires two heat treatments to obtain the desired mechanical and thermal properties: solution annealing (SA) to generate a supersaturated solution and age hardening (AH) to form fine precipitates dispersed in the copper matrix. As already described in [Section 1.3.3.2](#), the LPBF process generates a supersaturated solution due to its high cooling rates, and therefore it is possible to age harden directly the as-built parts (DAH – direct age hardened).

Firstly, this work presents the tuning of the parameters to obtain dense parts. The focus then shifts to the thermomechanical characterization of the heat-treated component using SA + AH and DAH.

The DAH heat treatment does not affect the columnar microstructure [113], [117]. The mechanical anisotropy of LPBF components has been associated with crystallographic texture in many studies [39], [187]. Therefore, this study investigates the effect of the microstructural recrystallization obtained with the solution annealing heat treatment. The anisotropy of the mechanical and thermal properties is analysed by testing samples printed in the horizontal and vertical directions. The effect of the heat treatments on the electrical properties was also analysed.

5.1.2 Material and methods

5.1.2.1 Feedstock Material

The CuCrZr copper powder used to produce the specimens was gas atomized and had spherical morphology, with a particle size range between 15 to 45 μm . The producer provided the chemical composition, reported in Table 5.1, and the powder characteristics: particle size distribution, apparent density and flow rate, reported in Table 5.2.

Table 5.1 Chemical composition of the starting CuCrZr copper powder.

Element	Cr	Zr	Si	Fe	Cu
Mass Fraction [wt%]	0.8	0.08	0.01	0.02	Bal.
min – Max [wt%]	0.5 – 1.2	0.03 – 0.3	0.1 Max	0.08 Max	

Table 5.2 Powder characteristics provided by the producer.

	Virgin Powder	Reused Powder	
Particle Size D10 [μm]	18.5	18.0	Min – Max 15 – 21 μm
Particle Size D50 [μm]	27.3	25.6	
Particle Size D90 [μm]	40.4	37.5	Min – Max 35 – 45 μm
Apparent density [g/cm ³]	4.79		
Flow rate [s/50g] (Carney Flow Testing, 5mm)	3.12		

Since it was not possible to use virgin powder for each manufacturing process, the morphology of the recycled powder and its particle size distribution were also analysed. The recycled powder has been reused five times and sieved with 230 mesh size (63 μm of aperture). The chemical composition of the powder was checked with EDS analyses, and the oxygen and nitrogen concentration was measured with the inert gas analysis using an Eltra N/O of both the recycled powder and printed material. The PSD of the reused powder was measured; the D-values of the recycled powder are reported in Table 5.2.

5.1.2.2 LPBF Setup and Heat Treatments

The fabrication parameters are listed in Table 5.3; the varied parameters were the scan speed, the hatching distance, and the laser power, while the layer thickness was kept constant. The scan strategy adopted was a bidirectional (zigzag) 5mm stripe pattern with a rotation angle of 67° between neighbouring layers.

Table 5.3 Fabrication parameters of the LPBF process

LPBF Parameters	Values
Layer thickness [μm]	20
Laser Power [W]	200 ÷ 370
Scan Speed [mm/s]	400 ÷ 1000
Hatching distance [μm]	70 ÷ 110
Protective atmosphere	N_2
Scanning strategy	Bidirectional, 67° Rotation angle

The heat treatments performed on the specimen are the solution annealing (SA) heat treatment and the age-hardening (AH) heat treatment. The specimens are named “direct age-hardened” (DAH) when only the AH heat treatment is performed and “solution annealed and age hardened” (SA+AH) when also the SA heat treatment is performed. No heat treatments have been performed in the as-built (AB) samples. The samples were solution annealed at 980°C for 30 min and water-quenched with a reducing $\text{Ar}+\text{H}_2$ atmosphere and age hardened at 580°C for 300 min with a reducing $\text{Ar}+\text{H}_2$ atmosphere

followed by air cooling. The AH heat treatment was selected in order to obtain the highest thermal conductivity, as reported in Wallis et al. [113].

5.1.3 Experimental results

5.1.3.1 Powder characterization

Figure 5.1 shows the recycled powder morphology and the chemical composition observed with EDS.

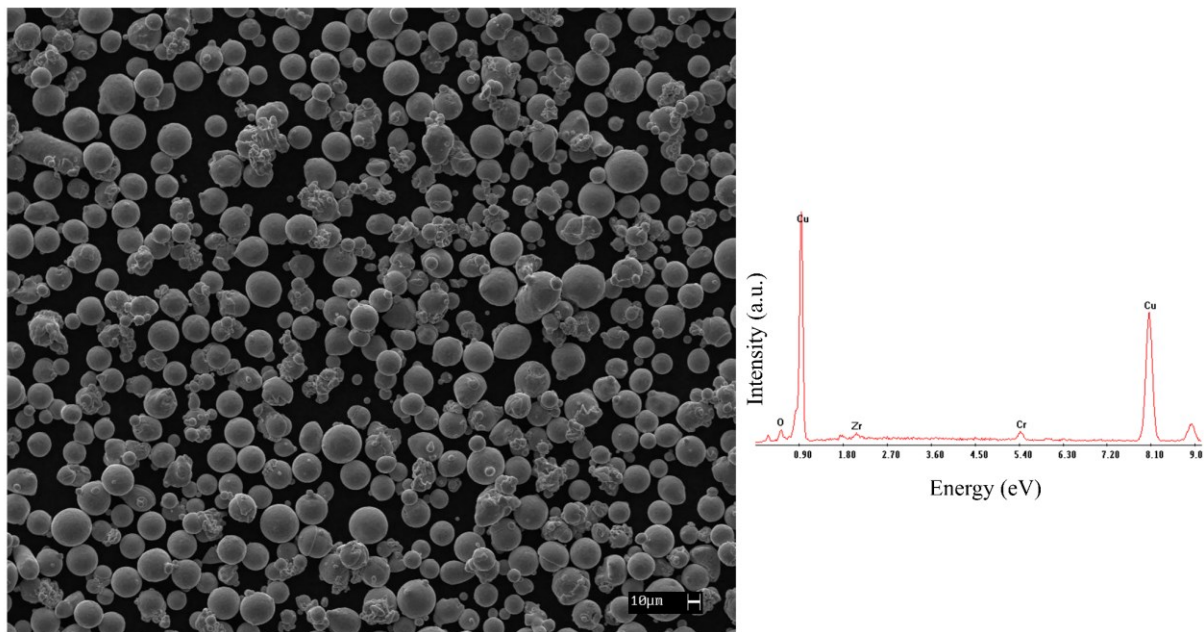


Figure 5.1 Morphology of the CuCrZr powder and EDS analysis.

The majority of the particles have a spherical shape, and some particles present smaller satellites attached to them. Among the spherical particles, it is possible to observe particles with irregular shapes, mainly clusters of particles, and particles with an elongated shape and broken particles. As discussed in [Section 3.1](#), the presence of clusters could be attributed to the collision of liquid metal splatters generated during the LPBF process with the powder bed [160]. Irregularly shaped particles have a negative influence on the powder flowability [151], however no distribution issues have been encountered during each manufacturing step.

The EDS spectrum shows the pick of the major elements present in the copper alloy and a small pick of oxygen due to the oxidation of the powder. The inert gas analysis also confirmed the oxidation

of the powder; the recycled powder had an oxygen concentration of 283 ppm. The oxygen concentration of printed parts has been measured, and the manufacturing process increases the amount of oxygen up to 485 ppm. This shows that the processing chamber's oxygen concentration should be reduced to reduce oxidation.

The reuse of the powder also led to a small change in the particle size distribution: a reduction of all D-values (D10, D50, D90) was observed (see Table 5.2). The D90 has decreased the most, approximately 3 μm , showing a higher reduction of the larger particles. Compared to the recycling of pure copper powder observed in [Section 4.2.2](#), where the reuse of the powder led to broader PSD, the PSD of the reused CuCrZr powder has shrunk. According to Condruz et al. [188], the narrowing of the PSD is a result of the powder layer spreading: the larger particles are carried away by the wiper blade and pushed towards the sides of the machine. However, the D-values of the reused powder remained in the recommendation range provided by the vendor.

The different behaviour of the PSD of recycled powder is an argument that will be studied in future research, but it is outside the scope of this thesis.

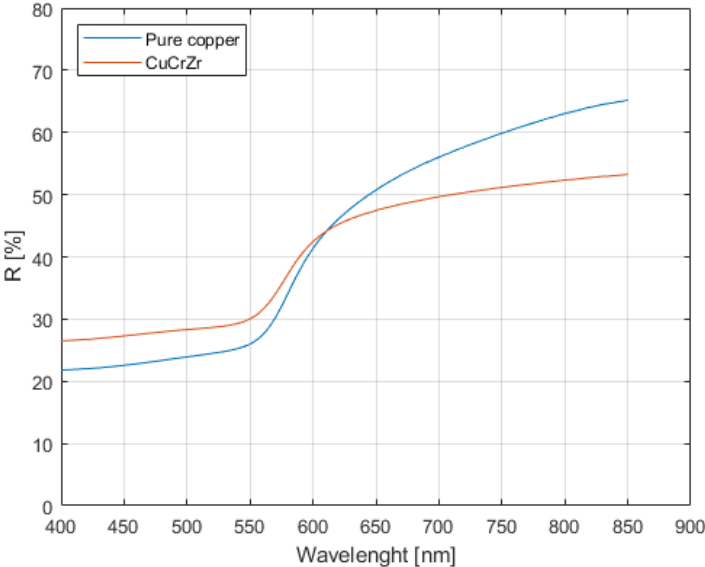


Figure 5.2 Laser reflectance measurements of pure copper (powder A) and CuCrZr.

The reflectivity spectrum of CuCrZr alloy is reported in Figure 5.2, and it is compared with pure copper with similar PSD (powder A). At 800 nm, the CuCrZr alloy shows ~12 % less reflectivity than

pure copper. It seems that the difference in reflectivity increases with the wavelength, and therefore it is likely that the CuCrZr alloy will absorb more energy at 1064 nm (wavelength used in EOSINT M280).

5.1.3.2 *Parameter tuning*

The processing parameters were fine-tuned in two stages. The objective was to achieve the lowest internal porosity while maintaining the highest possible production rate. The first parameters analysed were the laser power and the laser scan speed; Figure 5.3 reports the relative density of the specimens. The hatching distance has been kept constant at 90 μm and the layer thickness at 20 μm . The laser power has been varied between 200 W and 350 W, and the scan speed between 400 mm/s and 1000 mm/s.

The ratio between the laser power and scan speed P/v is defined as Linear Energy Density (LED). Low LED causes discontinuous and irregular scan tracks [189], which compromises their successful overlap, resulting in an increased lack of fusion porosity. This can be observed at low laser power (<300 W) when increasing the laser scan speed (and therefore reducing the LED) causes the relative density to drop. However, the laser power has a stronger influence on the relative density than the LED itself. Samples manufactured at higher laser power show lower porosities despite having lower LED. For example, the relative density of the sample produced with 350 W and 1000 mm/s (LED=0.35 J/mm) is 99.34%, whereas the sample manufactured using 200 W and 400 mm/s (LED=0.5 J/mm) shows a relative density of 96.37%. The process parameters of the sample with the highest relative density (99.78%) were 350 W of laser power and 800 mm/s of scan speed. Further increasing the scan speed led to a decrease in relative density.

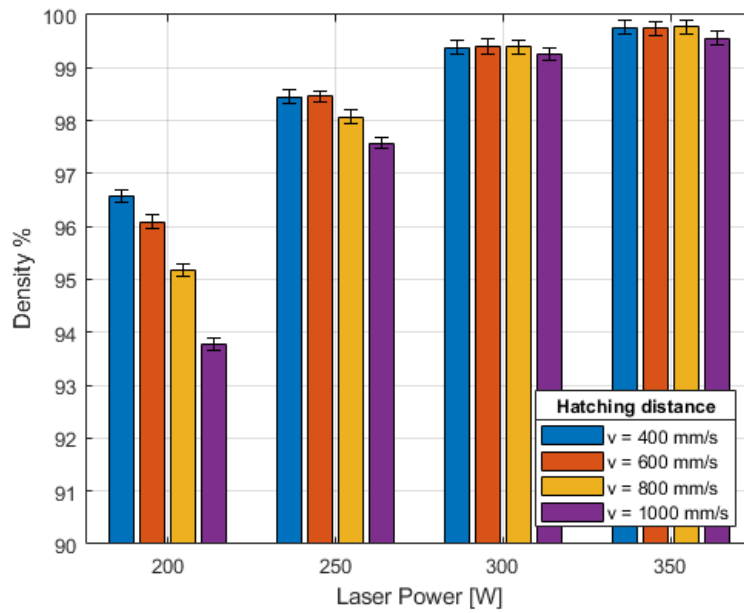


Figure 5.3 Relative densities of CuCrZr samples manufactured using different laser powers and scan speeds.

The goal of the second tuning stage was to determine the best combination of laser scan speed and hatching distance. The laser power was set to 370 W, which is the maximum feasible, and the layer thickness was kept at 20 μm . The results of the tuning of the parameters are reported in Figure 5.4.

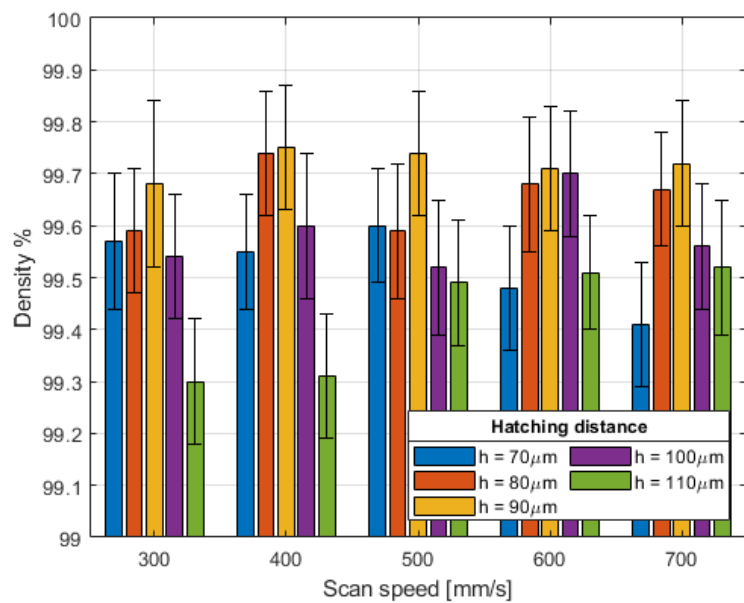


Figure 5.4 Relative densities of CuCrZr samples manufactured using different scan speeds and hatching distances.

Relative densities above 99 % were attained while maintaining the highest laser power. The highest relative density measured was 99.75 %, using 400 mm/s of scan speed and a hatching distance

of 90 μm . In the range of 300 – 700 mm/s, the influence of the scan speed while using 370 W of laser power is low, meaning that it should be possible to further increase the scan speed before measuring a significant decrease in relative density.

On the other hand, the optimal hatching distance was found. At 90 μm of hatching distance, the samples showed the highest relative density, meaning that this is the optimal overlap ratio between scan tracks to avoid lack of fusion porosities. Therefore the selected parameters for the manufacturing of the test specimens were: laser power of 370 W, layer thickness of 20 μm , scan speed of 800 mm/s, and hatching distance of 90 μm .

5.1.3.3 Microstructural characterization and XRD analysis

Microstructural analysis was conducted by observing the optical images of the etched sections of heat-treated samples. Figure 5.5 shows the XY planes of AB and DAH, while Figure 5.6 reports the XY planes of SA and SA+ AH samples.

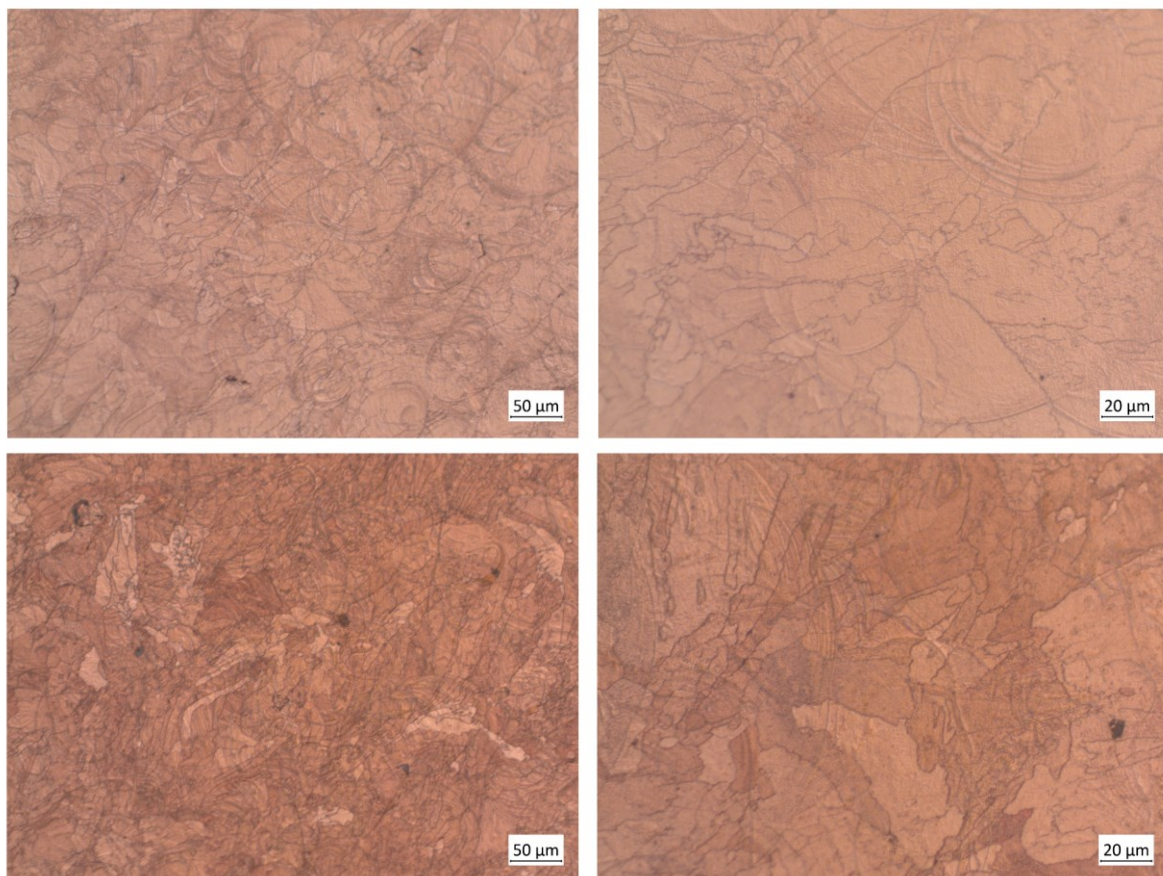


Figure 5.5 Microstructural analyses of XY sections of an AB sample (TOP) and a DAH sample (BOTTOM).

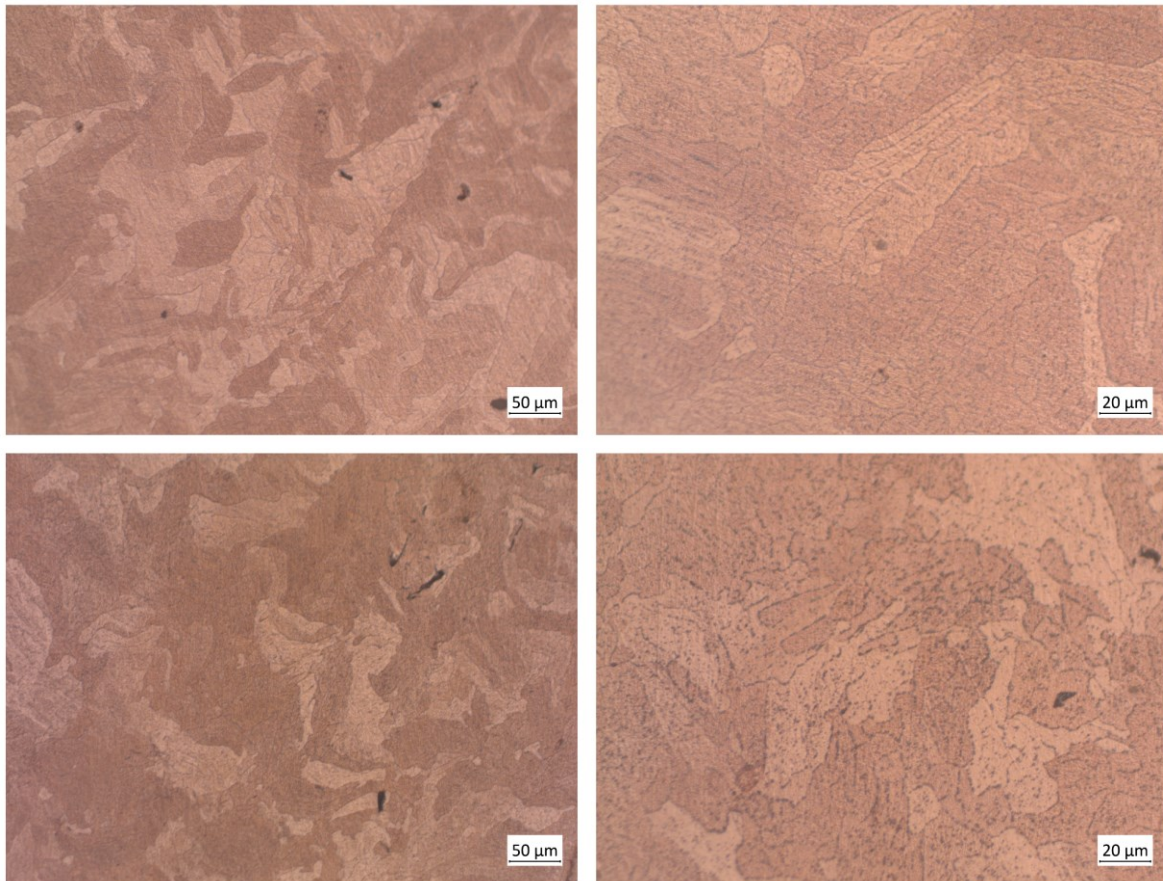


Figure 5.6 Microstructural analyses of XY sections of an SA sample (TOP) and a SA+AH sample (BOTTOM).

The microstructures of AB samples and DAH samples observed in Figure 5.5 are the same. They show grains of various sizes, from 10 μm to 100 μm , representing the cross-section of the columnar microstructure that develops from the high thermal gradients generated by the LPBF process. The difference in grain size is due to the partial recrystallization process that occurs because of the repeated fusion of the layers. Heat-treating at 580 $^{\circ}\text{C}$ for 360 min does not affect the microstructure, and no precipitates were observed. However, the variation of the mechanical properties and conductivity presented in the following sections confirms that the precipitation of Cr occurs. This means that the dimension of precipitates was too fine to be observed under an optical microscope. It was impossible to detect the presence of the precipitates even using high magnification at SEM. According to Wallis et al. [113], the DAH heat treatment generates precipitates of a few nanometers.

In both micrographs, it is also possible to observe the melt pools' boundaries, however the rotation angle between each layer makes them hard to distinguish.

A different microstructure is observed in Figure 5.6. The solution annealing heat treatment recrystallizes the microstructure. It consists of larger grains, and no trace of melt pool boundaries is present. Few precipitates near the grain boundaries were observed in the SA sample, meaning that the precipitation already starts with solution annealing heat treatment. The number of precipitates with a dimension of a few microns drastically increases in the SA + AH heat treatment.

Figure 5.7 shows the micrographs of the XZ planes of DAH and SA + AH samples, both presenting a few lack of fusion porosities. The columnar microstructure and the melt pool boundaries are clearly distinguishable in the DAH specimen. While the SA heat treatment vanishes the melt boundaries, it does not fully recrystallize the microstructure since columnar grains are still present. Higher temperatures or longer durations are required to recrystallize the microstructure fully.





Figure 5.7 Microstructural analyses of XZ section of (a) DAH sample and (b) SA+AH sample.

The XRD analyses on the powder and printed samples are presented in Figure 5.8. The diffraction peaks of α -Cu are detected in all the presented samples. Compared to the powder, the intensity of the Bragg peak of (220) is much higher in the LPBF samples. The same discrepancy in peak intensity was observed by Ma et al. [112]. The crystallographic texture in the LPBF components is due to the competitive grain growth towards the building direction, which is caused by the high thermal gradients generated by the LPBF process. Although the (220) peaks are still the most intense peaks, in the SA and SA+AH samples, the peaks have more uniform intensities, confirming that the partial recrystallization process has occurred.

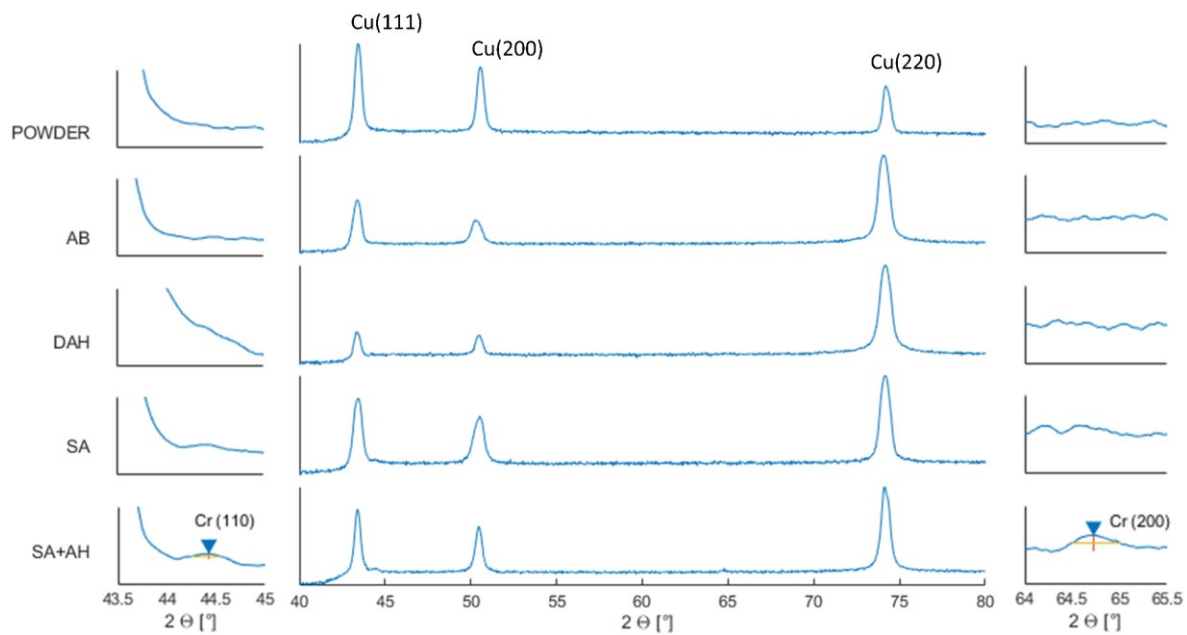


Figure 5.8 XRD-spectra of CuCrZr alloy in various heat-treated states, with close up view of the detected Cr peaks.

Only in the SA+AH specimen peaks other than α -Cu were detected. Two low-intensity peaks have been detected at $44.4^\circ 2\theta$ angle and $64.7^\circ 2\theta$ angle, which correspond to the(110) and (200) crystal planes of metallic chromium. Therefore, the observed precipitates correspond to metallic Cr. The precipitates in the DAH sample were too fine to be identified.

Compared to the AB samples, the peaks of the heat-treated samples are slightly shifted towards larger diffraction angles. The Bragg diffraction law (Equation (5.1)) explains this behaviour:

$$2d\sin(\theta) = n\lambda \quad (5.1)$$

Where d is the lattice constant, θ is the diffraction angle, λ is the wavelength, and n is the diffraction order. Because the wavelength and diffraction order are constants, increasing diffraction angles correlate to lowering lattice constants. The rapid cooling of the LPBF process generates a supersaturated solid solution of Cr atoms. The substitutional solution of Cr in the Cu matrix increases the lattice spacing because Cr atoms are smaller than Cu ones [190]. As a result, the heat-treated samples show larger Bragg diffraction peaks due to the precipitation of Cr, which brings the lattice spacing down to its lower equilibrium value.

5.1.3.4 Mechanical properties

The mechanical characterization of the CuCrZr alloy consisted of microhardness measurements and tensile tests on both AB and heat-treated samples. The micro-hardness measurements are reported in Figure 5.9. Before any heat treatment, the microhardness of the AB sample is 91.6 HV0.3, Wallis et al. [113] and Jahns et al. [115] obtained similar values.

The hardness of the material was increased by directly ageing it at 580 °C for 300 minutes, resulting in a hardness of ~133 HV0.3, confirming that Cr precipitation happened, even though it was not observed or detected.

When subjected to a solution annealing, the hardness of the as-built state reduces to 72.4 HV0.3. The partial recrystallization of the component increases the grain size and decreases the dislocation density, both of which affect the micro-hardness of the material [113], [114], [117]. The precipitation obtained with the subsequent ageing heat treatment improves the micro-hardness of the part up to 100 HV0.3.

Despite being subjected to the same ageing heat treatment, the micro-hardness of the SA+AH sample is ~25% lower than the DAH sample. According to Wegener et al. [116], the decrease of dislocation density caused by the solution annealing heat treatment accounts for the less obvious rise in hardness. Because a rise in dislocation density accelerates the kinetics of precipitation formation [191], samples aged immediately from the as-built state have a greater microhardness.

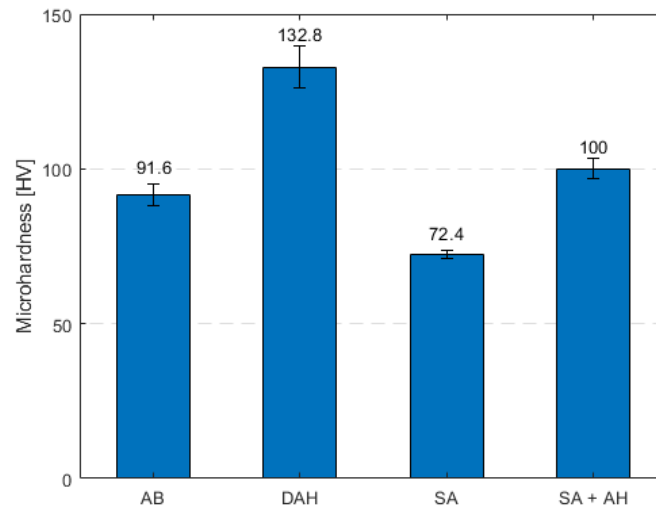


Figure 5.9 Micro-hardness of LPBF CuCrZr samples in the as-built state and after various heat treatments.

The results of the tensile tests are reported in Table 5.4, and the stress-strain curves are shown in Figure 5.10.

Table 5.4 Tensile test results of CuCrZr manufactured in two printing directions and at different heat-treating states.

Heat Treatment	Ys [MPa]	UTS [MPa]	E [GPa]	Elongation at Break [%]
As Built H	238 ± 2	281 ± 1	131	28
As built V	214 ± 4	239 ± 3	124	51
Direct Age Hardened H	272	366	142	21
Direct Age Hardened V	248 ± 4	318 ± 3	131	23
Solution Annealed + Age Hardened H	131 ± 3	265 ± 1	138	41
Solution Annealed + Age Hardened V	123 ± 2	232 ± 1	132	40

The specimens show mechanical anisotropy in each tested condition. Vertical samples have lower strength than the specimens built horizontally, probably due to the lack of fusion porosities between the layers (as observed in Figure 5.7), which severely diminishes the interlayer bonding. As already explained in [Section 3.3.3.2](#), the relative position between the loading direction and the lack of

fusion porosities of samples built vertically increases the stress concentration and favours crack initiation [168]. Heat-treating the samples slightly reduces the mechanical anisotropy. In the vertical direction, yield and tensile strength reduction were 10% and 15% for AB samples, 9% and 13% for DAH samples, and 6% and 12% for SA+AH samples. The SA + AH samples have a more homogenous microstructure as a result of partial recrystallization, which reduces mechanical anisotropy. Despite this, the anisotropy was not entirely removed because of the lack of fusion porosities.

More constant elongations at break were obtained by heat-treating the samples. The deviation between vertical and horizontal samples went from 20% in the AB state to ~2% in the heat-treated states. Vertical specimens have a higher ductility than horizontal ones because vertical specimens are manufactured with more layers. Since each layer is a “slipping surface”, the vertical specimens are more ductile [44]. The vertical specimen's elongation at break was extremely high because there were no precipitates to hinder the dislocations' motions in the AB state.

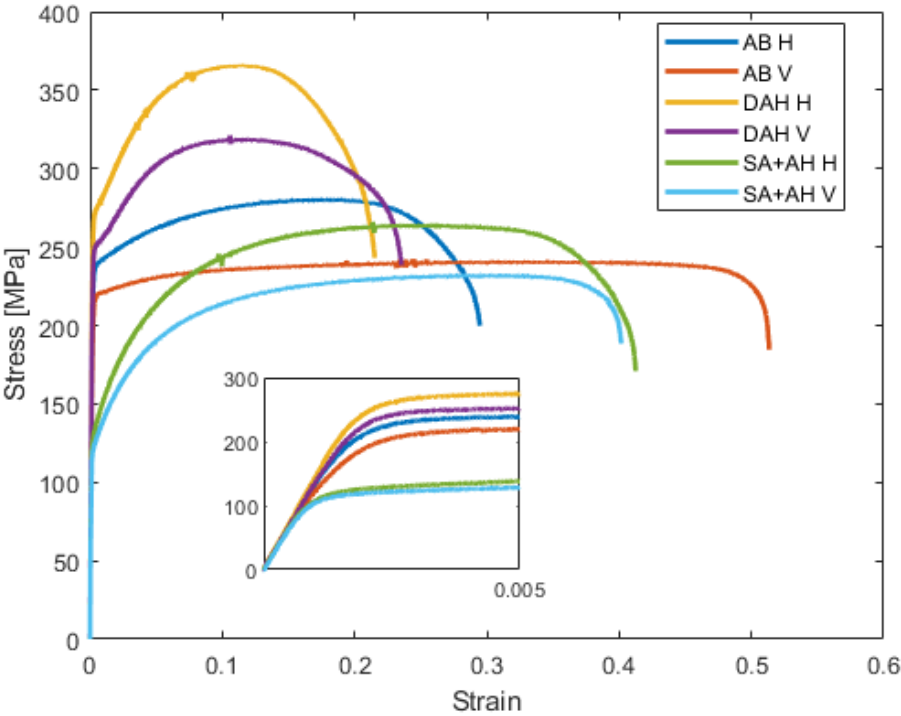
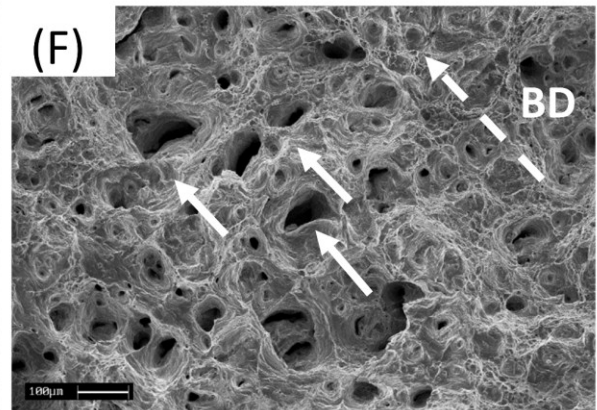
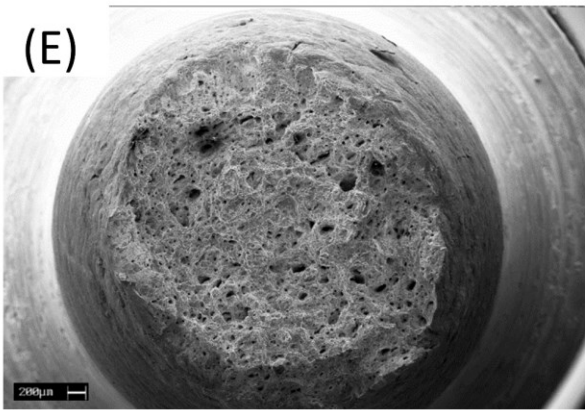
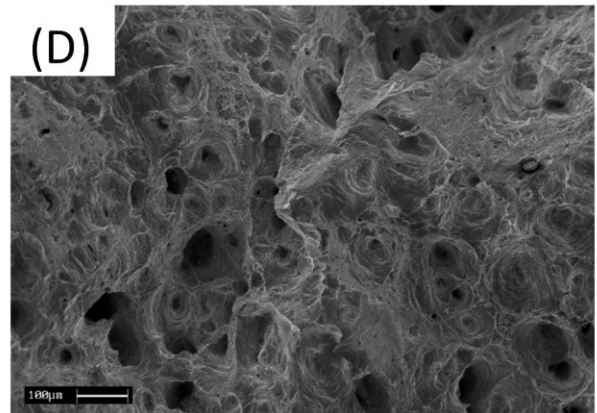
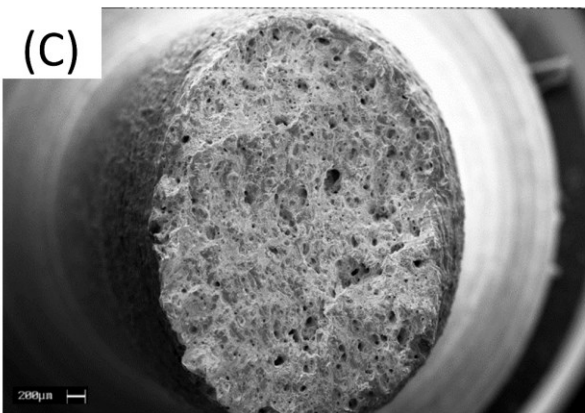
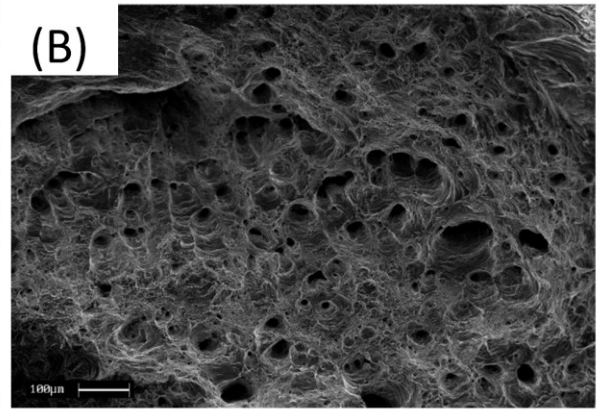
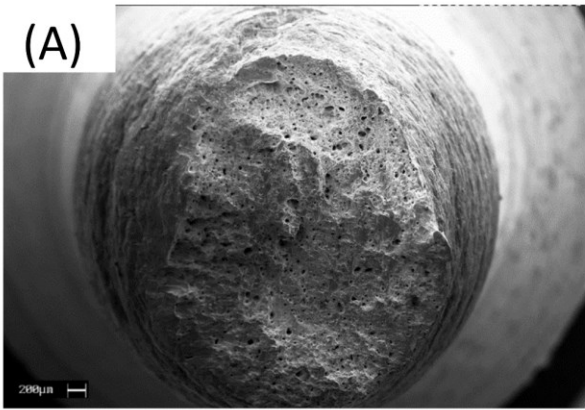


Figure 5.10 Stress-strain curves of CuCrZr manufactured in horizontal and vertical direction in AB, DAH, and SA+AH states.

The vertical specimens show the lowest mechanical strengths, and therefore only they will be considered for the mechanical characterization. The sample in the AB state had a yield strength of 214 MPa and UTS of 239 MPa. Similar values strength of the AB condition are found in open literature [113], [116], [118], [192]. The key reason for the discrepancies in the results is the variation in porosity levels achieved between the experiments [117]. The highest mechanical properties were obtained with the DAH heat treatment: the vertical specimens showed 248 MPa yield strength and 318 MPa of UTS. The increment of mechanical properties is obtained through the fine precipitation of the solute elements, which hinder the movements of the dislocations. The elongation at break, on the other hand, is diminished.

Compared to the DAH samples, the coarse precipitates in the SA+AH samples block the dislocations to a lower extent, and the mechanical properties are not as affected. The SA+AH samples showed lower yield strength than the AB specimens (123 MPa) and similar UTS. Wegener et al. [117] obtained a similar behaviour while testing overaged CuCrZr. Work hardening is more severe in the overaged samples. The partly recrystallized microstructure, which is made of bigger grains and coarse precipitates, and the decreased dislocation density are the causes of this behaviour.

Finally, Figure 5.11 displays the tensile fracture morphologies of the tested samples. All the specimens show the typical features of ductile fracture. The presence of large and deep dimples distributed all over the fracture surface was observed in all the samples. Lack of fusion holes were present, clearly distinguishable in the horizontal DAH sample (Figure 5.11 F). The porosity pointed with the white arrows are holes formed due to a lack of bonding between the melt pool and the layer underneath. The internal defects maintained their initial shape since the DAH samples did not undergo such strong plastic deformation as the other samples. On the other hand, the samples that showed the highest plasticity (all the SA+AH samples and AB V) presented deeper holes. In addition, the un-melted powder was observed on the surface of the vertical DAH sample (circled in Figure 5.11 H). Moreover, the lower ductility of the DAH samples also led to wider fracture surface areas.



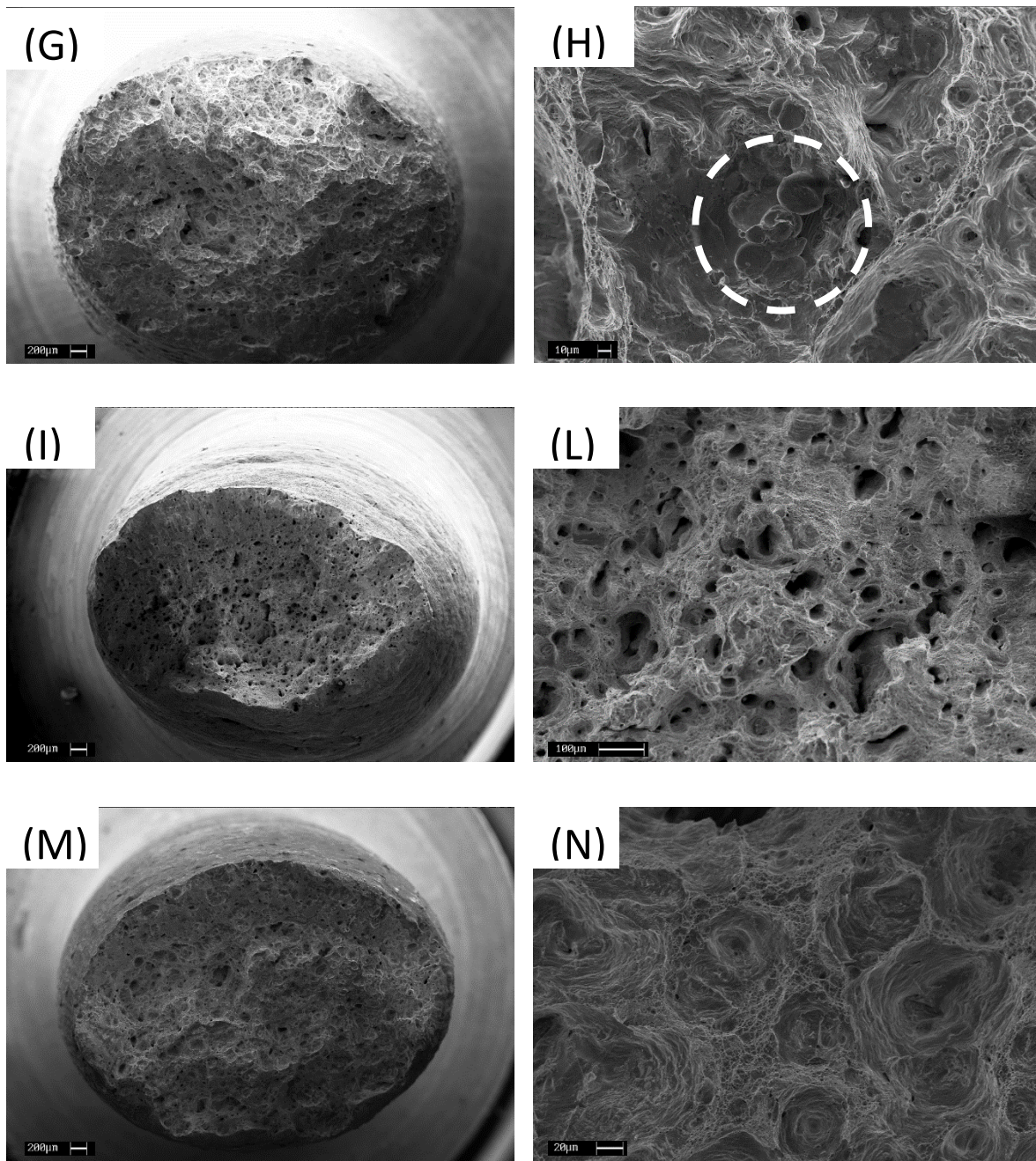


Figure 5.11 Tensile fracture morphologies of (A-B) AB H, (C-D) AB V, (E-F) DAH H, (G-H) DAH V, (I-L) SA+AH H, (M-N) SA+AH V

5.1.3.5 Electrical and Thermal Conductivity

Table 5.5 reports the results of the electrical resistivity measurements and the equivalent electrical conductivity compared to the international annealed copper standard (IACS). The samples

have been tested in AB, DAH, and SA+AH conditions. The effect of surface roughness was also evaluated by milling the surface of the squares.

Table 5.5 Results of the electrical resistivity measurements of heat-treated CuCrZr sample with different surface roughness.

	AB	AB Polished	DAH	DAH Polished	S+A	S+A Polished
ρ [ohm*cm]	9,36E-06	8,62E-06	3,54E-06	2,13E-06	2,57E-06	2,03E-06
DEV [ohm*cm]	5E-08	4E-08	4E-08	4E-08	6,0E-08	4,0E-08
% IACS	18,42	20,00	69,61	80,79	67,01	85,02

The surface quality has a strong impact on electrical resistivity. As-built LPBF samples have a surface roughness in the 15-30 μm range. The milling of the surface removes any oxide coating that may have formed after the manufacturing process and all open porosities that contain air and act as insulators.

Both heat treatments increase the electrical conductivity. The age hardening heat treatment removes the alloy elements from the copper matrix in the form of precipitates. In the AB state, the electrical conductivity of the polished part was 20%. The component's poor conductivity is due to the high Cr and Zr solute concentration, which causes lattice distortion and increases lattice electron scattering. The precipitation of the solute atoms greatly improves the electrical conductivity. The DAH heat treatment increased the electrical conductivity up to 80.79% IACS. A superior increment was obtained with the complete heat cycle, 85% IACS. This is because the solution annealing heat treatment increases the dimension of the grains, which has a beneficial effect on the material's conductivity.

The results are in agreement with what was found by Wegener et al. [117]. Their AB samples had 22% IACS, while similar heat treatments led to almost the same electrical conductivity measured in this study.

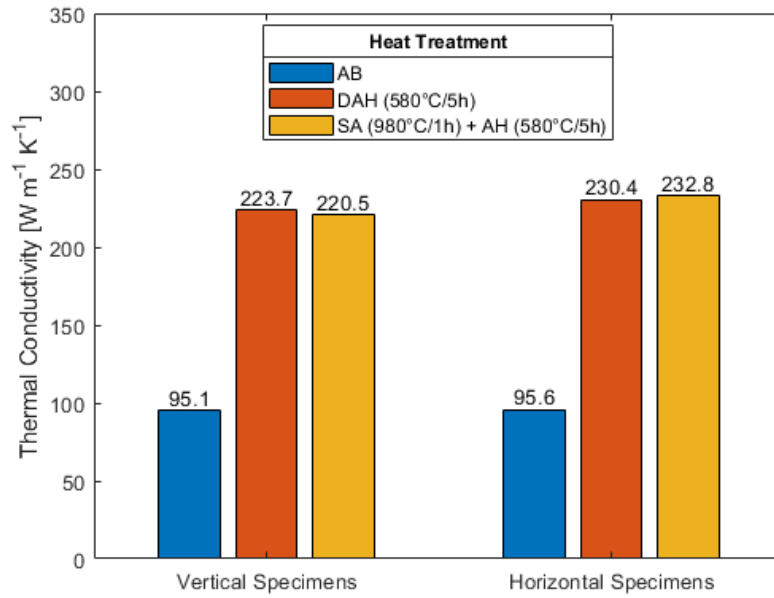


Figure 5.12 Thermal conductivities of CuCrZr samples in different heat-treating states and manufacturing orientations.

The results of the thermal conductivity measurements are shown in Figure 5.12. As seen with the electrical conductivity, the heat treatments increased the thermal conductivity of the samples. The specimens in the AB condition have a thermal conductivity of ~ 95 W/(mK). There were no significant changes between the two heat treatments. The horizontal direction of printing led to thermal conductivities of ~ 230 W/(mK), while slightly lower values (~ 220 W/(mK)) were measured in the vertical direction. This could be due to the columnar grains that are oriented perpendicularly to the heat flux direction. In this configuration, the grain borders obstacle the movement of the electrons to a greater extent than when oriented parallel to the heat flux.

However, as observed for the oxidized samples, there is a high discrepancy between the measured thermal conductivity and the one calculated using the Wiedemann-Franz relationship. According to the electrical conductivity of the samples, the thermal conductivity should be approximately 350 W/(mK) for the SA+ AH sample and 330 W/(mK) for the DAH sample. Hence, the obtained thermal conductivity was again far below the expected values.

Therefore, an alternative approach was used to check the thermal conductivity measurements performed with the Hot Disk method.

5.1.3.6 Alternative approach to measuring the thermal conductivity

Using the Laser Flash technique, the thermal conductivity of a bulk C10100 copper sample and a sample made from powder C (copper powder from Section 3) were determined. Two external laboratories performed the measurements on cylinders with a diameter of 12.7 mm and thickness of 2.5 mm by two external laboratories. The results are shown in Figure 5.13.

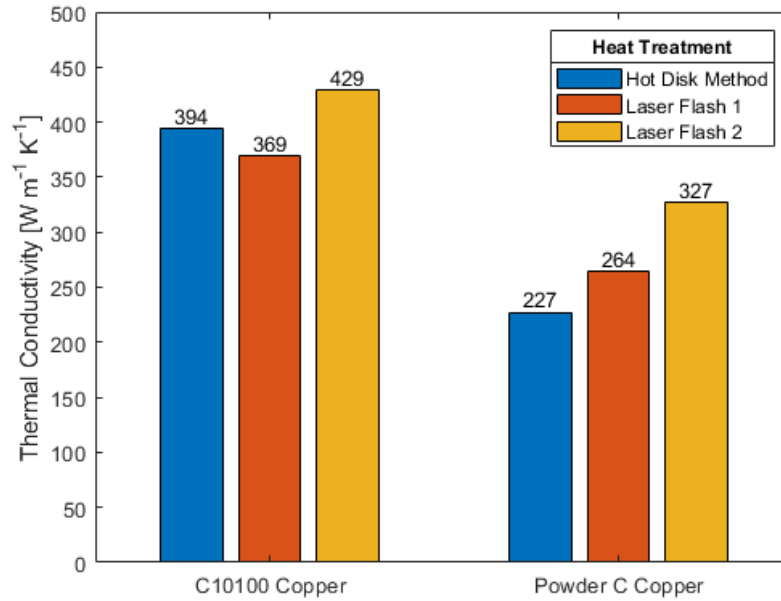


Figure 5.13 Thermal conductivities of copper samples obtained with Hot Disk and Laser Flash methods.

Both approaches measured high thermal conductivity of bulk copper, 394 W/(mK) for Hot Disk (HD) and 369 and 429 W/(mK) for Laser Flash (LF). Because of its chemical contamination and residual porosity, lower thermal conductivities have been obtained with the 3D printed sample. However, while the LF methods measured a reduction of ~25%, the reduction measured using the HD method was 44%, showing a high discrepancy between the values obtained with the two methods.

In order to decide which method leads to a more accurate result, an experimental setup has been designed to measure the thermal conductivity directly. The experimental method is based on the physical principle of Fourier law (Equation(5.2)):

$$|\bar{q}| = k \cdot \frac{dT}{dx} \quad (5.2)$$

Where heat flux \bar{q} is known and constant, $\frac{dT}{dx}$ is measured, and the thermal conductivity k is computed from the Fourier law.

The experimental setup comprises four elements: a heater cone equipped with an electrical cartridge, a reference sample, a test sample and a 3D printed water cooler. In Figure 5.14, the four main elements are reported.

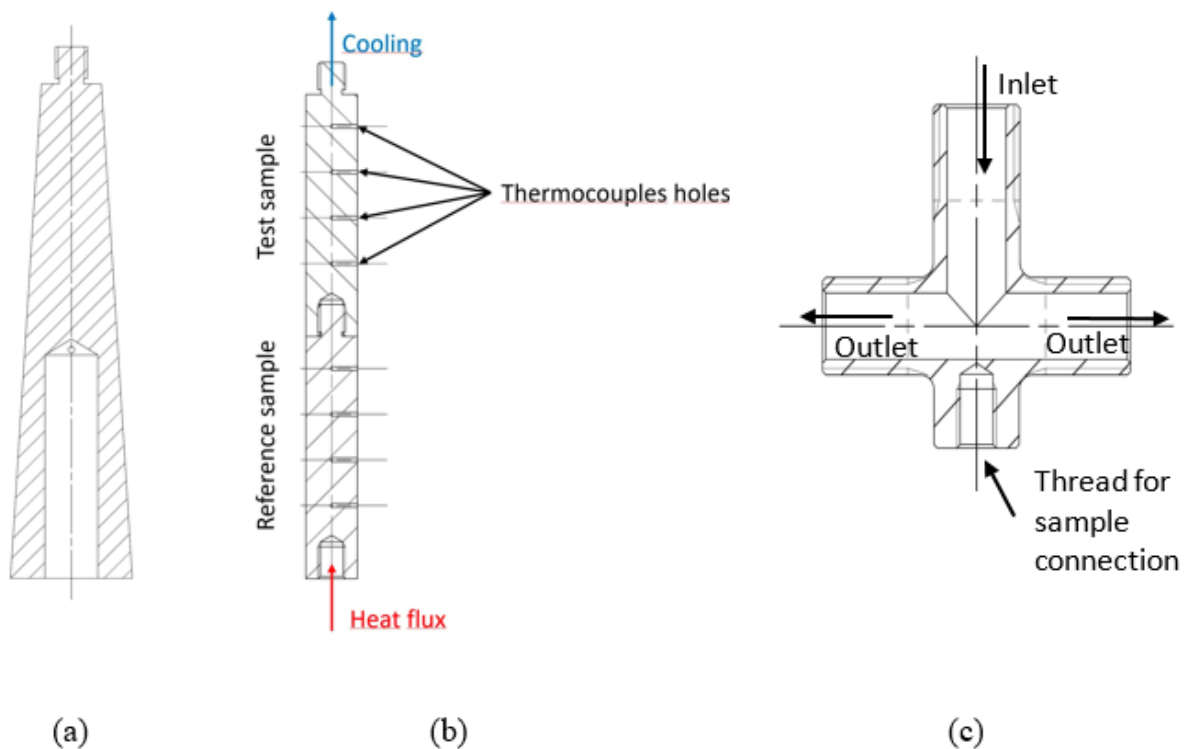


Figure 5.14 Experimental setup components: (a) pure copper heater cone made, (b) test sample and reference samples, (c) water cooler made by 3D printed pure copper.

The four elements are linked to each other through threaded pins and holes. The samples are cylinders with a diameter of 11.7 mm and a height of 60 mm. The printing direction was perpendicular to the cylinder height. The orientation of the columnar grains is therefore perpendicular to the heat flux.

The fillets and threads were machined, and four lateral holes were drilled at a 10 mm distance to allocate the thermocouples. Also, the lateral surface was machined to reach a good surface roughness.

The thermocouples measured the temperature at the centre of transversal sections of the samples at different locations. The system was thermally isolated with glass wool. Figure 5.15 displays the

experimental setup assembled and ready for experimental tests. To improve thermal connections, a conductive paste was used in threaded connections and inside the holes for thermocouples. Four T-type thermocouples (± 0.05 °C) have been installed in each sample.

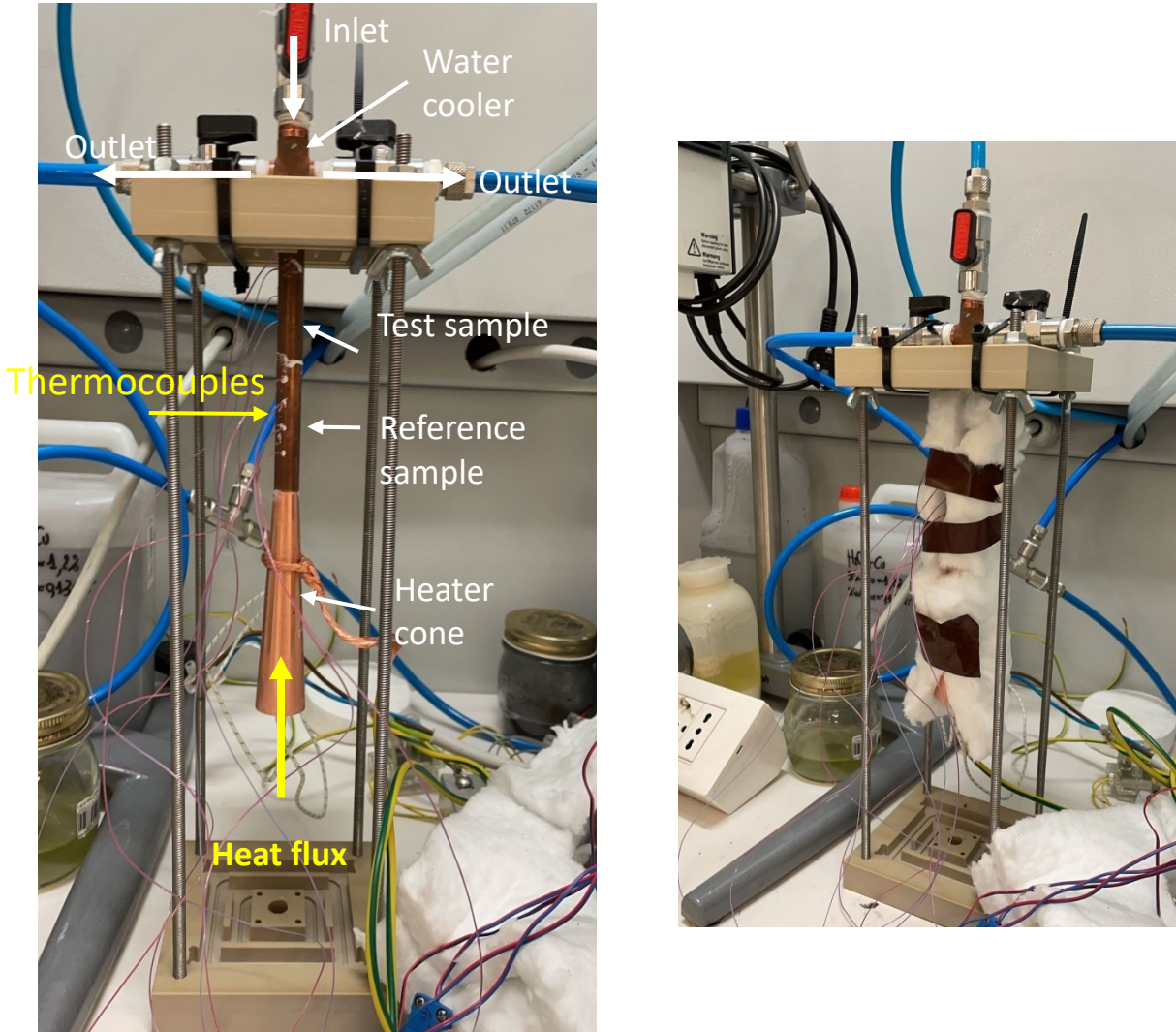


Figure 5.15 On the left: the final experimental setup connected with all components. On the right: the experimental setup covered with glass wool.

Heat flux is imposed on two connected cylinders, and their temperature along their height is measured using thermocouples. The bottom cylinder is the reference, made of C10100 bulk copper, while the top cylinder is the tested one. Since the heat flux is the same for both components, it is possible to calculate the thermal conductivity using Equation (5.3).

$$k_{TOP} = \frac{k_{ref} \left(\frac{dT}{dx} \right)_{ref}}{\left(\frac{dT}{dx} \right)_{TOP}} \quad (5.3)$$

Where k_{ref} is the thermal conductivity of the reference sample, and k_{TOP} is the thermal conductivity of the test sample.

For the calibration test, two C10100 samples were machined, instrumented with T-type thermocouples and installed in the experimental setup. Four independent tests were run at different heat flux grades. The theoretical pure copper thermal conductivity (400 w/(mK)) was used as a reference. Once the steady-state conditions are reached, the temperature values are collected, and the results are reported in Figure 5.16 and Table 5.6.

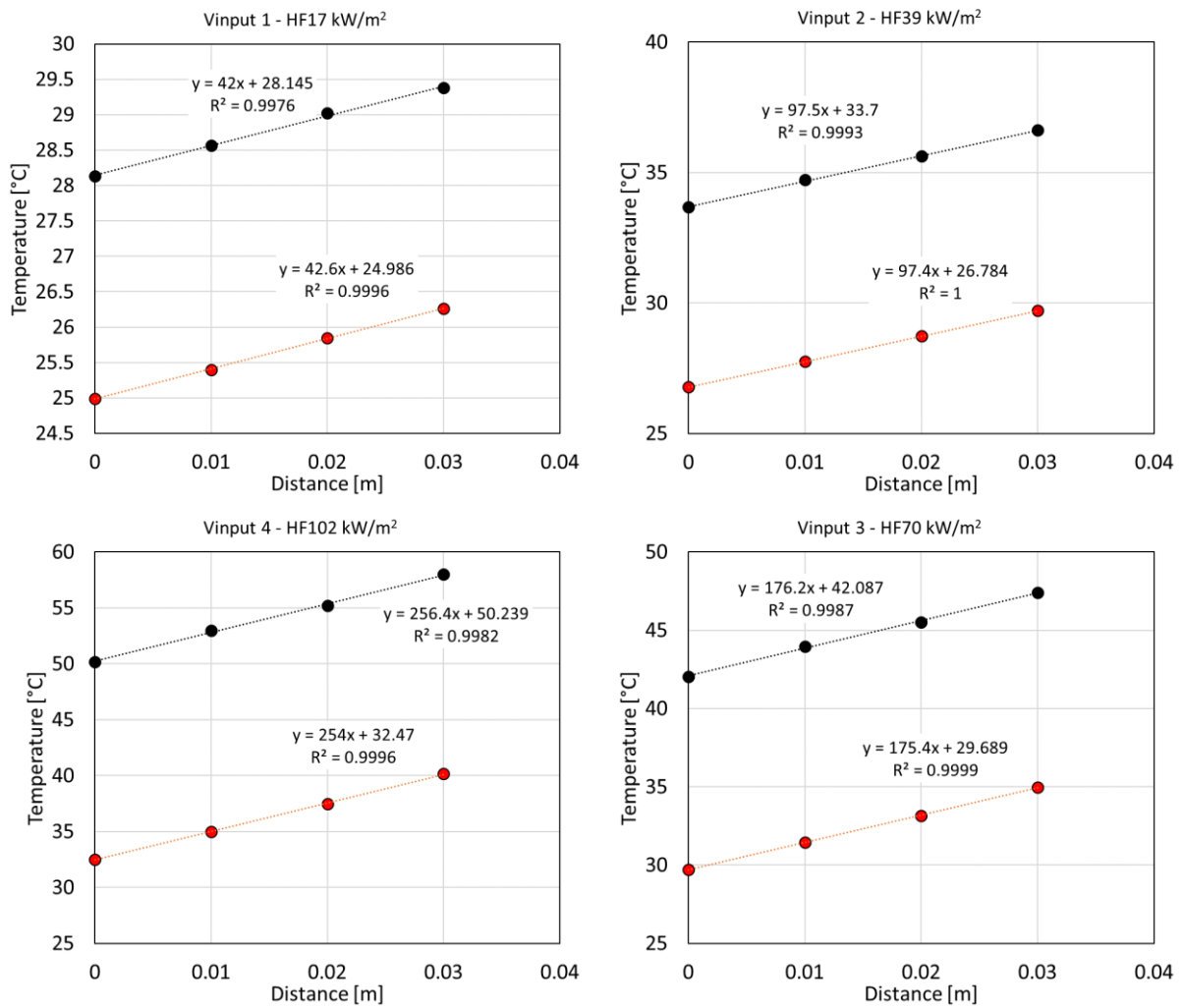


Figure 5.16 Calibration experimental tests at different heat fluxes imposed. The red and black data points are referred to as the test sample and reference sample, respectively.

Table 5.6 Thermal conductivity results for bulk C10100 copper samples.

q	(dt/dx) Ref	(dT/dx) TOP	dev	k ref	k TOP
[kW/m²]	[K/m]	[K/m]	[%]	[W m⁻¹ K⁻¹]	[W m⁻¹ K⁻¹]
17	42	42.6	-1.4	400	394.4
39	97.5	97.4	0.1	400	400.4
70	176.2	175.4	0.5	400	401.8
102	256.4	254	0.9	400	403.8

The reported heat fluxes have been calculated using equation 5.2 and the reference values (k_{ref} and $(dt/dx)_{ref}$). The results show a good agreement between the two samples made with the same material. There is a little deviation in the test when the heat flux is low. This evidence is explained because the result is more influenced by uncertainty.

A SA+AH and a DAH sample have been tested with the described setup. Table 5.7 and Figure 5.17 show the results obtained.

Table 5.7 Thermal conductivity of DAH and SA+AH CuCrZr samples obtained with the experimental setup. The C10100 values shown in figure 5.13 were used as k_{ref} . The obtained k TOP are compared with the theoretical k calculated using the Wiedemann-Franz relationship (k W-F).

Sample	q	(dt/dx) Ref	(dT/dx) TOP	dev	k ref	k TOP	k W-F	dev
	[kW/m²]	[K/m]	[K/m]	[%]	[W/(mK)]	[W/(mK)]	[W/(mK)]	[%]
DAH	132	357.3	418.9	-17.2	394	336	330	1.8
					369	314	330	-4.9
					429	366	330	9.8
SA+AH	144	390.2	402.5	-3.2	394	382	350	8.4
					369	357.7	350	2.2
					429	415	350	15.8

All of the observed values of thermal conductivity of C10100 bulk copper presented in Figure 5.13 were used as k_{ref} to calculate the thermal conductivity of the CuCrZr samples. The thermal

conductivities of CuCrZr that correlate the most with the Wiedemann-Franz law are obtained by using the LF 1 value (369 W/(mK)), as both values have a deviation inside of 5%. Therefore, the results obtained with Laser Flash 1 are considered the more accurate. Moreover, the thermal conductivities obtained using 369 W/(mK) as a reference agree with what was found by Wallis et al. [113].

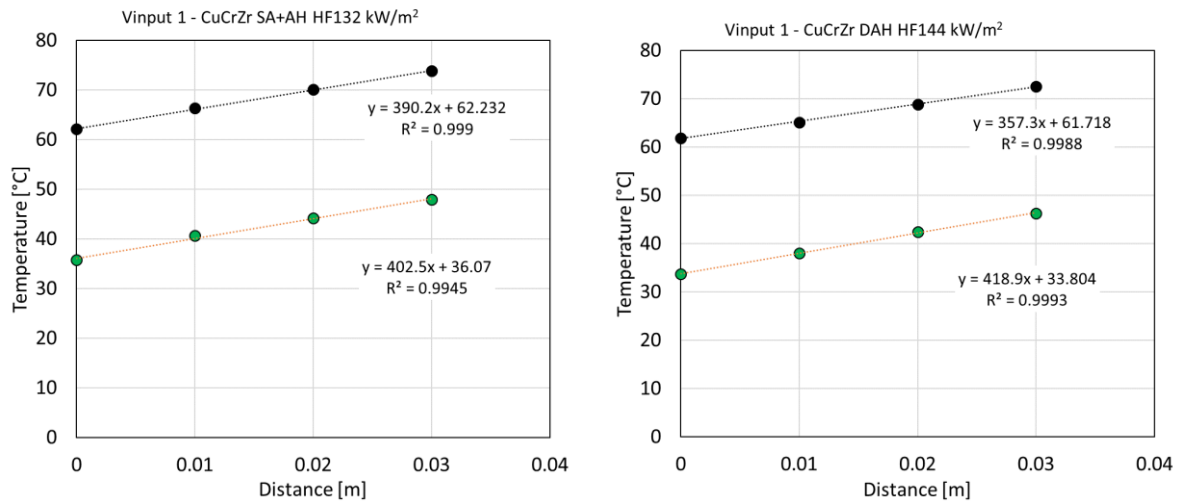


Figure 5.17 Temperature gradients obtained in the reference sample (Black) and in the CuCrZr samples (Green). On the left: SA + AH. On the right: DAH.

The anisotropy of the thermal conductivity was not tested with the experimental method. However, the small gap in results detected with the HD method shows that samples with columnar grains oriented parallel to the heat flux have higher thermal conductivities. In the experimental setup, the orientation of the columnar grains of the tested samples was perpendicular to the heat flux. As a result, altering the printing orientation of the samples may enhance the thermal conductivity.

5.2 Surface roughness improvements

The characterization of the CuCrZr alloy has proven that it is possible to manufacture dense CuCrZr components with a good combination of mechanical and thermal properties. Therefore, the alloy could be easily implemented in heat exchange applications, such as the production of accelerator grids. However, a known problem of the LPBF process is the high surface roughness of the components [193].

Since the surface roughness has a deep influence on the performance of the cooling channels [156], it is essential to study and characterize all the factors that affect the surface quality of the part.

Before performing the surface roughness characterisation, a second tuning of the process parameter was conducted. The layer thickness was raised to 30 μm to boost the alloy's building rate. Laser power of 370 W, hatching distance of 90 μm , and scan speed of 700 mm/s were the settings that resulted in the maximum density (98.56%). [Appendix A](#) lists the process parameters that were examined as well as the relative densities that were produced.

Several factors influence the surface roughness of an LPBF component. First and foremost, the part's orientation is critical since it dictates which surfaces are upward-facing (upskin) and which are downward-facing (downskin), and hence where the supports will be placed. The removal of the supports often deteriorates the quality of the surface [21]. In addition, the degree of the inclination of the surface has an impact on the surface roughness [194]–[198]. Surface quality is often low on unsupported downskin surfaces with a high slope [194], [198], whereas the staircase effect is seen on mildly inclined upskin surfaces [197], [199]. The roughness of the components is influenced by process factors such as laser power [200], scan speed [198], hatching distance [59], and layer thickness [194], but their impact varies based on the orientation of the surface. Therefore, a process parameter tuning should be performed for each surface type (downskin, upskin, vertical, and horizontal). Finally yet importantly, the scanning approach is crucial. The skywriting strategy helps reduce the roughness of the vertical surfaces [198], and as already observed in [Section 3.3.4](#), the contour scan strategy can improve the quality of the surface. The number of contours also affects the quality [201].

Cooling channels with complex designs should not have support structures inside since removing them is impossible. To avoid supports, the orientation of the cooling channels should be vertical or with low inclination angles. As a result, it was determined to investigate the surface roughness of upskin (US) and downskin (DS) surfaces in this study. For the characterization process, it was decided to use a parallelepiped with a square section (3 x 3 mm) 6 mm high and with the two parallel faces

inclined at 55°. The geometry and its nominal dimensions are shown in Figure 5.18. All the samples have been manufactured using a laser power of 370 W.

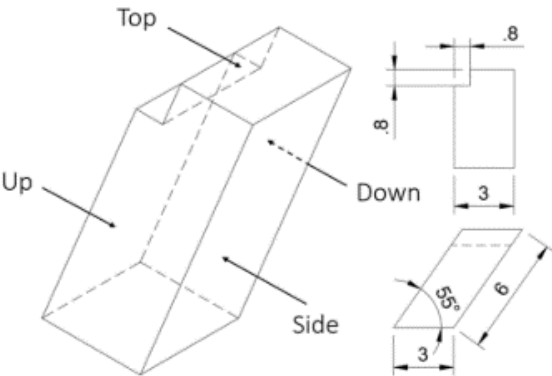


Figure 5.18 Sample geometry diagram used for roughness measurements: isometric (left), front (top right), side (bottom right) view. Dimensions in mm.

First and foremost, the roughness of the upskin and downskin surfaces were tested without using the contour scan approach, and the results were 20.97 μm and 21.24 μm , respectively. Following that, the number of contours and beam offset were investigated, as well as the effects of the inclination angle and the scan speed.

❖ **Beam offset**

The influence of the contour beam offset was investigated; the strategy and the findings are shown in Figure 5.19.

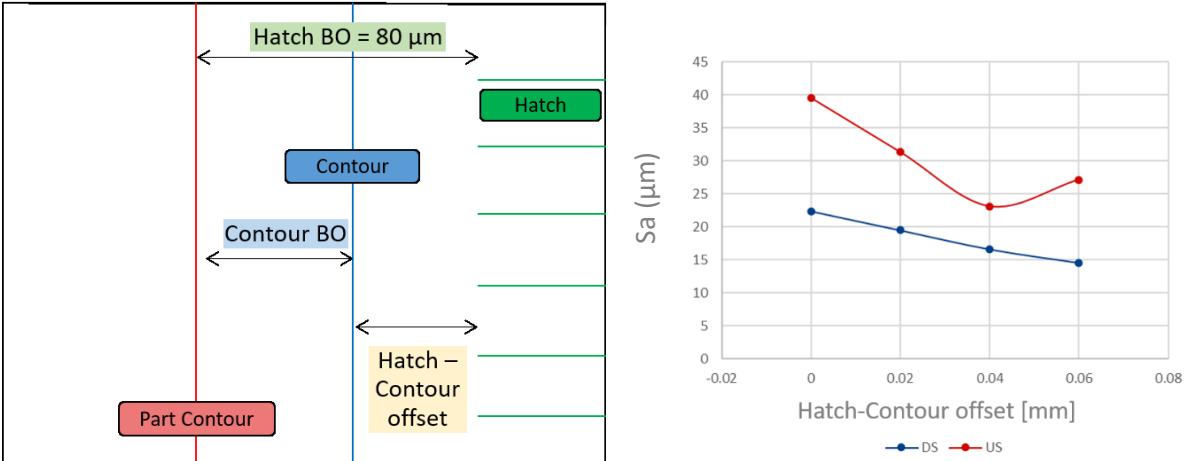


Figure 5.19 On the left: scheme of the used scan strategy. On the right: Sa parameters of US and DS surfaces at different beam offsets. The contour scan speed was 1000 mm/s.

The beam offset (BO) is defined as the distance of the applied scan strategy and the part nominal contour. The beam offset from the hatching lines (Hatch BO) was 80 μm and was kept constant. The contour BO was varied between 20 and 80 μm . Therefore, the relative distance between hatching lines and contour scan was varied between 0 and 60 μm .

Because the contour scans were done after the fusing of the inner section, low values of Hatch-Contour offset result in excessive re-melting of the core material. This leads to melt pool instabilities and hence to lower surface quality. However, an offset too high might result in lack of fusion porosities if the melt pool does not fully cover the gap between the two scan strategies. Therefore, the selected value of the beam offset was 40 μm .

The results also show that adding the contour scan strategy improves the DS surface quality but not the UP. None of the measured Sa of the US surfaces produced using the contour scan was below 21 μm (the value obtained without using the contour scan tracks). Another interesting finding is that the DS surfaces are produced with better surface quality. Due to dross production, the downskin surfaces generally have a greater surface roughness. However, the characterization of the surface roughness shows the opposite behaviour. Figure 5.20 depicts the cause of the high surface roughness of the US surfaces.

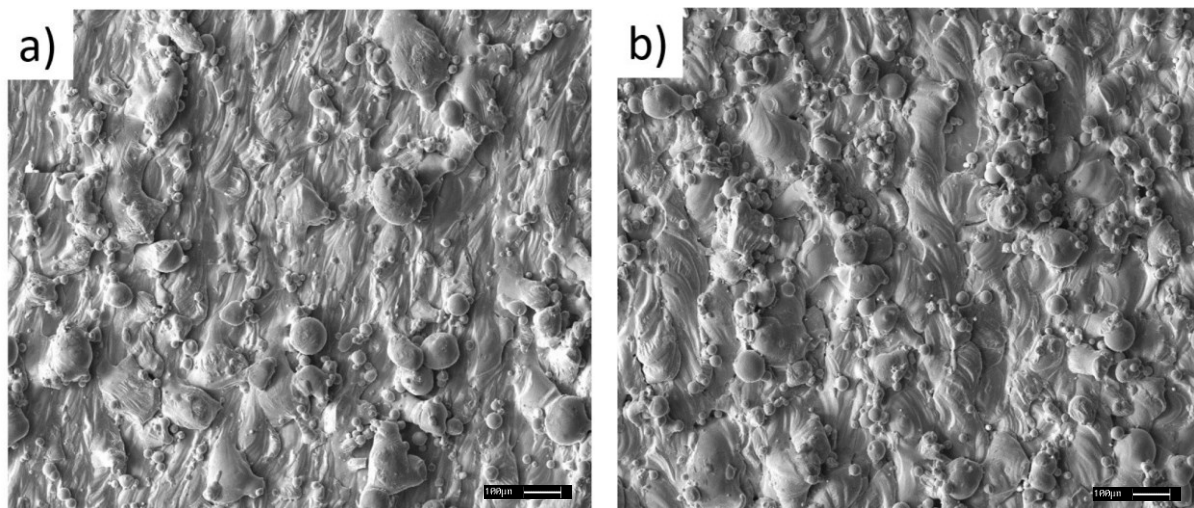


Figure 5.20 SEM images of US surfaces of samples manufactured using (a) 1 contour at 1000 mm/s ($S_a=25\ \mu\text{m}$) (b) no contour ($S_a=21\ \mu\text{m}$).

Figure 5.20 (a) shows the US surface of a sample manufactured using one contour at 1000 mm/s, while Figure 5.20 (b) presents the US surface produced without contour scan strategy. Both images show particles attached to the surface. The particles connected to the sample in (a) are spatter particles, whereas most of the particles in (b) are semi-molten powder particles of inferior dimension. In fact, the dimension of the powder particles lies in the range of the PSD, between 15 and 45 μm , while the spatter particles have diameters even larger than 100 μm . These spatter particles drastically hinder the surface quality of the US surface. However, aside from the spatter particles, the contour scan-generated US surface appears to be more regular, with reduced undulation. Hence, the contour scan strategy improves the surface quality, but the generation of spatter particles ultimately hinders this achievement.

Because the spatters near the DS surfaces sink into the powder bed, while those near the US surfaces remain attached, the US surfaces are more prone to englobe the spatter particles than the DS surfaces. For this reason, the surface roughness of DS surfaces is lower than the roughness of US surfaces.

❖ **Number of contours**

Figure 5.21 shows the Sa parameter of US and DS surfaces, using 1 to 3 contours with various scan speeds. The Hatch-Contour distance was 0, and the relative distance between the more external contours was 40 μm .

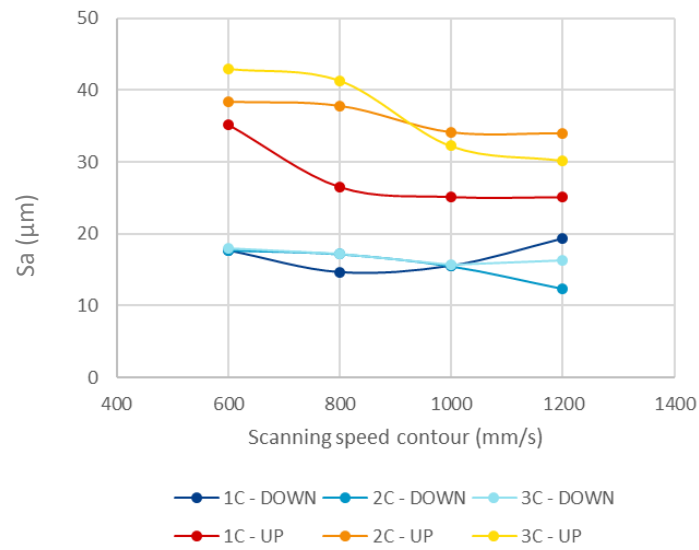


Figure 5.21 Sa parameters of US and DS surfaces with varying scanning speed and contour number. NC indicates the number of contours. Blue curves are downskin surfaces while the warm colour curves are upskin surfaces.

Again, for all scan speeds and the number of contours tested, upskin surfaces were rougher than downskin surfaces. The influence of the contour number is more noticeable in the US, leading to a progressive increase in the Sa parameter, but it appears not to affect the DS.

Increasing the number of contours increases the chances that the spatter particles will be englobed in the US surface, lowering the surface quality. Even scanning speed does not seem to impact the Sa parameter substantially.

❖ Inclination angle

Figure 5.22 depicts the surface roughness of the upskin and downskin at various inclination degrees. The examined angles were from 5° to 85° for the US surface and 35° to 85° for the DS surface, with a 10° increment. The roughness of a vertical surface (90°) is also reported.

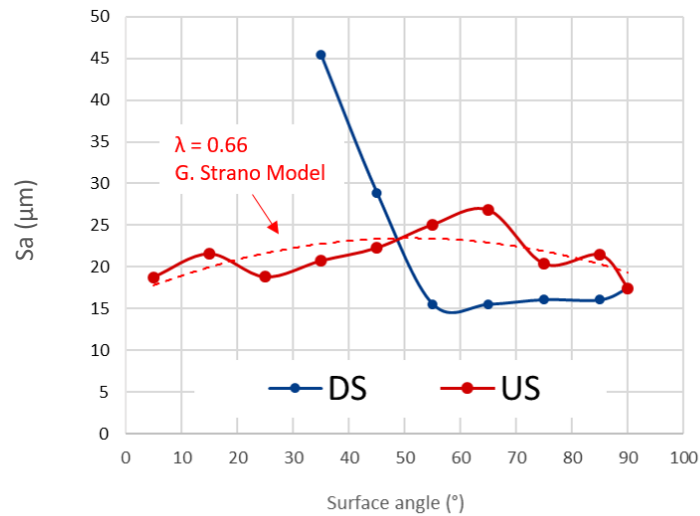


Figure 5.22 Trend of Sa parameter as the orientation of the surface varies (contour speed set at 1000 mm/s). The "dash-point" line in (a) represents the trend of the Sa parameter according to the model of G. Strano, with layer thickness at 30 μm and λ equal to 0.66.

For the US surfaces, the roughness is lower when the surface is inclined at 5° with respect to the XY plane (18.77 μm). It reaches a maximum when it is oriented at 65° (26.86 μm) and has a minimum Sa value when it is arranged vertically, i.e. oriented at 90° (17.47 μm). In the DS, the variation is not evident up to 55°, after which the phenomenon called dross formation begins to prevail, increasing the roughness up to too high values, making the measurement difficult and not very useful.

The surface roughness of US surfaces fits a model proposed by Strano et al. [197], which correlates the roughness of the upskin surfaces with the staircase effect and the particles adhering to the surface. The λ value, which ranges from 0 to 1, defines how much spatter and particles are stuck to the surface (at 1, there is the maximum concentration of particles). For this case, the best fit is obtained using λ equal to 0.66, confirming that a significant contribution to the surface roughness is given by the particle attached to the surface (rather than the waviness of the staircase effect).

❖ Scan speed

Finally, a wider range (between 100 and 2000 mm/s) of scan speed contours was investigated. As shown in Figure 5.23, the previously analysed scan speed range (400 – 1000 mm/s) favoured the downskin surface. The melt pool is more stable in this range and leads to a better surface finish. Scanning

at higher speeds produces unstable melt pools, whereas scanning at lower speeds increases the warp defect. Hence, outside the melt pool stability range, the roughness increases.

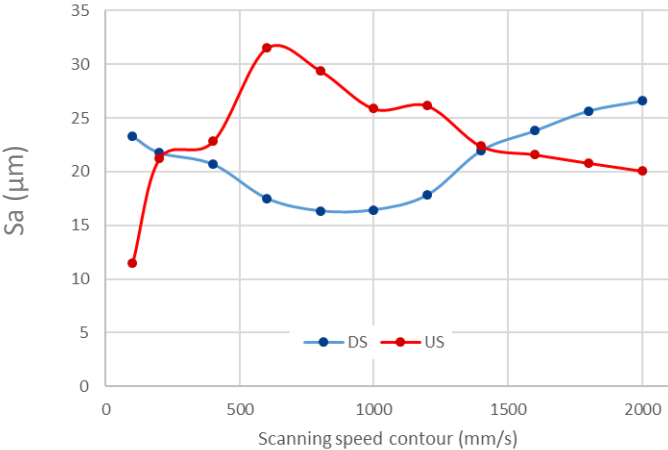


Figure 5.23 The contour scan speed effect on the US (red curve) and DS (blue curve) surfaces. The inclination angle was 55°.

Over 1400 mm/s and below 400 mm/s, the Sa parameter of upskin surfaces is lower than the downskin. Wang et al. [34] observed that increasing the energy input leads to stronger spattering intensity. When high energy input is used, the liquid metal flows more fiercely, and the recoil pressure increases. Both phenomena increase the spatter generation, which has been observed to be the most detrimental factor of the US surface quality. Over 1400 mm/s, the spattering intensity is low, and the roughness of the surface approaches the value obtained without contours.

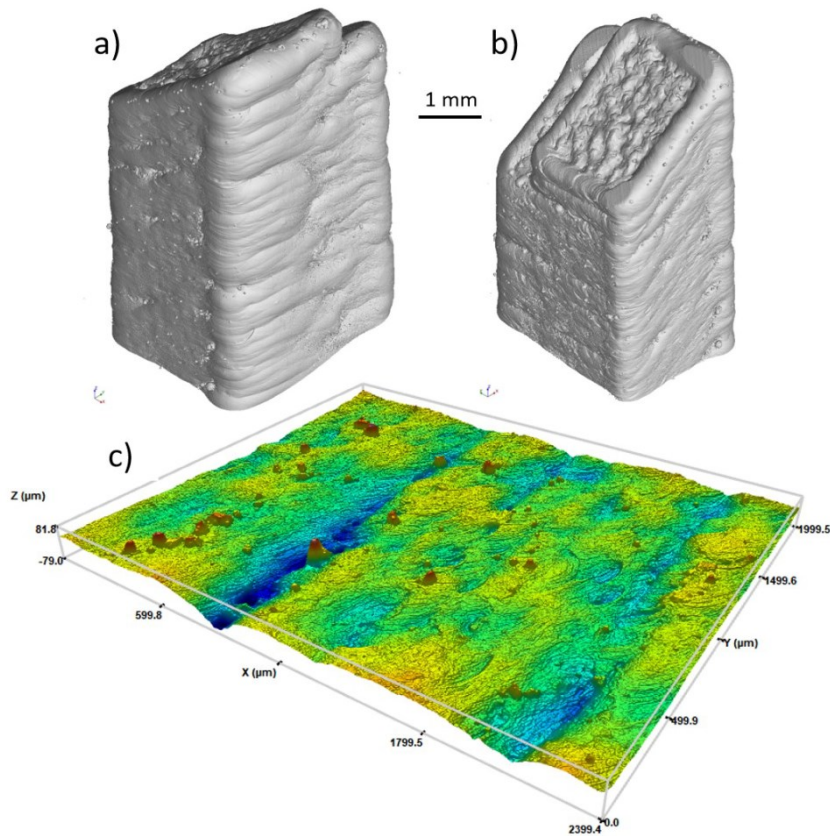


Figure 5.24 Isometric views of the volume reconstructed from the CT scans of the specimen printed with a contour scan speed of 100 mm/s, in which a) DS b) US surfaces can be observed; c) surface topography of the US surface of the same specimen.

The sole improvement on the upskin surface came from using the slowest scan speed. With a scan speed of 100 mm/s, the S_a resulted in 11.46 μm . Figure 5.24 c shows the topography of this surface. Despite the low S_a , the shape of the sample is severely compromised. The morphology of the upskin surface appears to be devoid of spatters (thus the low S_a value), yet ripples characterize the surface. The observed undulations are caused by wide melt pools formed at high energy input. Figure 5.24 a and b show the undulated DS and US surfaces reconstructed from the CT scans. The wide contour melt pools deviate the shape of the part from the original CAD design, which is a considerable problem when designing complex internal parts. For example, deviation of the cross-section of cooling channels from the CAD design can vary the flow rate and hence change the efficiency of the part. Therefore, using a low contour speed cannot be considered an acceptable solution for improving the surface quality.

5.3 Summary

The characterization of the CuCrZr alloy has proven that it is possible to manufacture dense parts with a good combination of mechanical and thermal properties. The tuning of the process parameter has led to a relative density of 99.75%. Compared to oxidized and impure copper, this result was obtained when using a higher scan speed (800 mm/s), meaning that the build rate is higher. The DAH heat treatment is superior to the SA + AH heat treatment. Both heat treatments increase the material's electrical and thermal conductivity (slightly less with the DAH heat treatment), but the mechanical properties are greatly enhanced when using the DAH heat treatment. Compared to the SA+AH samples, the fine dispersion of precipitates obtained with the DAH heat treatment resulted in a yield strength that was doubled and a UTS that was 40% higher. The partial recrystallization of the microstructure obtained with SA + AH heat treatment generates a more ductile material and reduces mechanical anisotropy. However, inferior mechanical strength in the vertical direction was still observed due to the lack of fusion porosities.

Moreover, the SA+AH heat treatment does not remove the thermal conductivity anisotropy, as the columnar microstructure is still present. Complete recrystallization of the part could be obtained by increasing the temperature and time of the heat treatment, but the mechanical properties would be further reduced. Therefore, directly ageing an LPBF part is the optimal choice to achieve an excellent combination of physical and mechanical properties.

The use of the contour scan strategy improved the surface roughness of only the downskin surface (from 21 to 17 μm). The contour scan technique did not enhance the surface quality of the upskin due to the high presence of spatters and melt-pool instability, maintaining Sa identical (or even higher) to the same surface obtained without the contour. A low scan speed could improve the roughness of the US surface, but the accuracy of the part is compromised.

CHAPTER 6

6 DEVELOPMENT OF AN AM DESIGN FOR ACCELERATOR GRIDS

The primary purpose of the characterization of copper and copper alloys produced via LPBF was to certify this technology for the production of accelerator grids. New feasible cooling channel designs have been created in parallel with the material characterisation process, and initial prototypes have been built and tested. Furthermore, while the results presented in this thesis suggest that the production of dense pure copper components is not practicable with low laser power, new LPBM machines were developed throughout the three-year study period. TRUMPF TruPrint 5000 (1kW laser with wavelength 515nm) and AMCM M 290-1 1kW (1kW laser with wavelength 1080 nm) have enough laser power to melt pure copper fully.

This chapter shows the characterization of test specimens manufactured by the producers. The high relative density of such components enabled the production of the first pure copper accelerator grids prototypes with AM design.

6.1 Preliminary AM design and prototypes of accelerator grids

Before the characterization of pure copper, two AM cooling channels designs were developed to improve the heat transfer efficiency. Figure 6.1 shows the CAD geometries of the conformal cooling channels.

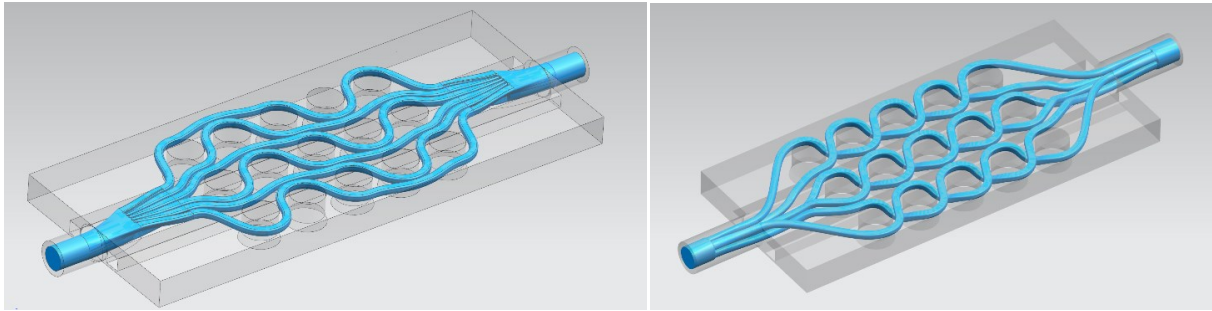
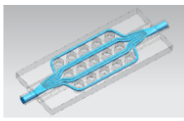
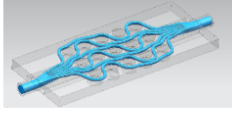
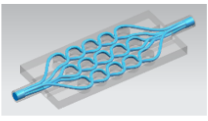
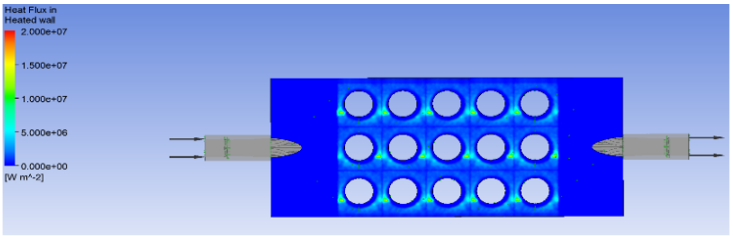


Figure 6.1 CAD geometries of AM cooling channels. On the left: Alternate Channels. On the right: Crossed Channels.

These cooling channel designs encircle the negative beam apertures, which are the zone where the heat loads concentrate. Table 6.1 reports the results of the CFD (Computational Fluid Dynamics) simulations of such designs using ANSYS workbench.

Table 6.1 Results obtained from CFD simulations of the acceleration grids prototypes. A straight channel prototype was designed to have reference results.

	Straight Channels	Alternate Channels	Crossed Channels
Geometry			
Power Density Distribution			
Inlet Speed [m/s]	6		
Inlet Water Temperature [°C]	35		
Maximum speed of the Fluid [m/s]	10	11,6	11,9
Load Loss [bar]	0,85	1,44	1,6
Maximum Temperature of the Solid [°C]	130	114	105
Maximum Temperature of the Fluid [°C]	92	91	88

The simulations were run using the CFX fluid dynamics program of Ansys. The tetrahedral element type was employed to mesh the channel shapes' complex geometry, and the mesh generation of each model was performed using the default parameters. The Navier-Stokes and continuity equations

have been solved using the $k - \epsilon$ turbulence model. The fluids' thermo-physical characteristics were supposed to be constant, and the flow was assumed to be three-dimensional, steady-state, and incompressible. The simulations were run using water as the fluid material and pure copper as the grid's material. The roughness of the cooling channels was not considered for these simulations. The processing conditions were obtained by the PhD thesis of Gambetta [202]. The inlet water temperature was 35°C, and the power density distribution was based on the EG grid (the Consorzio-RFX group provided it). An inlet speed of 6 mm/s was used for all the models.

The simulation results show that both AM cooling channel designs improve the cooling of the grids. The maximum temperature of the Straight Channels design is 130 °C, while the Alternate and Crossed Channels designs lead to a maximum temperature of 114 °C and 105 °C, respectively. However, the enhanced cooling is at the expense of a higher pressure drop. The pressure drop of the Alternate design is ~70% higher than the Straight Channels design, while the pressure drop of the Crossed Channels is almost doubled.

The geometries depicted in Figure 6.1 were built to test and compare the pressure drops of the AM cooling channels. Figure 6.2 shows the two grids still attached to the platform and one after the removal using a wire electrical discharge machining. The grids were manufactured using the LPBF machine EOSINT M280 and the material used was the aluminium alloy AlSi10Mg.

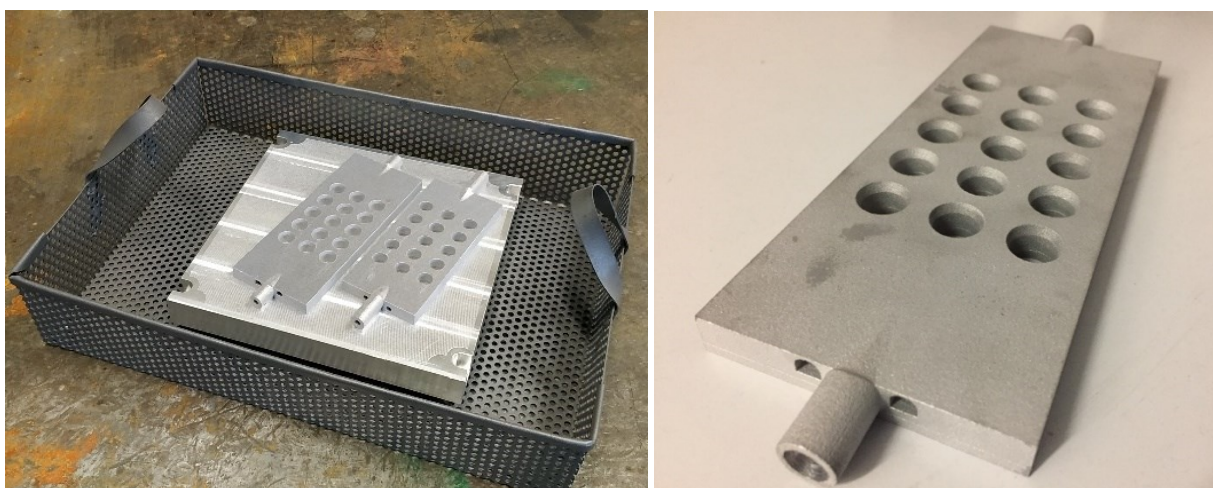


Figure 6.2 On the left: AM grids attached to the platform. On the right: AM grid after electro-discharging.

The pressure drop at different water flow rates was measured, and the results are shown in Figure 6.3. The Crossed Channels design has a larger pressure drop than the Alternate design. Because the cooling of the components could not be assessed, it was impossible to determine which design would best increase the grids' overall cooling efficiency. However, the experimental results of the pressure drop were helpful for the calibration of the CFD simulations. The calibrations of the CFD simulations are not reported as they are outside the scope of this thesis.

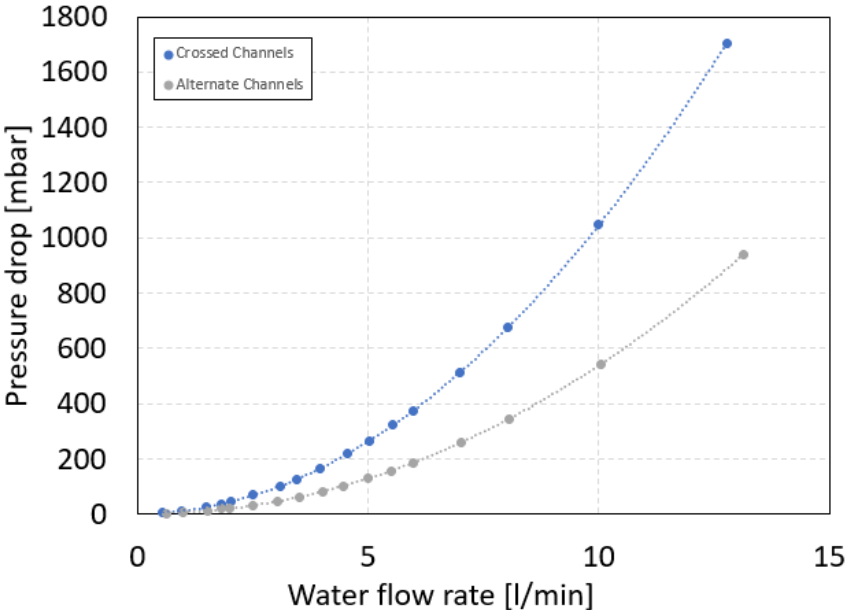


Figure 6.3 Pressure drops of Crossed and Alternate channels at various water flow rates.

Finally, a Computed Tomography (CT) of the crossed channels grid was performed at CERN using a Zeiss Metrotom 1500. Internal cooling channels were successfully built, as seen in Figure 6.4. Because of the printing orientation, dross and semi-molten particles formed on the unsupported surface of the channels. This divergence from the CAD design increases pressure drop and also has the potential to detach during operation, contaminating the refrigerating water. As a result, it was decided that the grids should be orientated throughout the manufacturing process with the direction of printing that most decreases the cooling channel surface roughness. This may be accomplished by vertically constructing the cooling channels.

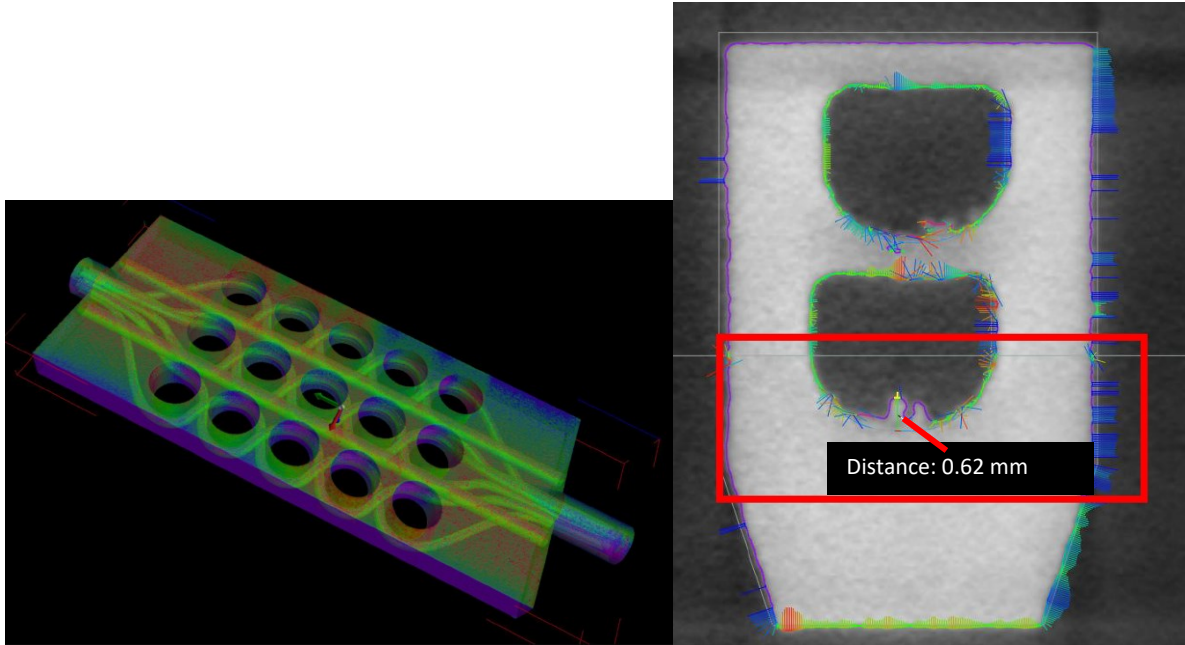


Figure 6.4 On the left: CT scan of crossed channel grid. On the right: focus on the highest scan deviation from the CAD geometry.

The reduction of the surface roughness of the cooling channels is critical for many reasons:

- ❖ low surface roughness reduces the pressure drop;
- ❖ asperities from the surface might detach and contaminate the water;
- ❖ the removal of such asperities might vary the heat exhaustion performance and produce inconsistent results.

6.2 Pure copper single-channel prototypes

Following the results obtained with the aluminium grids, a series of single channels prototypes have been manufactured using pure copper powder. The design of the cooling channels was based on the results shown in the PhD thesis of Gambetta [202]. As shown in Figure 6.5 a, the different channels were designed including two pressure taps (p1 and p2) located after the female connections, which were used to join the samples to the experimental setup. A straight channel (Figure 6.5 b) was used as a reference to tune and calibrate a new developed numerical model, which was then used for simulating the pressure drop of the more complex cooling channel designs named DUNED (Figure 6.5 c) and NICE

(Figure 6.5 d). Compared to the designs proposed by Gambetta [202], the cooling channel shapes were modified to be fabricated without the need for support structures and to boost cooling efficiency even further.

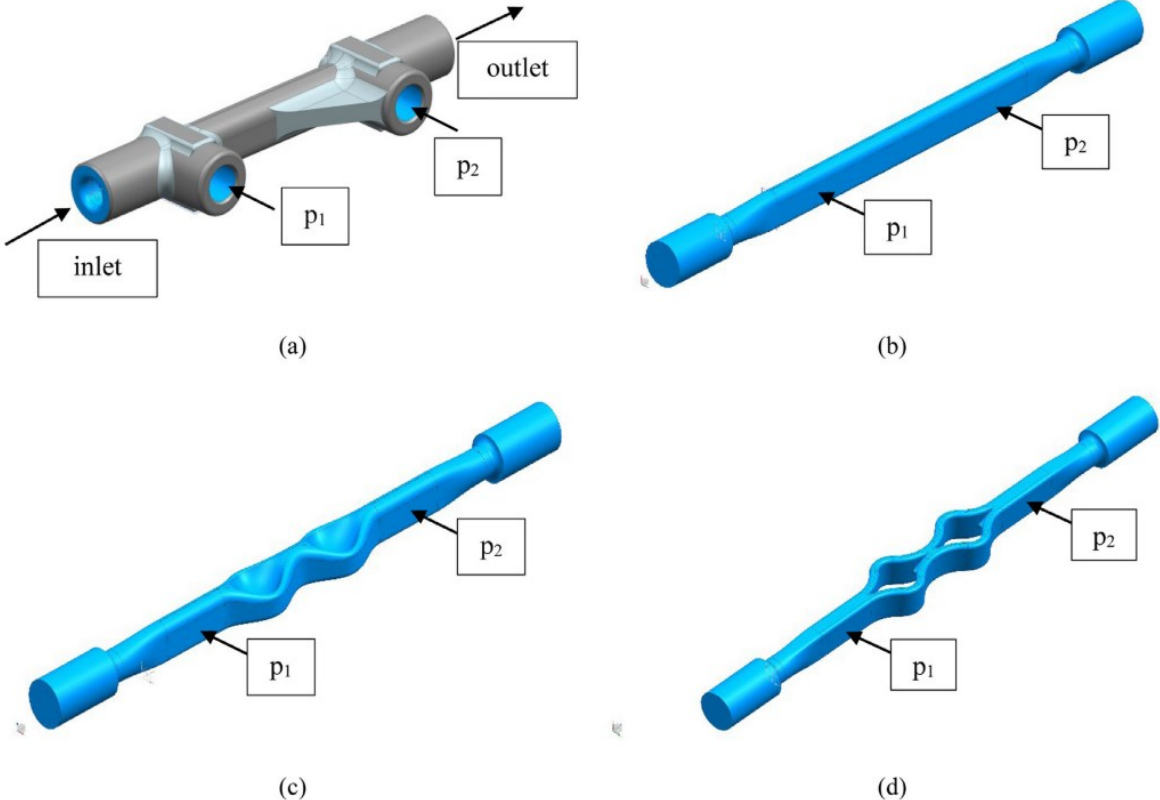


Figure 6.5 CAD design of the cooling channels: (a) test specimen design, (b) reference straight channel, (c) DUNED channel and (d) NICE channel [156].

For manufacturing the single-channel prototypes, the powder B studied in [Section 3](#) was employed, and the tuned process parameters were selected (layer thickness of 20 μm , hatching distance of 0.09 mm, laser power 370 W and scan speed of 400 mm/s). Figure 6.6 shows the samples as-built attached to the platform. The samples were threaded, and the supports were removed.

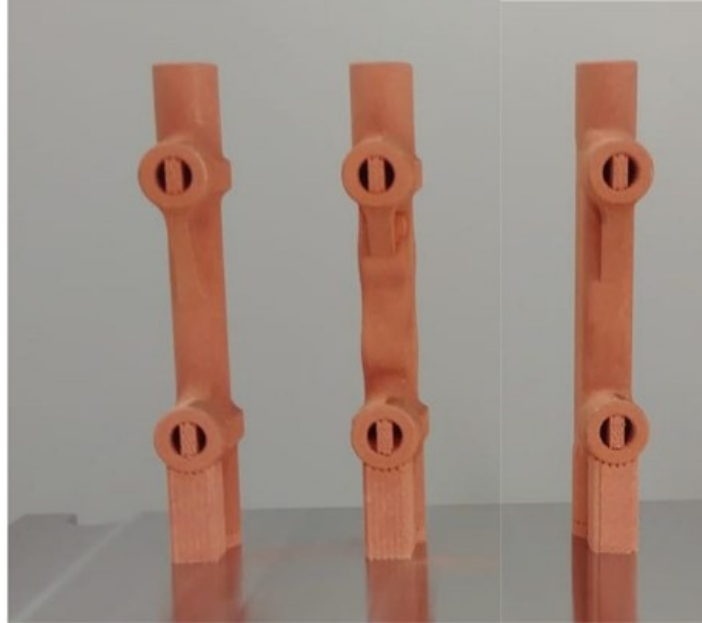


Figure 6.6 Image of the three cooling channels manufactured vertically [156].

Since the numerical modelling is outside the scope of this thesis, the calibration of the numerical model is not reported. However, the result can be found in the article presented by Favero et al. [156]. The main challenge was that the standard numerical tools could not correctly predict the fluid behaviour inside AM cooling channels because of the complex surface roughness of LPBF parts. Therefore, it was necessary to develop a novel calibration model. Figure 6.7 shows the excellent agreement between the experimental results and the new estimated values. The results show that it is possible to simulate the fluid dynamics of complex 3D printed cooling channels, which is extremely important when designing heat exhaustion components. Moreover, Figure 6.7 also shows that the DUNED cooling channel has the optimal design, as it leads to lower pressure drops.

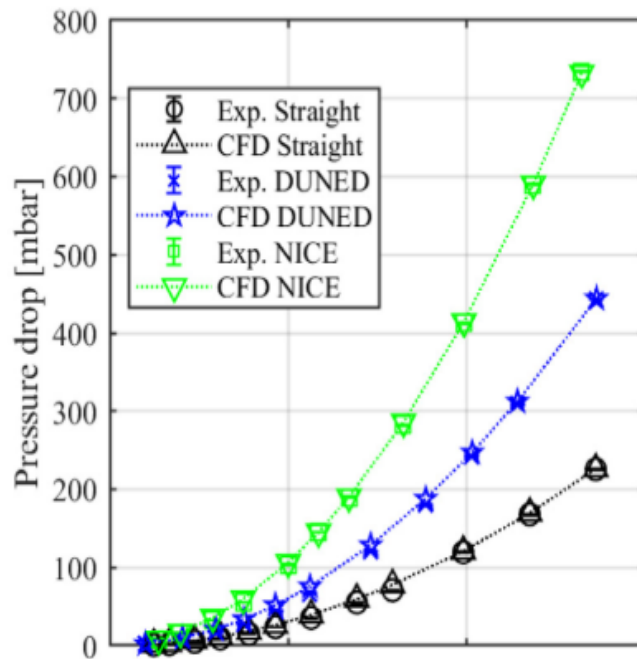


Figure 6.7 Plot with calibrated CFD and experimental results for the three different geometries [156].

6.3 Characterization of pure copper produced using high-power infrared and green lasers

The manufacturing of pure copper with low laser power (<400W) has proven to be challenging due to copper’s high thermal conductivity and reflectivity. The high concentration of lack of fusion porosities (~10%) observed in the pure copper components in [Section 3](#) leads to low mechanical properties and low thermal conductivity. Furthermore, the leak tightness of the grids may be compromised. Therefore, the EOSINT M280 was not suitable for producing pure copper accelerator grids prototypes.

However, during the final period of the research project, two commercial LPBF machines became available for the production of pure copper components. EOS has commercialized two LPBF machines (AMCM M 290-1 1kW and EOS M400) equipped with a 1kW infrared laser, while TRUMPF has commercialized (TRUMPF TruPrint 1000 Green Edition) and is developing (TRUMPF TruPrint 5000) LPBF machines equipped with green laser (515 nm).

Before requesting the production of pure copper grid prototypes from the manufacturers, the material had to be certified. Therefore, the characterization of samples provided by the producers was performed. The tested LPBF machines were the TRUMPF TruPrint 5000 (1kW laser with wavelength 515nm) and the AMCM M 290-1 1kW (1kW laser with wavelength 1080 nm).

The research was focused on characterizing the density and the mechanical properties. Three cylinders of 10 mm height and 12 mm diameter were manufactured for density measurements with the Archimedes method and optical analysis, and three tensile specimens were manufactured in the vertical and horizontal directions for the mechanical characterization.

Table 6.2 reports the average porosity levels measured with the Archimedes method and by analysing the optical images.

Table 6.2 Porosity level of 3D printed pure copper measured with Archimedes method and optical analysis.

Sample	Archimedes Porosity %	Optical Porosity %
AMCM M 290-1 1kW	0.64%	0.16%
TRUMPF TruPrint 5000	1.04%	0.13%

The samples were nearly fully dense, with few observed porosities. The porosity measured with the Archimedes method is higher due to the buoyant forces applied from the air bubbles attached to the surface during the weighing in water. The EOS samples were sanded, resulting in a smoother surface, which reduced trapped gas at the surface and, as a result, reduced the calculated porosity. Figure 6.8 shows two micrograph pictures of the cross-section of both materials. Both micrographs show a low amount of lack of fusion porosities.

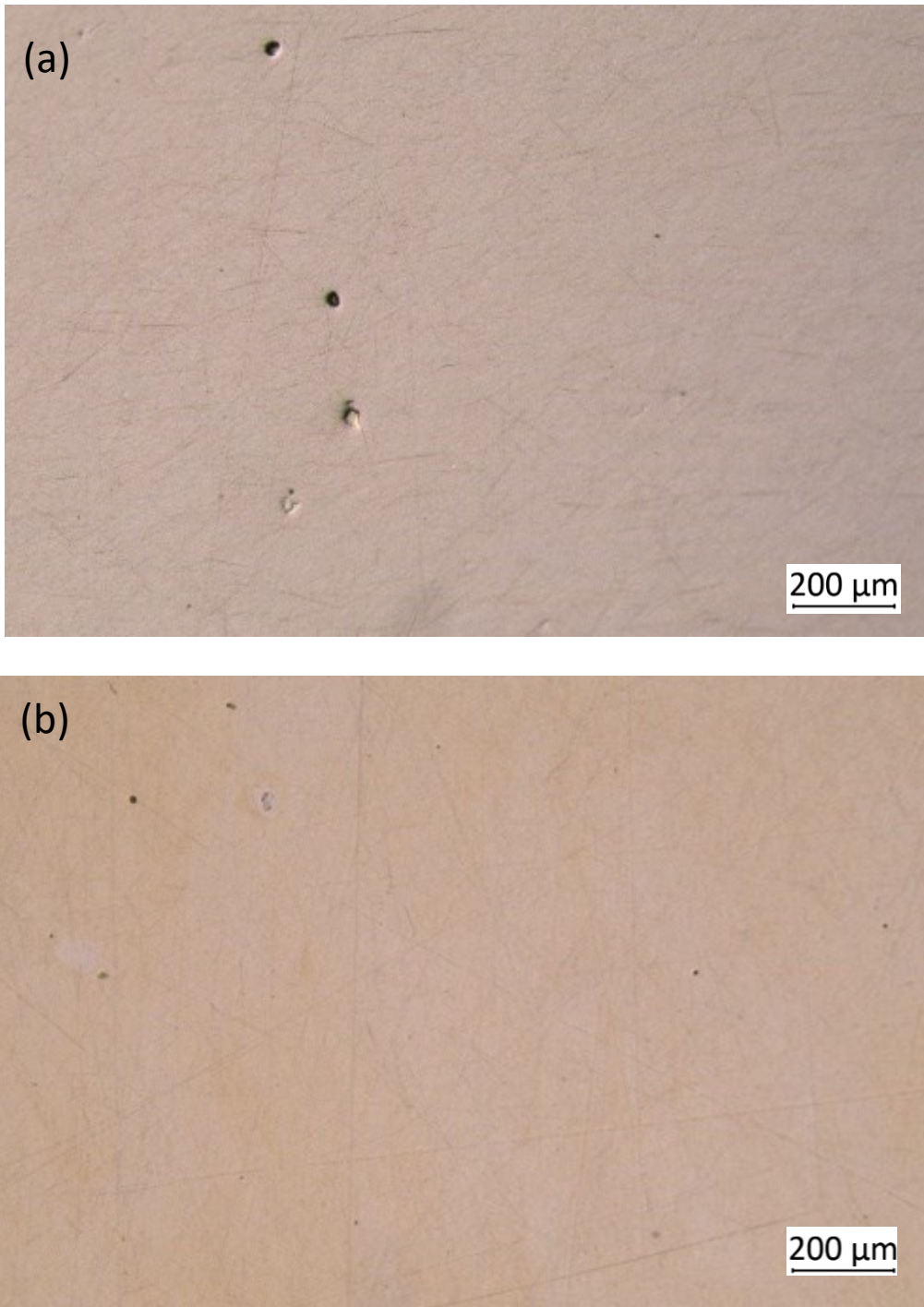


Figure 6.8 (a) cross section micrograph of pure copper AMCM M 290-1 1kW sample; (b) cross section micrograph of pure copper TRUMPF TruPrint 5000 sample.

Table 6.3 reports the results of the tensile tests of TRUMPF and EOS specimens, while the stress-strain curves are shown in Figure 6.9 and Figure 6.10, respectively. The results show that the

specimens manufactured with the same processing conditions have similar mechanical properties, all the measured properties have low standard deviations, and the stress-strain curves overlap.

Table 6.3 tensile test results of pure copper manufactured in two printing directions with AMCM M 290-1 1kW and TRUMPF TruPrint 5000.

	Yield Strenght [MPa]	Ultimate Tensile Strenght [MPa]	Young Module [GPa]	Elongation at Break
TRUMPF Vertical	137.3 ± 2.1	200.4 ± 0.1	124 ± 5	0.80 ± 0.02
TRUMPF Horizontal	139.7 ± 0.6	221.2 ± 1.4	136 ± 3	0.59 ± 0.02
EOS Vertical	165.3 ± 4.6	223.7 ± 0.5	124 ± 3	0.56 ± 0.01
EOS Horizontal	160.0 ± 2.8	224.9 ± 1.8	125 ± 4	0.53 ± 0.01

The samples manufactured with the infrared laser have superior mechanical properties and less anisotropy. The mechanical properties show low deviations between the horizontal and vertical printing directions. The horizontal specimens have a slightly inferior yield strength of 160 MPa, while the vertical samples have a yield strength of 165 MPa. The ultimate tensile strength (UTS) is almost constant at 224 MPa, as well as the Young module at 125 GPa. As observed in the CuCrZr samples, the vertical specimens have a higher elongation at break, 0.56 vs 0.53 obtained with the horizontal samples. The anisotropy of the elongation at break is even more evident with the TRUMPF specimens: the elongation at break of the vertical samples is 0.80, while for the horizontal ones is 0.59.

TRUMPF samples have lower mechanical properties than the EOS ones. The yield strength is almost constant for both printing directions, ~138 MPa, while the UTS is 200 MPa for the samples manufactured vertically and 221 MPa for the samples manufactured horizontally. Inferior interlayer bonding may be the reason for the TRUMPF specimens' lower strength and higher ductility. The slipping between layers is easier if the adhesion between layers is low.

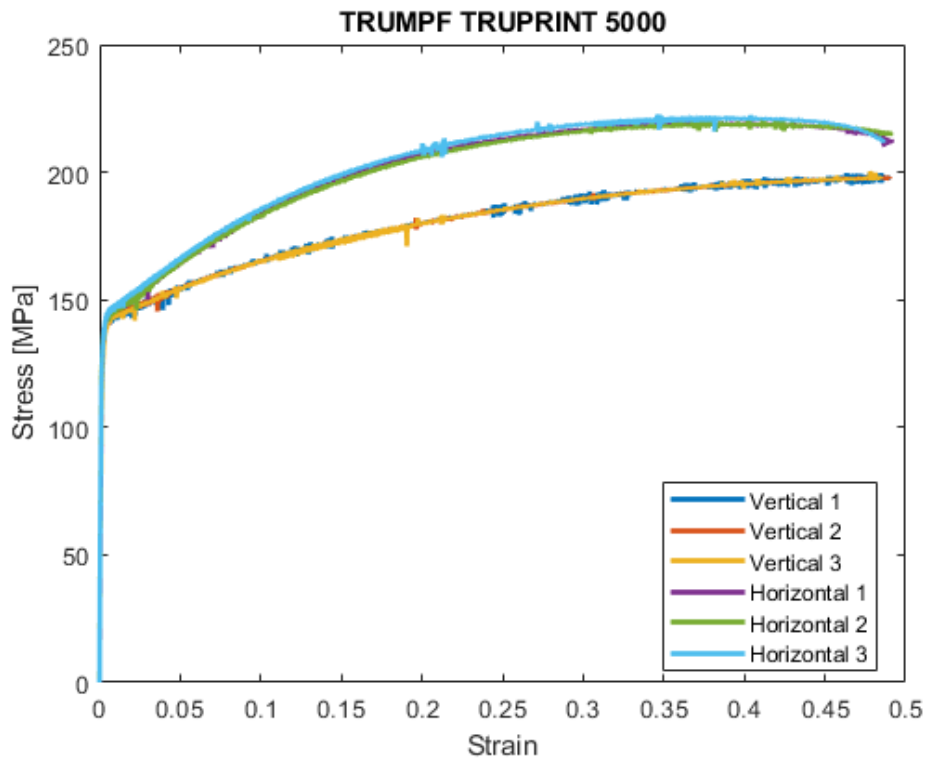


Figure 6.9 Stress-Strain curves of pure copper samples manufactured with TRUMPF TruPrint 5000.

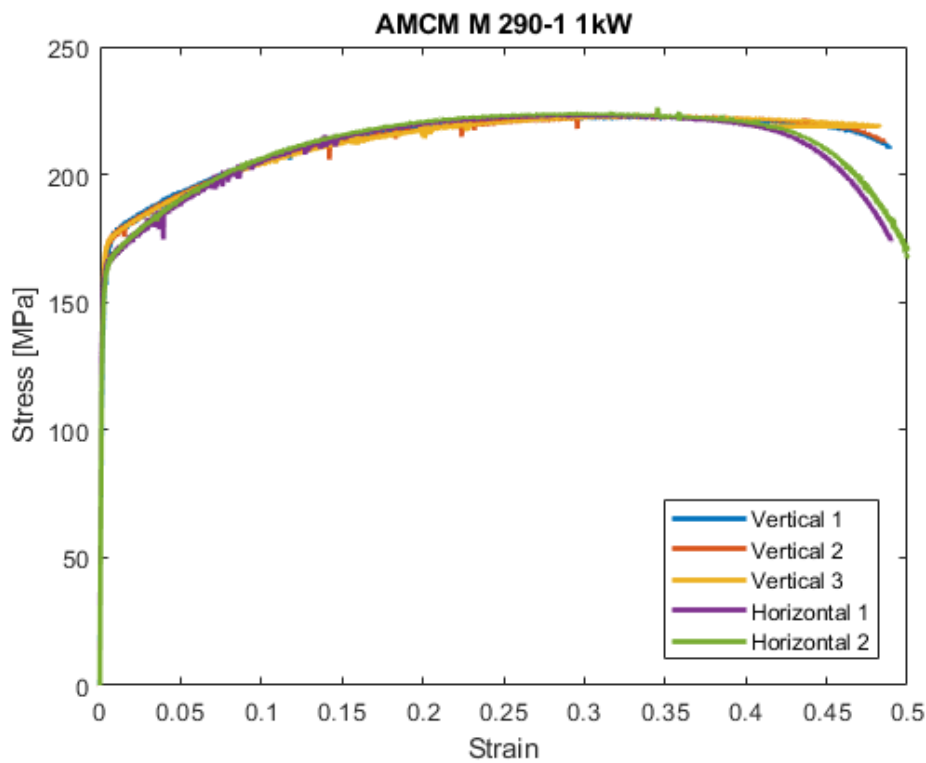


Figure 6.10 Stress-Strain curves of pure copper samples manufactured with AMCM M 290-1 1kW.

6.4 Production of accelerator grids prototypes

Since the components showed high relative densities and good mechanical properties, the following step was to request the production of the first grids prototypes from both producers. Figure 6.11 shows the grids prototypes. The prototype manufactured using the TruPrint 5000 is bigger (250x270x18 mm vs 200x210x18 mm) but has the inlet and outlet parts separated from the main component.

The main objectives of the prototyping are to check critical phases and eventually not predictable issues of the post-processing and to have an accurate analysis of the costs. The grids' post-processing consists of milling the external surfaces and electron beam welding the separate components.

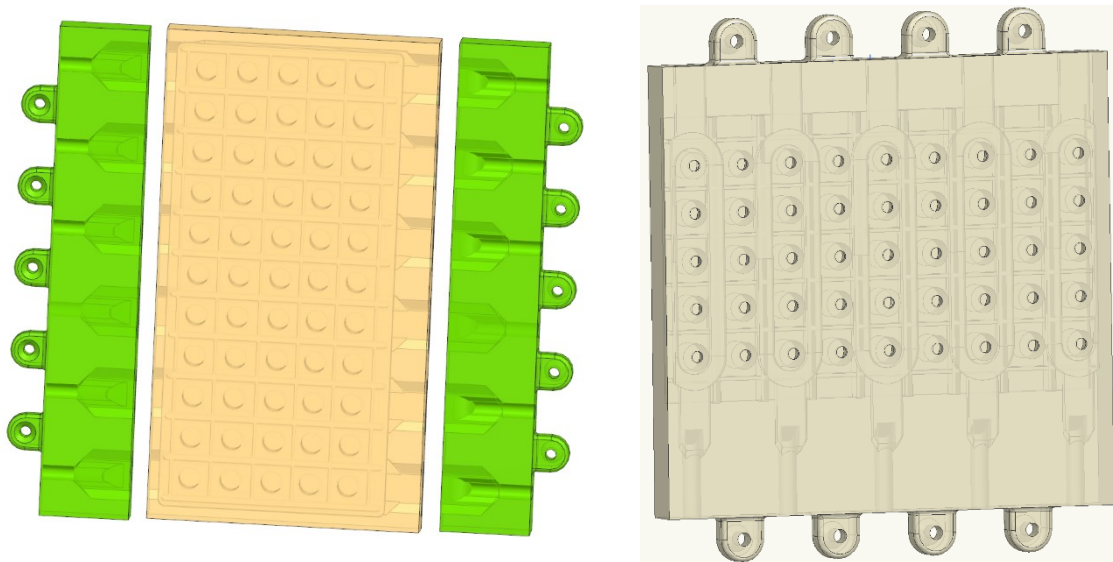


Figure 6.11 On the left: TruPrint 5000 accelerator grid prototype (250 x270x18 mm). On the right: AMCM M 290-1 1kW accelerator grid prototype (200x210x18 mm).

The designs presented in Figure 6.11 are oversized by a skin layer that the milling operation will remove to bring the part to the required tolerances. In particular, the grooves for the embedded magnets and the apertures for the negative beams require a good surface quality and tolerances of 0.1 mm and 0.05 mm, respectively. These features are only achievable by milling the surface. After the milling and electron beam welding of the grids, a leak test will be performed. Eventually, the grids will be tested on a beam-line.

To perform a thermal test using the DUNED configuration of the cooling channels, a smaller prototype (called “Power Test”- shown in Figure 6.12) was also requested from bot producers. The dimension of this grid is 149x146x11 mm. The heat loads are introduced in the system by some “C letters” that can be manufactured directly from the AM process. The “C letters” will be instrumented with T-thermocouples to register the temperature profile of the grids. Thermic resistances will be linked from a dug present at the top of the “C letters” to heat the samples, and water will be used to cool the grids.

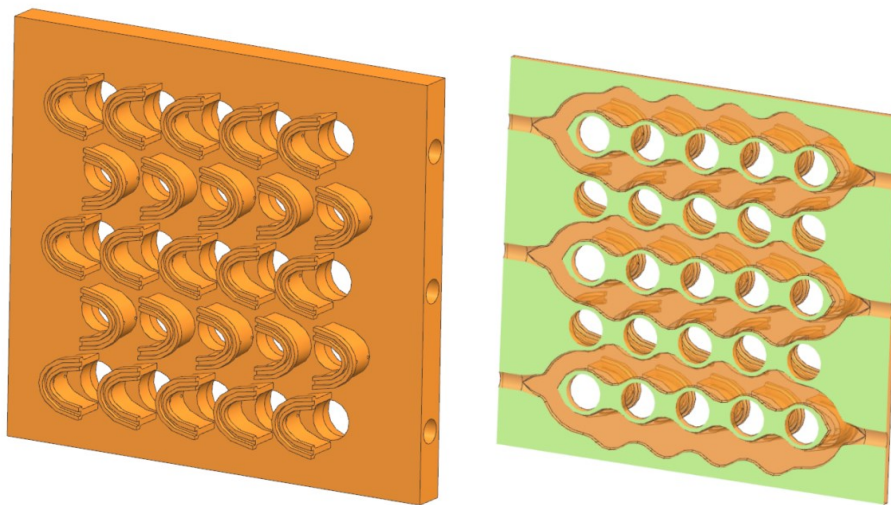


Figure 6.12 On the left: CAD design of the “Power Test” prototype. On the right: a section showing the DUNED cooling channels.

Before the manufacturing of the grids and the “Power Test” prototypes, it was agreed with both companies to deliver a “Leak Test” prototype to certify the tightness of the samples. The model chosen for this test is the same as the “Power Test” but without the “C” letters. A helium leak test will be performed at the grids. If the grids leak, an iterative process for improving the grids’ design will be performed until a leak-free prototype is delivered. Once the seal of the grids is confirmed, the grids prototypes will be manufactured.

During the last period of the research project, the “Leak Test” prototypes were delivered. Figure 6.13 b and c show the parts as delivered. The part produced by the LPBF machine TruPrint 5000 was CT scanned using a Zeiss Metrotom 1500 (the scan was performed at ProM’s Facility). Figure 6.13

shows the internal cooling channels of the grids, and the DUNED is recognizable.

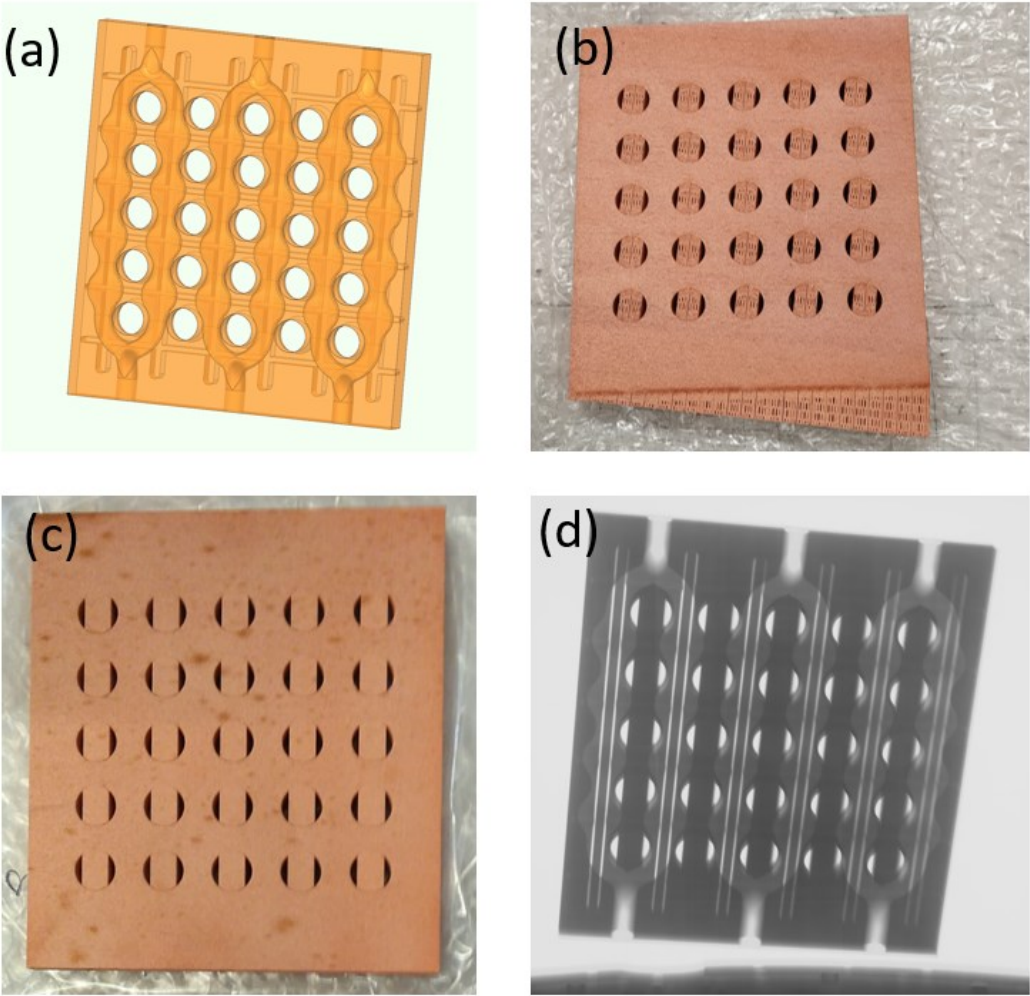


Figure 6.13 (a) CAD design of the “Leak Test” prototype. (b) Grid produced using EOS M290 1 kW. (c) Grid produced using TruPrint 5000. (d) CT scan of the “Leak Test” grid manufactured using TruPrint 5000.

7 CONCLUSIONS

The characterization of pure copper and CuCrZr alloy produced with the LPBD machine EOSINT M280 was performed. The results show that while using a laser power inferior to 400 W, it is not possible to manufacture dense pure copper parts. The high reflectivity of the infrared wavelength and high heat conductivity of pure copper reduce the energy input, and parts with high porosity are generated. The lack of fusion porosities reduces both the mechanical and physical properties of the parts.

The research on the PSD effect on the manufacturability of pure copper has shown that it has a low influence on the densification process. Despite having different granulometry, Powders A and B achieved the same relative density (~88%). A difference in the mechanical properties was recorded. Powder B, which had a broader PSD, led to inferior tensile and yield strengths (~14% lower). The cause of this behaviour was correlated to a higher concentration of unmelted particles inside the bulk material.

The effect of the PSD of Powder C could not be thoroughly assessed, as the composition of the material differed from powders was A and B. It presented a low level of contaminants, which reduced its thermal conductivity and reflectivity and led to better mechanical and thermal properties. The tuned parameters led to a 2% porosity, the mechanical properties of the parts were significantly higher than the pure copper parts (comparable to a 20% cold-worked pure copper), and also the thermal conductivity was improved due to the reduced porosity. Using the contour scan strategy reduced the roughness of vertical surfaces from 12 to 2.9 μm . Generally, LPBF parts have surface roughnesses within 10-30 μm (when a standard PSD is used). Therefore, this improvement was attributed to the PSD of the powder.

To improve the densification process of pure copper, powder A was oxidized at various times and temperatures. Heat treating the powder at 200°C for 1 h and at 150 °C for 15 h led to an oxygen concentration of 2000 ppm and to a reduction of reflectivity of ~28% (at a wavelength of 800 nm). Heat treating the powders at higher temperatures for a shorter duration of time leads to better results. The tuned parameters led to nearly full dense parts with higher micro-hardness. The thermal conductivity was also improved, but the obtained value is probably underestimated. During the research project, it

was proved that the Hot Disk method used to measure the thermal diffusivity of copper parts (i.e. high diffusivity values) underestimated the values. The measurement of the actual thermal conductivity of oxidized copper is a future work that will be conducted. It will be either performed by the Laser Flash method or by using the experimental setup described in this thesis.

More remarkable results were obtained while using the CuCrZr alloy. Compared to the oxidized copper, dense parts were obtained while using faster building rates. In addition, the LPBF process enables the direct ageing of the parts. The DAH parts showed a combination of high conductivity and high mechanical properties. The solution annealing heat treatment has the effect of partial recrystallizing the microstructure, which severely reduces the mechanical properties of the parts. The following ageing heat treatment raises the mechanical properties almost to the as-built condition (the yield strength is lower) and increases the material's conductivity. However, compared to the properties of DAH parts, the slight improvement of the conductivity is not worth the loss of mechanical properties. Furthermore, the material's anisotropy remains because of the lack of fusion porosities and partial recrystallization of the microstructure.

Although the downskin surface roughness was reduced from 21 to 15 μm , the upskin surface quality was harmed by the spatter particles created by the contour scan technique. Therefore, on the CuCrZr alloy, the contour scan strategy should be used only on the downskin surfaces.

The results obtained in this research project proved that the use of a copper alloy is the best solution to obtain copper parts with good conductivity and mechanical properties when using a low power laser. The manufacturing of pure copper is best performed with high laser power (1 kW), dense parts are obtained, and the building rate is faster.

The LPBF machines equipped with a 1 kW laser source were developed during the PhD period, and by the end of the research, it was possible to characterize the dense LPBF pure copper parts. The high quality of the parts enabled the production of the first accelerator grids prototypes with conformal cooling channels.

Based on the data acquired throughout this thesis study, new features that would be interesting to investigate have emerged. Firstly, the heat treatment of the CuCrZr alloy can be tuned to achieve the best combination of mechanical properties and conductivity. Then, an optimisation of the gas flow can be performed to remove the spatter particles and improve the surface quality of the parts. Other properties of the CuCrZr alloy can be characterized. Examples are fatigue resistance, corrosion resistance, and stress corrosion cracking susceptibility.

Another interesting aspect observed was the variation of relative density obtained by changing the number of samples manufactured (shown in [Appendix A](#)). The time interval between two consecutive layers affects the densification process and could be used to improve the quality of the printed parts. The effect of repeated reuse of CuCrZr powder should also be studied as the properties of the powder change. A hot isostatic pressing post-heat treatment can be performed and tuned to eliminate the lack of fusion porosity and hence the material anisotropy.

Since it was demonstrated that it is possible to manufacture copper alloys while using low laser power, other copper alloys can be characterized. For example, the CuCrNb is also a copper alloy that combines high thermal and mechanical properties. Besides characterizing alloys already developed for the traditional manufacturing process, novel copper alloy compositions specially intended for the LPBF process can be developed. In particular, the surface modification and carburization of powder proposed by Jadhav et al. [110],[120] are extremely interesting as they can be transferred to other copper alloys and highly reflecting materials.

Testing the AM accelerator grids is a research work that is currently being investigated. These tests will provide helpful information to improve the grid's design. For example, the wall thickness of the grids might be adjusted to avoid fluid leakages. The results of the heat exhaustion test and the pressure drop measurements can be used to validate the simulations that have been performed. These simulations will be then helpful for the designing of new accelerator grids or other heat exhaustion components.

Finally, polishing the interior channels is quite significant for thermal management devices. AM components' high surface roughness causes a high pressure drop, which should be decreased. While external surfaces could be easily finished by vibro-finishing and abrasive blasting processes, the polishing of small and complex cooling channels is more challenging. At the moment, single-channel prototypes made in CuCrZr are being polished using a chemical solution. Once the post process is tuned to achieve a low surface roughness for all inclination angles (as it was observed that the inclination angle affects the surface's quality), the samples will be used to evaluate the improvement of the channel's pressure drop. After the polishing process, the variation of the cross-section area of the cooling channels will also be measured, as it has to be taken into consideration when designing them.

APPENDIX A

Table A Relative density and process parameters of CuCrZr samples manufactured at 30 μm .

N	Laser Power [W]	Scan Speed [mm/s]	Hatching Distance [μm]	Density [g/mm^3]	RD [%]
1	310	400	80	8.690	97.75
2	370	400	80	8.719	98.07
3	310	1000	80	8.603	96.77
4	370	1000	80	8.698	97.84
5	310	400	100	8.660	97.41
6	370	400	100	8.716	98.05
7	310	1000	100	8.605	96.79
8	370	1000	100	8.718	98.06
9	310	700	90	8.699	97.85
10	370	700	90	8.762	98.56
11	340	400	90	8.736	98.26
12	340	1000	90	8.694	97.79
13	340	700	80	8.726	98.16
14	340	700	100	8.735	98.26
15	340	700	90	8.748	98.40
16	340	700	90	8.716	98.05
17	340	700	90	8.735	98.25
18	340	700	90	8.729	98.19
19	340	700	90	8.734	98.25
20	340	700	90	8.726	98.15

Several samples with the same process parameters have been manufactured to test the process reproducibility. The highest relative density (98.56 %) was obtained using the maximum laser power and a scan speed of 700 mm/s.

A second test was performed by manufacturing three samples using the maximum laser power, a scan speed of 600 mm/s and a hatching distance of 90 μm .

Table B Relative density and process parameters of the second set of CuCrZr samples manufactured at 30 μm .

N	Laser Power [W]	Scan Speed [mm/s]	Hatching Distance [μm]	Density [g/mm^3]	RD [%]
1	370	600	90	8.855	99.60
2	370	600	90	8.861	99.67
3	370	600	90	8.863	99.70

The relative density of the second set of specimens is remarkably higher; the three samples are nearly full dense with a relative density of ~99.7%.

While the reduction of scan speed (from 700 mm/s to 600 mm/s) might impact the increment of relative density, the primary reason for this increment is attributed to the different exposure times between the two printing jobs. In the first job, 20 samples were manufactured, while in the second only 3. The higher number of samples requires more time to manufacture, leading to an increment of time between two successive layer exposure. Instead, the samples in the second job have less time to cool, leading to heat accumulation during the manufacturing process.

While heat accumulation for many alloys could lead to various problems, such as residual stress and part deformation, it has the beneficial effect to reduce the lack of fusion porosity for the CuCrZr alloy. This result must be considered when manufacturing a low quantity of small samples, but it is not an available solution for producing larger parts, such as the acceleration grids. Therefore, only the first set of samples was considered for tuning the process parameters.

On the other hand, the acquired results serve as a starting point for future research into the impact of varying time exposure between layers on the physical properties of printed objects.

REFERENCES

- [1] ISO/ASTM 52900, “Standard Terminology for Additive Manufacturing – General Principles – Terminology,” vol. i, pp. 1–9, 2015.
- [2] W. J. Sames, F. A. List, S. Pannala, R. R. Dehoff, and S. S. Babu, “The metallurgy and processing science of metal additive manufacturing,” *International Materials Reviews*, vol. 61, no. 5, pp. 315–360, 2016, doi: 10.1080/09506608.2015.1116649.
- [3] X. Gong, T. Anderson, and K. Chou, “Review on powder-based electron beam additive manufacturing Technology,” *Manufacturing Review*, vol. 1, 2014, doi: 10.1051/mfreview/2014001.
- [4] F. Calignano *et al.*, “Overview on additive manufacturing technologies,” *Proceedings of the IEEE*, vol. 105, no. 4, pp. 593–612, 2017, doi: 10.1109/JPROC.2016.2625098.
- [5] J. Milberg and M. Sigl, “Electron beam sintering of metal powder,” *Production Engineering*, vol. 2, no. 2, pp. 117–122, 2008, doi: 10.1007/s11740-008-0088-2.
- [6] S. Liu and Y. C. Shin, “Additive manufacturing of Ti6Al4V alloy: A review,” *Materials and Design*, vol. 164, p. 107552, 2019, doi: 10.1016/j.matdes.2018.107552.
- [7] V. Petrovic and R. Niñerola, “Powder recyclability in electron beam melting for aeronautical use,” *Aircraft Engineering and Aerospace Technology*, vol. 87, no. 2, pp. 147–155, 2015, doi: 10.1108/AEAT-11-2013-0212.
- [8] D. Herzog, V. Seyda, E. Wycisk, and C. Emmelmann, “Additive manufacturing of metals,” *Acta Materialia*, vol. 117, pp. 371–392, 2016, doi: 10.1016/j.actamat.2016.07.019.
- [9] P. Li, D. H. Warner, A. Fatemi, and N. Phan, “Critical assessment of the fatigue performance of additively manufactured Ti-6Al-4V and perspective for future research,” *International Journal of Fatigue*, vol. 85, pp. 130–143, 2016, doi: 10.1016/j.ijfatigue.2015.12.003.
- [10] A. Dass and A. Moridi, “State of the art in directed energy deposition: From additive manufacturing to materials design,” *Coatings*, vol. 9, no. 7, pp. 1–26, 2019, doi: 10.3390/COATINGS9070418.

- [11] D. G. Ahn, *Directed Energy Deposition (DED) Process: State of the Art*, vol. 8, no. 2. Korean Society for Precision Engineering, 2021. doi: 10.1007/s40684-020-00302-7.
- [12] A. Vafadar, F. Guzzomi, A. Rassau, and K. Hayward, “Advances in metal additive manufacturing: A review of common processes, industrial applications, and current challenges,” *Applied Sciences (Switzerland)*, vol. 11, no. 3, pp. 1–33, 2021, doi: 10.3390/app11031213.
- [13] D. R. White, “Ultrasonic consolidation of aluminum tooling,” *Advanced Materials and Processes*, vol. 161, no. 1, pp. 64–65, Jan. 2003.
- [14] Y. Zhang *et al.*, “Additive Manufacturing of Metallic Materials: A Review,” *Journal of Materials Engineering and Performance*, vol. 27, no. 1, pp. 1–13, 2018, doi: 10.1007/s11665-017-2747-y.
- [15] G. D. J. Ram, C. Robinson, Y. Yang, and B. E. Stucker, “Use of ultrasonic consolidation for fabrication of multi-material structures,” *Rapid Prototyping Journal*, vol. 13, no. 4, pp. 226–235, 2007, doi: 10.1108/13552540710776179.
- [16] R. J. Friel and R. A. Harris, “Ultrasonic additive manufacturing A hybrid production process for novel functional products,” *Procedia CIRP*, vol. 6, no. December, pp. 35–40, 2013, doi: 10.1016/j.procir.2013.03.004.
- [17] M. Li, W. Du, A. Elwany, Z. Pei, and C. Ma, “Metal binder jetting additive manufacturing: A literature review,” *Journal of Manufacturing Science and Engineering, Transactions of the ASME*, vol. 142, no. 9, pp. 1–17, 2020, doi: 10.1115/1.4047430.
- [18] M. Vaezi, P. Drescher, and H. Seitz, “Beamless Metal Additive Manufacturing,” *Materials*, vol. 13, no. 4, 2020, doi: 10.3390/ma13040922.
- [19] B. Ferrar, L. Mullen, E. Jones, R. Stamp, and C. J. Sutcliffe, “Gas flow effects on selective laser melting (SLM) manufacturing performance,” *Journal of Materials Processing Technology*, vol. 212, no. 2, pp. 355–364, 2012, doi: 10.1016/j.jmatprotec.2011.09.020.
- [20] P. Hanzl, M. Zetek, T. Bakša, and T. Kroupa, “The influence of processing parameters on the mechanical properties of SLM parts,” *Procedia Engineering*, vol. 100, no. January, pp. 1405–1413, 2015, doi: 10.1016/j.proeng.2015.01.510.

- [21] J. Jiang, X. Xu, and J. Stringer, "Support structures for additive manufacturing: A review," *Journal of Manufacturing and Materials Processing*, vol. 2, no. 4, 2018, doi: 10.3390/jmmp2040064.
- [22] P. N. J. Lindecke, H. Blunk, J. P. Wenzl, M. Möller, and C. Emmelmann, "Optimization of support structures for the laser additive manufacturing of TiAl6V4 parts," *Procedia CIRP*, vol. 74, pp. 53–58, 2018, doi: 10.1016/j.procir.2018.08.029.
- [23] S. A. Khairallah, A. T. Anderson, A. Rubenchik, and W. E. King, "Laser powder-bed fusion additive manufacturing: Physics of complex melt flow and formation mechanisms of pores, spatter, and denudation zones," *Acta Materialia*, vol. 108, pp. 36–45, 2016, doi: 10.1016/j.actamat.2016.02.014.
- [24] A. Zakirov *et al.*, "Predictive modeling of laser and electron beam powder bed fusion additive manufacturing of metals at the mesoscale," *Additive Manufacturing*, vol. 35, no. April, p. 101236, 2020, doi: 10.1016/j.addma.2020.101236.
- [25] A. v. Gusarov, I. Yadroitsev, P. Bertrand, and I. Smurov, "Heat transfer modelling and stability analysis of selective laser melting," *Applied Surface Science*, vol. 254, no. 4, pp. 975–979, 2007, doi: 10.1016/j.apsusc.2007.08.074.
- [26] C. Meier, R. W. Penny, Y. Zou, J. S. Gibbs, and A. J. Hart, "Thermophysical Phenomena in Metal Additive Manufacturing By Selective Laser Melting: Fundamentals, Modeling, Simulation, and Experimentation," *Annual Review of Heat Transfer*, vol. 20, no. 1, pp. 241–316, 2018, doi: 10.1615/annualrevheattransfer.2018019042.
- [27] W. E. King *et al.*, "Laser powder-bed fusion additive manufacturing of metals; physics, computational, and materials challenges," *Additive Manufacturing Handbook: Product Development for the Defense Industry*, vol. 041304, pp. 461–506, 2015, doi: 10.1201/9781315119106.
- [28] C. Meier *et al.*, "Physics-based modeling and predictive simulation of powder bed fusion additive manufacturing across length scales," *GAMM Mitteilungen*, vol. 44, no. 3, pp. 1–26, 2021, doi: 10.1002/gamm.202100014.

- [29] D. Gu and Y. Shen, “Balling phenomena in direct laser sintering of stainless steel powder: Metallurgical mechanisms and control methods,” *Materials and Design*, vol. 30, no. 8, pp. 2903–2910, 2009, doi: 10.1016/j.matdes.2009.01.013.
- [30] C. Körner, A. Bauereiß, and E. Attar, “Fundamental consolidation mechanisms during selective beam melting of powders,” *Modelling and Simulation in Materials Science and Engineering*, vol. 21, no. 8, 2013, doi: 10.1088/0965-0393/21/8/085011.
- [31] X. Xiao, C. Lu, Y. Fu, X. Ye, and L. Song, “Progress on Experimental Study of Melt Pool Flow Dynamics in Laser Material Processing,” in *Liquid Metals*, S. J. S. Chelladurai, S. Gnanasekaran, and S. Mayilswamy, Eds. Rijeka: IntechOpen, 2021. doi: 10.5772/intechopen.97205.
- [32] B. Xiao and Y. Zhang, “Marangoni and Buoyancy effects on direct metal laser sintering with a moving laser beam,” *Numerical Heat Transfer; Part A: Applications*, vol. 51, no. 8, pp. 715–733, 2007, doi: 10.1080/10407780600968593.
- [33] C. Zhao *et al.*, “Real-time monitoring of laser powder bed fusion process using high-speed X-ray imaging and diffraction,” *Scientific Reports*, vol. 7, no. 1, pp. 1–11, 2017, doi: 10.1038/s41598-017-03761-2.
- [34] D. Wang *et al.*, “Mechanisms and characteristics of spatter generation in SLM processing and its effect on the properties,” *Materials and Design*, vol. 117, pp. 121–130, 2017, doi: 10.1016/j.matdes.2016.12.060.
- [35] M. J. Matthews, G. Guss, S. A. Khairallah, A. M. Rubenchik, P. J. Depond, and W. E. King, “Denudation of metal powder layers in laser powder bed fusion processes,” *Acta Materialia*, vol. 114, pp. 33–42, 2016, doi: 10.1016/j.actamat.2016.05.017.
- [36] J. Yin *et al.*, “Correlation between forming quality and spatter dynamics in laser powder bed fusion,” *Additive Manufacturing*, vol. 31, no. November 2019, p. 100958, 2020, doi: 10.1016/j.addma.2019.100958.
- [37] T. Mukherjee, J. S. Zuback, A. De, and T. DebRoy, “Printability of alloys for additive manufacturing,” *Scientific Reports*, vol. 6, pp. 1–8, 2016, doi: 10.1038/srep19717.

- [38] W. Kurz, B. Giovanola, and R. Trivedi, "Theory of Microstructural Development During Rapid Solidification.," *Acta Metallurgica*, vol. 34, no. 5, pp. 823–830, 1986, doi: 10.1007/978-94-009-4456-5_24.
- [39] T. DebRoy *et al.*, "Additive manufacturing of metallic components – Process, structure and properties," *Progress in Materials Science*, vol. 92, pp. 112–224, 2018, doi: 10.1016/j.pmatsci.2017.10.001.
- [40] P. A. Hooper, "Melt pool temperature and cooling rates in laser powder bed fusion," *Additive Manufacturing*, vol. 22, no. May, pp. 548–559, 2018, doi: 10.1016/j.addma.2018.05.032.
- [41] B. Vrancken, L. Thijs, J. P. Kruth, and J. van Humbeeck, "Microstructure and mechanical properties of a novel β titanium metallic composite by selective laser melting," *Acta Materialia*, vol. 68, pp. 150–158, 2014, doi: 10.1016/j.actamat.2014.01.018.
- [42] L. Thijs, K. Kempen, J. P. Kruth, and J. van Humbeeck, "Fine-structured aluminium products with controllable texture by selective laser melting of pre-alloyed AlSi10Mg powder," *Acta Materialia*, vol. 61, no. 5, pp. 1809–1819, 2013, doi: 10.1016/j.actamat.2012.11.052.
- [43] X. Liu, C. Zhao, X. Zhou, Z. Shen, and W. Liu, "Microstructure of selective laser melted AlSi10Mg alloy," *Materials and Design*, vol. 168, p. 107677, 2019, doi: 10.1016/j.matdes.2019.107677.
- [44] F. Trevisan *et al.*, "On the selective laser melting (SLM) of the AlSi10Mg alloy: Process, microstructure, and mechanical properties," *Materials*, vol. 10, no. 1, 2017, doi: 10.3390/ma10010076.
- [45] X. Wang and K. Chou, "Effects of thermal cycles on the microstructure evolution of Inconel 718 during selective laser melting process," *Additive Manufacturing*, vol. 18, pp. 1–14, 2017, doi: 10.1016/j.addma.2017.08.016.
- [46] R. Casati, J. Lemke, and M. Vedani, "Microstructure and Fracture Behavior of 316L Austenitic Stainless Steel Produced by Selective Laser Melting," *Journal of Materials Science and Technology*, vol. 32, no. 8, pp. 738–744, 2016, doi: 10.1016/j.jmst.2016.06.016.
- [47] L. Thijs, F. Verhaeghe, T. Craeghs, J. Van Humbeeck, and J. P. Kruth, "A study of the microstructural evolution during selective laser melting of Ti-6Al-4V," *Acta Materialia*, vol. 58, no. 9, pp. 3303–3312, 2010, doi: 10.1016/j.actamat.2010.02.004.

- [48] M. Schmitt *et al.*, “Influence of Part Geometry and Feature Size on the Resulting Microstructure and Mechanical Properties of the Case Hardening Steel 16MnCr5 processed by Laser Powder Bed Fusion,” *Procedia CIRP*, vol. 104, pp. 726–731, 2021, doi: 10.1016/j.procir.2021.11.122.
- [49] W. E. Frazier, “Metal additive manufacturing: A review,” *Journal of Materials Engineering and Performance*, vol. 23, no. 6, pp. 1917–1928, 2014, doi: 10.1007/s11665-014-0958-z.
- [50] A. Aversa *et al.*, “New Aluminum Alloys Specifically Designed for Laser Powder Bed Fusion: A Review,” *Materials*, vol. 12, no. 7, p. 1007, 2019, doi: 10.3390/ma12071007.
- [51] S. Sun, M. Brandt, and M. Easton, *Powder bed fusion processes*. Elsevier Ltd, 2016. doi: 10.1016/b978-0-08-100433-3.00002-6.
- [52] B. Vrancken, “Study of Residual Stresses in Selective Laser Melting,” *PhD Thesis; KU Leuven Arenberg Doctoral School Faculty of Engineering Science*, no. June, pp. 1–253, 2016, [Online]. Available: https://lirias.kuleuven.be/bitstream/123456789/542751/1/thesis+Bey+Vrancken+v01-06-2016+FINAL_compressed.pdf
- [53] P. Mercelis and J. P. Kruth, “Residual stresses in selective laser sintering and selective laser melting,” *Rapid Prototyping Journal*, vol. 12, no. 5, pp. 254–265, 2006, doi: 10.1108/13552540610707013.
- [54] K. Kempen, L. Thijs, B. Vrancken, S. Bols, J. Van Humbeeck, and J. P. Kruth, “Producing crack-free, high density M2 HSS parts by Selective Laser Melting: Pre-heating the baseplate,” *24th International SFF Symposium - An Additive Manufacturing Conference, SFF 2013*, no. August, pp. 131–139, 2013.
- [55] Z. Xiao *et al.*, “Study of residual stress in selective laser melting of Ti6Al4V,” *Materials and Design*, vol. 193, p. 108846, 2020, doi: 10.1016/j.matdes.2020.108846.
- [56] R. Mertens, S. Dadbakhsh, J. Van Humbeeck, and J. P. Kruth, “Application of base plate preheating during selective laser melting,” *Procedia CIRP*, vol. 74, pp. 5–11, 2018, doi: 10.1016/j.procir.2018.08.002.
- [57] M. Agarwala, D. Bourell, J. Beaman, H. Marcus, and J. Barlow, “Direct selective laser sintering of metals,” *Rapid Prototyping Journal*, vol. 1, no. 1, pp. 26–36, 1995, doi: 10.1108/13552549510078113.

- [58] M. Tang, P. C. Pistorius, and J. L. Beuth, “Prediction of lack-of-fusion porosity for powder bed fusion,” *Additive Manufacturing*, vol. 14, pp. 39–48, 2017, doi: 10.1016/j.addma.2016.12.001.
- [59] M. H. Hong, B. K. Min, and T. Y. Kwon, “The influence of process parameters on the surface roughness of a 3d-printed Co-Cr dental alloy produced via selective laser melting,” *Applied Sciences (Switzerland)*, vol. 6, no. 12, 2016, doi: 10.3390/app6120401.
- [60] Q. Bai, B. Wu, X. Qiu, B. Zhang, and J. Chen, “Experimental study on additive/subtractive hybrid manufacturing of 6511 steel: process optimization and machining characteristics,” *International Journal of Advanced Manufacturing Technology*, vol. 108, no. 5–6, pp. 1389–1398, 2020, doi: 10.1007/s00170-020-05514-4.
- [61] D. Wang, Y. Liu, Y. Yang, and D. Xiao, “Theoretical and experimental study on surface roughness of 316L stainless steel metal parts obtained through selective laser melting,” *Rapid Prototyping Journal*, vol. 22, no. 4, pp. 706–716, 2016, doi: 10.1108/RPJ-06-2015-0078.
- [62] H. Gong, “ThinkIR : The University of Louisville ’ s Institutional Repository Generation and detection of defects in metallic parts fabricated by selective laser melting and electron beam melting and their effects on mechanical properties .,” 2013.
- [63] A. Aversa *et al.*, “Single scan track analyses on aluminium based powders,” *Journal of Materials Processing Technology*, vol. 255, no. September 2017, pp. 17–25, 2018, doi: 10.1016/j.jmatprotec.2017.11.055.
- [64] H. Jia, H. Sun, H. Wang, Y. Wu, and H. Wang, “Scanning strategy in selective laser melting (SLM): a review,” *International Journal of Advanced Manufacturing Technology*, vol. 113, no. 9–10, pp. 2413–2435, 2021, doi: 10.1007/s00170-021-06810-3.
- [65] L. Thijs, “Microstructure and Texture of Metal Parts Produced by Selective Laser Melting (Microstructuur en textuur van metalen stukken geproduceerd via selectief laser smelten),” 2014.
- [66] R. Sharma and A. Kumar, “Track-Scale Simulations of Selective Laser Melting to Investigate Development and Mitigation of Thermal Stresses,” *Lasers in Manufacturing and Materials Processing*, vol. 6, no. 4, pp. 464–492, 2019, doi: 10.1007/s40516-019-00103-0.

- [67] P. Promopatum and S. C. Yao, "Influence of scanning length and energy input on residual stress reduction in metal additive manufacturing: Numerical and experimental studies," *Journal of Manufacturing Processes*, vol. 49, no. January 2019, pp. 247–259, 2020, doi: 10.1016/j.jmapro.2019.11.020.
- [68] J. A. Pakkanen, "Designing for Additive Manufacturing-Product and Process Driven Design for Metals and Polymers," 2018. doi: 10.6092/polito/porto/2714732.
- [69] Y. Tian, D. Tomus, P. Rometsch, and X. Wu, "Influences of processing parameters on surface roughness of Hastelloy X produced by selective laser melting," *Additive Manufacturing*, vol. 13, pp. 103–112, 2017, doi: 10.1016/j.addma.2016.10.010.
- [70] E. Yasa, J. Deckers, and J. P. Kruth, "The investigation of the influence of laser re-melting on density, surface quality and microstructure of selective laser melting parts," *Rapid Prototyping Journal*, vol. 17, no. 5, pp. 312–327, 2011, doi: 10.1108/13552541111156450.
- [71] D. Wang, Y. Yang, Z. Yi, and X. Su, "Research on the fabricating quality optimization of the overhanging surface in SLM process," *International Journal of Advanced Manufacturing Technology*, vol. 65, no. 9–12, pp. 1471–1484, 2013, doi: 10.1007/s00170-012-4271-4.
- [72] Y. Cao, H. L. Wei, T. Yang, T. T. Liu, and W. H. Liao, "Printability assessment with porosity and solidification cracking susceptibilities for a high strength aluminum alloy during laser powder bed fusion," *Additive Manufacturing*, vol. 46, no. February, p. 102103, 2021, doi: 10.1016/j.addma.2021.102103.
- [73] M. Leary, "Powder bed fusion," in *Design for Additive Manufacturing*, 2020, pp. 295–319. doi: 10.1016/b978-0-12-816721-2.00011-7.
- [74] Vin Calcutt, "Introduction to Copper: Applications," 2001. https://www.copper.org/publications/newsletters/innovations/2001/08/intro_to_copper.html (accessed Jan. 25, 2022).

- [75] D. Tiberto, U. E. Klotz, F. Held, and G. Wolf, "Additive manufacturing of copper alloys: influence of process parameters and alloying elements," *Materials Science and Technology (United Kingdom)*, vol. 35, no. 8, pp. 969–977, 2019, doi: 10.1080/02670836.2019.1600840.
- [76] T. Q. Tran *et al.*, "3D printing of highly pure copper," *Metals*, vol. 9, no. 7, pp. 12–20, 2019, doi: 10.3390/met9070756.
- [77] C. Silbernagel, L. Gargalis, I. Ashcroft, R. Hague, M. Galea, and P. Dickens, "Electrical resistivity of pure copper processed by medium-powered laser powder bed fusion additive manufacturing for use in electromagnetic applications," *Additive Manufacturing*, vol. 29, no. November 2018, p. 100831, 2019, doi: 10.1016/j.addma.2019.100831.
- [78] P. Frigola *et al.*, "Fabricating Copper Components with Electron Beam Melting," *Advanced Materials & Processes*, p. 20, 2014.
- [79] I. Yadroitsev, A. Gusarov, I. Yadroitsava, and I. Smurov, "Single track formation in selective laser melting of metal powders," *Journal of Materials Processing Technology*, vol. 210, no. 12, pp. 1624–1631, 2010, doi: 10.1016/j.jmatprotec.2010.05.010.
- [80] H. Siva Prasad, F. Brueckner, J. Volpp, and A. F. H. Kaplan, "Laser metal deposition of copper on diverse metals using green laser sources," *International Journal of Advanced Manufacturing Technology*, vol. 107, no. 3–4, pp. 1559–1568, 2020, doi: 10.1007/s00170-020-05117-z.
- [81] N. Yaragatti and A. Patnaik, "A Review on Additive Manufacturing of Pure Copper," *Materials Today: Proceedings*, vol. 44, pp. 4150–4157, 2020, doi: 10.1016/j.matpr.2020.10.490.
- [82] M. Sinico, G. Cogo, M. Benettoni, I. Calliari, and A. Pepato, "Influence of powder particle size distribution on the printability of pure copper for selective laser melting," in *30th Annual International Solid Freeform Fabrication Symposium*, 2019, pp. 1–11.
- [83] X. Yan *et al.*, "Microstructure and mechanical properties of pure copper manufactured by selective laser melting," *Materials Science and Engineering: A*, vol. 789, no. January, p. 139615, Jul. 2020, doi: 10.1016/j.msea.2020.139615.

- [84] F. Trevisan, F. Calignano, M. Lorusso, M. Lombardi, D. Manfredi, and P. Fino, "Selective laser melting of chemical pure copper powders," in *Euro PM 2017*, 2017, pp. 1–6.
- [85] P. A. Lykov, E. v. Safonov, and A. M. Akhmedianov, "Selective laser melting of copper," *Materials Science Forum*, vol. 843, no. September, pp. 284–288, 2016, doi: 10.4028/www.scientific.net/MSF.843.284.
- [86] T. T. Ikeshoji, K. Nakamura, M. Yonehara, K. Imai, and H. Kyogoku, "Selective Laser Melting of Pure Copper," *Jom*, vol. 70, no. 3, pp. 396–400, 2018, doi: 10.1007/s11837-017-2695-x.
- [87] M. Colopi, L. Caprio, A. G. Demir, and B. Previtali, "Selective laser melting of pure Cu with a 1 kW single mode fiber laser," *Procedia CIRP*, vol. 74, pp. 59–63, 2018, doi: 10.1016/j.procir.2018.08.030.
- [88] S. D. Jadhav, S. Dadbakhsh, L. Goossens, J. P. Kruth, J. van Humbeeck, and K. Vanmeensel, "Influence of selective laser melting process parameters on texture evolution in pure copper," *Journal of Materials Processing Technology*, vol. 270, no. July 2018, pp. 47–58, 2019, doi: 10.1016/j.jmatprotec.2019.02.022.
- [89] M. Colopi, A. G. Demir, L. Caprio, and B. Previtali, "Limits and solutions in processing pure Cu via selective laser melting using a high-power single-mode fiber laser," *International Journal of Advanced Manufacturing Technology*, vol. 104, no. 5–8, pp. 2473–2486, 2019, doi: 10.1007/s00170-019-04015-3.
- [90] S. D. Jadhav, L. R. Goossens, Y. Kinds, B. van Hooreweder, and K. Vanmeensel, "Laser-based powder bed fusion additive manufacturing of pure copper," *Additive Manufacturing*, vol. 42, no. April, p. 101990, Jun. 2021, doi: 10.1016/j.addma.2021.101990.
- [91] S. Qu, J. Ding, J. Fu, M. Fu, B. Zhang, and X. Song, "High-precision laser powder bed fusion processing of pure copper," *Additive Manufacturing*, vol. 48, no. PA, p. 102417, 2021, doi: 10.1016/j.addma.2021.102417.
- [92] K. Asano *et al.*, "Laser metal deposition of pure copper on stainless steel with blue and IR diode lasers," *Optics and Laser Technology*, vol. 107, pp. 291–296, 2018, doi: 10.1016/j.optlastec.2018.06.012.

- [93] “TRUMPF introduces precious metal and copper 3D printing powered by green laser - 3D Printing Industry.” <https://3dprintingindustry.com/news/trumpf-introduces-precious-metal-and-copper-3d-printing-powered-by-green-laser-143689/> (accessed Jan. 29, 2022).
- [94] S. Gruber, L. Stepien, E. López, F. Brueckner, and C. Leyens, “Physical and Geometrical Properties of Additively Manufactured Pure Copper Samples Using a Green Laser Source,” *Materials*, vol. 14, no. 13, p. 3642, 2021, doi: 10.3390/ma14133642.
- [95] Y. Chen, S. Ren, Y. Zhao, and X. Qu, “Microstructure and properties of CuCr alloy manufactured by selective laser melting,” *Journal of Alloys and Compounds*, vol. 786, pp. 189–197, 2019, doi: 10.1016/j.jallcom.2019.01.179.
- [96] S. D. Jadhav, J. Vleugels, J. Kruth, J. van Humbeeck, and K. Vanmeensel, “Mechanical and electrical properties of selective laser-melted parts produced from surface-oxidized copper powder,” *Material Design & Processing Communications*, vol. 2, no. 2, pp. 1–8, Apr. 2020, doi: 10.1002/mdp2.94.
- [97] V. Lindström *et al.*, “Laser powder bed fusion of metal coated copper powders,” *Materials*, vol. 13, no. 16, 2020, doi: 10.3390/MA13163493.
- [98] S. D. Jadhav *et al.*, “Highly conductive and strong CuSn0.3 alloy processed via laser powder bed fusion starting from a tin-coated copper powder,” *Additive Manufacturing*, vol. 36, no. September, p. 101607, 2020, doi: 10.1016/j.addma.2020.101607.
- [99] S. D. Jadhav *et al.*, “Influence of carbon nanoparticle addition (and impurities) on selective laser melting of pure copper,” *Materials*, vol. 12, no. 15, 2019, doi: 10.3390/ma12152469.
- [100] Z. Tan *et al.*, “Thermal effect on the microstructure of the lattice structure Cu-10Sn alloy fabricated through selective laser melting,” *Journal of Alloys and Compounds*, vol. 787, pp. 903–908, 2019, doi: 10.1016/j.jallcom.2019.02.196.
- [101] Z. Mao, D. Z. Zhang, J. Jiang, G. Fu, and P. Zhang, “Processing optimisation, mechanical properties and microstructural evolution during selective laser melting of Cu-15Sn high-tin bronze,” *Materials Science and Engineering A*, vol. 721, no. October 2017, pp. 125–134, 2018, doi: 10.1016/j.msea.2018.02.051.

- [102] D. Palousek *et al.*, “SLM process parameters development of Cu-alloy Cu7.2Ni1.8Si1Cr,” *Rapid Prototyping Journal*, vol. 25, no. 2, pp. 266–276, 2019, doi: 10.1108/RPJ-06-2017-0116.
- [103] S. J. Zinkle, “Applicability of copper alloys for DEMO high heat flux components,” *Physica Scripta*, vol. 2016, no. T167, 2016, doi: 10.1088/0031-8949/2015/T167/014004.
- [104] C. R. Pobel, M. A. Lodes, and C. Körner, “Selective Electron Beam Melting of Oxide Dispersion Strengthened Copper,” *Advanced Engineering Materials*, vol. 20, no. 8, pp. 1–7, 2018, doi: 10.1002/adem.201800068.
- [105] J. B. Correia, H. A. Davies, and C. M. Sellars, “Strengthening in rapidly solidified age hardened Cu-Cr and Cu-Cr-Zr alloys,” *Acta Materialia*, vol. 45, no. 1, pp. 177–190, 1997, doi: 10.1016/S1359-6454(96)00142-5.
- [106] S. C. Krishna, K. V. Radhika, K. Thomas Tharian, G. Sudarshan Rao, M. Swathi Kiranmayee, and B. Pant, “Effect of Simulated Brazing Cycle on the Microstructure and Mechanical Properties of Cu-Cr-Zr-Ti Alloy,” *Materials Science Forum*, vol. 710, pp. 626–631, 2012, doi: 10.4028/www.scientific.net/msf.710.626.
- [107] D. J. Chakrabarti and D. E. Laughlin, “The Cr-Cu (Chromium-Copper) system,” *Bulletin of Alloy Phase Diagrams*, vol. 5, no. 1, pp. 59–68, Feb. 1984, doi: 10.1007/BF02868727.
- [108] S. Uchida *et al.*, “Microstructures and electrical and mechanical properties of Cu-Cr alloys fabricated by selective laser melting,” *Materials and Design*, vol. 175, p. 107815, 2019, doi: 10.1016/j.matdes.2019.107815.
- [109] A. Morozova, R. Mishnev, A. Belyakov, and R. Kaibyshev, “Microstructure and properties of fine grained Cu-Cr-Zr alloys after termo-mechanical treatments,” *Reviews on Advanced Materials Science*, vol. 54, no. 1, pp. 56–92, 2018, doi: 10.1515/rams-2018-0020.
- [110] S. D. Jadhav, P. P. Dhekne, S. Dadbakhsh, J. P. Kruth, J. van Humbeeck, and K. Vanmeensel, “Surface Modified Copper Alloy Powder for Reliable Laser-based Additive Manufacturing,” *Additive Manufacturing*, vol. 35, no. June, 2020, doi: 10.1016/j.addma.2020.101418.

- [111] E. Uhlmann, A. E. Tekkaya, V. Kasjevko, S. Gies, R. Reimann, and P. John, “Qualification of CuCr1Zr for the SLM Process,” *7th International Conference on High Speed Forming*, no. April, pp. 173–182, 2016, [Online]. Available: <https://eldorado.tu-dortmund.de/handle/2003/34936>
- [112] Z. Ma, K. Zhang, Z. Ren, D. Z. Zhang, G. Tao, and H. Xu, “Selective laser melting of Cu–Cr–Zr copper alloy: Parameter optimization, microstructure and mechanical properties,” *Journal of Alloys and Compounds*, vol. 828, p. 154350, 2020, doi: 10.1016/j.jallcom.2020.154350.
- [113] C. Wallis and B. Buchmayr, “Effect of heat treatments on microstructure and properties of CuCrZr produced by laser-powder bed fusion,” *Materials Science and Engineering A*, vol. 744, no. September 2018, pp. 215–223, 2019, doi: 10.1016/j.msea.2018.12.017.
- [114] B. Buchmayr, G. Panzl, A. Walzl, and C. Wallis, “Laser Powder Bed Fusion – Materials Issues and Optimized Processing Parameters for Tool steels, AlSiMg- and CuCrZr-Alloys,” *Advanced Engineering Materials*, vol. 19, no. 4, 2017, doi: 10.1002/adem.201600667.
- [115] K. Jahns, R. Bappert, P. Böhlke, and U. Krupp, “Additive manufacturing of CuCr1Zr by development of a gas atomization and laser powder bed fusion routine,” *International Journal of Advanced Manufacturing Technology*, vol. 107, no. 5–6, pp. 2151–2161, 2020, doi: 10.1007/s00170-020-04941-7.
- [116] P. Guan *et al.*, “Effect of selective laser melting process parameters and aging heat treatment on properties of CuCrZr alloy,” *Materials Research Express*, vol. 6, no. 11, p. 1165c1, Oct. 2019, doi: 10.1088/2053-1591/ab4e2f.
- [117] T. Wegener, J. Koopmann, J. Richter, P. Krooß, and T. Niendorf, “CuCrZr processed by laser powder bed fusion—Processability and influence of heat treatment on electrical conductivity, microstructure and mechanical properties,” *Fatigue and Fracture of Engineering Materials and Structures*, vol. 44, no. 9, pp. 2570–2590, 2021, doi: 10.1111/ffe.13527.
- [118] Y. Bai, C. Zhao, Y. Zhang, J. Chen, and H. Wang, “Additively manufactured CuCrZr alloy: Microstructure, mechanical properties and machinability,” *Materials Science and Engineering A*, vol. 819, no. May, p. 141528, 2021, doi: 10.1016/j.msea.2021.141528.

- [119] S. D. Jadhav *et al.*, “Modification of Electrical and Mechanical Properties of Selective Laser-Melted CuCr0.3 Alloy Using Carbon Nanoparticles,” *Advanced Engineering Materials*, vol. 22, no. 2, pp. 1–14, 2020, doi: 10.1002/adem.201900946.
- [120] S. D. Jadhav *et al.*, “Laser powder bed fusion additive manufacturing of highly conductive parts made of optically absorptive carburized CuCr1 powder,” *Materials and Design*, vol. 198, p. 109369, 2021, doi: 10.1016/j.matdes.2020.109369.
- [121] “Energy Production and Consumption - Our World in Data.” <https://ourworldindata.org/energy-production-consumption> (accessed Mar. 14, 2022).
- [122] S. Li, H. Jiang, Z. Ren, and C. Xu, “Optimal Tracking for a Divergent-Type Parabolic PDE System in Current Profile Control,” 2014, doi: 10.1155/2014/940965.
- [123] A. Mimo, “Optimization of Caesium Dynamics in Large and Powerful RF Sources for Negative Hydrogen Ions,” 2018.
- [124] R. Koch, “Fast Particle Heating,” *Fusion Science and Technology*, vol. 57, no. 2T, pp. 185–195, Feb. 2010, doi: 10.13182/FST10-A9409.
- [125] P. Agostinetti *et al.*, “Detailed design optimization of the MITICA negative ion accelerator in view of the ITER NBI,” *Nuclear Fusion*, vol. 56, no. 1, p. 16015, 2016, doi: 10.1088/0029-5515/56/1/016015.
- [126] R. Nocentini, R. Gutser, B. Heinemann, M. Fröschele, and R. Riedl, “Optimization of the cooling circuit and thermo-mechanical analysis for the extraction grid of ELISE,” *Fusion Engineering and Design*, vol. 86, no. 6–8, pp. 916–919, 2011, doi: 10.1016/j.fusengdes.2011.01.147.
- [127] P. Agostinetti, G. Chitarin, G. Gambetta, and D. Marcuzzi, “Two key improvements to enhance the thermo-mechanic performances of accelerator grids for neutral beam injectors,” *Fusion Engineering and Design*, vol. 109–111, pp. 890–894, 2016, doi: 10.1016/j.fusengdes.2016.01.056.
- [128] P. Agostinetti *et al.*, “Thermo-mechanical design of the ITER neutral beam injector grids for radio frequency ion source and SINGAP accelerator,” *Proceedings - Symposium on Fusion Engineering*, pp. 4–7, 2007, doi: 10.1109/FUSION.2007.4337905.

- [129] P. Agostinetti, G. Chitarin, N. Marconato, D. Marcuzzi, and A. Rizzolo, "Manufacturing and testing of grid prototypes for the ITER neutral beam injectors," *IEEE Transactions on Plasma Science*, vol. 42, no. 3, pp. 628–632, 2014. doi: 10.1109/TPS.2013.2296743.
- [130] ASTM, "B213-17: Standard Test Methods for Flow Rate of Metal Powders Using the Hall Flowmeter," *ASTM Standards*, pp. 1–4, 2017, doi: 10.1520/B0213-17.2.
- [131] ASTM International, "B212-17: Standard Test Method for Apparent Density of Free-Flowing Metal Powders Using the Hall Flowmeter Funnel 1," *ASTM Standard*, vol. 99, no. Reapproved 2006, pp. 1–4, 2013, doi: 10.1520/B0212-17.2.
- [132] ASTM, "ASTM B311-17: Standard Test Method for Density of Powder Metallurgy (PM) Materials Containing Less Than Two Percent Porosity," *ASTM International*, pp. 1–5, 2019, doi: 10.1520/B0311-17.2.
- [133] D. R. Lide and ed., *CRC Handbook of Chemistry and Physics, Internet Version 2005*. Boca Raton, FL, 2005. doi: 10.1201/9781315380476-3.
- [134] C. G. Klingaa, M. K. Bjerre, S. Baier, L. de Chiffre, S. Mohanty, and J. H. Hattel, "Roughness Investigation of SLM Manufactured Conformal Cooling Channels Using X-ray Computed Tomography," *e-Journal of Nondestructive Testing*, no. 03, 2019, [Online]. Available: <https://www.ndt.net/search/docs.php3?showForm=off&id=23739>
- [135] Y. He, "Rapid thermal conductivity measurement with a hot disk sensor: Part 1. Theoretical considerations," *Thermochimica Acta*, vol. 436, no. 1–2, pp. 122–129, 2005, doi: 10.1016/j.tca.2005.06.026.
- [136] "Hall Effect Measurements | NIST." <https://www.nist.gov/pml/nanoscale-device-characterization-division/popular-links/hall-effect> (accessed Mar. 04, 2022).
- [137] ASTM E8, "ASTM E8/E8M standard test methods for tension testing of metallic materials 1," *Annual Book of ASTM Standards 4*, no. C, pp. 1–27, 2010, doi: 10.1520/E0008.

- [138] International Organization for Standardization, “ISO 4288:1998. Geometrical Product Specifications (GPS) - Surface texture: Profile method - Rules and procedures for the assessment of surface texture,” *Geometrical product specifications (GPS)*, vol. 1998, no. 1, p. 4288, 1998.
- [139] I. 25178-1, “BSI Standards Publication Geometrical product specifications (GPS) — Surface texture : Areal Part 1 : Indication of surface texture,” 2016.
- [140] S. Vock, B. Klöden, A. Kirchner, T. Weißgärber, and B. Kieback, “Powders for powder bed fusion: a review,” *Progress in Additive Manufacturing*, vol. 0, no. 0, p. 0, 2019, doi: 10.1007/s40964-019-00078-6.
- [141] J. H. Tan, W. L. E. Wong, and K. W. Dalgarno, “An overview of powder granulometry on feedstock and part performance in the selective laser melting process,” *Additive Manufacturing*, vol. 18, no. October, pp. 228–255, 2017, doi: 10.1016/j.addma.2017.10.011.
- [142] A. B. Spierings and G. Levy, “Comparison of density of stainless steel 316L parts produced with selective laser melting using different powder grades,” in *Proceedings of the Annual International Solid Freeform Fabrication Symposium*, 2009, pp. 1–12.
- [143] A. B. Spierings, N. Herres, and G. Levy, “Influence of the particle size distribution on surface quality and mechanical properties in additive manufactured stainless steel parts,” *21st Annual International Solid Freeform Fabrication Symposium - An Additive Manufacturing Conference, SFF 2010*, pp. 397–406, 2010.
- [144] M. Rombouts, L. Froyen, A. v. Gusarov, E. H. Bentefour, and C. Glorieux, “Photopyroelectric measurement of thermal conductivity of metallic powders,” *Journal of Applied Physics*, vol. 97, no. 2, 2005, doi: 10.1063/1.1832740.
- [145] M. Meisnar, S. Baker, C. Fowler, L. Pambaguian, and T. Ghidini, “Lessons learnt through the development of an application-specific methodology for metal powder characterisation for additive manufacturing,” *Proceedings Euro PM 2017: International Powder Metallurgy Congress and Exhibition*, pp. 3–9, 2017.

- [146] E. Santecchia, S. Spigarelli, and M. Cabibbo, “Material reuse in laser powder bed fusion: Side effects of the laser—metal powder interaction,” *Metals*, vol. 10, no. 3, pp. 1–21, 2020, doi: 10.3390/met10030341.
- [147] V. Seyda, N. Kaufmann, and C. Emmelmann, “Investigation of Aging Processes of Ti-6Al-4 v Powder Material in Laser Melting,” *Physics Procedia*, vol. 39, pp. 425–431, 2012, doi: 10.1016/j.phpro.2012.10.057.
- [148] S. Hoeges, A. Zwiren, and C. Schade, “Additive manufacturing using water atomized steel powders,” *Metal Powder Report*, vol. 72, no. 2, pp. 111–117, 2017, doi: 10.1016/j.mprp.2017.01.004.
- [149] R. Li, Y. Shi, Z. Wang, L. Wang, J. Liu, and W. Jiang, “Densification behavior of gas and water atomized 316L stainless steel powder during selective laser melting,” *Applied Surface Science*, vol. 256, no. 13, pp. 4350–4356, 2010, doi: 10.1016/j.apsusc.2010.02.030.
- [150] H. J. Niu and I. T. H. Chang, “Selective laser sintering of gas and water atomized high speed steel powders,” *Scripta Materialia*, vol. 41, no. 1, pp. 25–30, 1999, doi: 10.1016/S1359-6462(99)00089-5.
- [151] S. E. Brika, M. Letenneur, C. A. Dion, and V. Brailovski, “Influence of particle morphology and size distribution on the powder flowability and laser powder bed fusion manufacturability of Ti-6Al-4V alloy,” *Additive Manufacturing*, vol. 31, no. November 2019, p. 100929, 2020, doi: 10.1016/j.addma.2019.100929.
- [152] M. Khan and P. Dickens, “Selective laser melting (SLM) of gold (Au),” *Rapid Prototyping Journal*, vol. 18, no. 1, pp. 81–94, Jan. 2012, doi: 10.1108/13552541211193520.
- [153] A. Simchi, “The role of particle size on the laser sintering of iron powder,” *Metallurgical and Materials Transactions B: Process Metallurgy and Materials Processing Science*, vol. 35, no. 5, pp. 937–948, 2004, doi: 10.1007/s11663-004-0088-3.
- [154] ASTM, “ASTM B214-16: Standard Test Method for Sieve Analysis of Metal Powders,” *ASTM Interational*, pp. 1–4, 2016, doi: 10.1520/B0214-16.2.

- [155] ASTM, “ASTM B822-02: Standard Test Method for Particle Size Distribution of Metal Powders and Related Compounds by Light Scattering 1,” *ASTM Interational*, pp. 1–3, 2019, doi: 10.1520/B0822-02.2.
- [156] G. Favero, M. Bonesso, P. Rebesan, R. Dima, A. Pepato, and S. Mancin, “Additive manufacturing for thermal management applications: from experimental results to numerical modeling,” *International Journal of Thermofluids*, vol. 10, p. 100091, 2021, doi: 10.1016/j.ijft.2021.100091.
- [157] D. Chapman, “High Conductivity Coppers for Electrical Engineering,” *Anti-Corrosion Methods and Materials*, vol. 46, no. 2, 1999, doi: 10.1108/acmm.1999.12846bae.001.
- [158] A. B. Spierings, M. Voegtlin, T. Bauer, and K. Wegener, “Powder flowability characterisation methodology for powder-bed-based metal additive manufacturing,” *Progress in Additive Manufacturing*, vol. 1, no. 1–2, pp. 9–20, 2016, doi: 10.1007/s40964-015-0001-4.
- [159] R. Engeli, T. Etter, S. Hövel, and K. Wegener, “Processability of different IN738LC powder batches by selective laser melting,” *Journal of Materials Processing Technology*, vol. 229, pp. 484–491, 2016, doi: 10.1016/j.jmatprotec.2015.09.046.
- [160] A. N. D. Gasper *et al.*, “Spatter and oxide formation in laser powder bed fusion of Inconel 718,” *Additive Manufacturing*, vol. 24, no. September, pp. 446–456, 2018, doi: 10.1016/j.addma.2018.09.032.
- [161] Z. Dong, Y. Liu, W. Wen, J. Ge, and J. Liang, “Effect of hatch spacing on melt pool and as-built quality during selective laser melting of stainless steel: Modeling and experimental approaches,” *Materials*, vol. 12, no. 1, 2018, doi: 10.3390/ma12010050.
- [162] H. W. Mindt, M. Megahed, N. P. Lavery, M. A. Holmes, and S. G. R. Brown, “Powder Bed Layer Characteristics: The Overseen First-Order Process Input,” *Metallurgical and Materials Transactions A: Physical Metallurgy and Materials Science*, vol. 47, no. 8, pp. 3811–3822, 2016, doi: 10.1007/s11661-016-3470-2.
- [163] T. M. Wischeropp, C. Emmelmann, M. Brandt, and A. Pateras, “Measurement of actual powder layer height and packing density in a single layer in selective laser melting,” *Additive Manufacturing*, vol. 28, no. April, pp. 176–183, 2019, doi: 10.1016/j.addma.2019.04.019.

- [164] C. Vincent, J. F. Silvain, J. M. Heintz, and N. Chandra, "Effect of porosity on the thermal conductivity of copper processed by powder metallurgy," *Journal of Physics and Chemistry of Solids*, vol. 73, no. 3, pp. 499–504, 2012, doi: 10.1016/j.jpics.2011.11.033.
- [165] J. v. Gordon *et al.*, "Defect structure process maps for laser powder bed fusion additive manufacturing," *Additive Manufacturing*, vol. 36, p. 101552, 2020, doi: 10.1016/j.addma.2020.101552.
- [166] S. R. Pogson, P. Fox, C. J. Sutcliffe, and W. O'Neill, "The production of copper parts using DMLR," *Rapid Prototyping Journal*, vol. 9, no. 5, pp. 334–343, 2003, doi: 10.1108/13552540310502239.
- [167] J. A. Cherry, H. M. Davies, S. Mehmood, N. P. Lavery, S. G. R. Brown, and J. Sienz, "Investigation into the effect of process parameters on microstructural and physical properties of 316L stainless steel parts by selective laser melting," *International Journal of Advanced Manufacturing Technology*, vol. 76, no. 5–8, pp. 869–879, 2015, doi: 10.1007/s00170-014-6297-2.
- [168] T. Ronneberg, C. M. Davies, and P. A. Hooper, "Revealing relationships between porosity, microstructure and mechanical properties of laser powder bed fusion 316L stainless steel through heat treatment," *Materials and Design*, vol. 189, p. 108481, 2020, doi: 10.1016/j.matdes.2020.108481.
- [169] H. Ali, H. Ghadbeigi, and K. Mumtaz, "Effect of scanning strategies on residual stress and mechanical properties of Selective Laser Melted Ti6Al4V," *Materials Science and Engineering A*, vol. 712, no. December 2017, pp. 175–187, 2018, doi: 10.1016/j.msea.2017.11.103.
- [170] C. Phutela, N. T. Aboulkhair, C. J. Tuck, and I. Ashcroft, "The effects of feature sizes in selectively laser melted Ti-6Al-4V parts on the validity of optimised process parameters," *Materials*, vol. 13, no. 1, p. 117, 2020, doi: 10.3390/ma13010117.
- [171] M. F. Zaeh and G. Branner, "Investigations on residual stresses and deformations in selective laser melting," *Production Engineering*, vol. 4, no. 1, pp. 35–45, 2010, doi: 10.1007/s11740-009-0192-y.
- [172] O. Gokcekaya *et al.*, "Effect of scan length on densification and crystallographic texture formation of pure chromium fabricated by laser powder bed fusion," *Crystals*, vol. 11, no. 1, pp. 1–14, Dec. 2021, doi: 10.3390/cryst11010009.

- [173] B. S. Yilbas, K. Danisman, and Z. Yilbas, "Measurement of temperature-dependent reflectivity of Cu and Al in the range 30-1000 degrees C," *Measurement Science and Technology*, vol. 2, no. 7, pp. 668–674, 1991, doi: 10.1088/0957-0233/2/7/016.
- [174] P. Lykov, R. Baytimerov, S. Vaulin, E. Safonov, and D. Zhrebtsov, "Selective Laser Melting of Copper by 200 W CO2 Laser," *SAE Technical Papers*, pp. 2–5, 2016, doi: 10.4271/2016-01-0333.
- [175] S. M. Yusuf, E. Choo, and N. Gao, "Comparison between virgin and recycled 316l ss and alsi10mg powders used for laser powder bed fusion additive manufacturing," *Metals*, vol. 10, no. 12, pp. 1–18, 2020, doi: 10.3390/met10121625.
- [176] F. Yi, Q. Zhou, C. Wang, Z. Yan, and B. Liu, "Effect of powder reuse on powder characteristics and properties of Inconel 718 parts produced by selective laser melting," *Journal of Materials Research and Technology*, vol. 13, pp. 524–533, 2021, doi: 10.1016/j.jmrt.2021.04.091.
- [177] J. Zhang *et al.*, "Comparison of virgin and reused 15-5 PH stainless steel powders for laser powder bed fusion process," *Progress in Additive Manufacturing*, vol. 3, no. 1–2, pp. 11–14, 2018, doi: 10.1007/s40964-018-0038-2.
- [178] Q. B. Nguyen, M. L. S. Nai, Z. Zhu, C. N. Sun, J. Wei, and W. Zhou, "Characteristics of Inconel Powders for Powder-Bed Additive Manufacturing," *Engineering*, vol. 3, no. 5, pp. 695–700, 2017, doi: 10.1016/J.ENG.2017.05.012.
- [179] A. H. Maamoun, M. Elbestawi, G. K. Dosbaeva, and S. C. Veldhuis, "Thermal post-processing of AlSi10Mg parts produced by Selective Laser Melting using recycled powder," *Additive Manufacturing*, vol. 21, no. May, pp. 234–247, 2018, doi: 10.1016/j.addma.2018.03.014.
- [180] F. del Re *et al.*, "Statistical approach for assessing the effect of powder reuse on the final quality of AlSi10Mg parts produced by laser powder bed fusion additive manufacturing," *International Journal of Advanced Manufacturing Technology*, vol. 97, no. 5–8, pp. 2231–2240, 2018, doi: 10.1007/s00170-018-2090-y.

- [181] M. R. Pinnel, H. G. Tompkins, and D. E. Heath, "Oxidation of copper in controlled clean air and standard laboratory air at 50°C to 150°C," *Applications of Surface Science*, vol. 2, no. 4, pp. 558–577, 1979, doi: 10.1016/0378-5963(79)90047-3.
- [182] C. Zhong, Y. M. Jiang, Y. F. Luo, B. Deng, L. Zhang, and J. Li, "Kinetics characterization of the oxidation of Cu thin films at low temperature by using sheet resistance measurement," *Applied Physics A: Materials Science and Processing*, vol. 90, no. 2, pp. 263–266, 2008, doi: 10.1007/s00339-007-4259-3.
- [183] S. Choudhary *et al.*, "Oxidation mechanism of thin Cu films: A gateway towards the formation of single oxide phase," *AIP Advances*, vol. 8, no. 5, 2018, doi: 10.1063/1.5028407.
- [184] Y. Unutulmazsoy, C. Cancellieri, M. Chiodi, S. Siol, L. Lin, and L. P. H. Jeurgens, "In situ oxidation studies of Cu thin films: Growth kinetics and oxide phase evolution," *Journal of Applied Physics*, vol. 127, no. 6, 2020, doi: 10.1063/1.5131516.
- [185] W. Yu, S. L. Sing, C. K. Chua, and X. Tian, "Influence of re-melting on surface roughness and porosity of AlSi10Mg parts fabricated by selective laser melting," *Journal of Alloys and Compounds*, vol. 792, pp. 574–581, 2019, doi: 10.1016/j.jallcom.2019.04.017.
- [186] S. J. Raab, R. Guschlbauer, M. A. Lodes, and C. Körner, "Thermal and Electrical Conductivity of 99.9% Pure Copper Processed via Selective Electron Beam Melting," *Advanced Engineering Materials*, vol. 18, no. 9, pp. 1661–1666, 2016, doi: 10.1002/adem.201600078.
- [187] J. M. Jeon *et al.*, "Effects of microstructure and internal defects on mechanical anisotropy and asymmetry of selective laser-melted 316L austenitic stainless steel," *Materials Science and Engineering A*, vol. 763, no. March, p. 138152, 2019, doi: 10.1016/j.msea.2019.138152.
- [188] M. R. Condruz, G. Matache, and A. Paraschiv, "Characterization of in 625 recycled metal powder used for selective laser melting," *Manufacturing Review*, vol. 7, pp. 1–8, 2020, doi: 10.1051/mfreview/2020002.

- [189] J. Guan, X. Zhang, Y. Jiang, and Y. Yan, "Insights into fabrication mechanism of pure copper thin wall components by selective infrared laser melting," *Rapid Prototyping Journal*, vol. 25, no. 8, pp. 1388–1397, 2019, doi: 10.1108/RPJ-06-2018-0143.
- [190] F. Sun, P. Liu, X. Chen, H. Zhou, P. Guan, and B. Zhu, "Mechanical Properties of High-Strength Cu–Cr–Zr Alloy Fabricated by Selective Laser Melting," *Materials*, vol. 13, no. 21, p. 5028, Nov. 2020, doi: 10.3390/ma13215028.
- [191] K. Gururaj and S. Pal, "Influence of dislocation density and grain size on precipitation kinetics on P92 grade steel," *Materials Today: Proceedings*, vol. 18, pp. 1364–1374, 2019, doi: 10.1016/j.matpr.2019.06.602.
- [192] S. Zhang, H. Zhu, L. Zhang, W. Zhang, H. Yang, and X. Zeng, "Microstructure and properties of high strength and high conductivity Cu-Cr alloy components fabricated by high power selective laser melting," *Materials Letters*, vol. 237, pp. 306–309, 2019, doi: 10.1016/j.matlet.2018.11.118.
- [193] M. Doubenskaia, A. Domashenkov, I. Smurov, and P. Petrovskiy, "Study of Selective Laser Melting of intermetallic TiAl powder using integral analysis," *International Journal of Machine Tools and Manufacture*, vol. 129, no. August 2017, pp. 1–14, 2018, doi: 10.1016/j.ijmactools.2018.02.003.
- [194] B. Vandenbroucke and J. P. Kruth, "Selective laser melting of biocompatible metals for rapid manufacturing of medical parts," *Rapid Prototyping Journal*, vol. 13, no. 4, pp. 196–203, 2007, doi: 10.1108/13552540710776142.
- [195] A. Triantaphyllou *et al.*, "Surface texture measurement for additive manufacturing," *Surface Topography: Metrology and Properties*, vol. 3, no. 2, 2015, doi: 10.1088/2051-672X/3/2/024002.
- [196] P. B. Bacchewar, S. K. Singhal, and P. M. Pandey, "Statistical modelling and optimization of surface roughness in the selective laser sintering process," *Proceedings of the Institution of Mechanical Engineers, Part B: Journal of Engineering Manufacture*, vol. 221, no. 1, pp. 35–52, 2007, doi: 10.1243/09544054JEM670.

- [197] G. Strano, L. Hao, R. M. Everson, and K. E. Evans, "Surface roughness analysis, modelling and prediction in selective laser melting," *Journal of Materials Processing Technology*, vol. 213, no. 4, pp. 589–597, 2013, doi: 10.1016/j.jmatprotec.2012.11.011.
- [198] Y. Tian, D. Tomus, P. Rometsch, and X. Wu, "Influences of processing parameters on surface roughness of Hastelloy X produced by selective laser melting," *Additive Manufacturing*, vol. 13, pp. 103–112, 2017, doi: 10.1016/j.addma.2016.10.010.
- [199] F. Cabanettes *et al.*, "Topography of as built surfaces generated in metal additive manufacturing: A multi scale analysis from form to roughness," *Precision Engineering*, vol. 52, no. October 2017, pp. 249–265, 2018, doi: 10.1016/j.precisioneng.2018.01.002.
- [200] T. Yang *et al.*, "The influence of process parameters on vertical surface roughness of the AlSi10Mg parts fabricated by selective laser melting," *Journal of Materials Processing Technology*, vol. 266, no. July 2018, pp. 26–36, 2019, doi: 10.1016/j.jmatprotec.2018.10.015.
- [201] L. Wan *et al.*, "Parameter optimization of selective laser melting fabricated titanium alloy using skin-core and triple contour scanning strategy," *Journal of Laser Applications*, vol. 32, no. 4, p. 042001, 2020, doi: 10.2351/7.0000180.
- [202] G. Gambetta, "DEVELOPMENT, OPTIMIZATION AND TESTING OF HIGH PERFORMANCE COOLING SYSTEMS FOR FUSION DEVICES," 2018.